JSCSEN 80(1)1–125(2015)

ISSN 1820-7421(Online)

Journal of the Serbian Chemical Society

Volume 80 : : 2015 : : 85 Years of the Journal

1930 Glasnik Hemijskog Društva Kraljevine Jugoslavije
Journal of the Chemical Society of the Kingdom of Yugoslavia
1947 Glasnik hemijskog društva Beograd
Journal of the Chemical Society of Belgrade
1985 Journal of the Serbian Chemical Society

VOLUME 80

No 1

BELGRADE 2015

Available on line at
www.shd.org.rs/JSCS/

Journal of
the Serbian Chemical Society
eVersion electronic
JSCS-info@shd.org.rs • www.shd.org.rs/JSCS

J. Serb. Chem. Soc. Vol. 80, No. 1 (2015)

CONTENTS

Biochemistry and Biotechnology

Inorganic Chemistry

Theoretical Chemistry

Physical Chemistry

Electrochemistry

Analytical Chemistry

Polymers

Materials

Environmental

Published by the Serbian Chemical Society
Karnegijeva 4/III, P.O. Box 36, 11120 Belgrade, Serbia
Printed by the Faculty of Technology and Metallurgy
Karnegijeva 4, P.O. Box 35-03, 11120 Belgrade, Serbia

Journal of the Serbian Chemical Society

JSCS-info@shd.org.rs • www.shd.org.rs/JSCS

J. Serb. Chem. Soc. *80* (1) 1–8 (2015)
JSCS–4691

UDC 582.282.123.4:547.26’11+577.152.3+
543.24:665.327.3
Original scientific paper

Optimization of the fermentation conditions and substrate specifity of mycelium-bound ester hydrolases of *Aspergillus oryzae* Cs007

HONG DE YAN*, HONG CAI LIU and ZHAO WANG

College of Biological and Environmental Engineering, Zhejiang University of Technology, 310014 Hangzhou, People’s Republic of China

(Received 1 April, revised 6 July, accepted 7 July 2014)

Abstract: In order to improve the activities of mycelium-bound ester hydrolases of *Aspergillus oryzae* Cs007, the main production conditions were investigated. The activities of the ester hydrolases were simultaneously determined by titration assay and spectrophotometric assay methods, using olive oil and *p*-nitrophenyl esters as substrates, respectively. The optimum carbon source and nitrogen source were olive oil and peptone, at concentrations of 1 and 2.2 %, respectively. The effects of the carbon source, the nitrogen source and their concentrations on the production of the enzymes were identical when the enzymes activities were assayed by the two methods. The mycelium-bound enzymes showed hydrolytic activity toward all the tested *p*-nitrophenyl esters, triglycerides and fatty acid ethyl esters, but it showed greater preference for long-chain triglycerides and short-chain *p*-nitrophenyl esters.

Keywords: ester hydrolases; lipases; carboxylesterases; *Aspergillus oryzae*; *p*-nitrophenyl esters; olive oil.

INTRODUCTION

Ester hydrolases represent a diverse group of enzymes that catalyze the cleavage and formation of ester bonds. Two typical and important classes of ester hydrolases are lipases (EC3.1.1.3, triacylglycerol hydrolases) and carboxylesterases (EC3.1.1.1, carboxyl ester hydrolases). Lipases can be distinguished from other ester hydrolases by the phenomenon of interfacial activation, which is a unique characteristic for lipases. Furthermore, lipases prefer water-insoluble substrates, typically triglycerides composed of long-chain fatty acids, whereas carboxylesterases preferentially hydrolyze “simple” esters (*e.g.* ethyl acetate) and usually only triglycerides bearing fatty acids shorter than C6.[1] The most reported of the reactions realized by ester hydrolases, especially by lipases or carboxyl-

---

* Corresponding author. E-mail: yanhongde@zjut.edu.cn

doi: 10.2298/JSC140401071D

esterases, are hydrolysis, esterification, alcoholysis, acidolysis, transesterification and aminolysis. In addition, lipases or carboxylesterases show high regio- and stereospecificity. These make them attractive biocatalysts for use in detergent formulation,[2–5] food ingredients,[3–5] the pulp and paper industry,[3–5] the production of cosmetics,[4,5] biofuels production[4–6] and the synthesis of enantiopure compounds.[1,3,4,7–11] Ester hydrolases widely exist in animals, plants and microorganisms. However, the most frequently used ester hydrolases are of microbial origin, mainly bacteria[1,3,4,6,11–13] and fungi.[1,3–6] *Aspergillus oryzae* are one of the common fungal producers of ester hydrolases. In particular, they have the ability to produce extracellular and intracellular enzymes. A strain of *A. oryzae* WZ007 was isolated from soil that produced ester hydrolases showing high stereospecificity, which was used for the resolution of a biotin intermediate,[14] α-lipoic acid[15] and ethyl 2-(4-hydroxyphenoxy)propanoate.[16] In addition, it was a promising biocatalyst in the synthesis of flavour esters.[17] A mutant strain of *A. oryzae* Cs007 was obtained by ^{137}Cs gamma radiation of strain WZ007 that displayed high mycelium-bound ester hydrolases activity. To further improve production by the mycelium-bound ester hydrolases Cs007, the most important fermentation factors, including carbon source, nitrogen source and production time, were investigated in detail. Then the substrate specificities of the mycelium-bound enzymes for three typical esters, *i.e.*, *p*-nitrophenyl (*p*-NP) esters, triglycerides and straight-chain fatty acid ethyl esters, were investigated. To the best of our knowledge, most studies of the ester hydrolases from *A. oryzae* investigated systems with extracellular enzymes in the fermentation liquid. Mycelium-bound hydrolases were considered in only a few studies[14–17] and a mycelium-bound carboxylesterase, responsible for catalyzing ester synthesis in another.[18] Mycelium-bound enzymes could be conveniently used without additional immobilization. Therefore, it is very important to improve production by such bound enzymes.

EXPERIMENTAL

Chemicals

p-Nitrophenyl acetate (*p*-NPA), *p*-nitrophenyl octanoate (*p*-NPO) and *p*-nitrophenyl palmitate (*p*-NPP) were purchased from Alfa (Ward Hill, MA). *p*-Nitrophenyl butyrate (*p*-NPB) was purchased from Sigma (St. Louis, MO). Corn oil and soybean oil were purchased from a local supermarket. All other chemicals were of the highest commercially available purity.

Microorganism, medium and growth conditions

A. oryzae Cs007, a mutant strain, was obtained by ^{137}Cs gamma radiation of *A. oryzae* WZ007, which was isolated from soil samples and stored in the China Center for Type Culture Collection with the accession number of CCTCC No. M206105.[14] The microorganisms were maintained on potato slant medium consisting of potato 200 g L^{-1}, sucrose 20 g L^{-1} and agar 20 g L^{-1}. Shake flask culturing was performed in a 250 mL Erlenmeyer flask containing 50 mL of the medium. The basal medium was composed of glucose 10 g L^{-1}, peptone 10 g L^{-1}, KH_2PO_4 1 g L^{-1}, $MgSO_4$ 0.5 g L^{-1}, NaCl 0.5 g L^{-1} and gum arabic 4 g L^{-1} with an initial pH of 5. The basal medium was supplemented with a range of carbon sources, mainly sucrose, maltose, starch, glycerol, olive oil, soybean oil and corn oil, which were screened to examine their capacities to support the growth of *A. oryzae* Cs007 and the production of enzymes. Each carbon source was added into the basal medium at a concentration of 10 g L^{-1} instead of glucose. Suspensions of spores of *A. oryzae* Cs007 with about 10^6 spores per millilitre were used as inoculums. The culture was incubated at 30 °C for 48 h on a rotatory shaker maintained at 200 rpm. The fermentation cultures were filtered through cotton gauze. The mycelia were washed with distilled water two times and used as the crude mycelium-bound enzymes sample.

Biomass measurement

The amount of biomass was determined by the dry weight of mycelia. The fermentation cultures were filtered through cotton gauze. The mycelia were washed two times with distilled water and then dried to a constant weight at 100 °C.

Ester hydrolases activity

Spectrophotometric assay (p-NPA assay). The ester hydrolases activity was assayed with spectrophotometric method using *p*-NPA as substrate, according to a modified version of the Moreau method.[19] The reaction mixture consisting of 0.1 mL of 30 mM *p*-NPA in acetonitrile, 2.8 mL of 50 mM Tris–HCl buffer (pH 7.5) and 20 mg wet-mycelia was incubated at 40 °C for 3 min. The released *p*-nitrophenol was measured at 405 nm in a spectrophotometer. One unit of enzyme activity was defined as the amount of enzyme required to release 1 μmol of *p*-nitrophenol per min under the assay conditions.

Titration assay (olive oil assay). The titration assay method was used according to the Watanabe method with some modifications.[20] An olive oil emulsion was prepared by mixing 50 mL of olive oil and 150 mL of 4 % poly(vinyl alcohol) solution (*Mw* = 1750±50, Sinopharm Chemical Reagent Co., Ltd., Shanghai, China). The poly(vinyl alcohol) solution was prepared by dissolving poly(vinyl alcohol) in 50 mM phosphate buffer (pH 7.5). Prior to the assay, the olive oil emulsion was homogenized. The reaction mixture containing 5 mL of olive oil emulsion, 4 mL of 50 mM phosphate buffer (pH 7.5) and 50 mg wet-mycelia was incubated at 40 °C and 150 rpm for 10 min on a shaker. The enzyme reaction was terminated by adding 15 mL of ethanol to the reaction mixture. Then the liberated free fatty acids were titrated with 0.05 M NaOH. One unit of enzyme activity was defined as the amount of enzyme required to liberate 1 μmol of fatty acid per minute under the assay conditions.

Substrate specificity

Hydrolysis of p-NP esters. Substrate specificities of the ester hydrolases of *A. oryzae* Cs007 for *p*-NP esters were determined by a spectrophotometric method[19,21] using the following *p*-NP esters with different chain length of fatty acids: *p*-NPA (C2), *p*-NPB (C4), *p*-NPO (C8) and *p*-NPP (C16). The solutions of *p*-NPA and *p*-NPB were prepared by adding 0.1 mL of 10 mM *p*-NP esters in acetonitrile into 2.8 mL of 50 mM Tris–HCl buffer (pH 7.5). The solutions of *p*-NPO and *p*-NPP were prepared by adding 0.1 mL of solution A (10 mM *p*-NP esters in acetonitrile) into 2.8 mL of solution B (2.22 g of Triton X-100 in 500 mL of 50 mM Tris–HCl buffer, pH 7.5). The reaction mixtures consisting of 2.9 mL of *p*-NP esters solution and 20 mg wet-mycelia were incubated at 40 °C for the appropriate time.

Hydrolysis of triglycerides and fatty acid ethyl esters. Substrate specificities of the ester hydrolase of *A. oryzae* Cs007 for triglycerides and fatty acid ethyl esters were determined by a previously described titration method.[20] Triglycerides, including triacetin and triolein, and natural olive oil were selected as substrates. Ethyl esters of different carboxylic acid chain lengths (C_1, C_2, C_6, C_8 and C_{12}) were chosen as the substrates.

RESULTS AND DISCUSSION

Effect of carbon source

As indicated in Table I, a better growth of the strain *A. oryzae* Cs007 on oils and glycerol than on carbohydrates was observed. Olive oil gave the best enzyme production. Similarly, oils as inducers or carbon sources enhanced lipase production.[22–24] The activities of mycelium-bound ester hydrolases achieved 160.2 and 472.6 U g^{-1} biomass according to the *p*-NPA assay and olive oil assay, respectively.

TABLE I. Effect of different carbon sources on cell growth and production of mycelium-bound ester hydrolases of *A. oryzae* Cs007

Carbon source	Biomass, g L^{-1}	Enzymes activity, U g^{-1} biomass	
		p-NPA assay	Olive oil assay
Glucose	5.0	18.5	0
Sucrose	7.2	20.6	0
Maltose	5.6	20.2	0
Starch	6.4	28.5	0
Glycerol	8.4	110.0	100.2
Olive oil	10.2	160.2	472.6
Soybean oil	9.8	134.3	356.3
Corn oil	10.3	146.7	282.7

Then the optimal concentrations of olive oil for ester hydrolases production and cell growth were determined. The results are given in Table II, which indicates that the biomass increased with increasing concentrations of olive oil. The mycelium-bound ester hydrolases activities increased with increasing concentration of olive oil up to 1 % after which the enzyme activities decreased with increasing concentration of olive oil. Therefore, 1 % olive oil was used in the subsequent experiments. Significantly, the optimum carbon source and its concentration for the production of enzymes were identical when the ester hydrolases activities were assayed by two methods.

TABLE II. Effect of different concentrations of olive oil on the cell growth and production of mycelium-bound ester hydrolases by *A. oryzae* Cs007

Concentration of olive oil, %	Biomass, g L^{-1}	Enzymes activity, U g^{-1} biomass	
		p-NPA assay	Olive oil assay
0.6	5.6	50.6	134.2
0.8	8.4	104.8	378.3
1.0	10.3	160.2	472.6
1.2	11.9	138.4	400.5
1.4	14.2	121.2	245.2
1.6	15.8	70.9	233.6

Effect of nitrogen source

Using 1 % olive oil as the carbon source, various nitrogen sources including: peptone, yeast extract, beef extract, soybean powder, corn powder, ammonium sulphate and sodium nitrate were selected to investigate growth of *A. oryzae* Cs007 and the production of enzymes. Each nitrogen source was added into the basal medium at a concentration of 10 g L^{-1} instead of peptone. As indicated in Table III, the organic mixed nitrogen sources, especially peptone, yeast extract and soybean powder, resulted in excellent cell growth. However, the inorganic nitrogen sources, such as ammonium sulphate and sodium nitrate, could not be utilized for cell growth. Peptone was overwhelmingly superior to the other nitrogen sources for the production of enzymes. In particular, soybean powder was a good nitrogen source for cell growth, but not a good one for the production of enzymes, with the mycelium-bound enzymes exhibiting low activity.

TABLE III. Effect of different nitrogen sources on cell growth and production of mycelium-bound ester hydrolases by *A. oryzae* Cs007

Nitrogen source	Biomass, g L^{-1}	Enzyme activity, U g^{-1} biomass	
		p-NPA assay	Olive oil assay
Peptone	10.2	160.2	472.5
Yeast extract	9.2	45.6	150.1
Beef extract	6.2	38.8	120.6
Soybean powder	9.3	16.0	109.7
Corn powder	6.4	15.0	99.7
Ammonium sulphate	0	0	0
Sodium nitrate	0	0	0

To find the optimal concentration of peptone for cell growth and enzyme production, various concentrations of peptone from 10 to 30 g L^{-1} were investigated. The obtained results are presented in Table IV. The biomass increased with increasing the concentration of peptone to 18 g L^{-1}, reaching a constant value of about 11.6 g L^{-1} even though higher concentrations of peptone were used. Similarly, the mycelium-bound ester hydrolases activities increased with

TABLE IV. Effect of different concentrations of peptone on the cell growth and production of mycelium-bound ester hydrolases by *A. oryzae* Cs007

Concentration of peptone, g L^{-1}	Biomass, g L^{-1}	Enzymes activity, U g^{-1} biomass	
		p-NPA assay	Olive oil assay
10	10.2	160.2	472.5
14	11.0	188.5	623.3
18	11.6	363.8	1100.1
22	11.4	365.5	1150.5
26	11.8	359.7	1018.3
30	11.5	361.7	970.2

increasing the concentration of peptone to 22 g L^{-1}, achieving a maximum value of 365.5 U g^{-1} biomass by *p*-NPA assay and 1150.5 U g^{-1} biomass by olive oil assay. Thus, 22 g L^{-1} peptone was selected as the optimal concentration for the production of ester hydrolases of *A. oryzae* Cs007. The effects of the nitrogen source and its concentration on the production of the mycelium-bound enzymes were also identical when the enzymes activities were assayed by the two methods.

Time course of cell growth and the production of ester hydrolases of A. oryzae *Cs007*

The time courses of cell growth and production of ester hydrolases of *A. oryzae* Cs007 using the optimal medium are depicted in Fig. 1. The maximum biomass was obtained at 36 h. The activity of the mycelium-bound ester hydrolases showed a sharp increase from 24 to 36 h. The activity of enzymes reached maximum values at 36 h using the *p*-NPA assay but attained maximum values at 42 h using the olive oil assay. A further increase in the incubation time did not lead to increases in the activity of the enzymes and a slow decrease was evidenced up to 48 h.

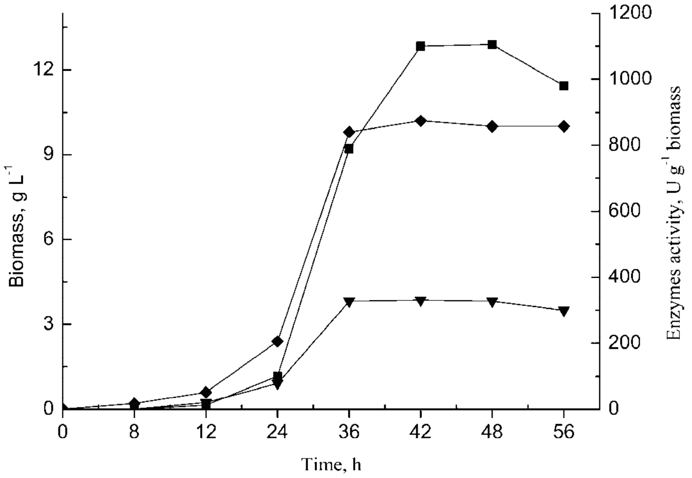

Fig. 1. Time courses of cell growth (◆), mycelium-bound ester hydrolases activity (▼) by the *p*-NPA assay and (■) by the olive oil assay of *A. oryzae* Cs007.

Substrate specificity

As shown in Table V, the mycelium-bound ester hydrolases of *A. oryzae* Cs007 showed a broad range of substrate specificities, with hydrolytic activity toward all tested *p*-NP esters, triglycerides and fatty acid ethyl esters. Of the *p*-NP esters, the enzymes showed greater preference for those with short-chain fatty acids. The highest hydrolytic activity was found toward *p*-NPA, with a specific activity of 365.5 U g^{-1} biomass. The enzymes showed the lowest hydrolysis of medium- and long-chain *p*-NP esters, such as *p*-NPO (C8) and *p*-NPP (C16). Similarly, lipases from *A. fumigatus*[25] also showed preference for *p*-NP esters with short-chain fatty acids, especially toward *p*-NPA. For triglycerides and fatty acid ethyl esters, the highest hydrolytic activity was found towards triolein with specific activity of 1975.4 U g^{-1} biomass. Moderate enzymes activities were observed towards the short-chain triglyceride (triacetin) and all the tested fatty acid ethyl esters. Of the tested fatty acid ethyl esters, ethyl caproate afforded a relatively high activity with a specific activity of 659.2 U g^{-1} biomass. The enzymes showed greater preference for long-chain triglycerides (triolein) and natural oil (olive oil). The preference of ester hydrolases of *A. oryzae* Cs007 for long-chain triglycerides may due to the hydrophobic nature of the long-chain fatty acid, which promotes helix lid opening, making the catalytic residues accessible to the substrates and exposing the hydrophobic surface of the enzyme. Thus, the enzymatic activity increased dramatically.[26]

TABLE V. Substrate specificities of mycelium-bound ester hydrolases of *A. oryzae* Cs007

Substrate	Enzymes activity, U g^{-1} biomass
p-NPA	365.5
p-NPB	238.7
p-NPO	32.9
p-NPP	44.6
Ethyl formate	394.6
Ethyl acetate	491.3
Ethyl caproate	659.2
Ethyl caprylate	559.1
Ethyl laurate	461.4
Olive oil	1150.5
Triolein	1975.4
Triacetin	395.8

CONCLUSIONS

This work showed the main production conditions and substrate specificities of mycelium-bound enzymes from *A. oryzae* Cs007. The main production conditions, including the optimum carbon and nitrogen sources, the optimal concentration of the carbon and nitrogen source and the production time, were optimized as follows. Olive oil and peptone were the optimum carbon and nitrogen source, and the optimal concentrations of the carbon and nitrogen source were 1 and 2.2 %, respectively. The activity of the enzymes reached maximum values at 36 h using the *p*-NPA assay and 42 h using the olive oil assay. The mycelium-bound enzymes showed hydrolytic activity toward all the tested *p*-NP esters, triglycerides and fatty acid ethyl esters. However, it was interesting that the enzymes preferred short-chain *p*-NP esters and long-chain triglycerides.

Acknowledgment. The authors are grateful for financial support from Zhejiang Provincial Education Department (Project No. Y201121810).

ИЗВОД

ОПТИМИЗАЦИЈА УСЛОВА ФЕРМЕНТАЦИЈЕ И СУПСТРАТНА СПЕЦИФИЧНОСТ ЕСТАРСКИХ ХИДРОЛАЗА ИЗ *Aspergillus oryzae* CS007 ВЕЗАНИХ ЗА МИЦЕЛИЈУМ

HONG DE YAN, HONG CAI LIU и ZHAO WANG

College of Biological and Environmental Engineering, Zhejiang University of Technology, 310014 Hangzhou, P. R. China

Испитивани су производни услови у циљу побољшања активности естарских хидролаза из *Aspergillus oryzae* Cs007 везаних за мицелијум. Активности естарских хидролаза су истовремено одређиване методом титрације и спектрофотометријски, користећи маслиново уље и *p*-нитрофенил естре као супстрате. Оптимални извори угљеника и азота су били маслиново уље и пептон, у концентрацијама 1, односно 2,2 %. Исти резултати су добијени применом обе методе праћења активности ензима. Ензими везани за мицелијум су испољили хидролитичку активност спрам свих тестираних *p*-нитрофенил естара, триглицерида и етил-естара масних киселина. Највећа активност је испољена спрам дуголанчаних триглицерида и кратколанчаних *p*-нитрофенил естара.

(Примљено 1. априла, ревидирано 6. јула, прихваћено 7. јула 2014)

REFERENCES

1. U. T. Bornscheuer, *FEMS Microbiol. Rev*. **26** (2002) 73
2. F. Hasan, A. A. Shah, S. Javed, A. Hameed, *Afr. J. Biotechnol*. **9** (2010) 4836
3. K.-E. Jaeger, M. T. Reetz, *Trends Biotechnol*. **16** (1998) 396
4. F. Hasan, A. A. Shah, A. Hameed, *Enzyme Microb. Technol*. **39** (2006) 235
5. A. K. Singh, M. Mukhopadhyay, *Appl. Biochem. Biotechnol*. **166** (2012) 486
6. A. Bajaj, P. Lohan, P. N. Jha, R. Mehrotra, *J. Mol. Catal., B* **62** (2010) 9
7. A. Ghanem, H. Y. Aboul-Enein, *Tetrahedron: Asymmetry* **15** (2004) 3331
8. A. Ghanem, H. Y. Aboul-Enein, *Chirality* **17** (2005) 1
9. H. Monti, G. Audran, *Mini-Rev. Org. Chem*. **2** (2005) 265
10. A. Ghanem, *Tetrahedron* **63** (2007) 1721
11. T. Panda, B. S. Gowrishankar, *Appl. Microbiol. Biotechnol*. **67** (2005) 160
12. J. L. Arpigny, K.-E. Jaeger, *Biochem. J*. **343** (1999) 177
13. R. Gupta, N. Gupta, P. Rathi, *Appl. Microbiol. Biotechnol*. **64** (2004) 763
14. J.-Y. Zheng, Z. Wang, Q. Zhu, Y.-J. Zhang, H.-D. Yan, *J. Mol. Catal., B* **56** (2009) 20
15. H.-D. Yan, Z. Wang, L.-J. Chen, *J. Ind. Microbiol. Biotechnol*. **36** (2009) 643
16. J.-Y. Zheng, J.-Y. Wu, Y.-J. Zhang, Z. Wang, *J. Mol. Catal., B* **97** (2013) 62
17. H.-D. Yan, Q. Zhang, Z. Wang, *Catal. Commun*. **45** (2014) 59
18. F. Molinari, R. Gandolfi, A. Converti, M. Zilli, *Enzyme Microb. Technol*. **27** (2000) 626
19. H. Moreau, A. Moulin, Y. Gargouri, J.-P. Noël, R. Verger, *Biochemistry* **30** (1991) 1037
20. N. Watanabe, Y. Ota, Y. Minoda, K. Yamada, *Agric. Biol. Chem*. **41** (1977) 1353
21. U. K. Winkler, M. Stuckmann, *J. Bacteriol*. **138** (1979) 663
22. N. Kulkarni, R. V. Gadre, *Biotechnol. Lett*. **21** (1999) 897
23. Y.-Q. He, T.-W. Tan, *J. Mol. Catal., B* **43** (2006) 9
24. R. Kaushik, S. Saran, J. Isar, R. K. Saxena, *J. Mol. Catal., B* **40** (2006) 121
25. J.-J. Shangguan, Y.-Q. Liu, F.-J. Wang, J. Zhao, L.-Q. Fan, S.-X. Li, J.-H. Xu, *Appl. Biochem. Biotechnol*. **165** (2011) 949
26. M. S. M. Ali, C. C. Yun, A. L. T. Chor, R. N. Z. R. A. Rahman, M. Basri, A. B. Salleh, *Protein J*. **31** (2012) 229.

JSCS-info@shd.org.rs • www.shd.org.rs/JSCS

J. Serb. Chem. Soc. 80 (1) 9–20 (2015)
JSCS–4692

UDC 638.27:543.544.3+66.095.23:547.466.3
Original scientific paper

An effective GC method for the determination of the fatty acid composition in silkworm pupae oil using a two-step methylation process

JUN WANG[1,2]*, WEIWEI WU[1], XUDONG WANG[1], MIN WANG[1] and FUAN WU[1,2]**

[1]School of Biotechnology, Jiangsu University of Science and Technology, Zhenjiang 212018, P. R. China and [2]Sericultural Research Institute, Chinese Academy of Agricultural Sciences, Zhenjiang 212018, P. R. China

(Received 1 April, revised 9 July, accepted 11 July 2014)

Abstract: In the search for an accurate and effective method for the determination of the fatty acid composition in silkworm pupae oils, five methylation methods were evaluated for use in the gas chromatographic (GC) quantification of fatty acid methyl esters (FAMEs). These included two one-step acid-catalyzed (H_2SO_4 and BF_3) and two one-step base-catalyzed (KOH and $NaOCH_3$) esterification processes, as well as a two-step procedure catalyzed successively by KOH and H_2SO_4. These methods were comparatively adopted to quantify FAMEs in silkworm pupae oil using GC–MS and GC and then their precision, stability and average recovery rates were validated. The results indicated that compared with the four one-step methyl esterification methods, the two-step methylation effectively improved the synthesis yield of FAMEs, conserved the agents and eliminated the usage of potential harmful reagents. The proposed GC method was validated, exhibited good accuracy and precision, and was successfully applied to the quantification of FAMEs in several varieties of silkworm pupae oils. The short analytical run time leads to low costs and a fast chromatographic procedure. In summary, two-step pretreatment had superior performance, providing technical references for the determination and analysis of fatty acids in other oils.

Keywords: fatty acid; fatty acid methyl ester; gas chromatography; silkworm pupae oil; two-step methylation.

INTRODUCTION

Recently, much attention has been given to the silkworm (*Bombyx mori* L.) pupa as a human food source due to its nutritional value, especially in some Asian countries.[1] Silkworm pupae are reported to be 30 % oil and 50 % protein; thus, approximately 133–270 tons of oil is likely to be available annually in

---

Corresponding authors. E-mails: (*) wangjun@just.edu.cn; (**) fuword@163.com
doi: 10.2298/JSC140401073W

China as byproducts of the silk industry.[2] Silkworm pupae oil is also a highly nutritional and exploitable food resource that lowers cholesterol, improves memory and serves as an anti-oxidant by eliminating free radicals in the body.[3] The fatty acid composition of silkworm pupae oil varies according to its variety and origin, usually consisting of α-linolenic, oleic, linoleic, palmitic, palmitoleic and other fatty acids, with a total of more than 75 % unsaturated fatty acids (UFAs) and approximately 20 % saturated fatty acids (SFAs).[4] Among these fatty acids, α-linolenic acid, the precursor of n-3 polyunsaturated fatty acids (n-3 PUFAs), is an essential fatty acid that is found in high concentrations in certain plant oils, such as flaxseed, walnut, and canola oils. The beneficial effects of n-3 PUFAs on normal health and chronic disease, such as the regulation of lipid levels, cardiovascular disease, and immune function were elucidated.[5] Beneficially for humans, the proportion of saturated, monounsaturated and polyunsaturated fatty acids in silkworm pupae oil tends strongly to the optimum ratio of fatty acids recommended by current nutritionists for the human body. As the fatty acid composition is a major factor that influences the properties of silkworm pupae oil, the determination of fatty acids content is important.

There are several analytical methods that could be used for the identification and quantification of fatty acids in oils. These techniques include gas chromatography–mass spectrometry (GC–MS),[6] gas chromatography (GC),[7] high-performance liquid chromatography–mass spectrometry (HPLC–MS),[8] high-performance liquid chromatography (HPLC),[9] high-performance size exclusion chromatography (HPSEC),[10] nuclear magnetic resonance (NMR),[11] Raman spectroscopy,[12] Fourier transform-infrared spectroscopy (FTIR)[13] and near-infrared spectroscopy (NIR).[14] However, GC–MS and GC are the most widely used techniques for the determination of individual fatty acid profiles and contents, respectively, in vegetable and animal oils. Several studies showed that GC–MS,[15] and GC with flame ionization detection (GC–FID)[16] are also applicable for investigating the fatty acid profiles in silkworm pupae oil.

The critical process in GC analysis of fatty acids is the required methylation of the fatty acids to obtain fatty acid methyl esters (FAMEs). Many different methylation methods are described in the literature but the most commonly used are those catalyzed by an acid, base or boron trifluoride and methylation with diazomethane, each of which have advantages and disadvantages and differ in their applicable range.[17]

For the determination of fatty acids in silkworm pupae oil by GC, acid- or base-catalyzed and boron trifluoride methylation methods were reported. The advantage of acid-catalyzed and boron trifluoride methylation, in which H_2SO_4 and BF_3 are widely used, is that free fatty acids (FFAs) can be catalyzed for esterification.[18] However, higher temperatures, usually between 60 and 90 °C, and longer reaction times, which could affect the compositions of fatty acids, easily lead to not only inaccurate results but also the occurrence of side reactions, loss of the unsaturated FAMEs and isomerization.[19] On the other hand, the advantages of base-catalyzed methylation are mild reaction conditions and fast reaction rate; however, there are two significant disadvantages. This method cannot catalyze the methyl esterification of FFAs, and the reaction must be conducted without water, which would otherwise often lead to saponification. In general, these methods are not necessarily convenient and must frequently be optimized for reaction conditions, including the catalyst and temperature. Thus, an accurate and effective method must be chosen for the methylation of fatty acids in silkworm pupae oil.

Silkworm pupae oils are lipid derivatives, so their compositions are very complex; therefore, an appropriate method is required to analyze their contents by converting both fatty acid salts and the acyl components in all lipid classes, such as triacylglycerols, phospholipids, sphingolipids, and waxes, to methyl esters using an effective esterification procedure. Recently, O'Fallon *et al.* presented a method to directly methylate fatty acids from muscle tissue, oils, and feedstuffs in aqueous solution that is based on a surprising concept, the addition of water to the fatty acid methyl ester synthesis reagents.[20] Usually, synthetic methods of FAMEs have rigorously avoided water as a matter of standard procedure. However, by adding water, the dynamics of sample preparation and methyl ester formation can be revisited, and the ideal outcome of the synthesis of FAMEs is enabled. Although the method described herein requires two steps, only one reaction tube is required. In summary, the developed protocol can simply obtain FAMEs from any sample. However, to the best of our knowledge, no report has been published concerning two-step methylation of fatty acids in silkworm pupae oil prior to GC analysis.

The aim of this work was to develop a validated method to determine the fatty acid composition in silkworm pupae oil by GC with two-step methylation. For this purpose, different varieties of silkworm pupae oils were extracted using a Soxhlet extractor, analyzed and determined by five methyl esterification methods, potassium hydroxide–methanol (KOH–MeOH), sodium methoxide–methanol ($NaOCH_3$–MeOH), sulfuric acid–methanol (H_2SO_4–MeOH), boron trifluoride–methanol (BF_3–MeOH), and a two-step methylation.

EXPERIMENTAL

Materials

Varieties of silkworm pupae including 5078, 220, 5082, HK3, and Qingsong×haoyue were supplied by the Sericultural Research Institute of the Chinese Academy of Agricultural Sciences.

The FAME standards, including methyl heptadecanoate (internal standard), methyl palmitate, methyl palmitoleate, methyl stearate, methyl oleate, methyl linoleate and methyl linolenate, were purchased from Sigma (St. Louis, MO, USA). Potassium hydroxide, methanol, BF_3–MeOH (14 %), sodium methoxide, sulfuric acid, *n*-hexane, petroleum ether, and all other reagents and solvents were of analytical grade (Sinopharm Chemical Reagent, Shanghai, China). Water was purified using an Elga Purelab Option-Q purification system (Elga Labwater, High Wycombe, Buckingham, UK) and had a minimum resistivity of 18.0 MΩ cm.

Preparation of silkworm pupae oil samples

Silkworm pupae oil was extracted with petroleum ether using the Soxhlet method. Approximately 5 g of dried silkworm chrysalis and 80 mL of petroleum ether (60–90 °C) were used in each Soxhlet extraction, which was realized at 80 °C for 8 h. After the extraction procedure, the solvents were evaporated under vacuum, and the samples were subsequently stored at 4 °C.

Different methylation methods for FAME synthesis

*Two-step methylation***.** Lipids obtained after the extraction of silkworm pupae samples were converted to the corresponding FAMEs according to the literature.[20] In this procedure, 40 μL of silkworm pupa oil was placed into 10 mL centrifuge tubes to which 0.7 mL of potassium hydroxide (10 M) solution and 5.3 mL of methanol were added. The reaction was performed at 55 °C for 1.5 h with mixing for 5 s every 20 min. After cooling to room temperature, 0.58 mL of sulfuric acid (10 M) solution was added and the reaction was continued at 55 °C for 1.5 h with mixing for 5 s every 20 min. After cooling to room temperature, 3 mL of *n*-hexane was added and mixed for 5 min. Subsequently, the tubes were centrifuged for 5 min and the extracts were removed for GC analysis.

*BF_3–MeOH methylation***.** The methods and conditions of FAME preparation were realized according to the literature.[20] In this procedure, 40 μL of silkworm pupa oil was placed into 10 mL centrifuge tubes to which 2 mL of boron trifluoride in methanol solution (14 %) was added. The tubes were reacted at 55 °C for 1.5 h, with mixing for 5 s every 20 min. Then, 2 mL of saturated sodium bicarbonate solution and 3 mL of *n*-hexane were added, and the tubes were well mixed. The extracts were removed for GC analysis.

*$NaOCH_3$–MeOH methylation***.** The methods and conditions of FAME preparation were set up according to the literature.[20] Here, 40 μL of silkworm pupa oil was placed into 10 mL centrifuge tubes to which 2 mL of 0.5 M sodium methoxide solution was added. The tubes were reacted at 55 °C for 1.5 h with mixing for 5 s every 20 min. Then, 2 mL of saturated sodium bicarbonate solution and 3 mL of *n*-hexane were added, and the tubes were well mixed. The extracts were removed for GC analysis.

KOH–MeOH methylation. The methods and conditions of FAME preparation were set up according to the literature.[21] Here, 40 μL of silkworm pupa oil was placed into 10 mL centrifugal tubes to which 3 mL of KOH–MeOH solution (0.5 M) was added. The mixture was heated at 60 °C for 15 min. After cooling to room temperature, 3 mL of *n*-hexane and 2 mL of distilled water were added and mixed thoroughly. The extracts were removed for GC analysis.

H_2SO_4–MeOH methylation. The methods and conditions of FAME preparation were set up according to the literature.[21] In this procedure, 40 μL of silkworm pupa oil was placed into 10 mL centrifugal tubes to which 2 mL of H_2SO_4–MeOH solution (1 %) was added. The mixture was heated at 70 °C for 1 h. After cooling to room temperature, 3 mL of *n*-hexane and 2 mL of distilled water were added and mixed thoroughly. The extracts were removed for GC analysis.

Analysis of FAME products by GC–MS and GC

GC–MS analysis was carried out using an Agilent 6890 gas chromatograph with a 5973 MS detector equipped with 60 m×0.25 mm, i.d. 0.25 μm/MS DB-WAX capillary column (Agilent). The following temperature ramp was used: injector at 250 °C, oven initially at 200 °C, held for 1 min and heated to 230 °C (1.5 °C min^{-1}, then held for 10 min). The characterization and identification of FAMEs from silkworm pupae oil was completed in the SCAN mode with the *m*/*z* range varied from 35 to 450. The flow rate of the nitrogen as carrier gas was 1 mL min^{-1}; manual injection; the injection volume was 1 μL.

The fatty acid composition of the FAMEs from silkworm pupae oil was determined using an Agilent 6820 gas chromatograph equipped with a Supelco capillary column (hp-innowax, Agilent, 100 m×0.25 mm, i.d. 0.20 μm), a flame ionization detector and split injection port. The initial oven temperature was 200 °C, which was held for 1 min, subsequently increased to 230 °C at 1.5 °C min^{-1} and then held for 1 min. The injector was set at 250 °C, and the detector at 280 °C. Nitrogen was used as the carrier gas at a flow rate of 1 mL min^{-1}. The split ratio was 50:1, and the sample size was 1 μL.

Statistical analysis

Triplicate experiments were performed for each parameter investigated. The standard deviation of the measurements was calculated to check the reliability of the results. Statistical analysis was performed using the ANOVA method. Significant differences ($p < 0.05$) between the means were determined.

RESULTS AND DISCUSSION

Chromatogram analysis of FAME standards

With methyl C17:0 as the internal standard, GC–FID was used to analyze quantitatively the FAME content in the five types of samples of silkworm pupae oils. The chromatogram of the FAME sample prepared using the two-step methylation of the pupae oil from silkworm variety 5078 is shown in Fig. 1 as an example and the chromatograms of the FAME samples obtained by the single-step methylation procedures of the oil from the same silkworm variety are presented in Fig. S-1 of the Supplementary material to this paper. As could be seen,

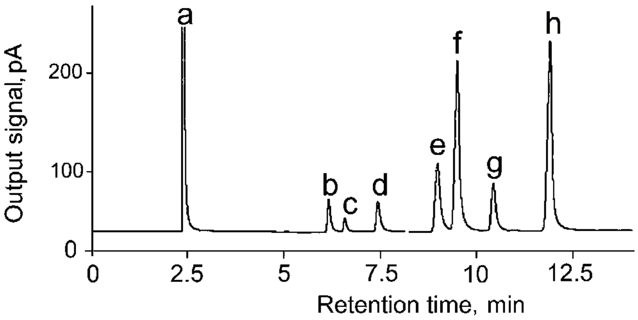

Fig. 1. GC chromatogram of FAMEs in pupae oil from silkworm variety 5078 prepared by the two-step methylation procedure. (a, *n*-hexane; b, methyl palmitate; c, methyl palmitoleate; d, methyl heptadecanoate; e, methyl stearate; f, methyl oleate; g, methyl linoleate; h, methyl linolenate).

all the main components of the samples were completely separated. The peaks were identified by comparison with the peaks of the chromatogram of the six FAME standards, which is shown in Fig. S-2 of the Supplementary material. All six FAME components, except for methyl heptadecanoate (internal standard), were also verified using MS and the obtained mass spectra are presented in Fig. S-3 (Supplementary material).

In the GC chromatograms, peaks at the same retention time represent the same compound, and the height and area of peaks directly reflect the content of each fatty acid methyl ester in the samples that indirectly responded to the effect of methyl esterification. The retention times of the FAME standards are listed in Table S-I of the Supplementary material. The results indicated that each fatty acid component in silkworm pupae oil was well separated and the analysis only took 12.5 min, avoiding thereby such problems as long analysis time and baseline drift. The short analytical run time leads to low costs and a rapid chromatographic procedure. Generally, the GC analysis method resulted in good separation, meeting both requirements of accuracy and precision.

Calibration curve for individual standards

The internal standard method was chosen as the quantification method to determine the response factor and concentration of each component present in the sample; methyl heptadecanoate was chosen as an internal standard. Response linearity was evaluated using gas chromatography, with a constant amount of the internal standard and varying amounts of the individual FAME standards. Standard FAME mixtures at different concentrations were prepared. In each standard mixture, 0.1 mg methyl heptadecanoate was added that was kept constant for all sample mixtures. Each sample preparation and subsequent injection and calculation for each concentration was performed in triplicate to verify the consistency, reliability and reproducibility of the GC method. The peak areas of the analyte and internal standard were calculated as the area ratio between the analyte and internal standard. The area ratio was plotted against the concentration ratio. The area ratios was calculated from the peak areas, which were automatically generated by the GC assistant software, and the concentration of each of FAMEs was calculated from the respective linear regression equations given in Table S-I of the Supplementary material to this paper. Table S-1 also includes the R^2 values and linear ranges for all six components. The results indicated that the six FAMEs (methyl palmitate, methyl palmitoleate, methyl stearate, methyl oleate, methyl linoleate and methyl linolenate) had good linearity ($R^2 > 0.9995$) in the ranges 1–10, 0.05–0.5, 0.25–2.5, 1–10, 0.5–2.5 and 1–10 mg mL^{-1}, respectively. Thus, the calibration curves for the individual FAME standards could be used to calculate and analyze the oil samples of silkworm pupae.

Comparison of the methylation methods for different silkworm pupae oil

The FAME contents of the five varieties of silkworm chrysalis oil that were obtained using the five methylation procedures are given in Table I. The results indicated significant differences among the five methylation methods. Employing the two-step methylation method always resulted in higher contents of FAMEs than those using the KOH–MeOH, NaOCH$_3$–MeOH, H$_2$SO$_4$–MeOH, or BF$_3$–MeOH methylation procedures ($p > 0.05$).

TABLE I. FAME contents (mg mL^{-1}) in pupae oil from five varieties of silkworm obtained using the five methylation methods; a–e: the mean values in the same row for FAME contents in silkworm pupae oil using varying reaction condition are significantly different ($p < 0.05$)

Variety	Component						
	Method	Methyl palmitate	Methyl palmitoleate	Methyl stearate	Methyl oleate	Methyl linoleate	Methyl linolenate
5078	KOH	0.822 ±0.026^{c}	0.060 ±0.001^{c}	0.234 ±0.025^{c}	0.815 ±0.116^{e}	0.520 ±0.020^{d}	1.453 ±0.150^{c}
	H$_2$SO$_4$	1.221 ±0.034^{b}	0.099 ±0.002^{b}	0.324 ±0.003^{b}	1.827 ±0.031^{b}	0.651 ±0.006^{b}	2.288 ±0.052^{b}
	BF$_3$	0.626 ±0.055^{de}	0.054 ±0.005^{cd}	0.189 ±0.011^{de}	0.918 ±0.020^{c}	0.506 ±0.015^{ed}	1.374 ±0.046^{cd}
	NaOCH$_3$	0.517 ±0.022^{e}	0.039 ±0.003^{e}	0.185 ±0.006^{e}	0.835 ±0.039^{cd}	0.522 ±0.007^{cde}	0.976 ±0.047^{e}
	Two-step	1.425 ±0.083^{a}	0.128 ±0.006^{a}	0.370 ±0.018^{a}	2.227 ±0.053^{a}	0.741 ±0.033^{ab}	2.756 ±0.084^{a}
220	KOH	0.976 ±0.113^{c}	0.067 ±0.006^{d}	0.200 ±0.006^{c}	1.365 ±0.068^{c}	0.536 ±0.009^{c}	1.439 ±0.072^{c}
	H$_2$SO$_4$	1.479 ±0.005^{b}	0.113 ±0.003^{b}	0.270 ±0.003^{c}	1.992 ±0.007^{b}	0.673 ±0.001^{b}	2.232 ±0.008^{b}
	BF$_3$	0.739 ±0.052^{e}	0.059 ±0.001^{d}	0.167 ±0.006^{b}	0.982 ±0.054^{d}	0.518 ±0.015^{c}	1.349 ±0.092^{d}
	NaOCH$_3$	0.765 ±0.069^{de}	0.099 ±0.007^{c}	0.228 ±0.008^{c}	1.099 ±0.098^{d}	0.487 ±0.016^{c}	1.164 ±0.851^{d}
	Two-step	2.155 ±0.080^{a}	0.193 ±0.012^{a}	0.344 ±0.010^{a}	2.978 ±0.091^{a}	0.879 ±0.018^{a}	3.314 ±0.086^{a}
5082	KOH	0.660 ±0.041^{d}	0.044 ±0.004^{e}	0.211 ±0.002^{cd}	1.101 ±0.064^{d}	0.495 ±0.010^{d}	1.219 ±0.010^{d}
	H$_2$SO$_4$	1.392 ±0.061^{ab}	0.093 ±0.004^{b}	0.367 ±0.014^{b}	2.206 ±0.047^{ab}	0.732 ±0.011^{ab}	2.662 ±0.072^{b}
	BF$_3$	0.505 ±0.120^{de}	0.048 ±0.003^{de}	0.172 ±0.003^{de}	0.796 ±0.022^{e}	0.479 ±0.010^{de}	1.118 ±0.044^{de}
	NaOCH$_3$	0.933 ±0.134^{c}	0.067 ±0.013^{c}	0.277 ±0.019^{c}	1.564 ±0.149^{c}	0.583 ±0.025^{c}	1.780 ±0.158^{c}
	Two-step	1.581 ±0.128^{a}	0.114 ±0.002^{a}	0.402 ±0.004^{a}	2.461 ±0.010^{a}	0.782 ±0.008^{a}	3.075 ±0.030^{a}

TABLE I. Continued

Variety	Method	Component					
		Methyl palmitate	Methyl palmitoleate	Methyl stearate	Methyl oleate	Methyl linoleate	Methyl linolenate
Jingsong ×haoyue	KOH	0.727 ±0.055^{cd}	0.056 ±0.004^{c}	0.187 ±0.009^{c}	0.959 ±0.059^{c}	0.502 ±0.016^{c}	1.553 ±0.053^{c}
	H_2SO_4	1.138 ±0.008^{ab}	0.075 ±0.002^{b}	0.257 ±0.001^{b}	1.400 ±0.012^{b}	0.630 ±0.006^{b}	2.496 ±0.019^{b}
	BF_3	0.431 ±0.069^{e}	–^{e}	0.141 ±0.005^{e}	0.584 ±0.031^{e}	0.440 ±0.023^{de}	1.038 ±0.078^{e}
	$NaOCH_3$	0.767 ±0.111^{c}	0.050 ±0.008^{cd}	0.185 ±0.005^{cd}	0.809 ±0.058^{cd}	0.470 ±0.039^{d}	1.320 ±0.103^{d}
	Two-step	1.385 ±0.023^{a}	0.105 ±0.001^{a}	0.283 ±0.015^{a}	1.742 ±0.029^{a}	0.701 ±0.009^{a}	3.157 ±0.037^{a}
HK3	KOH	0.531 ±0.026^{d}	0.040 ±0.006^{d}	0.157 ±0.001^{d}	0.832 ±0.005^{d}	0.445 ±0.020^{d}	0.913 ±0.001^{d}
	H_2SO_4	0.958 ±0.059^{b}	0.066 ±0.007^{bc}	0.213 ±0.006^{b}	1.325 ±0.090^{b}	0.562 ±0.017^{b}	1.412 ±0.081^{b}
	BF_3	0.428 ±0.014^{de}	–^{e}	0.135 ±0.003^{e}	0.605 ±0.025^{e}	0.423 ±0.002^{de}	0.674 ±0.023^{e}
	$NaOCH_3$	0.871 ±0.140^{c}	0.071 ±0.001^{b}	0.184 ±0.038^{c}	1.259 ±0.345^{bc}	0.505 ±0.041^{c}	1.198 ±0.253^{c}
	Two-step	1.101 ±0.124^{a}	0.098 ±0.007^{a}	0.248 ±0.018^{a}	1.723 ±0.166^{a}	0.651 ±0.028^{a}	1.937 ±0.078^{a}

This result is closely related to the nature of silkworm pupae oil. There is a certain amount of free fatty acid in silkworm pupae oils, more than 2 mg KOH g^{-1}.[21] In general, FFAs always produce negative effects because their presence causes soap formation that consumes catalyst and reduces the catalytic effectiveness,[22] which leads to an increased solubility of FAMEs in the glycerol layer. Overall, the effects of KOH or $NaOCH_3$ catalysts were not suited for methylation of the highly acidic oils. Moreover, BF_3 methylation has often been applied to test neutral components, but its results were affected by reaction time.[23] However, BF_3 is not suitable for the transesterification of triglycerides due to its potential for producing many artifacts.[24,25] Furthermore, in the presence of sulfuric acid as a catalyst, the method is suitable for the methylation of FFAs.[21] However, the reactions catalyzed by sulfuric acid are generally time-consuming, require high temperatures and did not result in complete conversion. In the two-step methylation, the first step was to hydrolyze fatty acid esters to FFAs under alkaline conditions, and the second step was esterification of the formed FFAs with methanol. Although the method consisted of two steps, the whole process was completed in one container. This methylation method was different from the others because some water was added to the reaction; water is known to facilitate the reaction.[20] Therefore, for FAME synthesis from silkworm pupae oil, the two-step methylation was superior among the five tested methods.

Method validation and precision

The precision of the five methylation methods was evaluated in terms of repeatability, which was expressed as relative standard deviation (*RSD*). The precision in terms of repeatability was obtained at different levels by the analysis of the FAMEs in pupae oil from silkworm variety 5078. The ANOVA of the chrysalis oil FAME was calculated using PROCGLM (SAS Inst. Inc., Cary, NC, USA).[26] The precision test results of FAME content of pupae oil from silkworm variety 5078 are given in Table S-II of the Supplementary material. The percent *RSD* of the FAME content with the two-step synthetic method ranged from 2.39 to 4.97 %, except for methyl palmitate (5.82 %). The FAME precisions with the other methods were between 1 and 11 %, while less than 3 % *RSD* was observed with the acid catalyst H_2SO_4. In addition, the methyl linoleate precisions of the five methylation methods (0.98–4.44 %) were higher than those for the other FAMEs. The *p*-values for the five methylation methods were all less than 0.05, indicating that the difference in the data was significant and that the data were valid.

Stability

A stability test was conducted on the five methylation methods of the pupae oil from silkworm variety 5078 after a week, and the corresponding stability analysis is given in Table S-III of the Supplementary material. Compared with the data in Table I, the content of all FAMEs produced by five methylation methods in Table S-III were slightly increased after one week. Using the two-step method, the contents of C16:0 and C18:3 were increased from 1.425±0.058 mg mL^{-1} to 1.909±0.009 mg mL^{-1} and from 2.756±0.084 mg mL^{-1} to 3.641± ±0.010 mg mL^{-1}, respectively. Thus, there is a possible correlation between the increase in FAMEs content and the precision of five methyl esterification methods. However, using the H_2SO_4–MeOH methylation, the fatty acid content remained essentially unchanged after a week. For example, the content of C16:0 was just decreased from 1.392±0.061 to 1.302±0.005 mg mL^{-1} ($p < 0.05$). This is because the fatty acids easily deteriorate after a few days of unfavorable conditions due to their poor stability.[27] Therefore, it was inferred that the samples of silkworm pupae oil should be determined as soon as possible.

Average recovery

After methyl esterification by the five methylation methods, the FAMEs standards were added to the samples to achieve 80, 100 and 120 % of the corresponding amount in the samples. GC was used to detect the total amount of the FAMEs, and the recovery rate was calculated. A summary of the average recovery rates of FAMEs in pupae oil obtained from silkworm variety 5078 using the five methylation methods is presented in Table S-IV of the Supplementary material. The average recovery rates of FAMEs ranged from 114.30 to 120.66 % for methyl palmitate, from 80.62 to 116.01 % for methyl palmitoleate, from 100.91 to 119.96 % for methyl stearate, from 89.36 to 108.77 % for methyl oleate, from 114.40 to 123.31 % for methyl linoleate and from 76.13 to 85.02 % for methyl linolenate. Except for the recovery rate of methyl linoleate using the H_2SO_4–MeOH methylation (123.31 %), the average recovery rate of methyl linolenate using the two-step method was the highest (85.02 %), and the average recovery rates of other FAMEs were tolerable (75–120 %). There were significant differences in the *RSD*. The *RSD* of the two-step method was lower than those of the other methods, which indicated that the reproducibility using the two-step method was more favorable.

Therefore, the results above indicate that FAME formation and GC analysis using two-step methylation of pupae oil from silkworm variety 5078 had high average recovery rates, with acceptable values of the *RSD* percentage. Importantly, this method is more effective and has a better reproducibility than the other methods as water could be used and was not antagonistic to the methylation. Lengthy preparation times are not required for lyophilization a sample (usually takes days) or perform prior organic solvent extractions and no evaporations (usually hours), which are required to eliminate water in the other fatty acid methods.[20] In addition, the two-step methylation not only improves the FAMEs yield, but it also eliminates the potential harmfulness of solvents.

Determination of oil content and fatty acid composition in different silkworm pupae

The Soxhlet extracted weights of the oils from different silkworm pupae samples are given in Table II. Among the five varieties of silkworm pupae, the oil content of silkworm variety HK3 was the greatest (56.4 %); the least was that of silkworm variety 220 (27.4 %), while the others were between 30 and 40 %. Therefore, the result corresponds with those previously reported that the oil contents of different varieties of silkworm pupae were significantly different.[2]

TABLE II. Pupae oil weights of five varieties of silkworm

Variety	Oil weight, g/5 g of dried silkworm chrysalis[a]	Oil content, %
5078	1.58	31.6
220	1.37	27.4
5082	1.71	34.2
HK3	2.82	56.4
Jingsong × haoyue	1.99	39.8

[a] 80 mL petroleum ether, 80 °C for 8 h

In addition, as shown in Table I, the fatty acid contents in the oils from different varieties of silkworm pupae determined by the same methylation procedures were significantly different, suggesting that fatty acid compositions were different in different varieties of silkworm pupae. As a whole, the fatty acid components in silkworm pupae oil were palmitic, palmitoleic, stearic, oleic, linoleic, and linolenic whereby the content of linolenic acid was the highest. The contents of linolenic acid determined using the two-step method were clearly higher than those determined using the other methylation methods. Among the oils from the five varieties of silkworm pupae, the content of linolenic acid in the oil from silkworm variety 220 was the highest (3.314±0.086 mg mL^{-1}).

The obtained results indicate that silkworm pupae oil is a good source of linolenic acid. As many human diets are deficient in n-3 PUFAs, enrichment of food products is an alternative to increasing the intake of these fatty acids.[2] Thus the procurement of linolenic acid concentrate from silkworm pupae is important for pharmaceutical and dietary purposes.

CONCLUSIONS

A quantitative method for preparing FAMEs for assessing the fatty acid content of silkworm pupae oils using GC with two-step methylation was developed. Compared with the other four methyl esterification methods (KOH, $NaOCH_3$, H_2SO_4, BF_3–MeOH methylation), the two-step methylation not only simplifies the experimental procedure of FAME synthesis and saves chemicals, but also eliminates the employment of potential harmful reagents. The proposed GC–FID method was validated and successfully applied to the quantification of FAMEs in the oils from various varieties of silkworm pupae. Thus, the developed methodology could be used for the convenient and effective determination of FAMEs in silkworm pupae oil and other samples.

SUPPLEMENTARY MATERIAL

GC chromatograms of FAMEs, Figs. S-1–S-3, details on statistics, Tables S-I and S-II, as well as FAME content in silkworm pupae oil, Table S-III, are available electronically from http://www.shd.org.rs/JSCS/, or from the corresponding author on request.

Acknowledgements. This work was financially supported by the Science and Technology Support Program of Jiangsu Province (BE2013405), the Qing Lan Project of Jiangsu Province, and the Modern Agro-industry Technology Research System of China (CARS-22).

ИЗВОД

УСПЕШНИ ГАСНО–ХРОМАТОГРАФСКИ МЕТОД ЗА ОДРЕЂИВАЊЕ САДРЖАЈА МАСНИХ КИСЕЛИНА У УЉУ ЛУТКЕ СВИЛЕНЕ БУБЕ ПРИМЕНОМ ДВОСТЕПЕНОГ МЕТИЛОВАЊА

JUN WANG[1,2], WEIWEI WU[1], XUDONG WANG[1], MIN WANG[1] и FUAN WU[1,2]

[1]*School of Biotechnology, Jiangsu University of Science and Technology, Zhenjiang, P. R. China* и
[2]*Sericultural Research Institute, Chinese Academy of Agricultural Sciences, Zhenjiang, P. R. China*

У потрази за успешним методом одређивања масних киселина гасном хроматографијом (GC) у уљу лутке свилене бубе, испитано је пет метода метиловања за добијање метил-естара масних киселина (FAME), укључујући једностепену естерификацију катализовану киселином (H_2SO_4 или BF_3) или базом (KOH или $NaOCH_3$), као и двостепену катализовану прво са KOH, па H_2SO_4. Ови поступци метиловања су упоређивани у методама GC–MS и GC, а затим валидирани кроз прецизност, стабилност и повраћај. Резултати су показали да се поступком двостепеног метиловања добија већи принос FAME, постиже се већа стабилност и избегава се употреба потенцијално штетних реагенаса. Предложени GC метод је испољио задовољавајућу тачност и прецизност и успешно је примењен за одређивање FAME у неколико варијетета уља свилене бубе. Кратко време аналитичког корака смањује трошкове и убрзава хроматографски поступак. У закључку, двостепено метиловање је имало боље перформансе у односу на једностепено, отварајући могућност примене ове методе за анализу масних киселина и из других уља.

(Примљено 1. априла, ревидирано 9. јула, прихваћено 11. јула 2014)

REFERENCES

1. F. Mentang, M. Maita, H. Ushio, T. Ohshima, *Food Chem.* **127** (2011) 899
2. J. Wang, J. L. Zhang, F. A. Wu, *Eur. J. Lipid Sci. Tech.* **115** (2013) 791
3. Z. J. Wei, A. M. Liao, H. X. Zhang, J. Liu, S. T. Jiang, *Biores. Technol.* **100** (2009) 4214
4. J. Wang, F. A. Wu, Y. Liang, M. Wang, *Afr. J. Biotechnol.* **9** (2010) 2956
5. T. Longvah, K. Manghtya, S. Qadri, *J. Sci. Food Agr.* **92** (2012) 1988
6. J. Ecker, M. Scherer, G. Schmitz, G. Liebisch, *J. Chromatogr., B* **897** (2012) 98
7. K. Ichihara, Y. Fukubayashi, *J. Lipid Res.* **51** (2010) 635
8. P. Agozzino, G. Avellone, D. Bongiorno, L. Ceraulo, S. Indelicato, S. Indelicato, K. Vekey, *J. Mass Spectrom.* **45** (2010) 989
9. A. H. Wang, G. L. Li, J. M. You, Z. Y. Ji, *J. Sep. Sci.* **36** (2013) 3853
10. F. N. Arslan, H. Kara, H. F. Ayyildiz, M. Topkafa, I. Tarhan, A. Kenar, *J. Am. Oil Chem. Soc.* **90** (2013) 1179
11. M. F. Marcone, S. A. Wang, W. Albabish, S. P. Nie, D. Somnarain, A. Hill, *Food Res. Int.* **51** (2013) 729
12. A. M. Miranda, E. W. Castilho-Almeida, E. Ferreira, G. F. Moreira, C. A. Achete, R. Armond, H. F. Dos Santos, A. Jorio, *Fuel* **115** (2014) 118
13. S. Sherazi, S. Arain, S. A. Mahesar, M. I. Bhanger, A. R. Khaskheli, *Eur. J. Lipid Sci. Tech.* **115** (2013) 535
14. Z. R. Huang, S. Sha, Z. Q. Rong, H. Y. Liu, J. H. Chen, S. J. Zhu, *Chin. J. Anal. Chem.* **41** (2013) 922
15. V. A. Yaylayan, J. Pare, G. Matni, J. Belanger, *Nat. Prod. Lett.* **15** (2001) 187
16. S. S Gu, J. Wang, N. Pang, F. Q. Wang, C. Li, F. A. Wu, *Adv. Mater. Res.* **634–638** (2013) 711
17. M. Petrovic, N. Kezic, V. Bolanca, *Food Chem.* **122** (2010) 285
18. K. S. Liu, *J. Am. Oil Chem. Soc.* **71** (1994) 1179
19. P. W. Park, R. E. Goins, *J. Food Sci.* **59** (1994) 1262
20. J. O'Fallon, J. R. Busboom, M. L. Nelson, C. T. Gaskins, *J. Anim. Sci.* **85** (2007) 1511
21. J. Kramer, V. Fellner, M. Dugan, F. D. Sauer, M. M. Mossoba, M. P. Yurawecz, *Lipids* **32** (1997) 1219
22. A. Demirbas, *Fuel* **90** (2011) 2273
23. W. R. Morrison, L. M. Smith, *J. Lipid Res.* **5** (1964) 600
24. W. W. Christie, in *Advances in Lipid Methodology*, Vol. 2, W. W. Christie. Ed., Oily Press, Dundee, 1993. p. 69
25. C. Stavarache, M. Vinatoru,Y. Maeda, *Ultrason. Sonochem.* **13** (2006) 401
26. N. M. Niza, K. T. Tan, K. T. Lee, Z. Ahmad, *Appl. Energ.* **101** (2013) 198
27. T. Levandi, T. Pussa, M. Vaher, P. Toomik, M. Kaljurand, *Eur. J. Lipid Sci. Tech.* **111** (2009) 715.

Journal of the Serbian Chemical Society
JSCS@tmf.bg.ac.rs • www.shd.org.rs/JSCS

J. Serb. Chem. Soc. 80 (1) S1–S6 (2015)
Supplementary material

SUPPLEMENTARY MATERIAL TO

An effective GC method for the determination of the fatty acid composition in silkworm pupae oil using a two-step methylation process

JUN WANG[1,2]*, WEIWEI WU[1], XUDONG WANG[1], MIN WANG[1] and FUAN WU[1,2]**

[1]School of Biotechnology, Jiangsu University of Science and Technology, Zhenjiang 212018, P. R. China and [2]Sericultural Research Institute, Chinese Academy of Agricultural Sciences, Zhenjiang 212018, P. R. China

J. Serb. Chem. Soc. 80 (1) (2015) 9–20

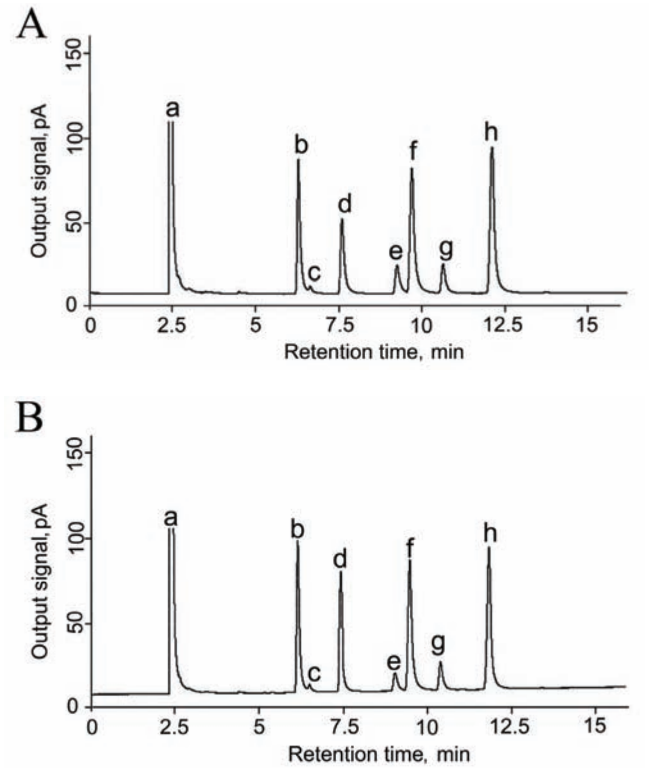

Corresponding authors. E-mails: (*) wangjun@just.edu.cn; (**) fuword@163.com

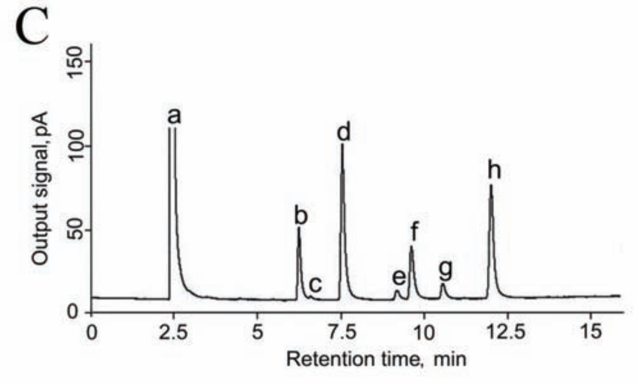

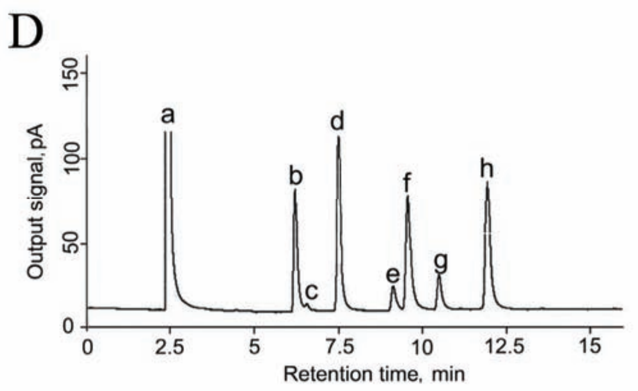

Fig. S-1. GC chromatograms of FAMEs in pupae oil from silkworm variety 5078 prepared by different one-step methylation methods. A, KOH–MeOH methylation; B, H_2SO_4–MeOH methylation; C, BF_3–MeOH methylation; D, $NaOCH_3$–MeOH methylation. (a, *n*-hexane; b, methyl palmitate; c, methyl palmitoleate; d, methyl heptadecanoate; e, methyl stearate; f, methyl oleate; g, methyl linoleate; h, methyl linolenate).

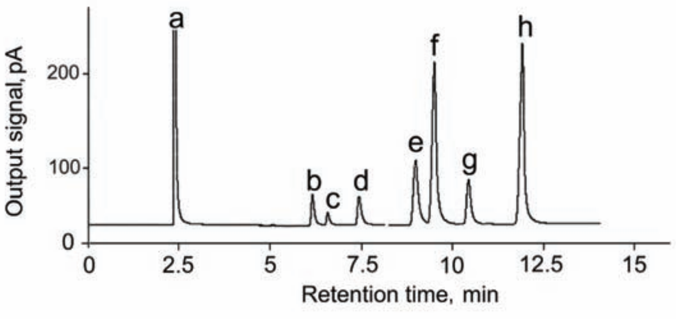

Fig. S-2. GC chromatogram of the six FAME standards (a, *n*-hexane; b, methyl palmitate; c, methyl palmitoleate; d, methyl heptadecanoate; e, methyl stearate; f, methyl oleate; g, methyl linoleate; h, methyl linolenate.)

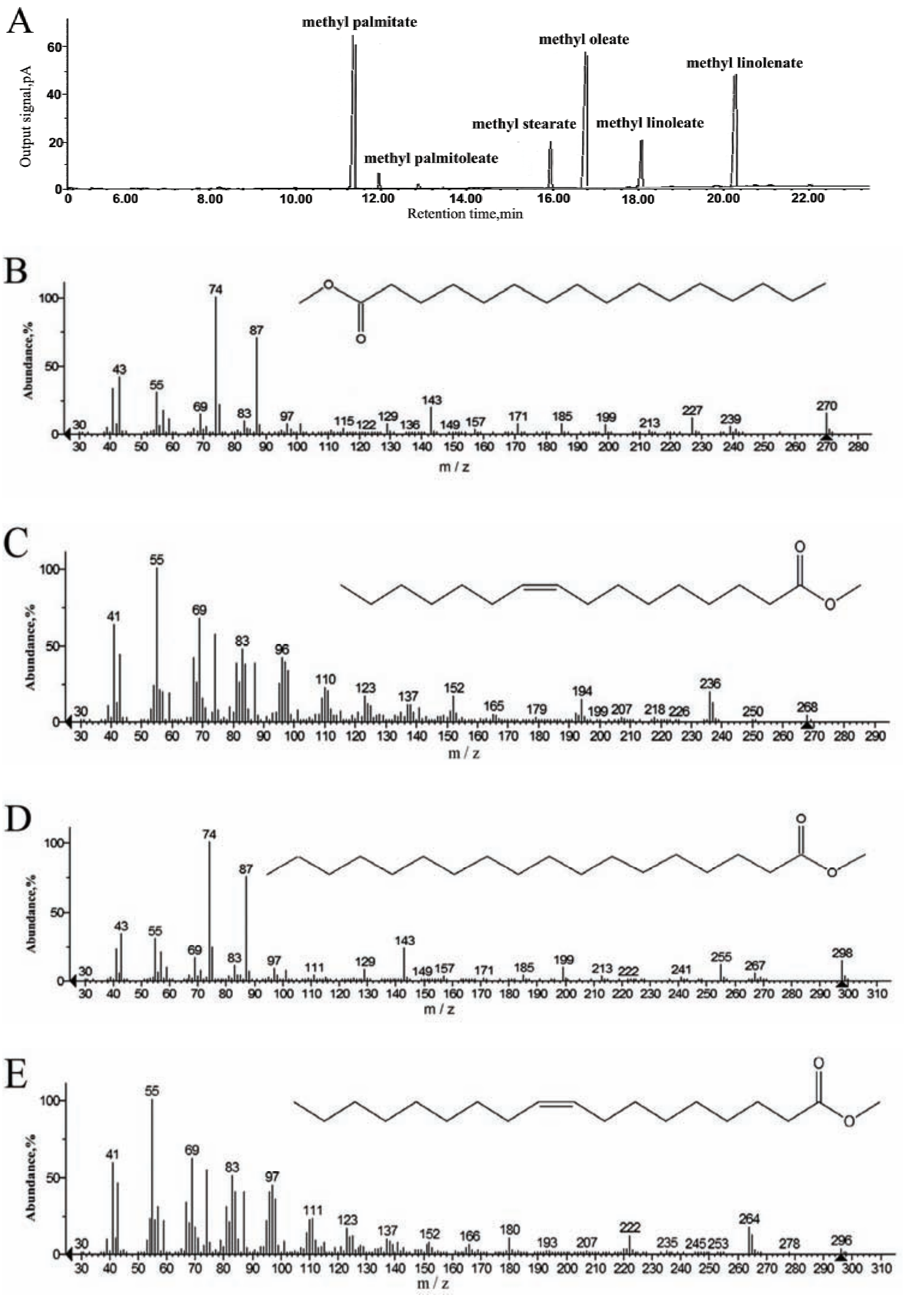
A
methyl palmitate
methyl palmitoleate
methyl stearate
methyl oleate
methyl linoleate
methyl linolenate
Output signal,pA
0
20
40
60
0
6.00
8.00
10.00
12.00
14.00
16.00
18.00
20.00
22.00
Retention time,min
B
Abundance,%
m / z
30
43
55
69
74
83
87
97
115
122
129
136
143
149
157
171
185
199
213
227
239
270
C
Abundance,%
m / z
30
41
55
69
83
96
110
123
137
152
165
179
194
199
207
218
226
236
250
268
D
Abundance,%
m / z
30
43
55
69
74
83
87
97
111
129
143
149
157
171
185
199
213
222
241
255
267
298
E
Abundance,%
m / z
30
41
55
69
83
97
111
123
137
152
166
180
193
207
222
235
245
253
264
278
296
O
O

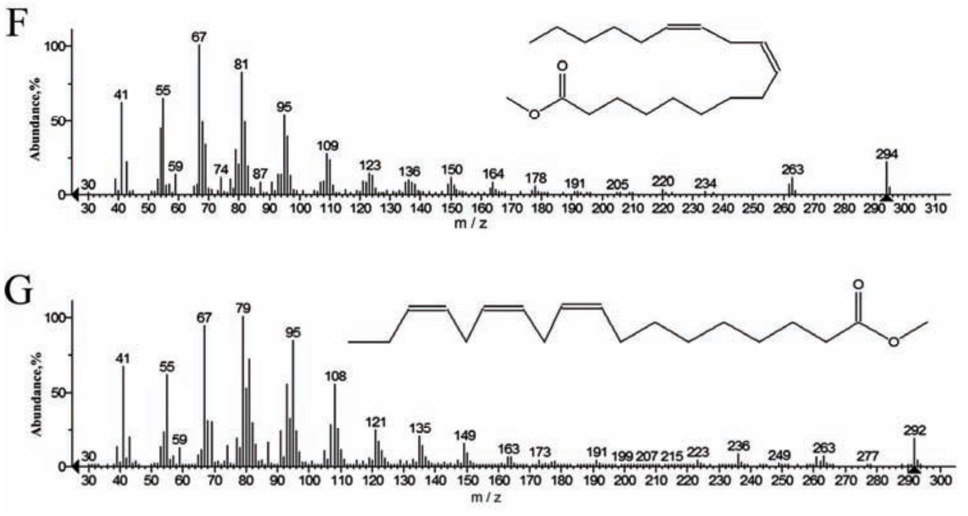

Fig. S-3. TIC chromatogram and mass spectra of FAMEs in silkworm pupae oil using GC–MS. A, GC–MS confirmation of FAMEs in silkworm pupae oil; B, mass spectrum of methyl palmitate, C, mass spectrum of methyl palmitoleate; D, mass spectrum of methyl stearate; E, mass spectrum of methyl oleate; F, mass spectrum of methyl linoleate; G, mass spectrum of methyl linolenate (*m*/*z* range from 35 to 450).

TABLE S-I. Linear regression equations of the FAME standard curves

Standard sample	Retention time, min	Linear range mg mL^{-1}	Regression equation	R^2
Methyl palmitate	6.3	1.00–10.00	$y = 1.0167x - 0.0944$	0.9996
Methyl palmitoleate	6.6	0.05–0.50	y = $0.8274x - 0.0033$	0.9999
Methyl stearate	9.2	0.25–2.50	$y = 1.4751x - 0.1339$	0.9999
Methyl oleate	9.6	1.00–10.00	$y = 0.9345x - 0.2010$	0.9998
Methyl linoleate	10.6	0.50–2.50	$y =1.0387x - 0.3547$	0.9998
Methyl linolenate	12.1	1.00–10.00	$y = 0.8789x - 0.1959$	0.9998

TABLE S-II. Precision test results of FAME content of silkworm pupae oil obtained using five methylation methods

Fatty acid methyl ester	Method	Average value, mg mL^{-1}	*RSD* / %	*SE*	*t*-Value	*p*-Value
Methyl palmitate (C16:0)	KOH	0.822	3.15	0.0614	13.39	0.0055
	H_2SO_4	1.221	2.76	0.0239	51.03	0.0004
	BF_3	0.626	8.76	0.0388	16.15	0.0038
	$NaOCH_3$	0.517	4.23	0.0126	40.92	0.0006
	Two-step	1.425	5.82	0.0587	24.29	0.0017

TABLE S-II. Continued

Fatty acid methyl ester	Method	Average value, mg mL^{-1}	*RSD* / %	*SE*	*t*-Value	*p*-Value
Methyl palmitoleate (C16:1)	KOH	0.060	1.02	0.0003	172.63	0.0001
	H_2SO_4	0.099	2.22	0.0013	78.10	0.0002
	BF_3	0.054	8.62	0.0033	16.41	0.0037
	$NaOCH_3$	0.039	8.36	0.0019	20.63	0.0023
	Two-step	0.128	4.37	0.0039	32.40	0.0010
Methyl stearate (C18:0)	KOH	0.234	10.64	0.0176	13.30	0.0056
	H_2SO_4	0.324	1.07	0.0024	132.45	0.0001
	BF_3	0.189	5.66	0.0076	25.01	0.0016
	$NaOCH_3$	0.185	3.11	0.0033	55.86	0.0003
	Two-step	0.370	4.97	0.0130	28.46	0.0012
Methyl oleate (C18:1)	KOH	1.220	9.52	0.1304	3.35	0.0112
	H_2SO_4	1.827	1.67	0.0216	84.46	0.0001
	BF_3	0.918	2.20	0.0586	15.67	0.0040
	$NaOCH_3$	0.835	4.65	0.0224	37.26	0.0007
	Two-step	2.227	2.39	0.0968	23.00	0.0019
Methyl linoleate (C18:2)	KOH	0.520	3.82	0.0219	23.80	0.0018
	H_2SO_4	0.651	0.98	0.0045	144.49	0.0001
	BF_3	0.506	2.95	0.0105	48.04	0.0004
	$NaOCH_3$	0.522	1.26	0.0720	7.24	0.0186
	Two-step	0.741	4.44	0.0233	31.84	0.0010
Methyl linolenate (C18:3)	KOH	1.453	10.30	0.1542	9.43	0.0111
	H_2SO_4	2.288	2.28	0.0368	62.10	0.0003
	BF_3	1.375	3.35	0.0872	15.74	0.0040
	$NaOCH_3$	0.976	4.79	0.0270	36.20	0.0008
	Two-step	2.756	3.05	0.1153	23.91	0.0017

TABLE S-III. FAME content (mg mL^{-1}) of silkworm pupae oil after a week obtained using five methylation methods

Method	Methyl palmitate	Methyl palmitoleate	Methyl stearate	Methyl oleate	Methyl linoleate	Methyl linolenate
KOH	1.313± 0.013	0.117± 0.001	0.330± 0.004	2.016± 0.096	0.667± 0.001	2.380± 0.002
H_2SO_4	1.302± 0.005	0.120± 0.008	0.333± 0.007	1.941± 0.014	0.674± 0.001	2.469± 0.026
BF_3	0.871± 0.015	0.074± 0.001	0.235± 0.003	1.295± 0.002	0.597± 0.011	1.884± 0.022
$NaOCH_3$	1.485± 0.027	0.126± 0.018	0.375± 0.005	2.288± 0.042	0.723± 0.011	2.792± 0.072
Two-step	1.909± 0.009	0.165± 0.012	0.449± 0.015	2.891± 0.049	0.863± 0.020	3.614± 0.010

TABLE S-IV. Average recovery results of FAMEs of silkworm pupae oil obtained using five methylation methods

Method	Fatty acid methyl ester	Average recovery, %	*RSD* / %
KOH	Methyl palmitate (C16:0)	120.47	0.71
	Methyl palmitoleate (C16:1)	80.62	17.17
	Methyl stearate (C18:0)	119.96	4.82
	Methyl oleate (C18:1)	89.36	8.00
	Methyl linoleate (C18:2)	114.84	3.38
	Methyl linolenate (C18:3)	77.78	0.67
H_2SO_4	Methyl palmitate (C16:0)	119.02	5.13
	Methyl palmitoleate (C16:1)	116.01	9.72
	Methyl stearate (C18:0)	119.96	1.57
	Methyl oleate (C18:1)	108.77	3.19
	Methyl linoleate (C18:2)	123.31	0.48
	Methyl linolenate (C18:3)	84.43	5.59
BF_3	Methyl palmitate (C16:0)	118.99	2.37
	Methyl palmitoleate (C16:1)	102.95	16.36
	Methyl stearate (C18:0)	111.54	19.50
	Methyl oleate (C18:1)	103.15	11.86
	Methyl linoleate (C18:2)	116.25	4.61
	Methyl linolenate (C18:3)	77.78	6.09
$NaOCH_3$	Methyl palmitate (C16:0)	114.34	1.62
	Methyl palmitoleate (C16:1)	103.86	1.33
	Methyl stearate (C18:0)	100.91	3.62
	Methyl oleate (C18:1)	101.74	8.17
	Methyl linoleate (C18:2)	115.68	4.66
	Methyl linolenate (C18:3)	76.13	7.22
Two-step	Methyl palmitate (C16:0)	120.66	0.47
	Methyl palmitoleate (C16:1)	112.61	3.24
	Methyl stearate (C18:0)	113.64	2.57
	Methyl oleate (C18:1)	109.66	3.06
	Methyl linoleate (C18:2)	114.40	0.40
	Methyl linolenate (C18:3)	85.02	4.47

Journal of the Serbian Chemical Society
eVersion electronic
JSCS-info@shd.org.rs • www.shd.org.rs/JSCS

J. Serb. Chem. Soc. 80 (1) 21–33 (2015)
JSCS–4693

UDC 547.565+631.576.4:641.3:615.27–188(497.11)
Original scientific paper

Fibre and polyphenols of selected fruits, nuts and green leafy vegetables used in Serbian diet

MARGARITA DODEVSKA*#, SLADJANA ŠOBAJIĆ and BRIŽITA DJORDJEVIĆ

University of Belgrade, Faculty of Pharmacy, Department of Bromatology, Belgrade, Serbia

(Received 4 April, revised 3 June, accepted 4 June 2014)

Abstract: Fruits and vegetables are known as good sources of numerous bioactive compounds among which polyphenols and dietary fibre are considered essential because of their protective health effects. The aim of this study was to characterize the quality of selected plant foods of Serbia regarding the amount of total phenols, fibres and ratio of certain fractions of fibre. Fifteen samples of plant foods (green leafy vegetables, fruits and nuts) were evaluated for their total antioxidant activity, total phenolic content, total, soluble and insoluble fibre and fractions of fibre: β-glucans, arabinoxylan, cellulose and resistant starch. Generally, nuts were the richest sources of fibre and total phenols. However, when serving size was taken into consideration, it appeared that raspberry and blackberry were the richest in total, soluble fibre and cellulose. Furthermore, almonds and hazelnuts were particularly rich in insoluble fibre, while walnuts had the highest polyphenol content. The analyzed plant foods were poor sources of arabinoxylan and β-glucan. Data on the presence of resistant starch in cashew nut was the first confirmation that resistant starch could be found in significant amount in some nuts. The results give rare insight into the quality of selected plant foods regarding dietary fibre and polyphenols from the nutritive point of view.

Keywords: total fibre; fractions of fibre; total phenols; antioxidant activity.

INTRODUCTION

The importance of fruits and vegetables in human diet is well established. Plant foods are low in fats and energy; they are good sources of vitamins, minerals and polyphenols and provide a significant amount of fibre. All these components are considered to be bioactive ingredients according to a new definition proposed by Guaadaoui *et al*.[1] These properties make them highly recommended for daily diet. When consumed in a proper way, fruits and vegetables offer many health benefits, including reduction of body weight, reduction of the risks of type

---

* Corresponding author. E-mail: margarit_bromi@yahoo.com

Serbian Chemical Society member.

doi: 10.2298/JSC140407062D

2 diabetes, cardiovascular disease and certain types of cancer.[2] The majority of noticed health benefits of fruits and vegetables are attributed to their bioactive ingredients and their specific combinations.

Total dietary fibre (TDF) is one of the bioactive compounds that are responsible for the protective effects of fruits and vegetables In their study, Ramulu & Rao[3] documented a significant amount of total, soluble and insoluble dietary fibres in fruits and vegetables. In terms of its chemistry, fibre is not a single defined compound but a combination of substances, such as cellulose, hemicelluloses, lignin, arabinoxylans, β-glucan, pectin, *etc*.[4] Different plant foods, even within the same food category, such as nuts, cereals, fruits, have different profiles of fibre fractions. Investigation of the profiles of food fibre is important because soluble and insoluble fibre, as well as individual specific fibre fractions, have distinct physiological effects. Soluble dietary fibre (SDF) reduces plasma glucose levels in diabetic patients, whereas insoluble fibre promotes laxative effects.[5] SDF derived from particular fruits and vegetables decrease serum cholesterol, thus lowering the risk of cardiovascular disease.[6] Soluble and insoluble dietary fibre (IDF) both play roles in cardiovascular risk reduction.[7,8]

Emerging evidence shows that different fibre fractions also have different physicochemical and physiological properties, and consequently express different protective effects. Cellulose is particularly known for its protective role in the development of colon cancer, while others, such as arabinoxylan and β-glucan, are effective as agents for reducing postprandial glucose response.[9] Pectins have hypolipidemic and hypoglycemic activity.[10,11]

Another important component of fruits and vegetables are polyphenols. Red wine, tea, coffee, chocolate and cereals are all sources of polyphenols in daily diet. Polyphenols exhibited anticancer, anti-inflammatory, antimicrobial, anti-mutagenic, anti-oxidant, and immunostimulant properties in numerous studies.[12]

A specific protective combination of polyphenols and fibres was defined by Saura-Calixto[13] as anti-oxidant dietary fibre (AODF), a natural product capable of combining the beneficial health effects of TDF and natural anti-oxidants, such as polyphenols. It seems that dietary fibre can entrap some polyphenols, thus protecting them from hydrolysis in the upper intestinal area. Such polyphenols entrapped in TDF easily reach the large intestine where they finally are fermented together with TDF. The end products of fermentation are metabolites such as phenylacetic, phenylpropionic, and phenylbutyric acids, which are easily absorbed and may exert systemic effects.[14] The remaining polyphenols that cannot be fermented and/or absorbed in the large intestine and remain unchanged may still contribute to a healthy antioxidant environment by acting as free radical scavengers and counteracting the pro-oxidants derived from food.[15] Foods and natural products that are rich in both fibre and polyphenols are considered to be of high nutritional and protective significance.

The objective of the present work was to study the characteristics of the fruits and vegetables that are produced and used in daily diet in Serbia regarding their dietary fibre content and profile, as well as polyphenol content and antioxidant capacity. The obtained results may be useful in preparing dietary regimes for specific health conditions by enabling the best combinations to be chosen from a broad range of dietary sources of fibre and polyphenols.

EXPERIMENTAL

Plant material

Three independent samples of fresh broccoli, spinach, lettuce, cabbage, parsley, cherry, strawberry, raspberry, blackberry, blueberry, apple, walnut, almond, hazelnut, and cashew nuts were purchased from three open local markets in Belgrade, Serbia, and used for the research. The vegetables, fruits (2.0 kg each), and nuts (300 g each) were randomly sampled. Except for the cashew nuts, the other samples originated from Serbian region.

Preparation of vegetables and fruits samples

Before analysis, the fruit and vegetable samples were washed in deionised water and dried at room temperature. After removal of occasional stalks from the strawberries, raspberries and blackberries, and deseeding of the apples and cherries, all fruit samples were homogenized separately in a blender. Subsequently, the samples were kept at –20 °C until analysed. The nuts were homogenized immediately after purchase and kept at room temperature.

Methods

For the analysis of the total fibre, the fibre fractions, polyphenols and anti-oxidative activity, reliable methods that were adequate according to their accuracy and precision, and are usually employed in similar investigations were used.

Determination of total phenolics

About 1 g of homogenized sample was extracted with methanol (50 mL) using a mechanical shaker for 2 h. The mixture was centrifuged at 10000 rpm for 10 minutes and the supernatant removed and filtered through Whatman No. 1 filter paper. The clear extract was used for phenolic content and antioxidant activity evaluation. The amount of total phenolic content was determined using the Folin–Ciocalteu reagent, as described by Singleton & Rossi (1965).[16] The absorbance was measured at 765 nm against gallic acid as a reference standard. Five calibration curves were prepared for the working solutions of gallic acid (Acros Organic, Lot: A0325987) in the concentration range of 1–10 µg mL^{-1}. The least-squares method was applied to calculate the equations of the lines: $y = (0.087\pm0.001)x + (0.048\pm0.007)$, resulting in a correlation coefficient: 0.9971. The relative standard deviation (*RSD*) of the slopes was 1.84 %, and for 6 µg GA mL^{-1}, *RSD* = 1.46 %.

Results are expressed as mg gallic acid equivalents (mg GAE) per 100 g wet weight of the sample.

Determination of antioxidant activity

The ferric reducing antioxidant power (FRAP) was determined according to Benzie and Strain.[17] Methanol extract prepared in the same way as for determination of the total polyphenols was used. The procedure is based on reduction of the yellow-coloured 2,4,6-tri2--pyridyl-*s*-triazine (TPTZ) complex that yields a blue-coloured end product. The reaction is performed at pH 3.6 in order to preserve good iron solubility. The reduction was monitored by measuring the absorbance at 593 nm. A standard curve was constructed using ferrous sulphate solution. The results are expressed as µmol Fe(II) per100 g wet sample.

Five calibration curves were prepared for the working solutions of $FeSO_4$ (Panreac, Lot: 0000491691) in the concentration range of 200–1000 µmol L^{-1}. The least-squares method was applied to calculate the equations of the lines: $y = (0.0009\pm0.001)x + (0.058\pm0.003)$, resulting in a correlation coefficient: 0.9997. The *RSD* of the slopes was 1.20 %, and for 500 µmol L^{-1} $FeSO_4$, *RSD* = 0.98 %.

Determination of D-xylose including xylan and arabinoxylan

D-Xylose, xylan and arabinoxylan were determined by a spectrophotometric method using the enzymatic assay kit K-XYLOSE (Megazyme, Bray, Ireland). The assay was performed according to the instruction manual of the kit producer. The measuring procedure is based on the interconversion of α-D-xylose to β-D-xylose. Interconversion of the α- and β-anomeric forms of D-xylose is catalysed by xylose mutarotase. The β-D-xylose is oxidised by NAD^+ to D-xylonic acid at pH 7.5 in the presence of β-xylose dehydrogenase. The amount of NADH formed in this reaction is proportional (directly correlated) to the D-xylose concentration and is measured by the increase in absorbance at 340 nm. The content of arabinoxylan is then calculated according to the formula:

$$\text{Arabinoxylan} = \text{Content of D-xylose (g/100 g)}\times100/62 \text{ (g/100 g)}$$

Internal analytic quality control was conducted using reference materials: D-xylose control (Megazyme, Lot 90401a). The repeatability (*RSD*) and recovery of the method were 2.0 and 99.2 %, respectively.

Determination of cellulose guide

Cellulose was determined by the official AOAC 950.37method.[18] The procedure was performed by cooking the sample with alkaline and acidic agents. Cooking in strong acids hydrolyses starch and proteins from the sample while alkaline pH hydrolyses the remaining non-hydrolysed proteins and saponification occurs. Residual raw cellulose was filtered, dried and weighed. Analytical internal quality control was conducted using reference materials: T1061 (FAPAS). The repeatability (*RSD*) and recovery of the method were 2.4 and 98.2 %, respectively.

Determination of total, soluble and insoluble dietary fibre

Samples were analyzed for soluble and insoluble fraction according to an enzymatic–gravimetric procedure (AOAC method 985.29), as described by Prosky *et al*.[19] The method requires phosphate buffer, pH 6.0 and the following enzymes: heat stable α-amylase, protease and amyloglucosidase. Heat stable α-amylase depolymerises starch, protease depolymerises and dissolves proteins, while amyloglucosidase converts starch into glucose. The total fibre was calculated as the sum of the soluble and insoluble fibre. Analytical internal quality control was conducted using reference materials: T2454 (FAPAS). The repeatability (*RSD*) and recovery of the method were 2.6 and 98.0 %, respectively.

Determination of β*-glucan*

β-Glucan was quantified according to McCleary and Codd[20] by a spectrophotometric method using the enzymatic assay kit K-BGLU (Megazyme, Bray, Ireland). The samples were suspended and hydrated in a buffer solution of pH 6.5 and then incubated with purified lichenase enzyme and then filtered. Afterwards, an aliquot of the filtrate is hydrolysed to completion with purified β-glucosidase. The D-glucose produced was assayed using a glucose oxidase/peroxidase reagent and measuring the absorbance at 510 nm. Analytical internal quality control was conducted using reference materials: *β*-glucan control (Megazyme, Lot 60301). The repeatability (*RSD*) and recovery of the method were 2.1 and 98.4 %, respectively.

Determination of resistant starch and starch

Resistant starch was quantified according to McCleary and Monaghan[21] by a spectrophotometric method using the enzymatic assay kit RSTAR (Megazyme, Bray, Ireland). The samples are incubated in the presence of *α*-amylase and amyloglucosidase derived from pancreas for 16 h at 37 °C. By the synergistic action of the two enzymes, the non-resistant starch was solubilised and hydrolyzed to glucose. After addition of ethanol, the hydrolysate was centrifuged. The resistant starch (RS) was obtained as a pellet, while the supernatant was used for measurement of the soluble non-resistant starch. The pellet was dissolved in 2 M KOH and the solution was neutralized with acetate buffer. Using amyloglucosidase, the RS was subsequently quantitatively hydrolyzed to glucose, which was, in turn, assayed with glucose oxidase/peroxidase reagent (GOPOD). The absorbance was measured at 510 nm. The soluble non-resistant starch was determined from the supernatant at the same wavelength as the resistant starch. This method offers the results that most approximately reflect the proportion of resistant starch and non-resistant starch *in vivo* and thus could be physiologically relevant. Analytical internal quality control was conducted using reference materials: Resistant Starch Control (Megazyme, Lot: 50904). The repeatability (*RSD*) and recovery of the method were 2.4 and 97.2 %, respectively.

Statistical analysis

The analyses were performed in triplicate. The results are presented as the mean values with the standard deviations.

RESULTS AND DISCUSSION

In this study, 15 samples belonging to 3 food groups, *i.e.*, fresh fruit, green leafy vegetables, and nuts, were investigated for the presence of total dietary fibre, the fibre fraction profile and antioxidant capacity. These food groups were chosen for investigation as they are highly recommended for everyday diet. The analyzed fibre fractions were cellulose and arabinoxylans from the insoluble fibre, and *β*-glucan and resistant starch from the soluble fibre. Data on their presence in plant foods are scarce or non-existent, especially when it comes to food of Serbian origin. Pectins are an important part of fruit fibre, and information on their content and profile in Serbian fruit was previously published.[22] All the selected plant foods were of Serbian origin, except for the cashew nuts.

The results for the contents of fibres are presented in Table I. Although the samples between the groups differed in their water content, the results are presented on a fresh weight basis since it is much easier to use such data to calculate the fibre intake necessary for achieving the desirable physiological effects.

In general, all the analyzed samples proved to be significant sources of dietary fibre. The total fibre contents were within the wide range of 1.09 to 14.88 g 100 g^{-1}. As expected, the total fibre content was the highest in nuts, then in fruits and green leafy vegetables.

TABLE I. Total, soluble, insoluble and fractional dietary fibre contents (g per 100 g fresh weight) in the analysed samples; n.d. – non detected; data are expressed on the original weight basis and presented as mean ± *SD* of three independent determinations. All values are given on a fresh weight basis

Sample	Arabinoxylan	Cellulose	β-glucan	RS	SDF	IDF	TDF	Moisture
			Green leafy vegetables					
Spinach	0.02	0.90	n.d.	n.d.	0.78	2.03	2.81	92.62
	±0.01	±0.16			±0.21	±0.35	±0.26	±1.02
Parsley	0.08	1.39	n.d.	n.d.	1.32	2.04	3.36	90.71
	±0.03	±0.21			±0.13	±0.29	±0.23	±0.98
Lettuce	0.05	0.90	n.d.	n.d.	0.20	0.91	1.09	95.84
	±0.02	±0.12			±0.03	±0.17	±0.12	±1.01
Cabbage	0.05	1.05	n.d.	n.d.	0.72	1.67	2.39	92.79
	±0.02	±0.10			±0.15	±0.19	±0.17	±0.89
Broccoli	0.07	1.26	n.d.	n.d.	0.85	2.09	2.94	91.07
	±0.03	±0.13			±0.21	±0.22	±0.22	±1.32
			Fruits					
Apple	0.11	0.49	n.d.	n.d.	0.60	1.66	2.26	86.72
(with skin)	±0.03	±0.11			±0.13	±0.10	±0.12	±2.18
Blueberry	0.07	0.79	n.d.	n.d.	0.8	2.11	2.90	85.22
	±0.04	±0.09			1±0.21	±0.17	±0.19	±1.43
Blackberry	0.11	1.93	n.d.	n.d.	1.77	3.36	5.13	88.14
	±0.04	±0.19			±0.23	±0.26	±0.25	±1.65
Raspberry	0.15	1.21	n.d.	n.d.	2.88	2.62	5.50	85.39
	±0.03	±0.22			±0.27	±0.21	±0.24	±0.99
Strawberry	0.14	0.71	n.d.	n.d.	1.06	1.14	2.20	90.25
	±0.05	±0.26			±0.10	±0.17	±0.14	±1.58
Cherry	0.08	0.64	n.d.	n.d.	1.09	1.02	2.11	83.94
	±0.03	±0.10			±0.15	±0.18	±0.17	±1.76
			Nuts					
Almond	0.53	3.64	0.05	0.16	1.01	13.87	14.88	4.78
	±0.18	±0.23	±0.02	±0.05	±0.10	±0.45	±0.28	±0.63
Hazelnut	0.44	2.67	0.04	0.17	1.37	8.09	9.46	3.39
	±0.13	±0.43	±0.02	±0.06	±0.32	±0.51	±0.42	±0.76
Cashew	0.21	1.02	0.02	0.93	0.95	4.21	5.16	3.97
nuts	±0.10	±0.20	±0.01	±0.23	±0.26	±0.29	±0.27	±0.48
Walnut	0.45	1.29	0.03	0.07	1.04	6.42	7.46	3.43
	±0.11	±0.36	±0.01	±0.03	±0.23	±0.53	±0.39	±0.64

Samples from the nut group were particularly rich in insoluble fibre, but contained soluble fibre as well (the ratio of IDF to SDF was from 4:1 to 14:1). Such a dominance of IDF in nuts was previously reported.[23] The IDF was the dominant fibre fraction in the analyzed fruits and vegetables. The descending sequence of the IDF content in the analyzed fruits was as follows: blackberry > raspberry > blueberry > apple > strawberry > cherry. The lowest SDF fraction in TDF was found in apple (26 %), whereas the highest was measured in raspberry

(52 %). Similar amounts of total fibre and IDF to SDF ratios were found in fruits collected from markets in North Carolina area, USA.[24] Among the green leafy vegetables, lettuce was the poorest source, while parsley and broccoli were the best sources of total, SDF and IDF. The green leafy vegetable samples examined in the present study demonstrated higher IDF and TDF contents than the vegetables of Canadian origin analyzed by Mongeau and Brassard.[25] IDF and SDF have different physiological properties and their balanced intake is of great nutritional importance. Since several studies found that the daily diets in European countries[26] and in Serbia[27] especially are low in SDF, the obtained data on the SDF content in the selected plant foods is important as an indicator for choosing appropriate food for increasing SDF.

The majority of published data reports the total, IDF and SDF fibre content of fruits and vegetables, while particular fibre fractions are hardly ever mentioned. Since individual fibre fractions often have specific and unique physiological effects, it is important to investigate fibre profile of regularly consumed foods. In the present study, several fibre fractions were investigated that were not previously studied in fruits and vegetables of Serbian origin: cellulose, arabinoxylan, β-glucan and resistant starch. Cellulose, classified as an insoluble fibre, was found in high percentages in all samples. Among the nuts, the highest cellulose content was detected in almonds (3.64 g 100 g^{-1}), while blackberry was the richest in cellulose (1.93 g 100 g^{-1}) in the fruit group. Parsley was the best source of cellulose in the green leafy vegetable group. The cellulose portion in nuts was about 20 % of the TDF, in fruits 20–40 %, and 40 % in green leafy vegetables, except for lettuce in which cellulose comprised up to 80 % of the TDF. Besides the common physiological properties ascribed to IDF, cellulose was specifically accredited as a protective agent in colon cancer.[8] Arabinoxylan is another insoluble fibre fraction, but unlike cellulose, it was present in very small quantities in 100 g of analyzed samples – from several milligrams in the fruits and vegetables to half gram in the nuts. Arabinoxylans are supposed to have influence on postprandial glucose response and insulin sensitivity.[28] The best dietary sources of arabinoxylans, according to the literature, are cereals[29] and the present results show that fruits, vegetables and nuts are not appropriate for increasing the daily intake of arabinoxylan.

Two fractions of soluble fibre, resistant starch and β-glucan, were analyzed for the first time in the chosen plant foods. The analyzed fruits and vegetables have low levels of starch, thus no resistant starch was detected in them, but it was found exclusively in the nuts. Resistant starch is defined as “the sum of starch and the products of starch degradation not absorbed in the small intestine of healthy individuals”.[30]

Starch is not a major component in almonds, hazelnuts and walnuts but cashew nuts are rich in starch. The starch contents in the analyzed nuts were as follows: 10.11±1.42 g/100 g in cashew nuts; 2.51±0.22 g/100 g in hazelnuts; 1.35±0.31 g/100 g in almonds; 0.97±0.34 g/100 g in walnuts (the results not shown in the table). Consequently, the values for resistant starch decreased in the same manner: the highest content was measured in cashew nut, the lowest in walnuts. Resistant starch share in total fibre was 1–18 %. Resistant starch has been proven to induce satiety, and intake of 15 g/day increased insulin sensitivity.[30,31] The obtained results confirmed that the analyzed fruit, vegetables, and nuts are generally not good sources of resistant starch, while the evidenced presence of resistant starch in cashew nut is the first confirmation that resistant starch could be found in significant amounts in some nuts.

β-Glucans are considered to be a very important class of fibres with proven hypocholesterolemic and hypoglycemic effects, but the analyzed fruits and vegetables contained no β-glucans.

The total polyphenol contents of the fruit, vegetable and nut samples were estimated using the Folin–Ciocalteu method and methanol as the extraction solvent. In the group of green leafy vegetables, by far the highest content was measured in broccoli, berries had the highest content in comparison with apples and cherries among the fruits and within the nut group, walnuts had 3.5–5 times more polyphenols than other analyzed nuts. The differences in polyphenol content that could be found in the literature largely depended on the plant family, genus and species, but were also dependent on the type of the used extraction agent and standards, which makes comparison of the present results with those of other authors difficult. Wu *et al.*[32] used acetone/water/acetic acid as an extraction solvent for fruit and nut samples purchased from 12 cities in United States. The results presented herein are in agreement with those of this previous study, with the exception for walnuts, where a lower content detected. However, in the vegetable group, lettuce had a higher phenolic content compared to previous studies.[32,33]

A broad spectrum of methods has been developed to measure antioxidant capacity. The methods are based on various anti-oxidative mechanisms, such as scavenging and inhibition of free radicals or chelating metallic ions which would otherwise lead to free radical formation. The FRAP test is based on electron transfer detection[34] and the assumption that the reducing capacity of a sample is directly proportional to its anti-oxidative capacity. The FRAP assay was used in the reported study to evaluate the anti-oxidant capacity of the analyzed fruits and vegetables and the results are given in Table II. As expected, all samples had high antioxidant capacity. In the group of green leafy vegetables, the highest FRAP value was found for spinach (1.61 mmol Fe^{2+} 100 g^{-1}), then broccoli (1.20 mmol Fe^{2+} 100 g^{-1}), while cabbage showed the lowest FRAP value (0.36 mmol Fe^{2+} 100 g^{-1}). In the group of fresh fruits, blueberries had the highest antioxidant capacity (FRAP value 4.98 mmol Fe^{2+} 100 g^{-1}), and apples the smallest

(0.98 mmol Fe^{2+} 100 g^{-1}). By far the highest FRAP value among all the analyzed samples was found for walnuts (13.24 mmol Fe^{2+} 100 g^{-1}).

TABLE II. Total antioxidant capacity and total phenolics in the analyzed samples; data are expressed on the original weight basis and presented as mean ± *SD* of three independent determinations. All values are given on a fresh weight basis

Samples	Total phenolic content mg GAE 100 g^{-1}	Antioxidant capacity (FRAP) mmol Fe^{2+} 100 g^{-1}
	Green leafy vegetables	
Spinach	230±23	1.61±0.34
Parsley	190± 78	1.10±0.04
Lettuce	140±54	0.42±0.09
Cabbage	170±39	0.36±0.12
Broccoli	376±67	1.20±0.41
	Fruits	
Apple with skin	103±43	0.98±0.33
Blueberry	310±76	4.98±0.51
Blackberry	259±23	3.54±0.61
Raspberry	262±41	2.98±0.23
Strawberry	305±54	2.69±0.37
Cherry	198±38	1.97±0.32
	Nuts	
Almond	408±49	0.54±0.21
Hazelnut	772±03	0.90± 0.34
Cashew nuts	269±87	0.24±0.09
Walnut	1456±235	13.24±1.99

Berry fruits are known for their high contents of phenolic acid and flavonoids, such as anthocyanins,[35] hence they demonstrate high antioxidant activity.[36] The present results for the antioxidative capacity obtained by the FRAP method for the berry fruit samples were in overall agreement with previous reports and the deviations that were found may be the consequence of the distinct geographic region and the altitude from where the cultivar samples originated.[37,38]

Fruits and vegetables are proven sources of multiple bioactive compounds, among which dietary fibre and polyphenolic antioxidants are of great importance. These two classes of plant ingredients and their physiological effects are usually studied separately. Saura-Calixto[13] was the first to combine the protective properties of fibre and polyphenols and to introduce the concept of anti-oxidant dietary fibre (AODF) – a natural product capable of combining the beneficial health effects of DF and natural antioxidants, such as polyphenols. Although this expression is not used for natural products but for functional ingredients derived from natural plant sources, it brought attention to the importance of combined and interrelated effects of these bioactive compounds. Epidemiological studies suggest that regular consumption of fruits and vegetables is negatively associated with the risk of several serious chronic diseases.[39,40] Five to seven daily portions or a minimum of 400 g of fruit and vegetables was proposed as population goals.[41,42] Simultaneously, several recommendations for individual phytonutrient intake, such as fibre and polyphenols, was also proposed. It is considered beneficial to consume >25 g day^{-1} of dietary fibre;[43] 6 g day^{-1} of arabinoxylan; 5 g day^{-1} cellulose[44] and >1 g day^{-1} of total polyphenols[45] as a part of ordinary daily diet. Similarly, the intake of 1 g SDF is considered important, since each additional gram of SDF in the diet was found to decrease serum total and LDL cholesterol concentration by 0.03 mmol L^{-1}.[46] One of the aims of this study was to evaluate the potential of selected plant foods as combined sources of antioxidative polyphenols and dietary fibre. These data could help in reaching dietary recommendations by choosing the best combinations from broad range of fibre and polyphenol dietary sources.

The best dietary sources of fibre and polyphenols among the analysed fruits and vegetables, expressed per average portion of original food item, are listed in Table III. The portion sizes were estimated according to the Dutch and Swiss dietary guidelines[42] since no estimates of Serbian standard portions exist. The criterion used for inclusion in the list of best dietary sources (Table III) was based on the potential of the analyzed plant foods to contribute in a significant way to the recommended intake of bioactive plant ingredients.

TABLE III. The best dietary sources of fibre and polyphenols among analysed fruits and vegetables (in descending order, expressed per one portion); 1 portion of fruit and vegetables, 100 g; 1 portion of nuts, 30 g. Serving size from Agundo, 2005[42]

Total fibre[a] g/portion	Soluble fibre[b] g/portion	Insoluble fibre[c] g/portion	Cellulose[d] g/portion	Polyphenols[e] mg GAE/portion	Polyphenol +total fibre[f] (g/portion)/(mg GAE/portion))
Raspberry (5.5) Blackberry (5.1) Blueberry (2.9) Almond (4.5) Hazelnut (2.8) Parsley (3.4) Broccoli (2.9) Spinach (2.8)	Raspberry (2.9) Blackberry (1.8) Cherry (1.1) Strawberry (1.1) Parsley (1.3)	Almond (4.2) Hazelnut (2.4) Blackberry (3.4) Raspberry (2.6) Blueberry (2.1) Broccoli (2.1) Parsley (2.0) Spinach (2.0)	Blackberry (1.9) Raspberry (1.2) Almond (1.1) Parsley (1.4) Broccoli (1.3) Cabbage (1.1)	Walnut (437) Blueberry (310) Strawberry (305) Raspberry (262) Blackberry (259) Broccoli (376) Hazelnut (232) Spinach (230)	Raspberry (5.5 / 262) Blackberry (5.1 / 259) Blueberry (2.9 / 310) Broccoli (2.9 / 376) Spinach (2.8 / 230) Hazelnut (2.8 / 232)

[a]Contributes > 2.5 g / portion; [b]contributes > 1 g/portion; [c]contributes > 2 g/portion; [d]contributes > 1 g/portion; [e]contributes > 200 mg GAE/portion; [f]contributes: polyphenol > 200 mg GAE/portion and total fibre > 2.5 g/portion

When dietary goal is increasing the total, IDF, and cellulose intake, the best choices among the analyzed food would be berries, almonds, parsley, and broccoli. The best dietary choices for SDF would be berries, cherries, and parsley. Although walnuts have by far the highest polyphenol content, when the combination of polyphenols and total fibre is considered, other plant foods could be of more importance. The best sources of combined polyphenols and total fibre was shown to be berries, hazelnut, broccoli, and spinach.

CONCLUSIONS

Based on the results presented in this paper, it is evident that daily consumption of 400 g of the analyzed fruits and vegetables would provide the quantity of dietary fibre and polyphenols that could be expected to give positive physiological effects. The combination of 100 g each of raspberry, blackberry, broccoli and spinach, per example, ensures an amount of 16.4 g day^{-1} TDF, approximately 1.2 g day^{-1} polyphenols, and 5.3 g day^{-1} cellulose. These are precisely the quantities that are being recommended for protective purposes.

In conclusion, the obtained data clearly demonstrate that no single food contains each and all the non-nutritive components relevant to human health. The analyzed plant foods of Serbian origin are rich sources of polyphenols and total, insoluble and soluble fibres, while some specific fibre fractions, such as arabinoxylans, β-glucans and resistant starch were only present in insignificant amounts. The analysis of individual fibre fractions should be encouraged, with aim of ensure proper and more knowledgeable food combinations that would help to supply a diet with the necessary ingredients. Possible synergistic effects of polyphenols and fibres are not well known and need further investigation in well-designed clinical studies.

Acknowledgment. This study was financed by a grant from the Ministry of Education, Science and Technology Development of the Republic of Serbia (III46001).

ИЗВОД

ПРОФИЛ ВЛАКАНА И САДРЖАЈ ПОЛИФЕНОЛА У ОДАБРАНОМ ВОЋУ И ПОВРЋУ

МАРГАРИТА ДОДЕВСКА, СЛАЂАНА ШОБАЈИЋ и БРИЖИТА ЂОРЂЕВИЋ

Универзитет у Београду, Фармацеутски факултет, Катедра за броматологију, Београд

Воће и поврће је познато као добар извор бројних биолошки активних једињења у које спадају и полифеноли и дијетна влакана. За ове састојке постоје докази да повољно утичу на смањење ризика од неких врста канцера, дијабетес, гојазност и хипертензију. Циљ овог рада био је да се провери квалитет биљних намирница са нашег подручја у погледу количине укупних фенола, влакана и односа појединих фракција влакана. Петнаест узорака зеленог лиснатог поврћа, воћа и језграстог воћа је испитивано на укупну антиоксидантну активност, укупан садржај фенола, укупна, растворљива и нерастворљива влакна и следеће фракције влакана: β-глукан, арабиноксилан, целулоза и резистентан скроб. Језграсто воће је било најбогатије у влакнима и укупним фенолима, међутим када је узета у обзир величина порције, бобичасто воће је било најбољи извор уку-

пних, растворљивих влакана и целулозе, лешници и бадеми су најбољи извор нерастворљивих влакана, док су ораси остали најбољи извор полифенола. У анализираним биљним намирницама нису нађене значајније количине арабиноксилана и β-глукана. Податак о присуству резистентног скроба у индијским орасима је прва потврда да резистентан скроб може да се нађе у значајној количини у језграстом воћу. Ови резултати дају редак приказ дијетарног значаја воћа и поврћа које се конзумира у Србији у смислу садржаја влакана и полифенола.

(Примљено 4. априла, ревидирано 3. јуна, прихваћено 4.јуна 2014)

REFERENCES

1. A. Guaadaoui, S. Benaicha, N. Elmajdoub, M. Bellaoui, A. Hamal, *Int. J. Nutr. Food Sci.* **3** (2014) 174
2. W. J. Lampe, *Am. J. Clin. Nutr.* **70** (1999) 475
3. P. Ramulu, P. U. Rao, *J. Food Compos. Anal.* **16** (2003) 677
4. J. Y. Thebaudin, A. C. Lafebvre, M. Harrington, C. M. Bourgeois, *Trends Food Sci. Tech.* **8** (1997) 41
5. J. L. Slavin, *Nutrition* **21**(2005) 411
6. W. D. Rosamond, *J. Am. Coll. Cardiol.* **39** (2002) 57
7. I. Flight, P. Clifton, *Eur. J. Clin. Nutr.* **60** (2006) 1145
8. C. F. Chau, P. C. K. Cheung, *Nutr. Res.* **19** (1999) 257
9. J. M. Lattimer, M. D. Haub, *Nutrients* **2** (2010) 1266
10. S. Hexberg, E. Hexberg, N. Willumson, R. K. Berge, *Br. J. Nutr.* **71** (1994) 181
11. G. Presannakumar, S. Sudheesh, N. R. Vijayalakshmi, *Planta Med.* **57** (1993) 330
12. A. Scalbert, C. Manach, K. Morand, C. Remesy, *Crit. Rev. Food Sci. Nutr.* **45** (2005) 287
13. F. Saura-Calixto, *J. Agric. Food Chem.* **46** (1998) 4303
14. C. Manach, G. Williamson, C. Morand, A. Scalbert, C. Remesy, *Am. J. Clin. Nutr.* **81** (2005) 230
15. I. Goni, J. Serrano, *J. Sci. Food Agric.* **85** (2005) 1877
16. V. L. Singleton, J. A. Rossi Jr., *Am. J. Enol. Vitic.* **16** (1965) 144
17. I. F. Benzie, J. J. Strain, *Anal. Biochem.* **239** (1996) 70
18. W. Horwitz, *Official Methods of Analysis of the Association of Official Analytical Chemists*, Gaithersburg, MD, 2000, p. 132
19. L. Prosky, N. G. Asp, T. F. Schweizer, J. W. DeVries, I. Furda, *J. Assoc. Off. Anal. Chem.* **75** (1992) 360
20. B. V. McCleary, R. Codd, *J. Sci. Food Agric.* **55** (1991) 303
21. B. V. McCleary, D. A. Monaghan, *J. Assoc. Off. Anal. Chem.* **85** (2002) 665
22. G. Niketić-Aleksić, *Technology of fruits and vegetables*, Faculty of Agriculture, Belgrade, 1982 (in Serbian)
23. J. A. Marlett, *J. Am. Diet. Assoc.* **92** (1992) 175
24. B. W. Li, K. W. Andrews, P. R. Pehrsson, *J. Food Compos. Anal.* **15** (2002) 715
25. R. Mongeau, R. Brassard, *J. Food Compos. Anal.* **2** (1989) 189
26. A. P. Pericki, M. L. Mandic, D. Kenjeric, Lj. Primorac, *Croat. J. Food Sci. Technol.* **1** (2009) 8
27. N. Djukic, S. Sobajic, B. Djordjevic, I. Miletic, I. Gajic, *Int. J. Food Sci. Nutr.* **60** (2009) 14
28. Z. X. Lu, K. Z. Walker, J. G. Muir, T. Mascara, K. O'Dea, *Am. J. Clin. Nutr.* **71** (2000) 1123
29. M. S. Dodevska, B. I. Djordjevic, S. S. Sobajic, I. D. Miletic, P. B. Djordjevic, V. S. Dimitrijevic-Sreckovic, *Food Chem.* **141** (2013) 1624

30. M. G. Sajilata, R. S. Singhal, P. R. Kulkarni, *Compr. Rev. Food Sci. Food Saf.* **5** (2006) 1
31. K. C. Maki, C. L. Pelkman, E. T. Finocchiaro, K. M. Kelley, A. L. Lawless, A. L. Schild, *J. Nutr.* **142** (2012) 717
32. X. Wu, G. R. Beecher, J. M. Holden, D. B. Haytowity, S. E. Gebhardt, R. L. Prior, *J. Agric. Food Chem.* **52** (2004) 4026
33. E. M. Zujko, A. M. Witkowska, A. Waskiewicz, E. Sygnowska, *Adv. Med. Sci.* **52** (2012) 375
34. D. Huang, B. Ou, R. L. Prior, *J. Agric. Food Chem.* **53** (2005) 1841
35. E. G. Pantelidis, M. Vasilakakis, A. G. Manganaris, G. Diamantidis, *Food Chem.* **102** (2007) 777
36. N. Pellegrini, M. Serafini, B. Colombi, D. Del Rio, S. Salvatore, M. Bianchi, F. Brighenti, *J. Nutr.* **133** (2003) 2812
37. B. L. Halvorsen, K. Holte, M. C. Myhrstad, I. Barikmo, E. Hvattum, S. F. Remberg, A. Wold, K. Haffner, H. Baugerod, L. F. Andersen, O. Moskaug, D. R. Jacobs, R. Blomhoff, *J. Nutr.* **132** (2002) 461
38. N. Ćujić, N. Menković, K. Šavikin, S. Tasić, G. Zdunić, T. Janković, M. Jovančević. 2011, *Lek. Sirov.* **31** (2011) 39
39. J. M. Genkinger, E. A. Platz, S. C. Hoffman, G. W. Comstock, K. J. Helzlsouer, *Am. J. Epidemiol.* **160** (2004) 1223
40. N. D. Freedman, Y. Park, A. F. Subar, A. R. Hollenbeck, M. F. Leitzmann, A. Schatzkin, C. C. Abnet, *Int. J. Cancer* **122** (2008) 2330
41. T. Pajk, V. Rezar, A. Levart, J. Salobir, *Nutrition* **22** (2006) 376
42. A. Agundo. *Measuring intake of fruit and vegetables*, in *Fruit and vegetables for health*, Report of a joint FAO/WHO workshop, 2004, Kope, Japan, p. 11, http://www.fao.org/ /ag/magazine/fao-who-fv.pdf (accessed 12. 01. 2015)
43. J. Tuomilehto, J. Lindstrom, G. J. Eriksson, T. T. Valle, H. Hamalainen, P. Ilanne-Parikka, *N. Engl. J. Med.* **344** (2001) 1343
44. K. C. Maki, M. L. Carson, W. H. Kerr Anderson, J. Geohas, M. S. Reeves, M. V. Farmer, M. Turowski, M. Miller, V. N. Kaden, M. R. Dicklin, T. M. Rains, *J. Clin. Lipidol.* **3** (2009) 159
45. V. Dilis, A. Trichopoulou, *J. Nutr.* **140** (2010) 1274
46. E. Theuwissen, R. P. Mensink, *Physiol. Behav.* **94** (2008) 285.

Journal of the Serbian Chemical Society
JSCS-info@shd.org.rs • www.shd.org.rs/JSCS

J. Serb. Chem. Soc. 80 (1) 35–43 (2015)
JSCS–4694

UDC 546.562+542.9+547.571+547.551+547.576+547.313.2–304.2
Original scientific paper

Cu(II) complexes of an ionic liquid-based Schiff base [1-{2-((2-hydroxybenzylidene)amino)ethyl}-3-methylimidazolium]PF_6: Synthesis, characterization and biological activities

SANJOY SAHA[1], DHIRAJ BRAHMAN[2] and BISWAJIT SINHA[2]*

[1]*Department of Chemistry, Kalimpong College, Kalimpong-734301, India and* [2]*Department of Chemistry, University of North Bengal, Darjeeling-734013, India*

(Received 1 February, revised 1 June, accepted 21 July 2014)

Abstract: Two Cu(II) complexes of an ionic liquid based Schiff base 1-{2-[(2--hydroxybenzylidene)amino]ethyl}-3-methylimidazolium hexafluorophosphate, were prepared and characterized by different analytical and spectroscopic methods such as elemental analysis, magnetic susceptibility, UV–Vis, IR and NMR spectroscopy, and mass spectrometry. The Schiff base ligand was found to act as a potential bidentate chelating ligand with N, O donor sites and formed 1:2 metal chelates with Cu(II) salts. The synthesized Cu(II) complexes were tested for their biological activity.

Keywords: ionic liquid based Schiff base; salicylaldehyde; Cu(II) complexes; 1-(2-aminoethyl)-3-methylimidazolium hexafluorophosphate.

INTRODUCTION

Ionic liquids (ILs) are defined as organic salts formed by the combination of bulky organic cations with a wide variety of anions, that are generally liquid at room temperature.[1] ILs are made up of large ions that are held together by electrostatic interactions. Due to these interactions, the properties of ILs are considerably different from those of molecular liquids.[2] ILs have been widely studied as alternatives to volatile organic solvents for organic synthesis in homogeneous as well as biphasic processes.[3–5] Such compounds have received attraction in synthetic chemistry in recent years due to their excellent characteristics, such as low vapor pressure, inflammability, high thermal and chemical stability, outstanding solubility and the possibility of easy recycling, *etc*.[6,7] Based on these properties, ILs have emerged as a novel class of compounds that have been employed in many fields, such as electrochemistry, organic synthesis, catalysis,

---

* Corresponding author. E-mail: biswachem@gmail.com
doi: 10.2298/JSC140201078S

gas separation, *etc*. The use of ionic liquids has also received much attention as eco-friendly reaction media in organic synthesis.[5,8] The hydrophobicity/hydrophilicity of ionic liquids can be altered by manipulating the structures of the cations and anions.[9] In recent years, a number of ionic liquids have been identified as solvents for the dissolution of biopolymers such as cellulose, starch, wood, lignin, feather, wool, *etc*.[10–17] Recently, many workers have focused on the preparation and application of functionalized ionic liquids (FILs) for special tasks, such as those carrying hydroxyl, amino, sulfonic acid or carboxyl groups and so on.[18–24] The FILs have shown great promise not only as alternative green solvents, but also as reagents or catalysts in many organic transformations.[25]

Among many potential organic compounds, Schiff bases are widely employed as ligands in coordination chemistry.[26] These ligands are readily available, versatile and, depending on the nature of the starting materials (primary amines and carbonyl precursors), they exhibit various denticities and functionalities.[27] Schiff bases and their complexes are widely applied in biochemistry, material science, catalysis, encapsulation, activation, transport and separation phenomena, hydrometallurgy, *etc*.[28,29] Schiff bases have been reported to show a variety of biological actions, such as antibacterial, antifungal, herbicidal, clinical and analytical activities by virtue of the azomethine linkage.[30,31] Schiff base metal complexes have been the subject intensive study due to their industrial and biological applications.[32–37] Salicylaldehyde and its derivatives are useful carbonyl precursors for the synthesis of a large variety of Schiff bases with wide variety of interesting properties. Hence in this study, an attempt was made to synthesize an ionic liquid grafted Schiff base 1-{2-[(2-hydroxybenzylidene)amino]ethyl}-3--methylimidazolium hexafluorophosphate, and its Cu(II) complexes. The synthesized compounds were characterized by various analytical methods and tested for their biological activities.

EXPERIMENTAL

Materials and measurements

All the employed reagents were of analytical grade and used as received without further purification. 1-Methylimidazole, 2-bromoethylamine hydrobromide and potassium hexafluorophosphate were procured from Sigma–Aldrich, Germany. Salicylaldehyde, $CuCl_2\cdot 2H_2O$, $Cu(NO_3)_2\cdot 3H_2O$ and all other chemicals were purchased from SD Fine Chemicals, India. The IR spectra were recorded in KBr pellets using a Perkin-Elmer Spectrum RX I FT-IR spectrometer, operating in the region 4000 to 400 cm^{-1}. The proton NMR spectra were recorded at room temperature on an FT-NMR Bruker Avance II 400 MHz spectrometer using DMSO-d_6 and D_2O as solvents. The chemical shifts are given in ppm downfield of internal standard tetramethylsilane (TMS). The melting points were recorded using the open capillary method. Elemental microanalyses (C, H and N) were realized using a Perkin–Elmer (Model 240C) analyzer. The Cu-content was determined by atomic absorption spectroscopy (AAS) employing a Varian SpectrAA 50B instrument using a standard Cu-solution from Sigma–Aldrich, Germany. The mass spectra were recorded on an Agilent 1100 LC equipped with an MSD trap. The purity of the Schiff base and its complexes were confirmed by thin layer chromatography (TLC) on silica gel plates and TLC visualization was realized by UV-light and iodine. The antibacterial activities (*in vitro*) of the synthesized ligand and the complexes were studied by the disc diffusion method against commonly known bacteria, *viz.*, *Bacillus subtilis* and *Escherichia coli* with respect to the standard drug ampicilin.

Physical, analytical and spectral data of the prepared compounds are given in Supplementary material to this paper.

Synthesis of ionic liquid 1-(2-aminoethyl)-3-methylimidazoliumhexafluorophosphate ([2-aemim]PF_6)

The amino functionalized ionic liquid was prepared by following literature procedure.[38] In a typical experiment, a mixture of 1-methylimidazole (4.10 g, 0.05 mol) and 2-bromoethylamine hydrobromide (10.25 g, 0.05 mol) in 25 mL of acetonitrile was heated with constant stirring at 80 °C for 4 h. On completion of the reaction, the solvent was removed by distillation and the residue was recrystallized from ethanol to afford the hydrobromide [2-aemim]Br as a white solid. Then KPF_6 (9.20 g, 0.05 mol) was added to the hydrobromide [2-aemim]Br in 20 mL of CH_3CN/H_2O (1:1, *V*/*V*). The solution was left for 24 h at room temperature and then NaOH (2.00 g, 0.05 mol) was added for neutralization. The solvents were evaporated under vacuum. This was followed by the addition of CH_3OH (2 mL) and $CHCl_3$ (10 mL). The precipitated KBr was filtered off and the solvents were evaporated. The obtained yellow oil was washed successively with chloroform (3×10 mL) and diethyl ether (3×10 mL). After drying for 6 h under vacuum at 80 °C, the expected ionic liquid was obtained.

Synthesis of the ionic liquid-grafted Schiff base

The ionic liquid based Schiff base ligand (L) was synthesized by slight modification of a literature procedure.[39] A mixture of salicylaldehyde (1.22 g, 10 mmol) and [2-aemim]PF_6 (2.71 g, 10 mmol) in 10 mL methanol was stirred at room temperature for 1 h. After completion of the reaction, as indicated by TLC, the reaction mixture was diluted with MeOH (10 mL). The precipitate was then filtered and dried to afford the expected ligand as a pale yellow solid in good yield.

Synthesis of Cu(II) complexes of the ionic liquid-based Schiff base

To a solution of ligand, LH (0.50 g, 1.30 mmol), in EtOH (20 mL), copper salts, *viz.*, $CuCl_2·2H_2O$ (0.11 g, 0.65 mmol) or $Cu(NO_3)_2·3H_2O$ (0.17 g, 0.65 mmol) were added and the reaction mixture was refluxed for 8 h at 25 °C until the starting material was completely consumed as monitored by TLC. On completion of the reaction, the solvent was evaporated and the reaction mixture was cooled to room temperature. The precipitate was collected by filtration, washed with C_2H_5OH (10 mL) and dry ether (10 mL) triply, and further dried in a desiccator to obtain the complex **2** as a deep green powder and complex **3** as a dark green powder.

Antibacterial activity

The newly synthesized Cu(II) complexes along with the ligand were tested against the gram-negative bacterium *Escherichia coli* ATCC 69905 and the gram-positive bacterium *Bacillus subtilis* ATCC 6633. Stock solutions of compounds were prepared by dissolving the compounds in distilled water and serial dilutions of the compounds were prepared in sterile distilled water for different concentrations to determine the minimum inhibition concentration (*MIC*). The concentrations of the tested compounds were 31.25, 62.5, 125 and 250 μg mL^{-1} in comparison to the standard drug ampicillin. The nutrient agar medium was poured into 0.5 mL culture containing Petri plates. Then the well diffusion technique[40,41] was performed. Petri plates were incubated at 37 °C for 24 h.

RESULTS AND DISCUSSION

All the isolated compounds were found to be air stable and were characterized based on elemental and different spectroscopic analyses. The data are given in the Supplementary material to this paper.

Infrared spectra of the Schiff base ligand and its complexes

The IR spectra of the free Schiff base and its Cu(II) complexes are presented in Figs. S-1–S-3 of the Supplementary material. In order to obtain conclusive insight concerning the coordination mode of the ligand (LH) to the metal ion and the structure of the metal complexes, the main IR bands were compared with those of the free ligand. The IR spectrum of the ligand showed a strong broad band at 3430–3151 cm^{-1}; this band was attributed to the hydrogen bonded –OH of the phenolic group with –N=C group of the ligand (OH···N=C).[42,43] This band was absent in the spectra of the complexes due to the involvement of the phenolic –OH group in coordination to the metal ion. A new band in the range of 3449.07 cm^{-1} appeared in case of Cu(II) complex **2** and this was assigned to coordinated water molecules in the complex,[44] although in case of the complex **3** no such band was observed in this region. This indicated the absence of coordinated water molecules in its structure A weak band at 3101–2923 cm^{-1} in the spectrum of the ligand was assigned to H–C(=N) stretching vibrations. The involvement of deprotonated phenolic moiety in metal complexes was confirmed by the shift of (–CO) of LH stretching band at 1465.5 cm^{-1} to lower frequency region of 1448–1445 cm^{-1} for the complexes **2** and **3**, respectively. In the spectrum of the ligand, a band corresponding to the azomethine group (–C=N) was found at 1640 cm^{-1}. On complexation, this band shifted to a lower wave number range of 1628–1622 cm^{-1}. This indicated the involvement of N-atom of the azomethine (–C=N) group in complex formation[45,46] and the band at 844.5–842.49 cm^{-1} in the spectra of the complexes **2** and **3** were assigned to P–F stretching frequency.

Therefore, the IR spectral data indicated that the coordination of ligand to metal ion occurred through the N-atom of the azomethine (–C=N) group and the O-atom of phenolic (O–Ar) group. Assignment of the proposed coordination sites was further supported by the appearance of medium bands at 634–620 cm^{-1} and 548–558 cm^{-1} due to M–O and M–N stretching frequencies, respectively.[47,48]

Mass spectra

The mass spectra of the compound [2-aemim]PF$_6$ and the ligand, LH, showed molecular ion peaks (*m*/*z*) at 126.20 and 231, which correspond to M$^+$, $[C_6H_{12}N_3]^+$ and M+1, $[C_{13}H_{16}N_3O +1]^+$ peaks, respectively. The observed mass spectra confirmed the formation of the proposed ligand. Again the mass spectra of the Cu(II) complexes **2** and **3** showed molecular ion peaks (*m*/*z*) at 557 and 523, respectively. These molecular ion peaks were assigned to $Cu(C_{26}H_{34}N_6O_4)^{2+}$ and M″+2 (where M″ = $Cu(C_{26}H_{30}N_6O_2)^{2+}$) peaks, respectively. These peaks support the proposed structure of the complexes and confirmed the ML_2 stoichiometry for the complexes. It is assumed that the Cu(II) complex **2** had an octahedral coordination site with two water molecules occupying two axial positions; however, the Cu(II) complex **3** has square planar geometry. The different molecular ion peaks, appeared in the mass spectra of the complexes, were attributed to different fragmentations of the metal complexes by successive rupture of different bonds in order to form stable ions. The fragmentation patterns of the complexes **2** and **3** are shown in Figs. 1 and 2, respectively. The mass spectra of the ligand and complexes were in good agreement with the structure as revealed by elemental analyses and spectral analyses.

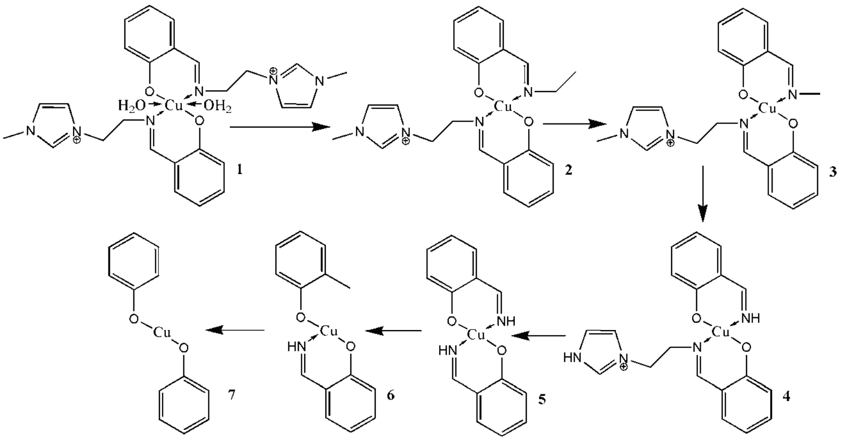

Fig. 1. The mass fragmentation pattern of the Cu(II) complex **2**. *m*/*z*: 1, 557; 2, 439; 3, 427; 4, 397; 5, 304; 6, 290 and 7, 250.

^{1}H-/^{13}C-NMR spectroscopy

The ^{1}H-NMR spectra of ligand and complexes were recorded in DMSO-d_6 and the spectra showed well-resolved signals as expected. The ^{1}H-NMR spectrum of the ligand showed a singlet at δ 3.82 ppm (3H, *s*, CH_3), a triplet at δ 3.99 ppm (2H, *t*, CH_2), a triplet at δ 4.52 ppm (2H, *t*, CH_2), a multiplet at δ 6.85–7.42 ppm (4H, *m*, Ar-H), a singlet at δ 7.67 ppm (1H, *s*, NCH) and a singlet at δ 7.33 ppm (1H, *s*, NCH). The spectrum of the ligand showed a sharp singlet at δ 8.56 ppm assignable to the proton of the azomethine group (–CH=N–), presumably due to the effect of the *ortho*-hydroxyl group in the aromatic ring. A sharp singlet in the downfield region at 12.56 ppm is attributed to the hydroxyl proton. The ^{13}C-

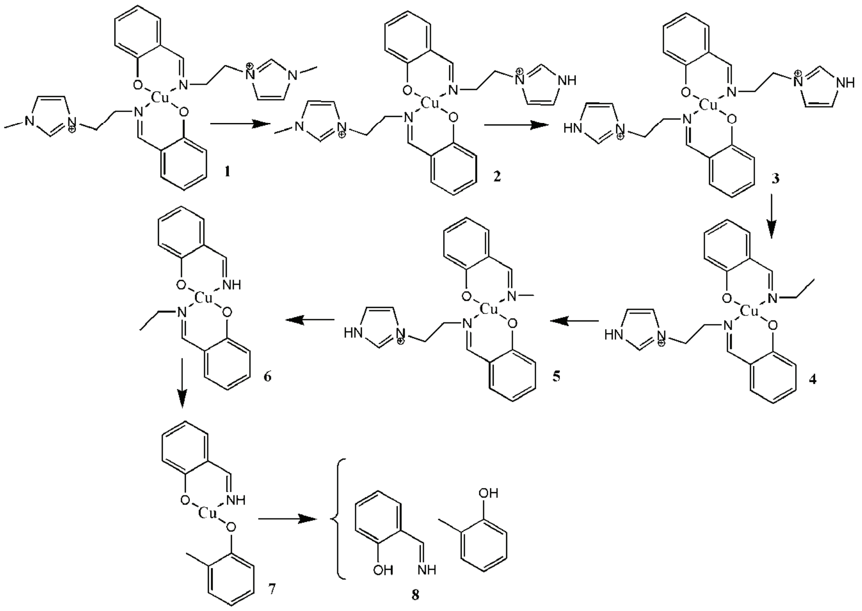

Fig. 2. The mass fragmentation pattern of the Cu(II) complex **3**. *m*/*z*: 1, 523; 2, 507; 3, 491; 4, 427; 5, 413; 6, 333; 7, 333; 8, 231 and 9, 231.

-NMR spectra of the ligand and complexes were recorded in DMSO-d_6 as solvent. The number of signals of sharp peaks represents the number of carbons of the compound that are chemically non-equivalent. The spectra exhibited the azomethine, C=N carbon at δ 159.91 ppm and the phenolic, C–OH carbon at δ 161.29 ppm. The chemical shifts of the aromatic carbons appeared at 137.31, 135.59, 123.75 and 122.41 ppm. The magnetic moment measurement of both the Cu(II) complexes, in which the electronic configuration is d^9, showed that these complexes are paramagnetic (the observed magnetic moments of Cu(II) complex **2** and complex **3** were 1.89 and 1.72 μ_B, respectively) and their ^{1}H-NMR spectra displayed only the broad signals assignable to the alkyl group as all of these proton signals are in close proximity. However, a signal for the Cu(II) center was not detectable.[49]

Antibacterial activity

The newly synthesized Cu(II) complexes along with the ligand were tested against the gram negative bacterium *E. coli* and the gram positive bacterium *B. subtilis* using the well diffusion technique.[40,41] No clear inhibition zone surrounding the well were formed against the ligand and its Cu(II) complexes (inhibition zones against *E. coli* are shown in Fig. 3), whereas $CuCl_2\cdot2H_2O$ and $Cu(NO_3)_2\cdot3H_2O$ showed antibacterial activities with clearly defined well diameters at a concentration of 250 μg mL^{-1} against the bacteria selected for this study.

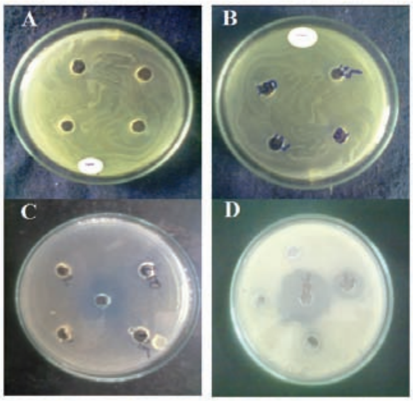

Fig. 3. Inhibition zones for anti-bacterial activities: A: for 1-{2-[(2-hydroxybenzylidene)amino]ethyl}-3-methyimidazolium hexaflurophosphate (**1**); B: for the Cu(II) complex **2**; C: for $CuCl_2 \cdot 2H_2O$; D: for $Cu(NO_3)_2 \cdot 3H_2O$ against *E. Coli*.

CONCLUSION

In this paper, the synthesis, characterization and biological activities of the synthesized ionic liquid based Schiff base and its two Cu(II) complexes were reported. The complexes were formed in 1:2 (metal:ligand) ratio, as confirmed by the spectral analysis. The results of different analytical and spectroscopic analyses revealed that the complexes have different coordination geometries. The Schiff base ligand acts as a bidentate ligand and binds to metal ions through the phenolic oxygen and the azomethine nitrogen Again the synthesized ligand and the complexes showed no antibacterial activities against two commonly known bacteria, *viz.*, *B. subtilis* and *E. coli.*

SUPPLEMENTARY MATERIAL

Physical, analytic and spectral data of the prepared compounds and their IR spectra are available electronically from http://www.shd.org.rs/JSCS/, or from the corresponding author on request.

Acknowledgement. The authors are grateful to the Departmental Special Assistance Scheme under the University Grants Commission, New Delhi (SAP-DRS-III, NO.540/12/DRS/2013) for financial support.

ИЗВОД

КОМПЛЕКСИ БАКРА(II) СА ШИФОВОМ БАЗОМ ДОБИЈЕНОМ ИЗ ЈОНСКЕ ТЕЧНОСТИ [1-{2-((2-ХИДРОКСИБЕНЗИЛИДЕН)АМИНО)ЕТИЛ}-3-МЕТИЛИМИДАЗОЛИЈУМ]PF_6: СИНТЕЗА, КАРАКТЕРИЗАЦИЈА И БИОЛОШКА АКТИВНОСТ

SANJOY SAHA[1], DHIRAJ BRAHMAN[2] AND BISWAJIT SINHA[2]

[1]*Department of Chemistry, Kalimpong College, Kalimpong-734301, India* и [2]*Department of Chemistry, University of North Bengal, Darjeeling-734013, India*

Синтетизована су два комплекса бакра(II) са Шифовом базом добијеном из јонске течности, 1-{2-[(2-хидроксибензилиден)амино]етил}-3-метилимидазолијум-хексафлуорофосфата. Добијени комплекси су окарактерисани применом различитих аналитичких и спектроскопских метода, као што су елементарна микроанализа, магнетна сусцептибилност, UV–Vis, IR и NMR спектроскопија и масена спектрометрија. Применом ових метода утврђено је да се Шифова база бидентатно координује преко атома азота и атома кисеоника, при чему настају комплекси у којима су два молекула лиганда координована за Cu(II) јон. Поред тога, испитивана је биолошка активност комплекса бакра(II).

(Примљено 1. фебруара, ревидирано 1. јуна, прихваћено 21. јула 2014)

REFERENCES

1. J. P. Hallett, T. Welton, *Chem. Rev.* **111** (2011) 3508
2. J. S. Wilkes, *Green Chem.* **4** (2002) 73
3. A. J. Carmichael, M. J. Earle, J. D. Holbrey, P. B. McCormac, K. R. Seddon, *Org. Lett.* **1** (1999) 997
4. N. V. Plechkova, K. R. Seddon, *Chem. Soc. Rev.* **37** (2008) 123
5. T. Welton, *Chem. Rev.* **99** (1999) 2071
6. K. R. Seddon, *J. Chem. Technol. Biotechnol.* **68** (1997) 351
7. P. Wasserscheid, W. Keim, *Angew. Chem., Int. Ed.* **39** (2000) 3772
8. R. Sheldon, *Chem. Commun*. (2001) 2399
9. M. G. Freire, L. M. N. B. F. Santos, A. M. Fernandes, J. A. P. Coutinho, I. M. Marrucho, *Fluid Phase Equilib.* **261** (2007) 449
10. H. Xie, S. Li, S. Zhang, *Green Chem.* **7** (2005) 606
11. R. P. Swatloski, S. K. Spear, J. D. Holbrey, R. D. Rogers, *J. Am. Chem. Soc.* **124** (2002) 4974
12. A. Biswas, R. L. Shogren, D. G. Stevenson, J. L. Willett, P. K. Bhowmik, *Carbohydr. Polym.* **66** (2006) 546
13. M. Zavrel, D. Bross, M. Funke, J. Büchs, A. C. Spiess, *Bioresour. Technol.* **100** (2009) 2580
14. S. S. Y. Tan, D. R. MacFarlane, J. Upfal, L. A. Edye, W. O. S. Doherty, A. F. Patti, J. M. Pringle, J. L. Scott, *Green Chem.* **11** (2009) 339
15. C. Azubuike, H. Rodríguez, A. Okhamafe, R. Rogers, *Cellulose* **19** (2012) 425
16. J. Gao, Z.-G. Luo, F.-X. Luo, *Carbohydr. Polym.* **89** (2012) 1215
17. M. E. Zakrzewska, E. Bogel-Lukasik, R. Bogel-Lukasik, *Energy Fuels* **2**4 (2010) 737
18. J. H. Davis, Jr., *Chem. Lett.* **33** (2004) 1072
19. J. Fraga-Dubreuil, J. P. Bazureau, *Tetrahedron Lett.* **42** (2001) 6097
20. W. Miao, T. H. Chan, *Org. Lett.* **5** (2003) 5003
21. F. Yi, Y. Peng, G. Song, *Tetrahedron Lett.* **46** (2005) 3931
22. E. D. Bates, R. D. Mayton, I. Ntai. J. H. Davis, *J. Am. Chem. Soc.* **124** (2002) 926
23. A. C. Cole, J. L. Jensen, I. Ntai, K. L. T. Tran, *J. Am. Chem. Soc.* **124** (2002) 5962
24. J. Li, Y. Peng, G. Song, *Catal. Lett.* **102** (2005) 159
25. S. Luo, X. Mi, L. Zhang, S. Liu, H. Xu, J. P. Cheng, *Angew. Chem., Int. Ed.* **45** (2006) 3093
26. S. Chandra, K. Gupta, *Trans. Met. Chem.* **27** (2002) 196
27. A. J. Atkins, D. Black, A. J. Blake, A. Marin-Bocerra, S. Parsons, L. Ruiz-Ramirez, M. Schröder, *Chem. Commun.* (1996) 457
28. B. Rihter, S. Srittari, S. Hunter, J. Masnovi, *J. Am. Chem. Soc.* **115** (1993) 3918
29. G. Occhipinti, V. R. Jensen, H. R. Bjrsvik, *J. Org. Chem.***72** (2007) 3561
30. S. K. Hadjikakou, N. Hadjiliadis, *Coord. Chem. Rev.* **253** (2009) 235
31. A. Garoufis, S. K. Hadjikakou, N. Hadjiliadis, *Coord. Chem. Rev.* **253** (2009) 1384
32. C. M. Liu, R. G. Xiong, X. Z. You, Y. J. Liu, K. K. Cheung, *Polyhedron* **15** (1996) 4565
33. S. S. Djebbar, B. O. Benali, J. P. Deloume, *Transition Met. Chem.* **23** (1998) 44
34. Y. J. Hamada, *IEEE Trans. Electron Devices* **44** (1997) 1208

35. R. Ramesh, M. Sivagamasundari, *Synth. React. Inorg. Met.-Org. Chem.* **33** (2003) 899
36. S. K. Bharti, G. Nath, R. Tilak, S. K. Singh, *Eur. J. Med. Chem.* **45** (2010) 651
37. K. Cheng, Q. Z. Zheng, Y. Qian, L. Shi, J. Zhao, H. L. Zhu, *Bioorg. Med. Chem.* **17** (2009) 7861
38. G. Song, Y. Cai, Y. Peng, *J. Comb. Chem.* **7** (2005) 561
39. Y. Peng, Y. Cai, G. Song, J. Chen, *Synlett* (2005) 21470
40. Clinical and Laboratory Standards Institute (NCCLS) 2006, *Performance Standards for Antimicrobial Disk Susceptibility Tests: Approved Standard*, 9th ed. M2-A9, Wayne, PA
41. Clinical and Laboratory Standards Institute (NCCLS) 2006, *Methods for Dilution Antimicrobial Susceptibility Tests for Bacteria that Grow Aerobically; Approved Standard*, 7th ed., M7-A7, Wayne, PA
42. M. Yıldız, Z. Kılıc, T. Hökelek, *J. Mol. Struct.* **1** (1998) 441
43. G.-Y. Yeap, S.-T. Ha, N. Ishizawa, K. Suda, P.-L. Boey, W. A. K. Mahmood, *J. Mol. Struct.* **658** (2003) 87
44. S. A. Abdel-Latif, H. B. Hassib, Y. M. Issa, *Spectrochim. Acta, A* **67** (2007) 950
45. G. A. Kohawole. K. S. Patel, *J. Chem. Soc., Dalton Trans.* (1981) 1241
46. P. Gluvchinsky, G. M. Mocler, *Spectrochim. Acta, A* **32** (1976) 1615
47. M. Thomas, M. K. M. Nair, R. K. Radhakrishan, *Synth. React. Inorg. Met.-Org. Chem.* **25** (1995) 471
48. K. Nakamoto, *Infrared and Raman Spectra of Inorganic and Coordination compounds*, 3rd ed., Wiley, New York, 1997
49. G.-Y. Yeap, B.-T. Heng, *J. Chem. Sci.* **126** (2014) 247.

Journal of the Serbian Chemical Society
JSCS@tmf.bg.ac.rs • www.shd.org.rs/JSCS
J. Serb. Chem. Soc. *80* (1) S7–S9 (2015)
Supplementary material

SUPPLEMENTARY MATERIAL TO

Cu(II) complexes of an ionic liquid-based Schiff base [1-{2-((2-hydroxybenzylidene)amino)ethyl}-3-methylimidazolium]PF_6: Synthesis, characterization and biological activities

SANJOY SAHA[1], DHIRAJ BRAHMAN[2] and BISWAJIT SINHA[2]*

[1]*Department of Chemistry, Kalimpong College, Kalimpong-734301, India and* [2]*Department of Chemistry, University of North Bengal, Darjeeling-734013, India*

J. Serb. Chem. Soc. 80 (1) (2015) 35–43

PHYSICAL, ANALYTIC AND SPECTRAL DATA OF THE PREPARED COMPOUNDS

[2-Aemim]PF$_6$. Yield: 67 %; yellow oil; Anal. Calcd. for $C_6H_{12}F_6N_3P$: C, 57.11; H, 9.59; N, 33.30 %. Found: C, 57.02; H, 9.42; N, 32.88 %; FT-IR (KBr, cm^{-1}): 3412, 3086, 2896, 1581, 1452, 1175, 847; ^{1}H-NMR (500 MHz, D_2O, δ / / ppm): 3.25 (2H, *m*, NH_2–C**H**$_2$), 4.12 (3H, *s*, CH_3), 4.49 (1H, *t*, N–CH_2), 4.52 (1H, *t*, N–CH_2), 7.68 (1H, *s*, NCH), 7.75 (1H, *s*, NCH), 8.63 (2H, *s*, NH_2), 8.99 (1H, *s*, N(H)CN); ^{13}C-NMR (400 MHz, D_2O, δ / ppm): 35.34, 41.04, 53.36, 122.30, 123.29, 136.87; ESI-MS (*m/z* (relative abundance, %)): 126.20 (92.6), M$^+$.

LH (***1***). Yield: 65–70 %; yellow solid; m. p.: 132–133 °C, Anal. Calcd. for $C_{13}H_{16}N_3OPF_6$: C, 40.81; H, 4.19; N, 10.99 %. Found: C, 41.61; H, 4.29; N, 11.20 %; FT-IR (KBr, cm^{-1}): 3430.12, 3151.5, 2923.9, 2866, 1640, 1616.2, 1569.9, 1508.2, 1465.50, 1278.31, 1167.87, 837; ^{1}H-NMR (500 MHz, DMSO-*d*$_6$, δ / ppm): 3.89 (3H, *s*, CH_3), 4.01 (2H, *t*, *J* = , CH_2), 4.48 (2H, *t*, CH_2), 6.79– –6.85 (4H, *m*, Ar-H), 7.66 (1H, *s*, NCH), 7.76 (1H, *s*, NCH), 8.56 (1H, *s*, N=CH), 9.12 (1H, *s*, CH), 12.56 (1H, *s*, OH); ^{13}C-NMR (400 MHz, DMSO-*d*$_6$, δ / ppm): 36.92, 43.54, 51.45, 116.25, 121.56, 122.41, 123.75, 124.62, 130.67, 135.59, 137.31, 159.91, 161.29; ESI-MS (*m/z* (relative abundance, %)): 231 (30.6), [M+1].

Cu(II) complex (***2***). Yield: 75 %; green solid; m. p.: 139–141 °C; Anal. Calcd for $C_{26}H_{34}CuF_{12}N_6O_4P_2$: C, 36.82; H, 4.04; N, 9.91 %. Found: C, 36.12; H, 3.92; N, 9.39 %; FT-IR (KBr, cm^{-1}): 3449.5, 1628, 1545, 1445, 1136, 842.49, 634, 548; ESI-MS (*m/z* (relative abundance, %)): 557 (29.5), [M+2].

Cu(II) complex (***3***). Yield: 77 %; green solid; m.p.: 145–147 °C; Anal. Calcd for $C_{26}H_{30}CuF_{12}N_6O_2P_2$: C, 38.46; H, 3.72; N, 10.35 %. Found: C, 38.01; H,

---

* Corresponding author. E-mail: biswachem@gmail.com

3.69; N, 10.11 %; FT-IR (KBr, cm^{-1}): 3152, 3093, 2867, 1622, 1505, 1448, 1100, 844.5, 620, 558; ESI-MS (*m/z* (relative abundance, %)): 523 (28.6), [M+2].

THE IR SPECTRA OF THE FREE SCHIFF BASE AND ITS Cu(II) COMPLEXES

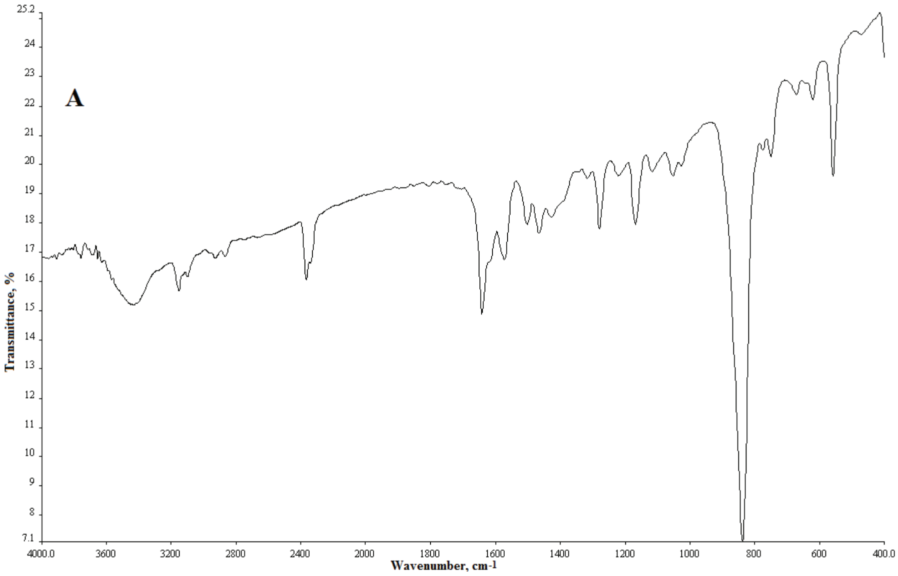

Fig. S-1. IR spectrum of 1-{2-[(2-hydroxybenzylidene)amino]ethyl}-3-methyimidazolium hexafluorophosphate (**1**).

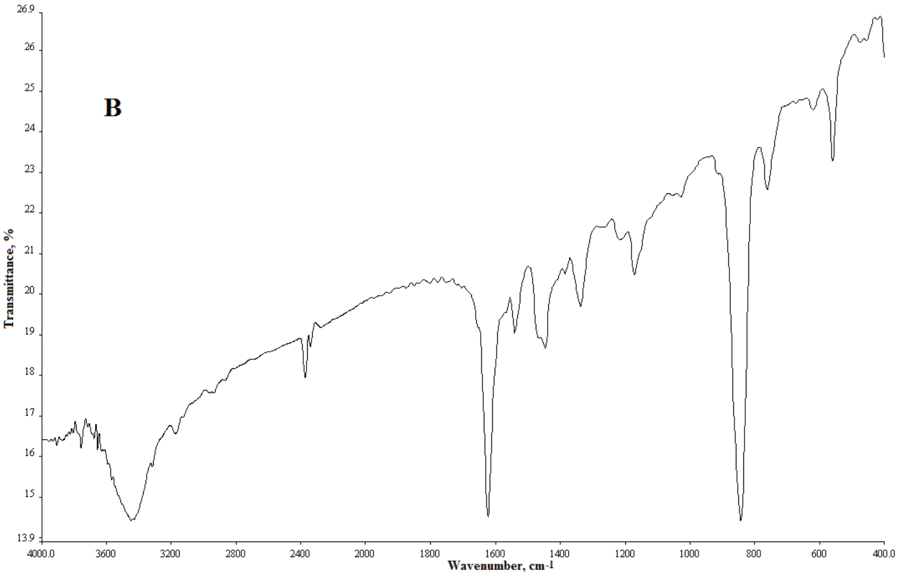

Fig. S-2. IR spectra of Cu(II) complex **2**.

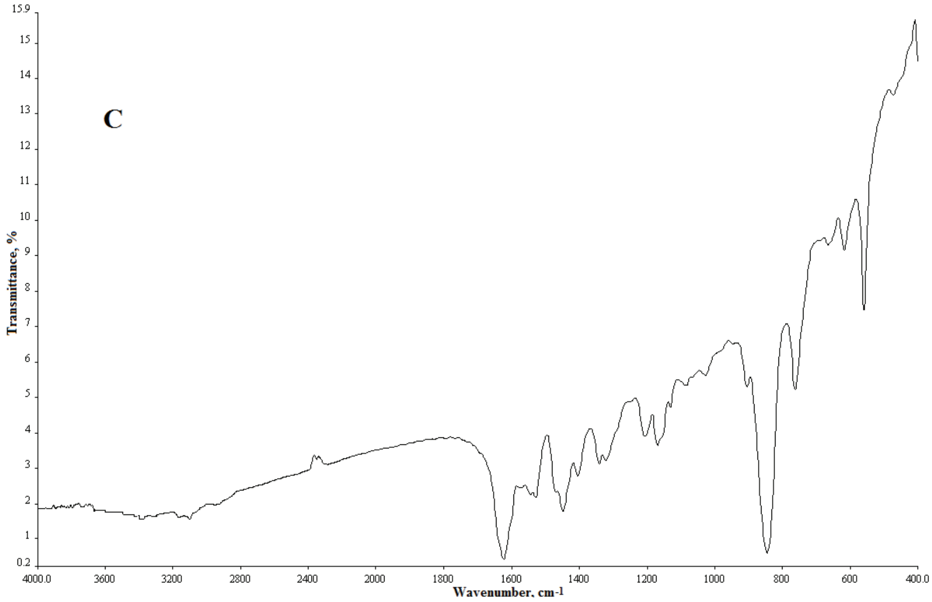

Fig. S-3. IR spectra of Cu(II) complex **3**.

Journal of the Serbian Chemical Society

JSCS-info@shd.org.rs • www.shd.org.rs/JSCS

J. Serb. Chem. Soc. 80 (1) 45–51 (2015) UDC 546.732+547.785.5+546.137:548.7:543.42

JSCS–4695 *Original scientific paper*

Synthesis, crystal structure and properties of $[Co(L)_2](ClO_4)_2$ (L = 1,3-bis(1*H*-benzimidazol-2-yl)-2-oxapropane)

AYDIN TAVMAN* and CIGDEM SAYIL

Department of Chemistry, Faculty of Engineering, Istanbul University, Avcilar, 34320, Istanbul, Turkey

(Received 15 April, revised 26 July, accepted 28 July 2014)

Abstract: The reaction of 1,3-bis(1*H*-benzimidazol-2-yl)-2-oxapropane (**L**) with $Co(ClO_4)_2 \cdot 6H_2O$ in absolute ethanol yielded the bis[1,3-bis(1*H*-benzimidazol-2-yl-κN^3)-2-oxapropane]cobalt(2+) diperchlorate chelate complex ([Co(**L**)$_2$](ClO$_4$)$_2$, **1**). Complex **1** was characterized by elemental analysis, magnetic moment and molar conductivity measurements, thermogravimetric analysis, FT-IR, UV–Vis and mass spectrometry, and its solid-state structure was determined by single crystal X-ray diffraction. According to the elemental and thermogravimetric analysis data, no water either coordinated or uncoordinated is present in **1**. Complex **1** has 1:2 M:L ionic characteristic according to the molar conductivity value. In the complex, the distances between the cobalt and the ethereal oxygen atoms (Co1–O2: 2.805(3); Co2–O1: 2.752(2) Å) show semi-coordination bonding and the Co(II) ion is six-coordinated with a N_4O_2 ligand set, resulting in a distorted octahedron.

Keywords: bis-benzimidazole; oxapropane; cobalt(II) perchlorate; semi-coordination; X-ray diffraction; spectroscopy.

INTRODUCTION

Bis-benzimidazoles are to be known strong chelating agents coordinating through both of the C=N nitrogen atoms. In addition, they have polymer-forming characteristics as typical multidentate ligands.[1,2]

Complexes of bridged bis-benzimidazole ligands with transition metals were examined as potential models of the structure of the metal-binding sites in metalloproteins, such as hemerythrin, hemocyanin, tyrosinase or azurin.[3–10]

The crystal structure of 1,3-bis(1*H*-benzimidazol-2-yl)-2-oxapropane (**L**) was reported by Chen *et al.*[11] Moreover, the crystal structures of some metal complexes of **L** were reported. For example, Cu(II)-dipicrate,[12] Zn(II)-diperchlorate,[13] various Cu(II) salts,[14] Co(II)-dipicrate,[15] Mn(II)-dipicrate[16] complexes

---

* Corresponding author. E-mail: atavman@istanbul.edu.tr

doi: 10.2298/JSC140415081T

were studied, as well as Cu(II) perchlorate mixed complex with bipyridine[17] complexes. In addition, Ni(II) and Zn(II) complexes of 1-benzyl derivative of L, 1,3-bis(1-benzylbenzimidazol-2-yl)-2-oxapropane, were reported.[18,19] Matthews *et al.* synthesized and characterized a series of asymmetric benzimidazolyl-2-oxapropane derivatives and their Cu(II), Zn(II), Cd(II), Hg(II) and Ag(I) complexes.[20] Co(II)[21] and Cd(II)[22] complexes of 1,3-bis(1-ethylbenzimidazol-2-yl)-2-oxapropane was also reported. $CoCl_2$ complex of **L** was used in the polymerization of butadiene as co-catalyst in combination with methylaluminoxane (MAO) and it was shown to catalyze the polymerization with high selectivity.[23] In most of the above mentioned complexes, the ligands acted as tridentate.

In this study, the crystal structure of the $Co(ClO_4)_2$ complex of **L**, bis[1,3-*bis*-(1*H*-benzimidazol-2-yl-κ*N*^{3})-2-oxapropane]cobalt(2+) diperchlorate ($C_{32}H_{28}N_8O_{10}Cl_2Co$, **1**, Fig. 1), is reported. The structure of **1** was also characterized by elemental analysis, molar conductivity, FT-IR, UV–Vis, mass spectrometry and thermogravimetric analysis.

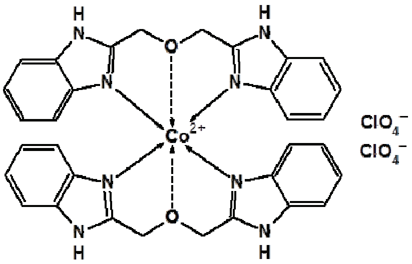

Fig. 1. Chemical diagram of the title compound.

EXPERIMENTAL

Elemental analysis data were obtained using a Thermo Finnigan Flash EA 1112 analyzer. The molar conductivity was measured on a WTW Cond315*i* conductivity meter in DMF at 25 °C. The magnetic moment measurement was realized on a Sherwood Scientific MK1 apparatus at room temperature by the Gouy method. The UV–Vis spectra were performed on a Perkin Elmer Lambda 25 UV/Visible spectrometer in ethanol (10^{-4} mol L^{-1}). The FT-IR spectra were recorded in KBr disks on a Mattson 1000 FT-IR spectrometer. Thee spray ionization-mass spectrometry (ESI-MS) analysis was performed in the positive ion mode using a Thermo Finnigan LCQ Advantage MAX LC/MS/MS instrument. The thermogravimetric (TG) study was realized on a Shimadzu TG-60WS instrument, at a heating rate of 10 °C min^{-1} under a dynamic air atmosphere at a flow rate of 50 mL min^{-1}.

Synthesis of **L**

The ligand was synthesized from a 1:2 mole ratio of diglycolic acid (also known as 2,2′-oxydiacetic acid), 1.34 g, 0.01 mol) and *o*-phenylenediamine (2.16 g, 0.02 mol) in 5.5 M HCl (20 mL) according to the literature.[17,24]

*Synthesis of [Co(**L**)$_2$](ClO$_4$)$_2$*

The ligand, **L** (0.209 g; 0.75 mmol), and Co(ClO$_4$)$_2$·6H$_2$O (0.275 g; 0.75 mmol) were dissolved separately in absolute ethanol (10 mL). Then the solutions were mixed and refluxed for 2 h. (After mixing the solutions, a purple turbidity formed). The mixture was filtered and the filtrate was kept at room temperature after the volume was reduced to 10 mL. Purple crystals suitable for X-ray diffraction studies were formed after 3 days. The crystals were filtered and dried at room temperature (0.232 g, yield: 76 %).

Crystallography

The diffraction measurements were performed at 20±1 °C on a Rigaku RAXIS RAPID imaging plate area detector using graphite monochromated Mo-Kα radiation (λ= 0.71070 Å), with the distance between the crystal and the detector being 127.40 mm (Istanbul University Advanced Analyses Laboratory, Turkey). For the structure solution, 127754 reflections were collected, 6775 were unique (R_{int} = 0.050); equivalent reflections were merged. An empirical absorption correction was applied that resulted in transmission factors ranging from 0.57 to 0.84. The data were corrected for Lorentz and polarization effects. The structure of **1** was solved by SIR92[25] and refined with CRYSTALS.[26] The non-hydrogen atoms were refined anisotropically. H atoms were treated as riding, with C–H = 0.95(6) Å and U_{iso}(H) = = 1.2U_{eq}(C) and were constrained refined. All calculations were performed using the CrystalStructure[27] crystallographic software package.

RESULTS AND DISCUSSION

General properties

Elemental analysis showed that the composition of **1** is [Co(**L**)$_2$](ClO$_4$)$_2$. Complex **1** is 2:1 electrolyte according to the molar conductivity data (126 S m^2 mol^{-1}) in DMF.[28] Thermogravimetric analysis data and elemental analysis showed that there are no coordinated or uncoordinated water in the structure of **1**. It started to decompose at about 250 °C and decomposed exactly above 550 °C to CoO (the weight percentage of CoO in the title compound is 9.1%, Fig. S-1 of the Supplementary material to this paper). The considerable weight loss near 300 °C should be due to the decomposition of the 1,3-bis(1*H*-benzimidazol-2-yl)-2-oxapropane ligand.

In the FT-IR spectrum of **1**, a strong band at 1115 cm^{-1} could be assigned to the stretching vibrations of the uncoordinated perchlorate anion, ν(Cl=O). In addition, the medium band at 627 cm^{-1} is due to the ν_4 mode of the perchlorate anion.[29–31] The new broad medium band at 698 cm^{-1} in the IR spectrum could be attributed to the ν(Co–N) coordination band.[32]

Compound **1** shows three absorption bands in the visible region with maxima at 558, 526 and 456 nm. The 558 and 526 nm bands may be assigned to $^4T_{1g}(F) \rightarrow {}^4T_{1g}(P)$ and $^4T_{1g}(F) \rightarrow {}^4A_{2g}(F)$ transitions, respectively, indicating a distorted octahedral geometry. The 456 nm shoulder may be due to ligand to metal charge transfer transitions.[32,33]

The observed magnetic moment value for **1** at room temperature, μ_B = 4.12 μ_B, is near the range reported for distorted octahedral Co(II) complexes having three unpaired electrons (high spin).[33,34]

In the ESI-MS spectrum, the molecular ion peak of **1** is appears at *m*/*z* 835.90 (19.2 %) as $[(M+23)–2]^+$ (sodiated molecular ion). The *m*/*z* 614.7 fragment is due to $[CoL(L–H)]^+$ ($[C_{32}H_{28}CoN_8O_2]^+$) and its intensity was 100 %. Furthermore, a fragment at *m*/*z* 279.7, corresponding to the ion peak of the ligand, was determined with an intensity of 18 %.

*Crystal structure of **1***

The details of the X-ray data collection, structure solution and structure refinements are given in Table I. Compound **1** crystallizes in the monoclinic system with space group *P*2/n. Selected bond distances and angles are listed in Table S-I and selected torsion angles are given in Table S-II in Supplementary material. The ORTEP 3 view of the molecular structure of the title compound is given in Fig. 2; a crystal-packing diagram of **1** is given in Fig. S-2 of the Supplementary material. Crystallographic data has been deposited with the Cambridge Crystallographic Data Base as CCDC reference number 836316 for the $[Co(\mathbf{L})_2](ClO_4)_2$ complex.

TABLE I. X-Ray crystallographic data for **1**

Empirical formula	$C_{32}H_{28}Cl_2CoN_8O_{10}$
Molecular weight, g mol^{-1}	814.46
Color, habit	Purple, chunk
Crystal system	Monoclinic
a / Å	19.448(2)
b / Å	9.6228(6)
c / Å	20.471(2)
V / Å^3	3576.6(6)
β (°)	110.999(4)
Space group	*P*2/*n*
Z value	4
d_{calc} / g cm^{-3}	1.512
μ(Mo-Kα) / cm^{-1}	6.97
F(000)	1668.00
Index ranges, h, k, l	$–23 \leq h \leq 23, –11 \leq k \leq 10, –24 \leq l \leq 24$
θ range for data collection, °	2.7–25.0
No. observations ($I > 3\sigma(I)$)	5899
No. variables	516
Residuals: R ($I > 3\sigma(I)$)	0.094
Residuals: R_w ($I > 3\sigma(I)$)	0.053
Goodness of fit indicator	1.161

The coordination cations ($[Co(L)_2]^{2+}$) are stabilized by weak $\pi\cdots\pi$ stacking between the benzimidazole rings. In addition, no inter- or intra-molecular hydrogen bonding was detected.

The ligand (**L**) is potentially tridentate of NON-type. In many complexes described in the literature, **L** acted as tridentate towards the metal ions coordinating through the ethereal oxygen atom and the C=N nitrogen atoms. Some of the found M–O bond lengths were as follows: Zn–O, 2.35;[13] Mn–O, 2.38;[16] Ni–O, 2.10;[18] Cu–O, 2.53;[17] Cd–O, 2.54 Å.[22] However, in the present study, the distances between the cobalt and the ethereal oxygen atoms [O1–Co2: 2.752(2) and Co1–O2: 2.805(3) Å] are longer than in a coordination bond. Metal–ligand interactions with such long distances are often viewed as semi coordination.[35,36] Likewise, the bending of the oxygen atoms towards the cobalt atom supports semi-coordination. Thus, **L** acted as tridentate towards $Co(ClO_4)_2$ in this study and the Co(II) ion is six coordinate with a N_4O_2 ligand set from two ligands and the complex is distorted octahedral.

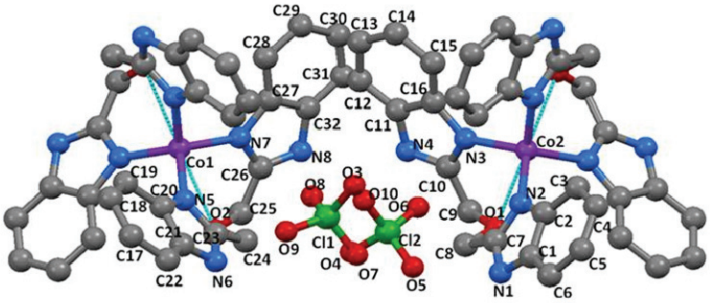

Fig. 2. A molecular drawing of the title compound. H atoms are omitted for clarity.

CONCLUSIONS

In this study, bis[1,3-bis(1*H*-benzimidazol-2-yl-κN^3)-2-oxapropane]cobalt(2+) diperchlorate was synthesized and recrystallized from ethanol as single crystals suitable for X-ray study. The complex was characterized by elemental analysis, magnetic moment and molar conductivity measurements, thermogravimetric analysis, and FT-IR, UV–Vis and mass spectrometry. The molar conductivity of 1 measured in DMF falls within the range of values typical for 2:1 electrolytes. The room temperature magnetic moment value, $\boldsymbol{\mu}_B$, of 4.12 μ_B falls within the range of values typical for high spin octahedral Co(II) complexes. The thermogravimetric analysis data showed that there was no coordinated or uncoordinated water molecule in compound **1**, which was supported by elemental analysis. In addition, the structure of **1** was determined by X-ray diffraction. The distances between the cobalt and the ethereal oxygen atoms (Co1–O2: 2.805(3); Co2–O1: 2.752(2) Å) indicate semi-coordination bonding. According to these data, the chelate complex **1** has four five-membered Co–N–C–CH$_2$–O rings, and the Co(II) ion has a distorted octahedral geometry with four nitrogen and two oxygen atoms from two ligands.

SUPPLEMENTARY MATERIAL

Analytical, conductivity, magnetic and spectral data, as well as TGA data and packing diagram of the title compound are available electronically from http://www.shd.org.rs/JSCS/, or from the corresponding author on request.

Acknowledgement. This work was supported by the Scientific Research Projects Unit of Istanbul University, Turkey.

ИЗВОД

СИНТЕЗА, КРИСТАЛНА СТРУКТУРА И СВОЈСТВА $[\mathrm{Co}(\mathbf{L})_2](\mathrm{ClO}_4)_2$ (**L** = 1,3-БИС(1*H*-БЕНЗИМИДАЗОЛ-2-ИЛ)-2-ОКСАПРОПАН)

AYDIN TAVMAN и CIGDEM SAYIL

Department of Chemistry, Faculty of Engineering, Istanbul University, Avcilar, 34320, Istanbul, Turkey

У реакцији 1,3-бис(1*H*-бензимидазол-2-ил)-2-оксапропана (**L**) са $\mathrm{Co(ClO_4)_2 \cdot 6H_2O}$ у апсолутном етанолу добијен је хелатни комплекс бис[1,3-бис(1*H*-бензимидазол-2-ил-κN^3)-2-оксапропан]кобалт(2+)-диперхлорат, $[\mathrm{Co}(\mathbf{L})_2](\mathrm{ClO}_4)_2$ (**1**). Овај комплекс је окарактерисан помоћу елементалне анализе, мерења магнетног момента и моларне проводљивости, термогравиметријске анализе, FT-IR, UV–Vis и масене спектрометрије. Кристална структура комплекса **1** је одређена методом дифракције X-зрака. На основу термогравиметријске и елементалне анализе нађено је да у комплексу **1** нема координованих и кристалних молекула воде. На основу мерења моларне проводљивости закључено је да су у комплексу **1** кобалт(II) и лиганд координовани у молском односу 1:2. На основу измерених растојања између Co(II) јона и атома кисеоника у аксијалном положају (Co1–O2: 2,805(3); Co2–O1: 2,752(2)) може се закључити да је у овом случају присутна парцијално-координативна веза и да је Co(II) јон хексакоординован са $\mathrm{N_4O_2}$ лигандним системом, као и то да комплекс **1** има деформисану октаедарску геометрију.

(Примљено 15. априла, ревидирано 26. јула, прихваћено 28. јула 2014)

REFERENCES

1. S. K. Chawla, *Polyhedron* **18** (1999) 1397
2. P. Lavrenko, O. Okatova, I. Strelina, M. Bruma, B. Schulz, *Polymer* **44** (2003) 2919
3. P. L. Holland, W. B. Tolman, *J. Am. Chem. Soc.* **122** (2000) 6331
4. H. Adams, A. B. Neil, J. D. Crane, D. E. Fenton, J. M. Latour, J. M. Williams, *J. Chem. Soc. Dalton Trans.* **1990** (1990) 1727
5. T. N. Sorrel, M. L. Garrity, *Inorg. Chem.* **30** (1991) 210
6. S. Chen, J. Richardson, *Inorg. Chem.* **33** (1994) 2376
7. S. Tandon, L. Thomson, J. Bridson, J. Dewan, *Can. J. Chem.* **70** (1992) 2771
8. J. Sessler, J. Hugdahl, B. Lynch, *Inorg. Chem.* **30** (1991) 334
9. A. van Steenberger, E. Bouwman, A. de Graaf, W. Driessen, J. Reedijk, P. Zanello, *J. Chem. Soc. Dalton Trans.* **1990** (1990) 3175
10. J. Lockhart, W. Clegg, M. Hill, D. Rushton, *J. Chem. Dalton Trans.* **1990** (1990) 3541
11. Y. Chen, J. Guo, R. Yun, H. Wu, *Acta Crystallogr., E* **65** (2009) o948
12. R. Yun, W. Ying, B. Qi, X. Fan, H. Wu, *Acta Crystallogr., E* **64** (2008) m1529

13. Q. H. Zhou, P. Yang, *Acta Chim. Sin.* **64** (2006) 793
14. R. P. Bonomo, E. Rizzarelli, M. Bressan, A. Morvillo, *Inorg. Chim. Acta* **186** (1991) 21
15. H. Wu, R. Yun, X. Huang, Q. Sun, B. Qi, *Acta Crystallogr., E* **65** (2009) m851
16. T. Sun, K. Li, Y. Lai, R. Chen, H. Wu, *Acta Crystallogr., E* **66** (2010) m1058
17. Y. T. Cheng, H. L. Chen, S. Y. Tsai, C. C. Su, H. S. Tsang, T. S. Kuo, Y. C. Tsai, F. L. Liao, S. L. Wang, *Eur. J. Inorg. Chem.* **2004** (2004) 2180
18. H. Wu, R. Yun, K. Li, K. Wang, X. Huang, T. Sun, *Synth. React. Inorg., Met.-Org., Nano-Met. Chem.* **39** (2009) 614
19. H. Wu, R. Yun, K. Li, S. Tao, K. Wang, *Acta Crystallogr., E* **65** (2009) m786
20. a) C. J. Matthews, T. A. Leese, W. Clegg, M. R. J. Elsegood, L. Horsburgh, J. C. Lockhart, *Inorg. Chem.* **35** (1996) 7563; b) C. J. Matthews, W. Clegg, S. L. Heath, N. C. Martin, M. N. S. Hill, J. C. Lockhart, *Inorg. Chem.* **37** (1998) 199
21. H.-L. Wu, F. Kou, F. Jia, B. Liu, J.-K. Yuan, Y. Bai, *J. Coord. Chem.* **64** (2011) 3041
22. H. Wu, F. Kou, B. Liu, F. Jia, J. Yuan, Y. Bai, R. Yun, X. Fan, *Synth. React. Inorg., Met.--Org., Nano-Met. Chem.* **42** (2012) 839
23. R. Cariou, J. J. Chirinos, V. C. Gibson, G. Jacobsen, A. K. Tomov, G. J. P. Britovsek, A. J. P. White, *Dalton Trans.* **39** (2010) 9039
24. D. Kong, Y. Xie, *Inorg. Chim. Acta* **338** (2002) 142
25. D. J. Watkin, C. K. Prout, J. R. Carruthers, P. W. Betteridge, CRYSTALS 10, PW, Chemical Crystallography Laboratory, Oxford, 1996
26. CrystalStructure 3.5.1, Crystal Structure Analysis Package, Rigaku and Rigaku/MSC 9009, New Trails Dr. The Woodlands, TX, 2000–2003
27. L. J. Farrugia, *J. Appl. Crystallogr.* **30** (1997) 565
28. W. Geary, *Coord. Chem. Rev.* **7** (1971) 81
29. B. Gu, J. D. Coates, *Perchlorate: Environmental Occurrence, Interactions and Treatment*, Springer Science + Business Media, Inc., New York, 2006
30. K. Nakamoto, *Infrared and Raman Spectra of Inorganic and Coordination Compounds, Part B*, Wiley, New York, 1997
31. A. Tavman, S. Ikiz, A. F. Bagcigil, Y. Ozgür, S. Ak, *Bull. Chem. Soc. Ethiop.* **24** (2010) 391
32. T. J. Hubin, N. W. Alcock, H. J. Clase, L. L. Seib, D. H. Busch, *Inorg. Chim. Acta* **337** (2002) 91
33. K. Pachori, S. Malik, S. Wankhede, *Res. J. Chem. Sci.* **4** (2014) 75
34. F. A. Cotton, G. Wilkinson, *Advanced Inorganic Chemistry*, Wiley, New York, 1988, p. 725
35. X.-Z. Li, X.-J. Kong, C.-Q. Li, H. Qu, L.-N. Zhu, D.-Z. Liao, *Inorg. Chem. Commun.* **27** (2013) 114
36. G. A. van Albada, P. Mutikainen, U. Turpeinen, J. Reedijk, *Polyhedron* **25** (2006) 81.

Journal of the Serbian Chemical Society
JSCS@tmf.bg.ac.rs • www.shd.org.rs/JSCS
J. Serb. Chem. Soc. 80 (1) S10–S12 (2015)
Supplementary material

SUPPLEMENTARY MATERIAL TO

Synthesis, crystal structure and properties of $[Co(L)_2](ClO_4)_2$ (L = 1,3-bis(1*H*-benzimidazol-2-yl)-2-oxapropane)

AYDIN TAVMAN* and CIGDEM SAYIL

Department of Chemistry, Faculty of Engineering, Istanbul University, Avcilar, 34320, Istanbul, Turkey

J. Serb. Chem. Soc. 80 (1) (2015) 45–51

IR DATA FOR THE LIGAND

*1,3-Bis(1*H*-benzimidazol-2-yl)-2-oxapropane (**L**)*. IR (KBr, cm^{-1}): 3049*m,br*, 2947*m*, 2846*m*, 2744*m*, 1625*m*, 1590*m*, 1457*s*, 1432*s*, 1336*s*, 1272*s*, 1232*s*, 1103*s*, 1038*m*, 923*m*, 748*s*, 433*m*.

ANALYTICAL, PHYSICAL AND SPECTRAL DATA OF THE TITLE COMPOUND

*Bis[1,3-bis(1*H*-benzimidazol-2-yl-κN^3)-2-oxapropane]cobalt(2+)-diperchlorate (**1**)*. M.p.: 234 °C; Anal. Calcd. for $C_{32}H_{28}Cl_2CoN_8O_{10}$: C, 47.19; H, 3.47; N, 13.76 %. Found: C 46.78, H 3.62, N 13.54 %; IR (KBr, cm^{-1}) 3273 (NH stretching), 3080*m* (CH stretching of aromatic ring), 2933 ($–CH_2–$ stretching), 1630*m* (C=N stretching), 1604*m* (C=C stretching), 1484*m*, 1462*s*, 1399*m*, 1283*m*, 1115*s* (Cl=O stretching of perchlorate anion), 1088*s*, 1046*s* (C–O stretching of ethereal bridge), 1009*m*, 745*s* (out of plane bending CH of aromatic ring), 698*m* (Co–N stretching), 627*m* (Cl=O ν_4 stretching mode of perchlorate), 584*w*; MS (*m*/*z*, (relative abundance, %)): 835.90 (19.2, $[(M+23)–2]^+$, {814.45+23 = 837.45}); 279.7 (11.8, $[ML+1]^+$ for the ligand); 614.7 (100, $[Co(L)2–1]^+$); 714.1 (26.5, $[2L+Co+ClO_4]^+$); 484.6 (16.7, $[L+Co+ClO_4]^+$); UV–Vis (MeOH, λ_{max} / nm): 558*w*, 526*sh*, 476*sh*, 280*m*, 274*s*, 268*sh*, 246*s,br*, 218*s*, 212*s*; Molar conductivity (DMF, 25 °C): 126 S m^2 mol^{-1}. Magnetic moment, $\boldsymbol{\mu}_{eff}$ / μB: 4.12.

---

* Corresponding author. E-mail: atavman@istanbul.edu.tr

TABLE S-I. Selected bond lengths and angles

Bond lengths, Å			
Co(1)–N(5)	2.034(2)	Co(1)–N(7)	2.032(4)
Co(2)–N(2)	2.028(2)	Co(2)–N(3)	2.053(4)
Co(1)–O(2)	2.805(3)	Co(2)–O(1)	2.752(2)
O(2)–C(24)	1.431(5)	O(2)–C(25)	1.435(5)
N(2)–C(2)	1.408(5)	N(2)–C(7)	1.333(4)
C(1)–C(2)	1.396(5)	C(7)–C(8)	1.474(5)
Bond angles, °			
N(5)–Co(1)–N(7)	114.3(2)	N(2)–Co(2)–N(3)	112.9(1)
O(1)–Co(2)–N(2)	162.3(6)	O(2)–Co(1)–N(5)	155.7(2)
C(8)–O(1)–C(9)	113.1(3)	C(24)–O(2)–C(25)	112.1(3)
C(2)–N(2)–Co(2)	131.0(2)	C(7)–N(2)–Co(2)	123.6(3)
C(10)–N(3)–Co(2)	125.1(4)	C(16)–N(3)–Co(2)	129.6(2)
C(23)–N(5)–Co(1)	123.8(3)	C(8)–C(7)–N(1)	125.2(3)
C(8)–C(7)–N(2)	122.5(3)	O(1)–C(8)–C(7)	104.0(3)
C(10)–C(9)–O(1)	108.6(3)	N(4)–C(10)–C(9)	122.5(3)
O(2)–C(24)–C(23)	104.7(3)	C(26)–C(25)–O(2)	109.2(3)

TABLE S-II. Selected torsion angles (°)

N(7)–Co(1)–N(5)–C(20)	149.9(3)	N(7)–Co(1)–N(5)–C(23)	–21.8(3)
N(5)–Co(1)–N(7)–C(26)	59.9(4)	N(5)–Co(1)–N(7)–C(27)	–116.7(4)
N(2)–Co(2)–N(3)–C(10)	–66.7(3)	N(3)–Co(2)–N(2)–C(7)	34.0(4)
C(9)–O(1)–C(8)–C(7)	–154.7(3)	C(8)–O(1)–C(9)–C(10)	73.9(3)
Co(1)–N(7)–C(26)–N(8)	–177.1(3)	O(2)–C(25)–C(26)–N(8)	150.5(4)
Co(1)–N(7)–C(27)–C(28)	–4.6(7)	Co(1)–N(7)–C(26)–C(25)	3.3(6)
N(1)–C(7)–C(8)–O(1)	–134.3(4)	Co(1)–N(7)–C(27)–C(32)	177.6(3)
N(5)–C(23)–C(24)–O(2)	–37.8(4)	N(2)–C(7)–C(8)–O(1)	44.2(6)
O(2)–C(25)–C(26)–N(7)	–29.9(6)		

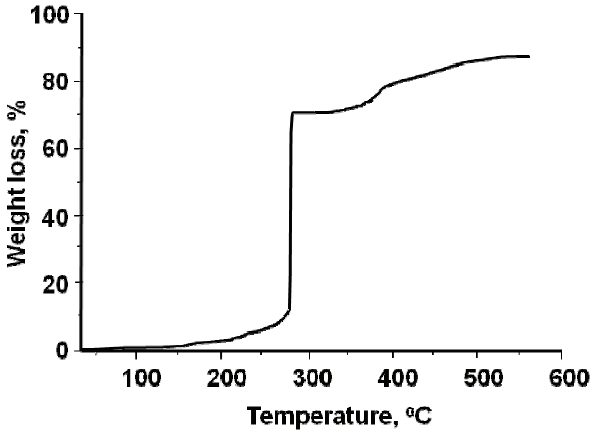

Fig. S-1. TGA curve of the title compound.

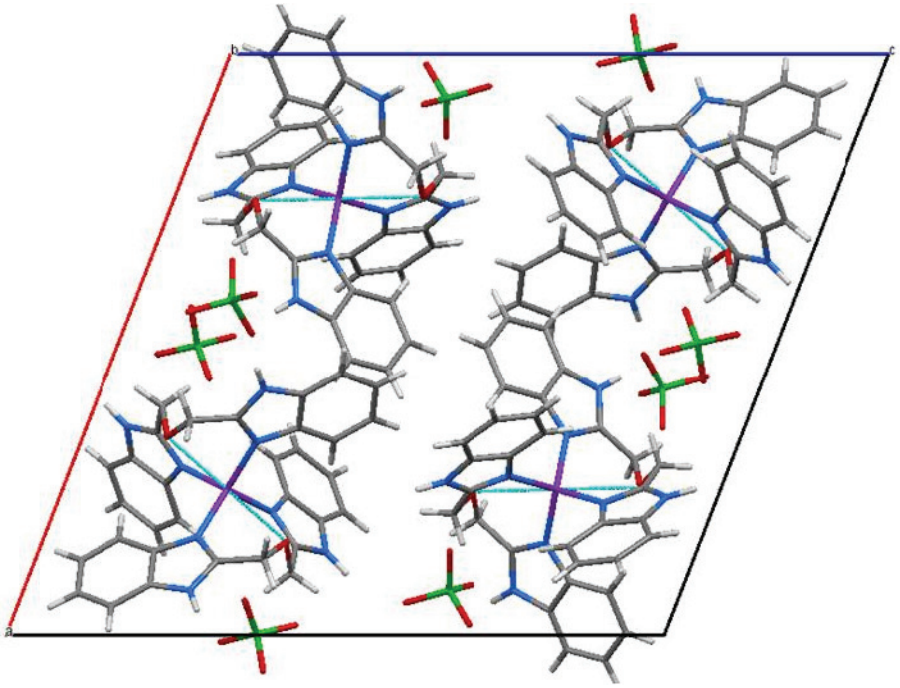

Fig. S-2. A packing diagram of the title compound (view *b*).

Journal of the Serbian Chemical Society
JSCS-info@shd.org.rs • www.shd.org.rs/JSCS

J. Serb. Chem. Soc. 80 (1) 53–62 (2015)
JSCS–4696

UDC 547.421.22–31+547.556.3:541.124
Original scientific paper

A theoretical study on the mechanism of the reaction between azacyclopropenylidene and oxirane

YING JING[1] and XIAOJUN TAN[2]*

[1]*The General Hospital of Jinan Military Command, Jinan, Shandong, 250031, P. R. China and* [2]*College of Biological Science and Technology, University of Jinan, Jinan, Shandong, 250022, P. R. China*

(Received 12 May, accepted 28 May 2014)

Abstract: The reaction mechanism between azacyclopropenylidene and oxirane was systematically investigated employing the second-order Møller–Plesset perturbation theory (MP2) method to understand better the reactivity of azacyclopropenylidene with the three-membered ring compound oxirane. Geometry optimization, vibrational analysis, and energy property for the involved stationary points on the potential energy surface were calculated. The energies of all the species were also further corrected by CCSD(T)/6-311+G* single-point calculations. The calculational results showed that there are two possible reaction pathways. From the kinetic viewpoint, the first pathway is primary. From the viewpoint of thermodynamics, the second dominates.

Keywords: azacyclopropenylidene; oxirane; reaction mechanism; MP2 method.

INTRODUCTION

Much attention has recently been paid to carbon chain molecules containing heteroatoms (N,[1–8] O,[9,10] S,[11–13] and Si[14–16]) due to their astrophysical abundance and interesting spectroscopic properties. A typical example is cyanopolyacetylenes, $HC_{2n+1}N$, in which $HC_{11}N$ is one of the largest carbon chain molecules observed in interstellar medium.[17] In contrast to $HC_{2n+1}N$ cyanopolyacetylenes, systematic studies on $HC_{2n}N$ molecules containing an even number of carbon atoms were relatively scarce. Despite this, $HC_{2n}N$ molecules and their geometrical isomers are still very important, as they are good candidates for astrophysical observations by microwave and infrared spectroscopy due to their rather large dipole moments. An exciting fact is that HC_2N was observed in interstellar space.[18] Many experimental and computational methods were utilized in studies on the structures and the relative energies of some isomers of this system. Numerous studies revealed that many isomers of HC_2N molecules of

---

* Corresponding author. E-mail: chem.2001@163.com
doi: 10.2298/JSC140509056J

similar energies exist with different kinds of geometries (linear, bent or cyclic) or different multiplicities (singlet or triplet).[19–30] Inostroza *et al*. characterized quasi-linear triplet, bent singlet, and cyclic singlet HC_2N isomers and determined their molecular properties in a series of highly accurate *ab initio* level of theory investigation.[27] In addition, the cyclic HC_2N isomer was found to be an intermediate between the interconversion of the bent HCCN and an unknown bent HCNC on the hypersurface of neutral, anionic, and cationic species where barriers are feasible.[31] The most stable singlet state of the HC_2N molecule is named azacyclopropenylidene and its structure, which was confirmed by spectroscopy and calculation, is displayed in Scheme 1.

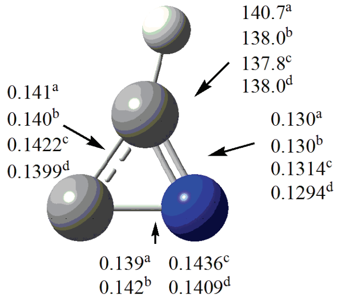

Scheme 1. Geometrical parameters for azacyclopropenylidene calculated at diverse levels. The bond lengths are in nm and the bond angle in degree (a: B3LYP/6-311++G**;[28] b: MP2/6-311++G**;[28] c: QCISD(T)/D95**;[21] d: CCSD(T)/cc-pVTZ[30]).

In 1998, matrix generations of singlet azacyclopropenylidene and singlet bromocyanocarbene (BrCCN) were researched by Maier and co-workers.[32] Casavecchia *et al*. reported the dynamics of a reaction of nitrogen atom with an unsaturated hydrocarbon by combining crossed molecular beam experiments and *ab initio* molecular orbital calculations. They found that azacyclopropenylidene is one of the products of the reaction of nitrogen atom with C_2H_2 in the upper atmosphere of Titan.[33] Thus, azacyclopropenylidene seems to be a good candidate for astrophysical detection, considering these various possible formation pathways and its large dipole moment.[34]

Computation of HC_2N molecules would be very helpful in the elucidation of the reactivity and kinetic stability of these molecules, but less attention has been paid to the reactivity of azacyclopropenylidene with active species containing small ring compounds until now. In the present study, a comprehensive theoretical investigation of the reaction mechanism between azacyclopropenylidene and oxirane was performed by employing the second-order Møller–Plesset perturbation theory (MP2) method in order to understand better the reactivity of azacyclopropenylidene. To the best of our knowledge, this study is the first report of the reaction mechanism between azacyclopropenylidene and small ring compounds. The present results will enrich the available data for the relevant azacyclopropenylidene chemistry and discuss the possibility of the formation of larger molecules by means of azacyclopropenylidene in interstellar space.

CALCULATION METHOD

The MP2 method in combination with 6-311+G* basis set was employed to locate all the stationary points along the reaction pathways. Frequency analyses were performed to confirm the nature of the minima and transition states. Moreover, intrinsic reaction coordinate (IRC) calculations were also performed to validate further the calculated transition states connecting reactants and products. Additionally, the relevant energy quantities, such as reaction energies and barrier heights, were corrected with zero-point vibrational energy (ZPVE) corrections.

To further refine the calculated energy parameters, single point energy calculations were performed at the CCSD(T)/6-311+G* level of theory based on the stationary points optimized at the MP2/6-311+G* level of theory. As summarized in Table I, both levels gave consistent results for the calculated reaction profile of the insertion reaction. For the sake of simplicity, mainly the energetic results at the CCSD(T)//MP2/6-31+G* level are discussed below if not noted otherwise.

All the calculations have been performed using the Gaussian 98 program.[35]

TABLE I. The calculated relative energy (in kJ mol^{-1}) with respect to the isolated reactants at the MP2/6-311+G* level of theory considering the ZPVE corrections; the data in the brackets refer to the results at the CCSD(T)//MP2/6-311+G* level of theory considering the ZPVE corrections

Pathway	Relative Energy			
	TS	IM		
	171.0 (173.2)	–273.4 (–255.6)		
Pathway (1)	TS1	P1		
	–87.8 (–93.3)	–181.3 (–186.0)		
Pathway (2)	TS2a	IM2a	TS2b	P2
	8.9 (19.3)	–126.0 (–124.9)	–57.8 (–60.8)	–260.0 (–255.8)

RESULTS AND DISCUSSION

The two proposed possible reaction pathways for the insertion reaction between azacyclopropenylidene and oxirane are displayed in Scheme 2. The geometric parameters for the reactants (azacyclopropenylidene (R1) and oxirane (R2)), transition states (TS), intermediates (IM), and products (P) involved in

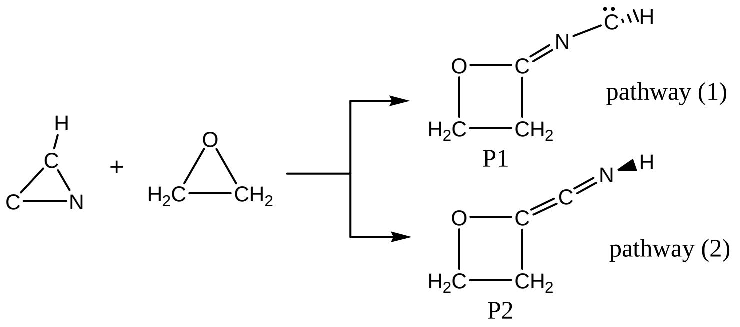

Scheme 2. The two proposed reaction pathways for the insertion reaction between azacyclopropenylidene and oxirane.

pathways (1) and (2) are shown in Fig. 1. Correspondingly, the calculated relative energies for the available stationary points are summarized in Table I. The corresponding reaction profile is illustrated in Fig. 2.

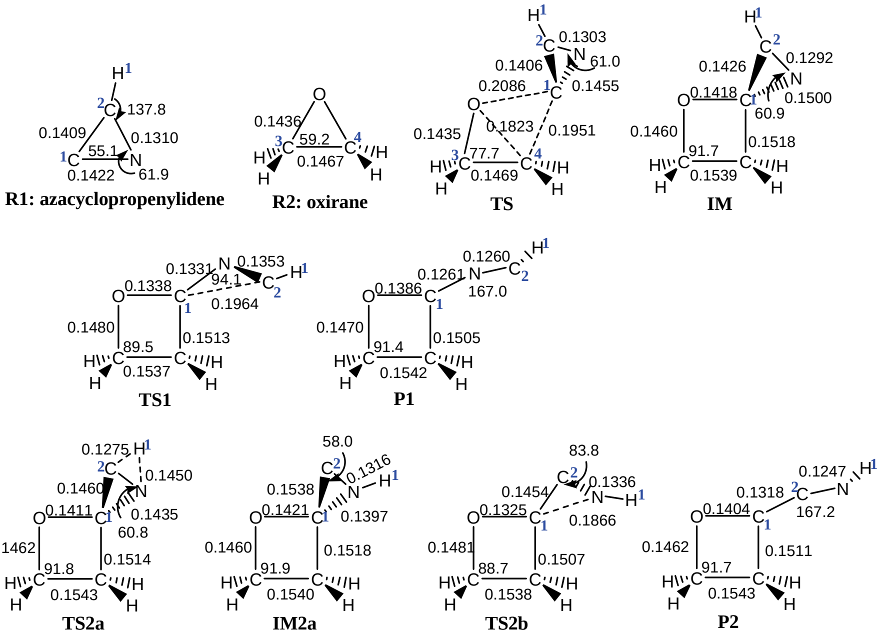

Fig. 1. Optimized structures of the reactants (azacyclopropenylidene and oxirane), transition states (TS), intermediates (IM), and products (P) in reaction pathways (1) and (2) at the MP2/6-311+G* level of theory, in which the bond lengths and bond angles are in nm and degree, respectively.

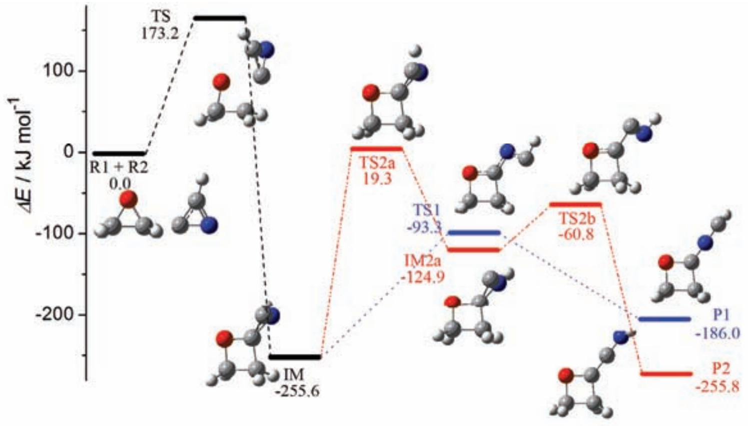

Fig. 2. Reaction profile for the reaction between azacyclopropenylidene and oxirane at the MP2/6-311+G* level of theory.

Insertion process to form a spiro intermediate IM

The first intermediate IM in the reaction between azacyclopropenylidene and oxirane was formed *via* a barrier of 173.2 kJ mol^{-1}. The calculated unique imaginary frequency of the transition state TS in the insertion process is 727*i* cm^{-1} at the MP2/6-311+G* level of theory.

As shown in Fig. 1, in the TS, the distance of C^1–O is 0.2086 nm, and C^1–C^4 is 0.1951 nm. The distance of O–C^4 in the R2 fragment of the TS has been elongated significantly to 0.1823 nm. Thus, in the transition state TS, two new bonds C^1–O and C^1–C^4 are to form and the O–C^4 bond is to break simultaneously. In other words, insertion of the C^1 atom of the R1 fragment into the O–C^4 bond of the R2 fragment is the process that resulted the formation of a spiro intermediate IM. Moreover, as shown in Fig. 3, these changes can be further validated by IRC calculations based on the TS.

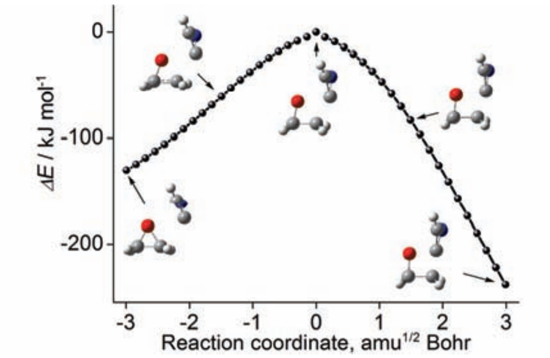

Fig. 3. IRC of TS and geometry evolution.

Qualitatively, the insertion process could be explained from the frontier molecular orbital theory since the frontier orbitals (*e.g.*, HOMO) of a chemical species are very important in defining their reactivity and determining the way in which the molecule interacts with other species.[36] As displayed in Fig. 4, the weak strength of the C–O bond can be deduced from the HOMO of oxirane. Obviously, the O–C^3 bond (or O–C^4 bond) is characterized by π antibonding orbital. As for azacyclopropenylidene, the activity of C^1 site could be deduced from the C^1 atom having the largest contributions to the components of the whole HOMO. Therefore, C^1 atom in azacyclopropenylidene could insert into the C–O bond of oxirane rather than into the C–C bond.

As shown in Fig. 1, C^2 and N adopt sp^2 hybridization in the IM. Compared with the isolated azacyclopropenylidene, the bond length of C^2–N in the IM is shortened by 0.0018 nm. The angle of C^{1}NC^2 in the IM is 60.9°, which is decreased slightly by 1.0° relative to that in isolated azacyclopropenylidene. Therefore, the ring-tension of the R1 fragment in the IM is larger than that of the isolated R1. Due to the existing large tension in the three-membered ring, the C^1–C^2 bond in the IM will break. Through the ring-opening step at the C–C bond, the IM can transfer to product P1, which is designated as pathway (1). On the other hand, through H-transfer step and subsequent ring-opening step at the C–N bond, the IM can turn into product P2, which is designated pathway (2). Therefore, the IM is the common intermediate for pathway (1) and pathway (2).

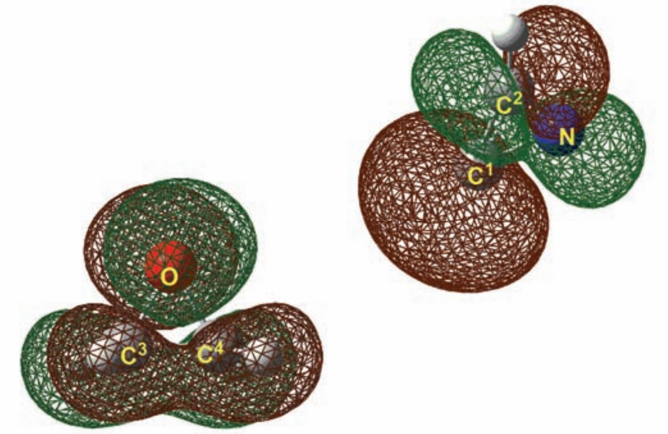

Fig. 4. The calculated HOMO orbitals for azacyclopropenylidene and oxirane.

Pathway (1): ring-opening process to form a carbene product

As mentioned above, the first step of pathway (1) is the formation of the IM. Through cleavage of the C^1–C^2 bond, the second step of pathway (1) is the conversion of the IM to P1 *via* TS1, where the barrier is 162.3 kJ mol^{-1}. The calculated only imaginary frequency of the transition state TS1 is 359*i* cm^{-1}. IRC calculations were performed based on the calculated TS1 to investigate the interactions between intermediate IM and product P1 in the pathway (1) process (see Fig. 5).

As shown in Figs. 1 and 5, the angle of C^1NC^2 in TS1 increases continuously along with the reaction. Simultaneously, the bond distance of C^1–C^2 increases along with the reaction process, implying the breakage of the three-membered ring involving C^1NC^2.

In P1, all the non-hydrogen atoms are located approximately on the same plane. The N atom adopts sp^2 hybridization and the bond length of C^1–N is 0.1261 nm, which is shorter than that of a normal C=N double bond. Moreover, the distance of N–C^2 (0.1260 nm) is shorter than that of a normal N–C single bond. Furthermore, the C^2 atom has a pair of lone electrons, making P1 exhibit the carbene characters. Therefore, from a thermodynamics viewpoint, P1 is not a stable product, which can be demonstrated by the calculated energy (–186.0 kJ mol$^{–1}$).

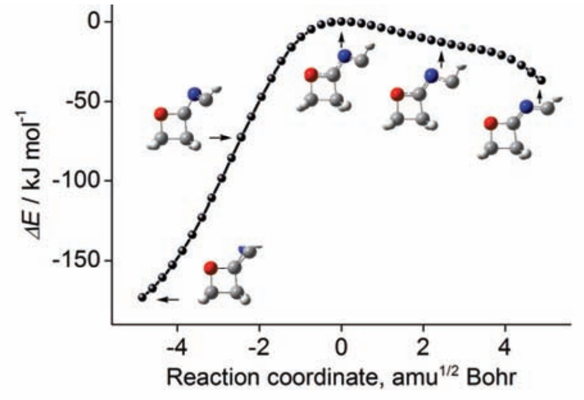

Fig. 5. IRC of TS1 and geometry evolution.

Pathway (2): H-transfer and ring-opening processes to form an allene product

The second step and the third step of pathway (2) are an H-transfer process to form the spiro intermediate IM2a, and a ring-opening process to form the allene product P2, respectively.

The second step of pathway (2) is hydrogen transfer from C^2 to the adjacent N, resulting in the conversion of IM into IM2a *via* TS2a. IRC calculations were performed based on the calculated TS2a and TS2b in the pathway (2) process (see Fig. 6). Here, the calculated barrier is 274.9 kJ mol$^{–1}$ and the imaginary frequency of TS2a is 1281*i* cm$^{–1}$. In details, as shown in Figs. 1 and 6, the distance of C^2–H^1 in TS2a is elongated to 0.1275 nm, and the distance of N–H^1 reaches 0.1450 nm, indicating that the H^1 atom can transfer from C^2 to N.

As IM, IM2a is a spiro intermediate. However, the bond between C^2 and N in IM2a is a single bond, whereas it is a double bond in IM. Therefore, there are

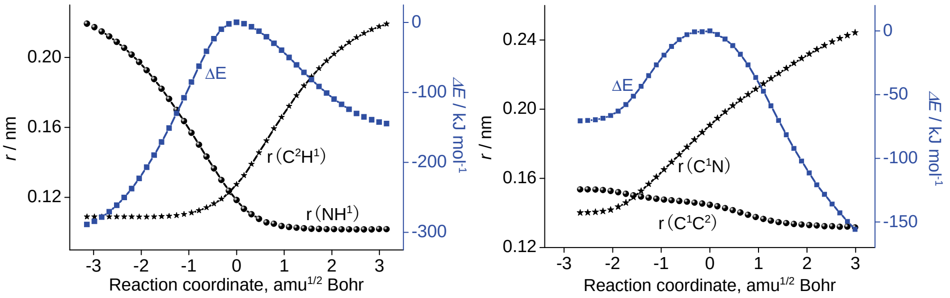

Fig. 6. Selected bond lengths and relative energy changes along the reaction coordinates based on the IRC of TS2a (left) and TS2b (right).

two unpaired electrons in the C^2 atom. In other words, IM2a has the character of an active carbene and can convert into a more stable configuration.

The third step of pathway (2) is a ring-opening process to form the allene product P2. Through cleavage of the C^1–N bond, IM2a is converted into P2 *via* TS2b, where the barrier is 64.1 kJ mol^{-1}. The calculated only imaginary frequency of the transition state TS2b is 429*i* cm^{-1}. As shown in Figs. 1 and 6, the bond distance of C^1–N in TS2b lengthens and the angle of C^1C^2N increases along with the reaction process, implying breakage of the three-membered ring involving C^1C^2N.

In P2, the bond length of C^1–C^2 is 0.1318 nm, which falls in the range intermediate between C=C and C≡C bond lengths. Similarly, the bond length of C^2–N (0.1247 nm) is between C=N and C≡N bond lengths. The three atoms, C^1, C^2 and N, are almost in the same line (the angle of C^1C^2N is 167.2°). Therefore, P2 has the typical structure of an allene. Along the reaction profile, P2 is the most stable species, which is exothermic with the value of 255.8 kJ mol^{-1} compared with those of the reactants.

CONCLUSIONS

In this study, the mechanism of the reaction between azacyclopropenylidene and oxirane was systematically investigated employing the MP2/6-311+G* level of theory. It is found that there are two pathways, denoted (1) and (2), which lead to the formation of two ultimate products, P1 and P2, respectively. The first step of the reaction is the formation of a common intermediate IM. The barrier heights of the rate-determining steps in reaction pathway (1) and (2) are 173.2 and 274.9 kJ mol^{-1}, respectively. Therefore, the reaction pathway (1) is the most favorable channel from the kinetic viewpoint. On the other hand, the corresponding two products P1 and P2 were stabilized by about 186.0 and 255.8 kJ mol^{-1} relative to the reactants, respectively. Therefore, the most favorable product P2 should be confirmed from the thermodynamic viewpoint.

Acknowledgment. This work was supported by a project of the Shandong Province Higher Educational Science and Technology Program (J13LM06).

ИЗВОД

ТЕОРИЈСКО ИСПИТИВАЊЕ МЕХАНИЗМА РЕАКЦИЈЕ ИЗМЕЂУ АЗАЦИКЛОПРОПЕНИЛИДЕНА И ОКСИРАНА

YING JING[1] и XIAOJUN TAN[2]

[1]*General Hospital of Jinan Military Command, Jinan, China и* [2]*University of Jinan, Jinan, China*

Механизам реакције између азациклопропенилидена и оксирана је систематски испитиван применом Møller–Plesset пертурбационе теорије другог реда (MP2). Циљ је био да се боље разуме реактивност азациклопропенилидена са једињењима која имају трочлани прстен, као што је оксиран. Израчунате су оптимизоване геометрије и енергије за одговарајуће стационарне тачке на површини потенцијалне енергије, и извршена вибрациона анализа. Енергије су затим додатно кориговане CCSD(T)/6-311+G* методом.

Прорачуни показују да су могућа два пута за одигравање реакције. Први је преферира са кинетичке а други са термодинамичке тачке гледишта.

(Примљено 12. маја, прихваћено 28. маја 2014)

REFERENCES

1. B. P. João, S. Da, N. R. Mozart, *Int. J. Quantum Chem.* **43** (1992) 215
2. J. A. Francisco, S. L. Richardson, *J. Chem. Phys.* **101** (1994) 7707
3. P. Botschwina, M. Horn, S. Seeger, J. Flugge, *Mol. Phys.* **78** (1993) 191
4. P. Botschwina, B. Schulz, M. Horn, M. Matuschewski, *Chem. Phys.* **190** (1995) 345
5. H. Suzuki, S. Yamamoto, M. Ohishi, N. Kaifu, S. Ishikawa, Y. Hirahara, S. Takano, *Astrophys. J.* **392** (1992) 551
6. H. E. Matthews, W. Irvine, P. Freiberg, R. D. Brown, P. D. Godfrey, *Nature* **310** (1984) 125
7. K. Aoki, S. Ikuta, A. Murakami, *Chem. Phys. Lett.* **209** (1993) 211
8. K. Aoki, S. Ikuta, O. Nomura, *J. Chem. Phys.* **98** (1993) 7661
9. W. M. Irvine, *Adv. Space Res.* **15** (1995) 35
10. B. Lee, *Chem. Phys. Lett.* **1–2** (1998) 171
11. S. Saito, K. Kawaguchi, S. Yamamoto, M. Ohishi, H. Suzuki, N. Kaifu, *Astrophys. J.* **317** (1987) L115
12. M. B. Bell, L. W. Avery, A. Feldman, *Astrophys. J.* **417** (1993) L37
13. S. Yamamoto, S. Saito, K. Kawaguchi, N. Kaifu, H. Suzuki, M. Ohishi, *Astrophys. J.* **317** (1987) L119
14. K. Kim, B. Lee, S. Lee, *Chem. Phys. Lett.* **297** (1998) 65
15. S. Lee, *Chem. Phys. Lett.* **268** (1997) 69
16. M. Ohishi, N. Kaifu, K. Kawaguchi, A. Murakami, S. Saito, S. Yamamoto, S. I. Ishikawa, Y. Fujita, Y. Shiratori, W. M. Irvine, *Astrophys. J.* **345** (1989) L83
17. M. B. Bell, P. A. Feldman, M. J. Travers, M. C. McCarthy, C. A. Gottlieb, P. Thaddeus, *Astrophys. J.* **483** (1997) L61
18. D. McGonagle, W. M. Irvine, *Astron. Astrophys.* **310** (1996) 970
19. M. C. McCarthy, C. A. Gottlieb, A. L. Cooksy, P. Thaddeus, *J. Chem. Phys.* **103** (1995) 7779
20. N. Goldberg, A. Fiedler, H. Schwarz, *J. Phys. Chem.* **99** (1995) 15327
21. K. Aoki, S. Ikuta, O. Nomura, *J. Chem. Phys.* **99** (1993) 3809
22. F. Sun, A. Kosterev, G. Scott, V. Litosh, R. F. Curl, *J. Chem. Phys.* **109** (1998) 8851
23. P. Y. Hung, F. Sun, N. T. Hunt, L. A. Burns, R. F. Curl, *J. Chem. Phys.* **115** (2001) 9331
24. J. E. Rice, H. F. Schaefer, *J. Chem. Phys.* **86** (1987) 7051
25. E. T. Seidl, H. F. Schaefer, *J. Chem. Phys.* **96** (1992) 4449
26. H. S.-W. Park, S. Lee, *Bull. Korean Chem. Soc.* **23** (2002) 1553
27. N. Inostroza, X. Huang, T. J. Lee, *J. Chem. Phys.* **135** (2011) 244310
28. M. Z. Kassaee, S. M. Musavi, N. Jalalimanesh, *J. Theor. Comput. Chem.* **7** (2008) 367
29. M. Z. Kassaee, M. Ghambarian, S. M. Musavi, *Heteroatom Chem.* **19** (2008) 377
30. K. Jacek, *J. Phys. Chem., A* **107** (2003) 4717
31. G. Maier, H. P. Reisenauer, K. Rademacher, *Chem. Eur. J.* **4** (1998) 1957
32. G. Maier, A. Bothur, J. Eckwert, H. P. Reisenauer, *Chem. Eur. J.* **4** (1998) 1964
33. N. Balucani, M. Alagia, L. Cartechini, P. Casavecchia, G. G. Volpi, K. Sato, T. Takayanagi, Y. Kurosaki, *J. Am. Chem. Soc.* **122** (2000) 4443
34. M. R. Nimlos, G. Davico, C. M. Geise, P. G. Wenthold, W. C. Lineberger, S. J. Blanksby, C. M. Hadad, G. A. Petersson, G. B. Ellison, *J. Chem. Phys.* **117** (2002) 4323

35. Gaussian 98, Gaussian, Inc., Pittsburgh, PA, 1998
36. P. Thaddeus, C. A. Gottlieb, R. Mollaaghababa, J. M. Vrtilek, *J. Chem. Soc. Faraday Trans*. **89** (1993) 2125.

Journal of the Serbian Chemical Society
JSCS-info@shd.org.rs • www.shd.org.rs/JSCS

J. Serb. Chem. Soc. 80 (1) 63–72 (2015)
JSCS–4697

UDC 547.979.4+548.7+542.913:
543.424.2:543.426.1
Original scientific paper

Facile synthesis of water-soluble curcumin nanocrystals

ZORAN M. MARKOVIĆ[1], JOVANA R. PREKODRAVAC[1], DRAGANA D. TOŠIĆ[1],
IVANKA D. HOLCLAJTNER-ANTUNOVIĆ[2], MOMIR S. MILOSAVLJEVIĆ[1],
MIROSLAV D. DRAMIĆANIN[1] and BILJANA M. TODOROVIĆ-MARKOVIĆ[1]*

[1]*Vinča Institute of Nuclear Sciences, University of Belgrade, P. O. Box 522, 11001 Belgrade, Serbia and* [2]*Faculty for Physical Chemistry, University of Belgrade, Studentski trg 14–16, 11000 Belgrade, Serbia*

(Received 19 August, revised 12 November, accepted 21 November 2014)

Abstract: In this paper, a facile synthesis of water-soluble curcumin nanocrystals is reported. Solvent exchange method was applied to synthesize curcumin nanocrystals. Different techniques were used to characterize the structural and photophysical properties of the curcumin nanocrystals. It was found that the nanocurcumin prepared by this method had good chemical and physical stability, could be stored in the powder form at room temperature, and was freely dispersible in water. It was established that the size of curcumin nanocrystals varied in the range of 20–500 nm. Fourier transform infrared spectroscopy and UV–Vis analyses showed the presence of tetrahydrofuran inside the curcumin nanocrystals. Furthermore, it was found that the nanocurcumin emitted photoluminescence with a yellow–green color.

Keywords: curcumin nanocrystals; atomic force microscopy; transmission electron microscopy; Raman spectroscopy; photoluminescence spectroscopy.

INTRODUCTION

Curcumin is a natural yellow–orange dye extracted from the rhizomes of the plant *Curcuma longa* L. Commercially available curcumin is a mixture of three curcuminoids, namely, curcumin, demethoxy- and bisdemethoxy-curcumin, the latter two amounting to nearly 30 % in samples labeled “pure”.[1] It shows a remarkable range of pharmacological activity, including antioxidant, anti-inflammatory and anticancer activity.[2–7] The anticancer potential of curcumin is mediated through the inhibition and modulation of several intracellular signaling pathways, as confirmed in various *in vitro* and *in vivo* cancer studies. Biomedical application of curcumin requires improvement of its bioavailability and its targeting capacity toward cancer tissue. Due to the low bioavailability of curcumin,

---

* Corresponding author. E-mail: biljatod@vinca.rs

doi: 10.2298/JSC140819117M

numerous approaches were undertaken,[8,9] *i.e.*, nanoparticle-based drug delivery in which curcumin is encapsulated in liposomes,[10] solid lipid microparticles, such as bovine serum albumin[11] and chitosan,[12] or complexed with phospholipids[13] and cyclodextrin.[14]

Various types of nanoparticles, such as polymer nanoparticles, polymeric micelles, liposome/phospholipid, nano-/microemulsions, nanogels, solid lipid nanoparticles, polymer conjugates, self-assemblies, *etc*., are suitable for the delivery of the active form of curcumin to tumors.[15] Previous studies showed that nanocurcumin has improved anticancer effects as compared to normal curcumin formulations.[16] Bhawana *et al*. demonstrated that the water solubility and antimicrobial activity of curcumin markedly improved by particle size reduction down to the nano range.[17] Recently it was demonstrated that curcumin nanoparticles under aqueous conditions exhibited similar or a much stronger antiproliferative effect on cancer cells compared to normal curcumin in dimethyl sulfoxide (DMSO).[18] Raghavendra *et al*. showed that aqueous-based nanocurcumin (nanoparticles of curcumin) impregnated gelatin cellulose fibers (NCGCFs) has a superior performance over curcumin impregnated gelatin cellulose fibers.[19] The activity of curcumin lies in its ability to scavenge active oxygen- or nitrogen-free radicals.[6,7,20–22]

Curcumin is practically insoluble in water but soluble in both polar and nonpolar organic solvents. It belongs to the group of β-diketones and exhibits tautomerism between enol- and keto-structures (Fig. 1). The relative contributions of the keto and enolic tautomers as well as their *cis* or *trans* form depend on factors such as solvent characteristics, temperature, polarity and substitution on the curcumin.[23–25] The enol form is characterized by a strong intermolecular hydrogen bond.

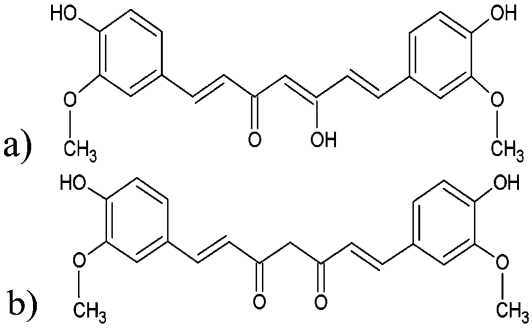

Fig. 1. Structure of the a) enol and b) keto form of curcumin.

In solution, curcumin can form intermolecular H-bonds with the solvent molecules and this strongly influences its physicochemical properties in both the ground and excited states.[26] The spectral properties of curcumin show a solvent polarity dependency. Curcumin dissolved in thirteen different solvents (cyclohexane, ethanol, hexane, dichloromethane (DCM), 1,2-dichlorobenzene (DCB), 1,4-dioxane, tetrahydrofuran (THF), methanol, acetonitrile, *n*-butyronitrile (*n*BN), dimethyl sulfoxide (DMSO) and *N*,*N*-dimethylformamide (DMF)) showed a double-exponential decay function with a short-lived component in the picoseconds time scale.[27]

Different methods have been applied to synthesize nano-sized curcumin: solvent-based processes, which include emulsification-solvent evaporation,[28] emulsification-solvent diffusion, and precipitation methods.[29,30] Margulis *et al*. demonstrated a method employing turbulent co-mixing of water with a curcumin-loaded emulsion using manually operated confined impingement jet mixers.[31] Another approach for increasing the rate of dissolution of curcumin is by increasing its surface area. This can be achieved by decreasing the particle size by methods such as milling and grinding.[17]

This paper describes facile synthesis of curcumin nanocrystals (nanocurcumin) by means of a solvent exchange method that was previously used regularly for nanoC_{60} synthesis.[32] THF was used to dissolve curcumin before mixing with water. THF is water-miscible organic liquid with low viscosity. This organic solvent transfers their charge to curcumin molecules. This organic solvent is intercalated inside curcumin crystal lattice, thereby improving water solubility. The aim of this paper was to obtain a stable water-soluble nanocurcumin colloid and further investigate its structural and photophysical properties.

EXPERIMENTAL

For the preparation of nanocurcumin colloid, an ethanol extract of commercially obtained curcumin was used. By applying a previously described solvent exchange method,[32] the dried ethanol extract was dissolved in fresh THF of HPLC purity (Carlo Erba, Milan, Italy) at a concentration of 1.33 mg mL^{-1}. After purging the mixture with argon to remove any dissolved oxygen, an equal amount of MiliQ water was then added to the THF/curcumin filtrate under continuously stirring. The more volatile THF was subsequently removed from the solution using a rotary evaporator at 45 °C. MiliQ water was added four times more and evaporated to the initial volume. The obtained solution was filtered through a 0.45 µm nylon filter and stored in the dark. After gravimetric estimation, the concentration of the nanocurcumin was adjusted to 0.38 mg mL^{-1}.

The nanocurcumin colloid was characterized by transmission electron microscopy (TEM), atomic force microscopy (AFM), Raman spectroscopy, Fourier transform infrared spectroscopy (FTIR), UV–Vis spectrometry and photoluminescence (PL) spectroscopy.

Transmission electron microscopy imaging was performed on a TEM Philips CM200 microscope operated at 200 kV. Samples were prepared by drop casting a dispersion of nanocurcumin onto a carbon-coated 300 mesh copper grid.

AFM measurements were performed using a Quesant microscope operating in the tapping mode in air at room temperature.[33] Curcumin dissolved in THF and nanocurcumin colloid were deposited on mica substrates by spin coating and imaged after drying. The freshly cleaved mica had a very small roughness (the mean roughness was 0.12 nm) favoring the formation of aggregates which appeared during drying of the thin layer of colloid due to capillary forces. To reduce aggregation on the substrate, a higher dilution was employed. Standard silicon tips (purchased from NanoAndMore) with a constant force (40 N m^{-1}) were used. The accuracy of the AFM mean diameter determination was improved by deconvolution. The mean diameter of the investigated particles was determined using Gwyddion software.[34]

The UV–Vis spectra of nanocurcumin suspensions were scanned within the wavelength range of 200–500 nm using an Avantes UV–Vis spectrophotometer. All UV–Vis measurements were performed at 20 °C and automatically corrected for the suspending medium, which was water.

For the FTIR analysis, a nanocurcumin suspension was dried on silicon wafers until thin films were formed. The FTIR spectra were measured at room temperature in the spectral range from 400 to 4000 cm^{-1} on a Nicollet 380 FT-IR, Thermo Electron Corporation spectrometer operating in the ATR mode.

Raman spectra of the nanocurcumin colloid on glass were obtained from a DXR Raman microscope (Thermo Scientific) using 532 nm excitation line from a diode pumped, solid state laser. The laser power was 5 mW. 50× Objectives were used to focus the excitation laser light on the right spot of the investigated samples. The spot size of laser beam was 0.7 µm. The spectral resolution was 0.5 cm^{-1}. The acquisition time was always 100 s (10×10 s).

The photoluminescence spectra of nanocurcumin deposited on SiO_2/Si were recorded at room temperature on a Fluorolog-3 Model FL3-221 spectrofluorometer system (HORIBA Jobin–Yvon). The emission spectra were measured utilizing a 450 W xenon lamp as the excitation source.

RESULTS AND DISCUSSION

Surface morphology of curcumin nanocrystals

Transmission electron microscopy and atomic force microscopy were used to visualize the structure and morphology of the curcumin nanocrystals. The shape and size of the curcumin nanocrystals were determined by AFM. A top view AFM image of curcumin nanoparticles dispersed in THF is presented in Fig. 2a, while AFM image of curcumin nanocrystals dispersed in water and corresponding histogram of nanocurcumin diameters are presented in Fig. 2b. As can see from Fig. 2a, the curcumin nanoparticles dissolved in THF had a bagel shape, while the curcumin nanocrystals were spherical. Based on surface analysis the average size of the curcumin nanocrystals was 250 nm. It was also established that about 25 % of the nanocurcumin crystals had a diameter smaller than 100 nm, while 41 % of the nanocurcumin particles had a diameter smaller than 150 nm (Fig. 2d).

TEM micrograph and electron diffraction pattern of nanocurcumin are presented in Fig. 2c. Average size of nanocurcumin based on calculations on large-scale TEM micrographs is about 200 nm. From an electron diffraction image (inset in Fig. 2c), it could be concluded that the nanocurcumin had a crystal structure.

The solubility process is the first step during interactions between polycrystalline curcumin powder and an organic solvent. Curcumin polycrystals obtain charge

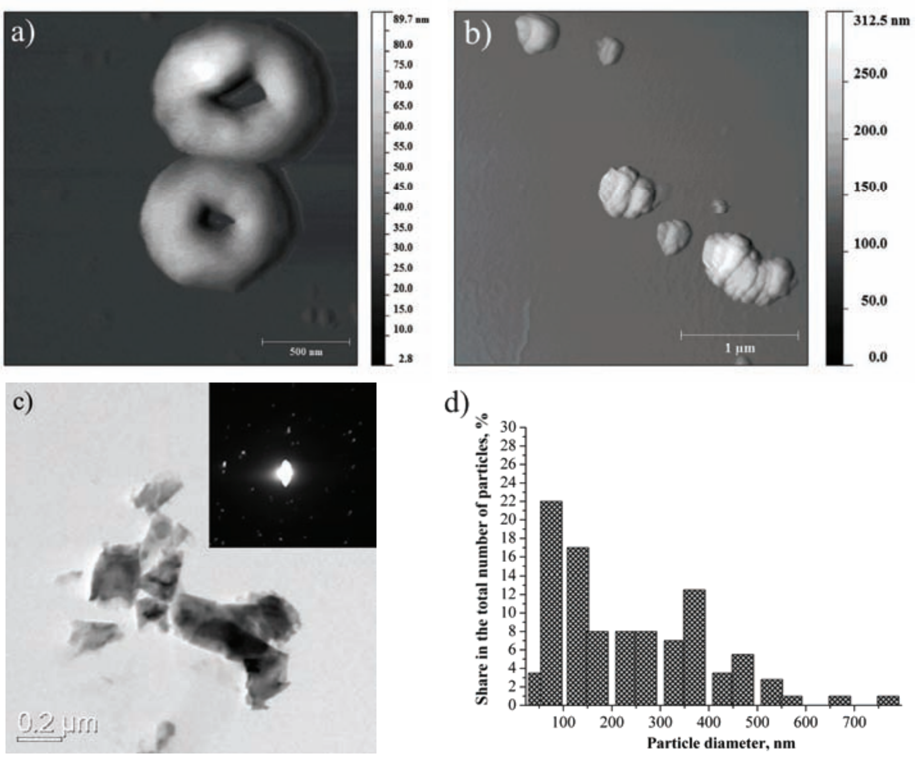

Fig. 2. a) Top-view AFM images of curcumin dissolved in THF and b) water soluble curcumin nanocrystals and the corresponding surface profile; c) bright field TEM micrograph and corresponding electron diffraction pattern of the water-soluble curcumin nanocrystals and d) particle size distribution.

from several thousand THF molecules depending on the size of polycrystal. Tetrahydrofuran is positioned along boundaries of the monocrystals and around the curcumin particles. The nanocurcumin colloid was stabilized electrostatically which was confirmed by its precipitation in 1 wt. % solution. Other authors synthesized curcumin nanoparticles with a narrower particle distribution (2–40 nm)[17] but they used a solvent whose LD_{50} value was lower than that for THF (the amount of a toxic agent sufficient to kill 50 % of a population of animals, usually within a certain time; the LD_{50} value for dichloromethane is 1.6 g kg^{-1} compared to 2−3 g kg^{-1} for THF).[35] Average diameter of nanocurcumin produced by solvent exchange method was larger than that produced by the milling and grinding technique due to particle aggregation. In previous investigations concerning nanoC_{60}, it was shown that THF itself is not toxic as it was completely unable to generate reactive oxygen species (ROS) and did not affect cell viability even at the concentrations >100-fold higher[36] than its estimated residual presence (10 %) in the nanoC_{60}.[37] The solubility of nanocurcumin can be improved significantly by using polymers such as poly(vinyl pyrrolidone) (PVP), poly(ethylene glycol) (PEG) but the disadvantage of this method is that it requires the addition of considerable amounts of surfactants to prevent coalescence during particle formation.[38]

FTIR spectra of curcumin nanocrystals

The composition of the prepared nanocurcumin colloid was investigated by FTIR spectroscopy – Fig. 3a. A detailed study on the vibrational spectra of curcumin was reported earlier by Kolev *et al.*[39] The FTIR spectrum of curcumin shows characteristic absorption bands at 2852 and 2922 cm^{-1} that represent sp^3 –C–H stretching while the band at 3011 cm^{-1} is due to sp^2 –C–H stretching vibrations. Broad band at 2540 cm^{-1} is due to –O–H stretching vibrations while the broad band between 1980 and 2020 cm^{-1} could be assigned to –C=C–

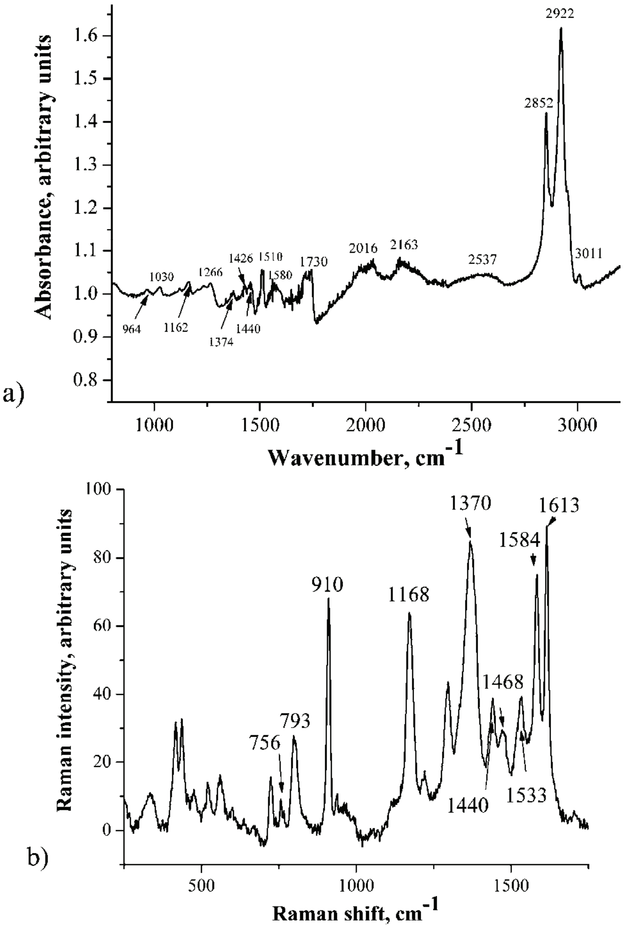

Fig. 3. a) FTIR and b) Raman spectra of nanocurcumin.

asymmetric stretch. The broad band between 1680 and 1730 cm$^{–1}$ corresponds to the –C=O asymmetric mode. The band between 1520 and 1610 cm$^{–1}$ could be assigned to –C=C– in ring while the broad band between 1400 and 1440 corresponds to –CH$_3$ deformations and the bands at 1030, 1270 and 1160 cm$^{–1}$ stem from –C–O– stretching vibrations. The band at 964 cm$^{–1}$ originates from –C–H bending vibrations.

FTIR analysis of the nanocurcumin colloid revealed two absorption bands at about 2852 and 2922 cm$^{–1}$, which reflect the presence of strained C–H covalent bonds. The shape and position of the two bands matches perfectly the strongest bands of a tetrahydrofuran liquid film according to the IR spectrum presented in the Spectral Database for Organic Compounds.[40] Since these two bands do not overlap with typical IR bands of nanocurcumin positioned in the range from 500 to 1800 cm$^{–1}$, tetrahydrofuran molecules are inserted into interstitial positions of curcumin nanocrystals.

Raman spectra of curcumin nanocrystals

Raman spectroscopy was used in earlier studies for the characterization of curcumin.[39] The Raman spectrum of nanocurcumin is shown in Fig. 3b. The peaks at 756 and 793 cm$^{–1}$ seen in Fig. 3b stem from out-of-plane C–C–H bending vibrations while the peak at 910 cm$^{–1}$ originates from in-plane C–C–H bending vibrations. The peaks at 1168, 1440 and 1468 cm$^{–1}$ could be assigned to in-plane –CH$_3$ bending vibrations while the peak at 1370 cm$^{–1}$ originates from in-plane C–O–H bending vibrations. The peak at 1533 cm$^{–1}$ stem from –C=O stretching vibrations and the peak at 1584 originates from –C–C– stretching vibrations. The peak at 1613 cm$^{–1}$ stems from –C=O stretching vibrations.

Absorption spectra of curcumin nanocrystals

The visible and ultraviolet spectra of organic compounds (such as curcumin) represent transitions between electronic energy levels. These transitions are generally between a bonding or lone-pair orbital and an unfilled non-bonding or anti-bonding orbital. The absorption bandwidth could indicate the degree of agglomeration.[41] The UV–Vis spectra of curcumin dissolved in ethanol and THF as well as of nanocurcumin are presented in Fig. 4a and b, respectively. The UV–Vis spectra of curcumin dissolved in ethanol and THF (Fig. 4a) overlap while the UV–Vis spectra of curcumin dissolved in THF and nanocurcumin differ (Fig. 4b). As can be seen, there is one peak at 427 nm that could be assigned to low-energy π–π* excitation of the chromophore (this peak is typical for curcumin dissolved in organic solvent such as tetrahydrofuran – curve 1) and one shoulder at 279 nm. As for nanocurcumin, there is a very broad absorption band at 410 nm and a shoulder (weak absorption band) at 283 nm – curve 2. A blue shift to 410 nm and broadening of the absorption peak at 427 nm due to effect of water were registered. The intensity of the absorption peak at 410 nm was also significantly reduced. The evolution of absorption peak at 410 nm for the π–π* transitions of curcumin in water as well as the decreasing intensity indicate a change in the tautomeric form of the keto–enol–enolate group in curcumin. The broadening of absorption band at 410 nm was caused by aggregation of the nanocrystals.

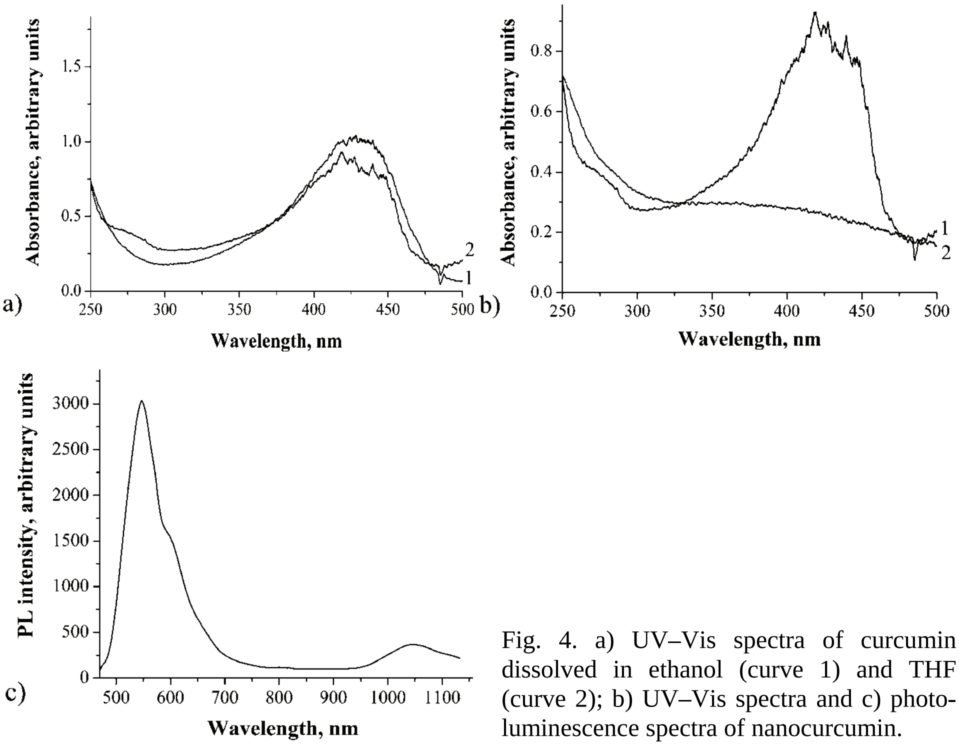

Fig. 4. a) UV–Vis spectra of curcumin dissolved in ethanol (curve 1) and THF (curve 2); b) UV–Vis spectra and c) photoluminescence spectra of nanocurcumin.

Photoluminescence spectra of curcumin nanocrystals

A photoluminescence spectrum of nanocurcumin is presented in Fig. 4c. Under excitation of 405 nm, there are two PL peaks at 547 and 595 nm, and their intensities decreased rapidly. One of the possible explanations for the multiple peaks could be variation in the size of the crystallites, and the emission would have come from a statistical average of the crystallites. The solvent polarity affects (the effect of THF) intramolecular charge transfer, which influences the fluorescence emission. Polar solvents also shift the emission to longer wavelength due to the stabilization of the excited states.[42]

CONCLUSIONS

In this paper, a facile synthesis of water-soluble curcumin nanocrystals was presented. It was established that the most important features of synthesized colloid were: the average size of the photoluminescent curcumin nanocrystals was around 250 nm and their long-term stability. Due to very low toxicity of tetrahydrofuran, nanocurcumin colloids could be applied in nanomedicine.

Acknowledgement. This research was supported by the Ministry of Education, Science and Technological Development of Republic of Serbia (Project No. 172003).

ИЗВОД

СИНТЕЗА ВОДОРАСТВОРНИХ НАНОКРИСТАЛА КУРКУМИНА

ЗОРАН М. МАРКОВИЋ[1], ЈОВАНА Р. ПРЕКОДРАВАЦ[1], ДРАГАНА Д. ТОШИЋ[1], ИВАНКА Д. ХОЛЦЛАЈТНЕР-АНТУНОВИЋ[2], МОМИР С. МИЛОСАВЉЕВИЋ[1], МИРОСЛАВ Д. ДРАМИЋАНИН[1] и БИЉАНА М. ТОДОРОВИЋ-МАРКОВИЋ[1]

[1]*Институт за нуклеарне науке „Винча“, Универзитет у Београду, Мике Аласа 12–14, 11001 Београд и*
[2]*Факултет за физичку хемију, Универзитет у Београду, Студентски Трг 14–16, 11000 Београд*

У раду је приказан нови начин синтезе нанокристала куркумина применом методе измене растварача. За испитивање структурних и фотофизичких особина нанокристала куркумина коришћене су различите технике карактеризације. Утврђено је да колоид нанокуркумина припремљен овим поступком има добру физичку и хемијску стабилност и да се лако раствара у води. Применом микроскопије атомске силе утврђено је да је величина нанокристала куркумина била у опсегу од 20−50 nm. Фуријеова инфрацрвена и UV–Vis спектроскопија су показале присуство тетрахидрофурана унутар нанокристала куркумина. Такође је утврђено да нанокуркумин емитује фотолуминесценцију у жуто-зеленој области спектра.

(Примљено 19. августа, ревидирано 12. новембра, прихваћено 21. новембра 2014)

REFERENCES

1. F. Jasim, F. Ali, *Microchem. J.* **38** (1988) 106
2. O. P. Sharma, *Biochem. Pharmacol*. **25** (1976) 1811
3. T. Masuda, Y. Toi, H. Bando, T. Maekawa, Y. Takeda, H. Yamaguchi, *J. Agric. Food Chem.* **50** (2002) 2524
4. K. Mehta, P. Pantazis, T. McQueen, B. Agarval, *Anti-Cancer Drugs* **8** (1987) 471
5. A. N. Nurfina, M. S. Reksoha Diprodjo, H. Timmerman, U. Jenie, D. Sigianto, H. J. van der Goot, *Med. Chem*. **32** (1997) 321
6. N. Sreejayan, M. N. A. Rao, K. I. Priyadarsini, A. T. P. Devasagayam, *Int. J. Pharm*. **15**1 (1997) 127
7. P. Venkatesan, M. N. Rao, *J. Pharm. Pharmacol.* **52** (2000) 1123
8. P. Anand, A. B. Kunnumakkara, R. A. Newman, B. B. Aggarwal, *Mol. Pharm.* **4** (2007) 807
9. P. Anand, H. B. Nair, B. Sung, A. B. Kunnumakkara, V. R. Yadav, R. R. Tekmal, B. B. Aggarwal, *Biochem. Pharmacol*. **79** (2010) 330
10. D. Wang, M. S. Veena, K. Stevenson, C. Tang, B. Ho, J. D. Suh, V. M. Duarte, K. F. Faull, K. Mehta, E. S. Srivatsan, M. B. Wang, *Clin. Cancer Res*. **14** (2008) 6228
11. V. Gupta, A. Aseh, C. N. Rios, B. B. Aggarwal, A. B. Mathur, *Int. J. Nanomed*. **4** (2009) 115
12. R. K. Das, N. Kasoju, U. Bora, *Nanomedicine* **6** (2010) 153
13. K. Maiti, K. Mukherjee, A. Gantait, B. P. Saha, P. K. Mukherjee, *Int. J. Pharm*. **330** (2007) 155

14. M. M. Yallapu, M. Jaggi, S. C. Chauhan, *Macromol. Biosci.* **10** (2010) 1141
15. I. Muqbil, A. Masood, F. H. Sarkar, R. M. Mohammad, A. S. Azmi, *Cancers* **3** (2011) 428
16. G. Flora, D. Gupta, A. Tiwari, *Crit. Rev. Ther. Drug* **30** (2013) 331
17. R. Bhawana, H. Kumar Basniwal, V. K. Singh Buttar, N. Jain, *J. Agr. Food Chem.* **59** (2011) 2056
18. R. Kumar Basniwala, R. Khoslab, N. Jain, *Nutr. Cancer* **66** (2014) 1015
19. G. Raghavendra, T. Jayaramudu, K. Varaprasad, S. Ramesh, K. Mohana Raju, *RSC Adv.* **4** (2014) 3494
20. M. Onoda, H. Inano, *Nitric Oxide* **4** (2000) 505
21. A. Gorman, V. Hamblett, V. Srinivasan, P. Wood, *Photochem. Photobiol.* **59** (1994) 389
22. K. Priyadarsini, *Free Radic. Biol. Med.* **23** (1997) 838
23. C. F. Chignell, P. Bilski, K. J. Reszka, A. G. Motten, R. H. Sik, T. A. Dahl, *Photochem. Photobiol.* **59** (1994) 295
24. V. Galasso, B. Kovac, A. Modelli, M. F. Ottaviani, F. Pichierri, *J. Phys. Chem., A* **112** (2008) 2331
25. S. M. Khopde, K. I. Priyadarsini, D. K. Palit, T. Mukherjee, *Photochem. Photobiol.* **72** (2000) 625
26. L. Nardo, R. Paderno, A. Andreoni, M. Masson, T. Haukvik, H. H. Tonnesen, *Spectroscopy* **22** (2008) 187
27. D. Patra, C. Barakat, *Spectrochim. Acta, A* **79** (2011) 1034
28. M. K. Modasiya, V. M. Patel, *Int. J. Pharm. Life Sci.* **3** (2012) 1490
29. Y.-M. Tsai, C.-F. Chien, L.-C. Lin, T.-H. Tsai, *Int. J. Pharm.* **416** (2011) 331
30. M. Kakran, N. G. Sahoo, I. L. Tan, L. Li, *J. Nanopart Res.* **14** (2012) 757
31. K. Margulis, S. Magdassi, H. S. Lee, C. W. Macosko, *J. Colloid Interf. Sci.* **434** (2014) 65
32. S. Deguchi, G. A. Rossitza, K. Tsujii, *Langmuir* **17** (2001) 6013
33. B. Todorović-Marković, S. Jovanović, V. Jokanović, Z. Nedić, M. Dramićanin, Z. Marković, *Appl. Surf. Sci.* **255** (2008) 3283
34. Gwyddion, http://www.gwyddion.net (accessed on July 20th, 2014)
35. D. E. Moody, *Drug. Chem. Toxicol.* **14** (1991) 319
36. Z. Marković, B. Todorović-Marković, D. Kleut, N. Nikolić, S. Vranješ-Djurić, M. Misirkić, L. Vučićević, K. Janjetović, A. Isaković, L. Harhaji, B. Babić-Stojić, M. Dramićanin, V. Trajković, *Biomaterials* **36** (2007) 5437
37. L. Harhaji, A. Isaković, N. Raičević, Z. Marković, B. Todorović-Marković, N. Nikolić, S. Vranješ-Djurić,I. Marković, V. Trajković, *Eur. J. Pharmacol.* **568** (2007) 89
38. S. D. Kumavat, Y. S. Chaudhari, P. Borole, K. Shenghani, P. Duvvuri, N. Bubera, P. Shah, *Int. J. Pharm. Research Sci.* **2** (2013) 693
39. T. M. Kolev, E. A. Velcheva, B. A. Stamboliyska, M. Spiteller, *Int. J. Quantum Chem.* **102** (2005) 1069
40. SDBS Compounds and Spectral Search, http://sdbs.db.aist.go.jp/sdbs/cgi-bin/ /direct_frame_top.cgi (accessed on July 21th, 2014)
41. J. Lee, J. H. Kim, *Environ. Sci. Technol.* **42** (2008) 1552
42. J. Lakowicz, *Principles of Fluorescence Spectroscopy*, 3rd ed. Springer, New York, 2006.

Journal of the Serbian Chemical Society
eVersion electronic
JSCS-info@shd.org.rs • www.shd.org.rs/JSCS

J. Serb. Chem. Soc. 80 (1) 73–86 (2015) UDC 546.47'73'74+543.421:544.654.2:620.193
JSCS–4698 *Original scientific paper*

Ternary Zn–Ni–Co alloy: anomalous codeposition and corrosion stability

MILORAD V. TOMIĆ[1], MILOŠ M. PETROVIĆ[2], SLAVKA STANKOVIĆ[3],
SANJA I. STEVANOVIĆ[4#] and JELENA B. BAJAT[3*#]

*[1]University of Eastern Sarajevo, Faculty of Technology Zvornik, Republic of Srpska, B & H, [2]Institute of Materials Research and Engineering, A*STAR (Agency for Science, Technology and Research) 3 Research link, Singapore 117602, Department of Mechanical Engineering, National University of Singapore, Singapore 117576, [3]Faculty of Technology and Metallurgy, University of Belgrade, P. O. Box 3503, 11120 Belgrade, Serbia and [4]ICTM – IEC, P. O. Box 473, 11001 Belgrade, Serbia*

(Received 28 August, revised 31 October, accepted 13 November 2014)

Abstract: Electrochemically deposited Zn–Ni–Co alloys under various deposition conditions were investigated using atomic absorption spectroscopy for the determination of the chemical composition, atomic force microscopy for surface morphology analysis, and electrochemical impedance spectroscopy for determination of corrosion properties. The influence of the ratio of the alloying elements, $[Co^{2+}]/[Ni^{2+}]$, in a chloride deposition solution, as well as the deposition current density, on the chemical content, morphology and corrosion properties of the ternary alloys was studied. The plating solutions used were with the same overall metal concentration, free of additives and the deposition was realized at room temperature. It was shown that the deposition of the ternary alloy coatings was of anomalous type and that the ratio of nickel to cobalt ions in the plating solution, as well as the deposition current density, had a significant influence on the chemical composition and corrosion stability of these coatings. The presence of both Ni and Co was beneficial for their corrosion stability. It was shown that morphology and porosity were important factors in the corrosion stability of these coatings. The coating deposited from the solution with higher $[Co^{2+}]/[Ni^{2+}]$ ratio at 8 A dm^{-2} was made up of the smallest crystalline aggregates, had a small surface roughness and porosity, and was with quite uniform distribution of agglomerates and it exhibited the best corrosion stability.

Keywords: electrodeposition; ternary alloy coatings; corrosion; EIS; AFM.

---

* Corresponding author. E-mail: jela@tmf.bg.ac.rs

[#] Serbian Chemical Society member.

doi: 10.2298/JSC260814113B

INTRODUCTION

Alloy electrodeposition is widely used in the production of new materials that require some particular mechanical, chemical and physical properties. It was shown that zinc alloys could provide improved corrosion resistance compared to pure zinc in the protection of ferrous-based metals. The most common zinc alloys are zinc–nickel,[1–3] zinc–cobalt[4–6] and zinc–iron.[7,8] Compared with Zn the Zn–Ni and Zn–Co binary alloys give corrosion protection and physical properties significantly superior to those obtained with pure zinc deposits. However, the binary Zn alloys, that provide good alloy properties, often have a rough, non-uniform and unattractive finish, so additives often have to be used in the plating solutions.

Therefore, it would be interesting to combine the properties of Zn–Ni and Zn–Co alloys in one alloy, which could be accomplished *via* the electrodeposition of ternary Zn–Ni–Co alloys. There are several literature data on Zn–Ni–Co ternary alloys. Younan[9] and Eliaz *et al.*[10] studied the deposition of such ternary alloys in the presence of additives (sodium dodecyl sulfate,[9] sulphanilic acid[10] and gelatine[10]) and showed the increased corrosion stability with respect to the corresponding binary alloys: the corrosion rates of Zn–Ni–Co coatings were 7–10 times lower than binary Zn–Co and Zn–Ni alloys. Younan showed that the increased corrosion stability of Zn–Ni–Co deposits is not only due to the formation of a high nickel γ-alloy phase, but also to the codeposition of Co, which caused a change in a crystal orientation and resulted in a finer grain size.[9] Namely, Zn–Ni alloy coatings with 13–17.8 % Ni were a γ-phase $Zn_{21}Ni_5$ solid solution with (330) and (411) crystal orientation. Upon incorporation of Co, the crystal orientation of the γ-phase changed to (442) and (600), and with increasing Co content, ε-$Zn(OH)_2$ was also formed.

Higher corrosion resistance of ternary alloys was also determined by other authors,[11–14] for alloy coatings deposited from sulfate solutions, mainly at high temperatures. Since it was shown in previous work[15,16] that Zn–Ni and Zn–Co alloys deposited from sulfate plating baths had lower corrosion stability as compared to binary alloys deposited from chloride bath, the aim of this work was to investigate Zn–Ni–Co codeposition from a simple chloride plating solution. Different ratios of alloying elements were tested in order to determine whether greater Ni or Co contents in the alloy coatings would be beneficial for better corrosion protection. The plating baths used were free of additives and deposition was performed at room temperature since the aim of the work was to investigate only the influence of different cobalt to nickel ratios in the solution.

EXPERIMENTAL

Electrodeposition of Zn–Ni–Co alloys

The Zn–Ni–Co alloys were deposited galvanostatically, at various current densities, from chloride baths of the following composition (pH 4.5±0.1): 0.38 mol dm^{-3} $ZnCl_2$; 0.24 mol dm^{-3}

H_3BO_3; 3.85 mol dm^{-3} KCl and either 0.34 mol dm^{-3} $NiCl_2\cdot 6H_2O$ and 0.04 mol dm^{-3} $CoCl_2\cdot 6H_2O$, or 0.20 mol dm^{-3} $NiCl_2\cdot 6H_2O$ and 0.18 mol dm^{-3} $CoCl_2\cdot 6H_2O$, at 25 °C. The employed electrolytes were prepared using p.a. chemicals and double distilled water.

The working electrodes were Zn–Ni–Co alloys deposited on: *i*) steel panel (20 mm×20 mm×0.25 mm), for electrochemical measurements: electrochemical impedance spectroscopy (EIS) and open circuit potential (E_{ocp}) measurements and atomic force microscopy (AFM) analysis and *ii*) Pt panel for determination of the chemical composition.

Prior to each electrodeposition the steel substrates were pretreated by mechanical cleaning (polishing successively with emery papers of the following grades: 280, 360, 800 and 1000) and then degreased in a saturated solution of sodium hydroxide in ethanol, pickled with a 1:1 hydrochloric acid solution for 30 s and finally rinsed with distilled water. The Pt panel was pretreated by mechanical polishing with a polishing cloth (Buehler Ltd.), impregnated with a water suspension of alumina powder (0.3 μm grade) and then rinsed with pure water in an ultrasonic bath.

The counter electrodes were: *i*) a zinc panel, placed parallel to a steel panel and *ii*) a Pt spiral wire for the EIS measurements.

The reference electrode used in all experiments was a saturated calomel electrode (SCE).

Chemical composition and surface morphology

The chemical compositions of the Zn–Ni–Co alloys were determined by atomic absorption spectrometry (AAS-PYE Unicam SP9, Philips).

The structural characterization was performed by atomic force microscopy, with a NanoScope 3D (Veeco, USA) microscope operated in the tapping mode under ambient conditions. Etched silicon probes with a spring constant 20–80 N m^{-1} were used.

Electrochemical measurements

The electrochemical measurements were performed in 3 % aqueous NaCl solution using a Gamry Reference 600 potentiostat/galvanostat/ZRA. A classic three-electrode cell arrangement was used. The working electrode was a coated steel panel situated in a special holder. The counter electrode was a platinum mesh with a surface area considerably greater than that of the working electrode. The reference electrode was a saturated calomel electrode (SCE). The cell assembly was located at a Faraday cage to prevent electrical interferences. The electrochemical impedance spectroscopy measurements were performed at the open-circuit potential (OCP), over a frequency range from 100 kHz to 10 mHz, using a 10 mV amplitude sinusoidal voltage. The impedance spectra were analyzed using the Gamry Elchem Analyst fitting procedure. The corrosion stability was also evaluated by determining the time to the appearance of red rust. The plated specimens (10 μm thick) were immersed in a 3 % aqueous NaCl solution and the open circuit potential was measured daily.

RESULTS AND DISCUSSION

Chemical composition of Zn–Ni–Co alloys

In order to define the composition of ternary alloys, three variables of composition should be fixed. The manner in which the composition of the plating solution is varied is very important.[17] The most convenient way is to keep the total metal content of the solution and one of the metal-percentages constant. In this manner, the chemical content of a ternary alloy then becomes a function of the metal percentage of one of the other two metals in the solution.[17] In this work the Zn content was held constant in both the examined plating solutions and the ratio of two alloying elements, Co and Ni, was varied. The influence of the deposition current density on the chemical content of Co, Ni and Zn in the Zn–Ni–Co alloys, determined by AAS, is shown in Figs. 1 and 2 for alloys deposited from plating solutions with different Co^{2+} to Ni^{2+} ratios. It can be seen that chemical content of the alloying elements depends on both the ion ratio in the plating solution and the deposition current density. Namely, the alloys deposited from a solution with $[Co^{2+}]/[Ni^{2+}] = 0.12$ contained a significantly greater amount of Ni as compared to Co (Fig. 1), whereas the differences among contents of Co and Ni were smaller for the alloys deposited from a solution with $[Co^{2+}]/[Ni^{2+}] = 0.90$ (Fig. 2). The total content of alloying elements, Ni and Co, was greater for alloy coatings deposited from the bath with higher cobalt to nickel ion ratio and it varied depending on the deposition current density. Namely, in this plating solution, the Co content in the alloy deposit increased with increasing deposition current density until 5 A dm^{-2} but a further increase in current density resulted in a decreased Co content (Fig. 2).

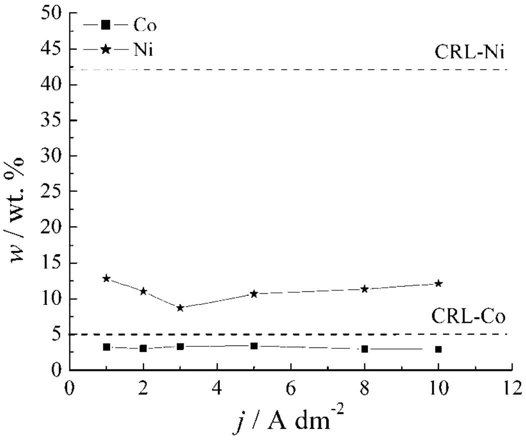

Fig. 1. Dependence of the Co and Ni contents in Zn–Ni–Co alloys on the deposition current density for alloys deposited from the solution with $[Co^{2+}]/[Ni^{2+}] = 0.12$.

The ratio of each alloying element to the total amount of metal cations in the plating solution is shown in Figs. 1 and 2 by composition reference lines (CRL) for both Co and Ni. Brenner[17] classified the electrodeposition of Zn with elements of the iron group as anomalous, when zinc, which is the less noble metal, deposits preferentially and the content of alloying element in the deposit is smaller than in the plating solution. The amount of Zn in ternary alloys does not change much with the deposition current density and in both plating solutions it was well above the CRL lines, which being ≈52 %, suggesting preferential Zn deposition (see Fig. S-1a and b in the Supplementary material to this paper).

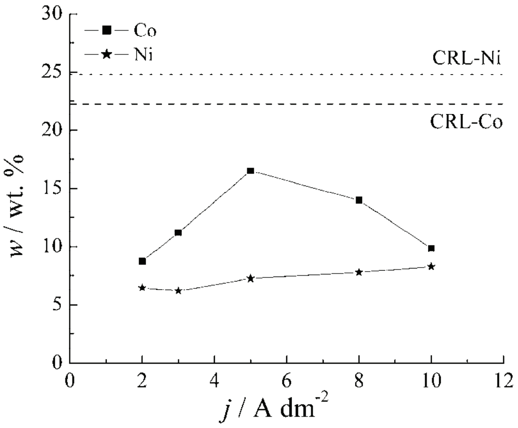

Fig. 2. Dependence of the Co and Ni contents in Zn–Ni–Co alloys on the deposition current density for alloys deposited from the solution with $[Co^{2+}]/[Ni^{2+}] = 0.90$.

Since the contents of both Co and Ni were below their corresponding composition reference lines and the zinc content was considerably above its CRL, and bearing in mind that Zn is less noble than both Co and Ni, it could be concluded that the two alloying elements form an anomalous plating system with Zn.

In one plating solution the ratio of the alloying elements, Co and Ni ions, was 0.12, whereas the ratios of these metals in the deposits were in the range 0.25–0.38, depending on the deposition current density. In the other plating solution, where ratio of the alloying elements was 0.90, their ratio in the deposit was even higher, ranging from 1.2 (at low and high current densities) to 2.3 (at intermediate current densities). In both cases, the ratio of Co and Ni in the deposit was much higher than their ratio in the plating solution, suggesting that these elements could have a synergistic beneficial effect in their codeposition and incorporation in a deposit. Eliaz *et al.* studied partial current densities for the deposition of Zn–Ni–Co alloys in the presence of gelatine and evidenced a mutual synergistic catalytic effect of Ni on Co.[10]

Corrosion protection

Since Zn alloys are mainly used in corrosion protection, their corrosion stability was determined by electrochemical measurements. The results of electrochemical impedance spectroscopy, a technique commonly used in corrosion testing of Zn alloy coatings,[1,10,18,19] are shown in Fig. 3a and b. Nyquist plots for the impedance of the Zn–Ni–Co deposits obtained from the solution with higher ratio of alloying elements, at different current densities, after 60 min of exposure to 3 % NaCl solution are shown in Fig. 3a. All EIS plots were characterized by two semicircles. According to the literature,[10,19,20] the time constant in the high frequency range relates to the presence of a porous oxide layer, while the second time constant, in the lower frequency range, accounts for a pseudo--barrier layer of alloy coating. The smallest impedance values, suggesting the

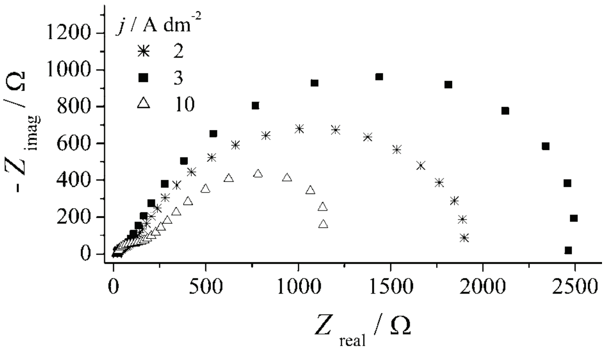

(a)

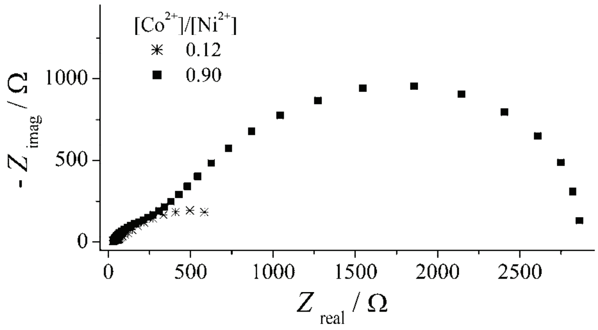

(b)

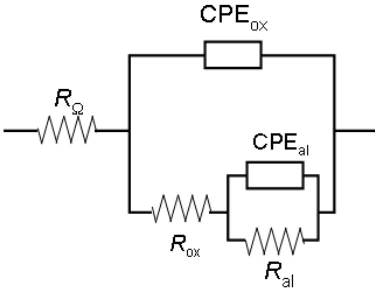

(c)

Fig. 3. Nyquist plots for Zn–Ni–Co alloy coatings deposited: a) from the solution with $[Co^{2+}]/[Ni^{2+}] = 0.90$ at different current densities and b) at 8 A dm^{-2} from the solution with different $[Co^{2+}]/[Ni^{2+}]$ ratios, after 60 min of exposure to 3 % NaCl; c) equivalent electrical circuit used for the impedance plots fitting.

smallest resistance, were obtained for the Zn–Ni–Co alloy coating deposited at the highest current, 10 A dm^{-2}, having 9.8 % Co and 8.3 % Ni. Higher impedance was determined for coatings deposited at smaller current densities. The overall impedance of the alloy coating deposited at 3 A dm^{-2} (with 11.2 % Co and 6.2 % Ni) was two times greater than that for the coating deposited at 10 A dm^{-2} with a smaller Co content and a higher Ni content.

The influence of the $[Co^{2+}]/[Ni^{2+}]$ ratio in the plating solution on the corrosion stability of Zn–Ni–Co alloys is shown in Fig. 3b, for coatings deposited at 8 A dm^{-2}. As can be seen, the differences in the corrosion stability were more dependent on the plating solution composition than on the current density. Deposition from the solution with higher ratio of the alloying elements, with 14 % Co and 7.8 % Ni, resulted in the almost three-fold increase in the overall impedance, as compared to the alloy with only 2.9 % Co and 11.3 % Ni. This could be the result of the differences in the chemical composition of the alloy coatings deposited from the different plating solutions. Namely, the overall content of the alloying elements in the deposits were greater when they were obtained from the solution with their higher ion ratio, as well as greater Co content.

The corrosion protection was analyzed by electrochemical impedance spectroscopy and the EIS data were fitted by the appropriate equivalent electrical circuit (Fig. 3c), having two time constants, (R_{ox}, C_{ox}) and (R_{al}, C_{al}). The elements of the equivalent electrical circuit are: R_{Ω} – the electrolyte resistance, R_{ox} – the oxide layer resistance, R_{al} – the resistance of the alloy coating with corrosion products, and CPE_{ox} and CPE_{al} are the constant phase elements, which are related to the capacitance of the oxide layer and alloy coating with corrosion products, respectively. The time constant related to the charge-transfer resistance and double layer capacitance (R_{ct}, C_{dl}) were not used in the equivalent electrical circuit. This time constant indicates that the corrosion processes on the steel substrate on initial exposure to a corrosive agent was negligible compared to the time constant related to the alloy coating, (R_{al}, C_{al}). Thus, the whole corrosion process, at this early stage, was characterized by the properties of the alloy coating and the time constant (R_{al}, C_{al}), and the oxide layer. The fitting of experimental data enabled the determination of R_{ox}, C_{ox}, R_{al} and C_{al} for the alloy coatings and the results are shown in Figs. 4 and 5. The capacitance C_{al} was determined in the Gamry Instruments Echem Analyst and also calculated using the proposed method from the literature.[21]

As can be seen from Figs. 3 and 4, the impedance of the thin, porous oxide layer was significantly smaller than the impedance of the inner pseudo-barrier layer on the alloy surface. The R_{al} values of the Zn–Ni–Co alloys deposited from the solution with low [Co^{2+}]/[Ni^{2+}] ratio, with around 3 % Co and 9–13 % Ni, were up to six times lower (indicating lower corrosion stability) than the alloy coatings deposited from the other plating solution, which containing a greater amount of Co and a smaller amount of Ni (9–16.5 % Co and 6–8 % Ni).

For the alloy coatings deposited from the solution with the low ratio of the alloying elements, the highest alloy coating resistance was determined for the ones with the same chemical content (2.9 % Co and 12 % Ni) deposited at 8 and 10 A dm^{-2} (822 and 905 Ω cm^2), while much higher resistances were found for alloy coatings deposited from the solution with high ion ratio at 3 and 8 A dm^{-2}, having greater Co and smaller Ni amounts (11.2 % Co, 6.2 % Ni and 14 % Co, 8.3 % Ni, respectively) (2640 and 2710 Ω cm^2).

The resistances of the corresponding binary alloy coatings were 800 Ω cm^2 for Zn–Ni (with 12.0 % Ni) and 450 Ω cm^2 for Zn–Co (11.3 % Co), deposited at

8 A dm^{-2} from the plating solutions free of one of the alloying element (Co and Ni, respectively). Hence, the ternary alloy coatings provided either comparable or greater corrosion stability, depending on both the deposition current density and the deposition solution.

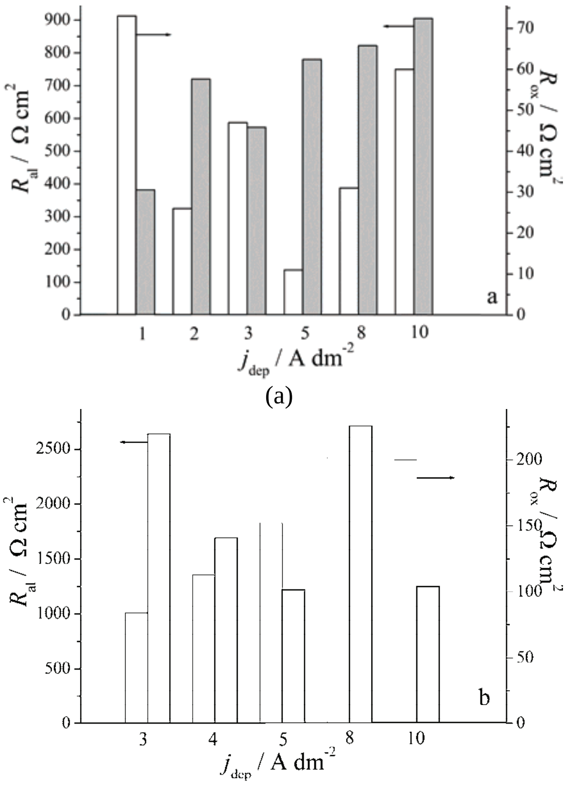

(a)

(b)

Fig. 4. The values of R_{ox} and R_{al} for the Zn–Ni–Co alloys deposited at different deposition current densities from the solution with [Co^{2+}]/ /[Ni^{2+}]: a) 0.12 and b) 0.90.

The values of alloy coating capacitances, C_{al}, are shown in Fig. 5. One to two order of magnitude higher C_{al} values were determined for alloy coatings deposited from the solution with the lower alloying ion ratio, having a smaller Co content. The smallest capacitances were determined for coatings deposited at 3 and 8 A dm^{-2} from the solution with [Co^{2+}]/[Ni^{2+}] = 0.90, suggesting they were less porous. The capacitances of the corresponding binary alloy coatings were 20 μF cm^{-2} and 310 μF cm^{-2} for Zn–Ni and Zn–Co alloys, respectively.

Based on the EIS plots and results shown in Figs. 4 and 5, it could be concluded that the higher content of either of the alloying element was not solely responsible for providing higher corrosion stability, as indicated by the high R_{al} and low C_{al} values, for coatings deposited from both the plating solutions. The highest corrosion stability (highest R_{al} and lowest C_{al} values) was observed for the Zn–Ni–Co (14 % Co, 8.3 % Ni) alloy deposited at 8 A dm^{-2} from the bath with a high $[Co^{2+}]/[Ni^{2+}]$ ratio.

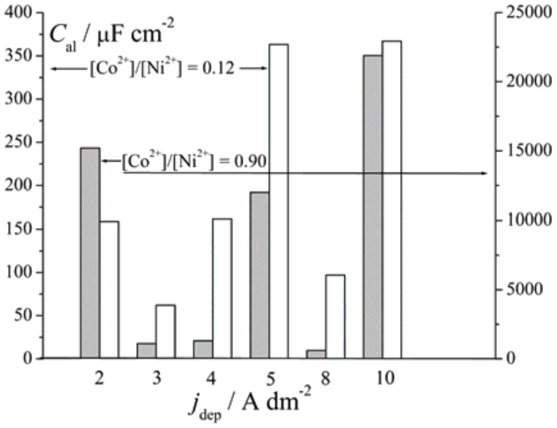

Fig. 5. The values of C_{al} for the Zn–Ni–Co alloys deposited at different deposition current densities from the solution with $[Co^{2+}]/[Ni^{2+}]$: 0.12 and 0.90.

The long-term protection was evaluated by following the change in the open circuit potential with time of exposure to a 3 % NaCl solution. The time dependence of E_{ocp} for steel coated by Zn–Ni–Co alloys deposited from different plating solutions at different current densities was analyzed (see Fig. S-2 of the Supplementary material). The potentials of all the Zn–Ni–Co alloys were more negative than the E_{ocp} value of the steel base; hence, these ternary alloy deposits offered sacrificial cathodic protection. The open circuit potentials of the alloys deposited from the solution with $[Co^{2+}]/[Ni^{2+}] = 0.12$ were more negative (lower than –1020 mV *vs*. SCE) as compared to those deposited from the solution with the higher ion ratio (–720 mV *vs*. SCE). The alloy coatings deposited from the latter solution have greater overall amounts of alloying elements and, consequently, a nobler E_{ocp}. The E_{ocp} values of steel coated with Zn–Ni–Co alloys increased with time of immersion and eventually reached the steel E_{ocp}, which represents loss of the deposit and the start of a steel corrosion process. Deposits obtained from the solution with the lower ion ratio reached the steel E_{ocp} more rapidly. The alloy coating deposited at 1 A dm^{-2} (3.2 % Co, 12.8 % Ni) reached the steel E_{ocp} already after 3 days, whereas the ones deposited at 3, 5 and 8 A dm^{-2} (≈3 % Co, 10.5–12 % Ni) lasted longer, 7–9 days. Among the coatings obtained from the solution with $[Co^{2+}]/[Ni^{2+}] = 0.90$, red rust appeared first on the alloy deposited at 10 A dm^{-2} (9 days). The longest time to red rust appearance (24 days), indicating the best corrosion stability, was observed for the Zn–Ni–Co alloy deposited from this plating solution at 8 A dm^{-2}.

The differences in corrosion stability among coatings could be the due to the greater overall content of the alloying elements, as well as the greater Co content, in deposits obtained from the solution with their higher ion ratio. It was shown that the chemical content of all the alloy coatings analyzed in this work was sufficient to provide better corrosion protection with respect to the protection offered by binary coatings. However, the results shown so far suggest that the chemical content of the alloys was not the only factor governing good corrosion stability.

Surface morphology

Homogenous and coherent coatings were obtained from both plating solutions up to a current density 10 A dm^{-2}. Already at 12 A dm^{-2}, the deposits were not so uniform and powdery at the edges. The differences in surface morphology of some of the electrodeposited Zn–Ni–Co alloys could be seen from the atomic force microscopy (AFM) images shown in Figs. 6 and 7. A large crystal agglomeration of hexagonal type, ranging from 900–1500 nm, could be seen in Fig. 6a for the deposit obtained from the plating solution with [Co^{2+}]/[Ni^{2+}] = 0.12 at 5 A dm^{-2}. A larger Co content in the plating solution, at the same current density, resulted in a deposit having a different shape of crystal agglomerations (Fig. 6b). They were smaller (500–700 nm), more narrow and flat and thus, more densely packed.

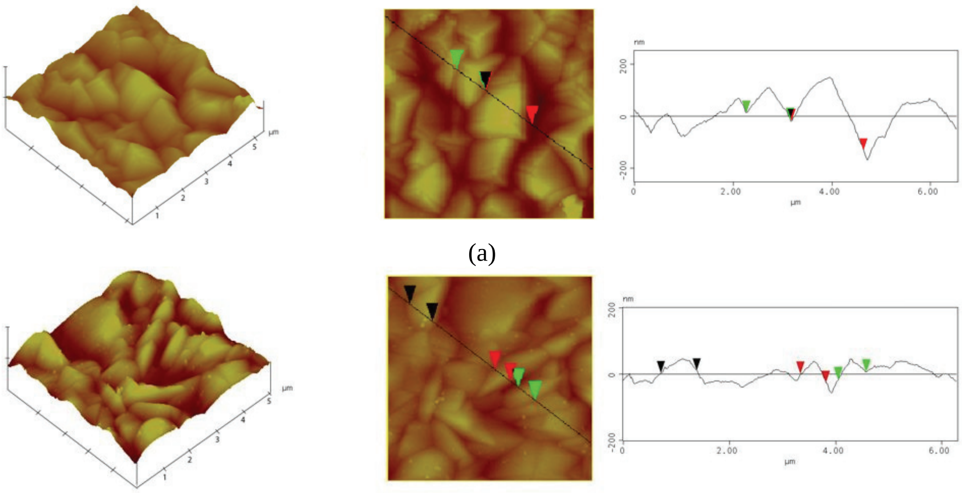

(a)

(b)

Fig. 6. 3D and 2D AFM images and height profiles of the Zn–Ni–Co alloy deposited at 5 A dm^{-2} from the solution with [Co^{2+}]/[Ni^{2+}]: a) 0.12 and b) 0.90.

Higher current densities modified the morphology of the alloys, decreasing the surface roughness, in both plating solutions. A smooth surface with large agglomerations, ranging from 1.3–1.7 μm, could be seen in Fig. 7a for the alloy deposited at 8 A dm^{-2} from the solution with the smaller Co to Ni ratio. Large agglomerations with high roughness no longer existed, suggesting the inhibition of vertical agglomeration growth on the surface. The deposit was composed of large, flat agglomerates that are not closely packed and hence, it does not seem very compact. The surface morphology of alloy deposited at 8 A dm^{-2} from the plating solution with [Co^{2+}]/[Ni^{2+}] = 0.90 was more compact and smoother, as can be seen in Fig. 7b, with agglomerates of smaller size, *i.e.*, 750–800 nm.

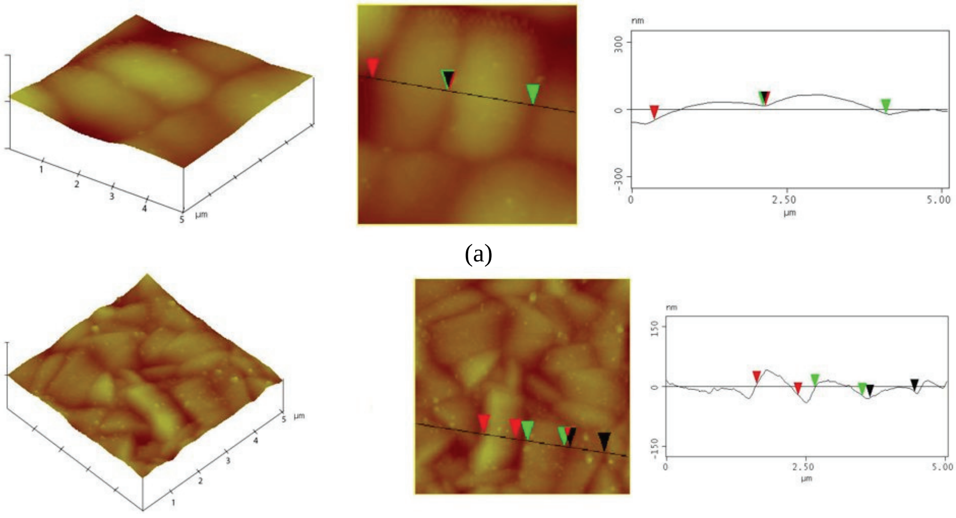

(a)

(b)

Fig. 7. 3D and 2D AFM images and height profiles of the Zn–Ni–Co alloy deposited at 8 A dm^{-2} from the solution with [Co^{2+}]/[Ni^{2+}]: a) 0.12 and b) 0.90.

The distribution of sizes of the agglomerates, determined from AFM images (not shown), indicated that the average agglomerate size of all deposits varied greatly with the [Co^{2+}]/[Ni^{2+}] ratio in the plating bath. Smaller agglomerates were observed for the alloy coatings deposited from the solution with the greater ion ratio and greater overall amounts of alloying elements. In addition, the homogeneity of agglomerates size distribution for these samples was also greater.

It is well known that Zn alloys corrode preferentially, thus providing sacrificial protection of steel. The protection mechanism for both Zn–Ni and Zn–Co alloy coatings was suggested by Lambert and confirmed by Short.[22,23] Namely, at the beginning of exposure to a corrosive agent, *i.e.*, during the early stage of corrosion, zinc, as a less noble metal, dissolves preferentially, providing galvanic protection of steel. Consequently, a dezincification process occurs, resulting in enrichment of the alloy surface layer with alloying elements. The dezincification of the Zn–alloy coating leads to an improved barrier layer, which reduces the corrosion rate. This, in turn, leads to a shift in the corrosion potential to more noble values. With further exposure to a corrosive agent, a layer of corrosion products forms on the surface that acts as a protective, barrier layer. It was shown that the layer of corrosion products on Zn-alloys in a chloride-containing environment is mainly made up of zinc hydroxychloride, $Zn_5(OH)_8Cl_2$.[4,25,26] It has a very low solubility, $10^{-14.2}$,[27] providing a pseudo-passive layer that enables high protective ability. If porosity of this pseudo-barrier layer were smaller, the corrosion protection would be improved.

The more densely packed morphology of the alloy coatings obtained from the plating solution with greater $Co^{2+}]/[Ni^{2+}]$ ratio, with a greater amount of Co and considerably smaller crystal agglomerates, resulted in a less porous deposit. The smaller porosity was indicated by AFM images and confirmed by the at least order of magnitude smaller capacitances (Fig. 6). Eliaz *et al.*[10] also found that the minimal corrosion rates of Zn–Ni–Co alloy coatings neither corresponded to the highest content of the more noble element (iron-group metal) in the coating nor to the highest thickness of the coatings. They showed that the coatings with the lower corrosion resistance were those with a higher degree of porosity. Hence, the chemical content was not the sole factor determining the corrosion stability of the ternary alloy coatings examined in this work.

Hence, it could be concluded that the chemical content and surface properties, such as homogeneity, agglomeration size and their distribution, depend on the plating solution, as well as on deposition current density. The agglomerates obtained from the plating solution with a smaller ion ratio were larger, with considerable differences in size, with respect to the ones deposited from the plating solution with the higher ion ratio. More compact alloy coatings, with a uniform distribution of agglomerates, are deposited from the solution with the higher ion ratio, especially at 8 A dm^{-2}. Hence, the pseudo-passive layer of the corrosion products formed on the surface of this alloy was more compact, with a higher resistivity and a smaller permeability (reflected by the smaller capacitance values), which, in turn, resulted in improved corrosion stability.

CONCLUSION

Ternary Zn–Ni–Co alloy coatings were successfully deposited from chloride, additive free, plating solutions. Based on the presented results, it could be concluded that the ratio of nickel to cobalt ions in the plating solution and deposition current density had a significant influence on the chemical composition, morphology and corrosion stability of Zn–Ni–Co electrodeposited alloys.

The contents of both Co and Ni are below their corresponding composition reference lines and the zinc content is considerably above its CRL, so the two alloying elements form an anomalous plating system with Zn. The ratio of Co and Ni is much higher than their ratio in the plating solution, in all examined deposits, suggesting that these elements could have a beneficial synergistic effect in their codeposition and incorporation in a deposit.

It was shown that the ternary alloy coatings provide either comparable or greater corrosion stability, depending both on the deposition current density and the deposition solution. A higher impedance of the ternary alloys deposited from the solution with the greater [Co^{2+}]/[Ni^{2+}] ratio was determined. These deposits also showed significantly smaller capacitances, suggesting improved corrosion stability. The longest time to red rust appearance, indicating the best corrosion stability, was observed for the Zn–Ni–Co alloy deposited from this plating solution at 8 A dm^{-2}.

Homogenous and coherent coatings were obtained from both plating solutions up to a current density of 10 A dm^{-2}. Smaller crystalline aggregates were formed by deposition from the solution with the higher [Co^{2+}]/[Ni^{2+}] ratio, *i.e.*, in deposits with the greater Co content. In addition, the homogeneity of the size distribution of the agglomerates for these samples was also greater and the corresponding corrosion stability was higher. It is assumed that more compact alloy coatings with uniform distribution of agglomerates, which were deposited from the solution with the higher ion ratio, especially at 8 A dm^{-2}, resulted in an improved corrosion stability.

SUPPLEMENTARY MATERIAL

Figures S-1 and S-2 along with corresponding discussion are available electronically from http://www.shd.org.rs/JSCS/, or from the corresponding author on request.

Acknowledgement. This research was financed by the Ministry of Education, Science and Technological Development of the Republic of Serbia, Contract No. III 45019, and the Ministry of Science and Technology of the Republic of Srpska (Project: “Electrochemical deposition and characterization of environmentally friendly protective ternary Zn–Ni–Co alloys on steel”).

ИЗВОД

ТРОЈНЕ Zn–Ni–Co ЛЕГУРЕ: АНОМАЛНО ТАЛОЖЕЊЕ И КОРОЗИОНА СТАБИЛНОСТ

МИЛОРАД В. ТОМИЋ[1], МИЛОШ М. ПЕТРОВИЋ[2], СЛАВКА СТАНКОВИЋ[3], САЊА И. СТЕВАНОВИЋ[4]
и ЈЕЛЕНА Б. БАЈАТ[3]

[1]*Универзитет у Источном Сарајеву,Технолошки факултет Зворник, Каракај бб, Зворник, Република Српска, БиХ,* [2]*Institute of Materials Research and Engineering, A*STAR (Agency for Science, Technology and research) 3 Research link, Singapore 117602, Department of Mechanical Engineering, National University of Singapore, Singapore 117576,* [3]*Технолошко–металуршки факултет, Универзитет у Београду, Карнегијева 4, 11120 Београд и* [4]*ИХТМ – Центар за електрохемију, Универзитет у Београду, Његошева 12, Београд*

У овом раду су проучаване Zn–Ni–Co легуре електрохемијски таложене под различитим условима. Хемијски састав је одређиван AAS техником, морфологија AFM анализом а корозиона стабилност применом EIS. Испитиван је утицај односа легирајућих елемената, [Co^{2+}]/[Ni^{2+}], у хлоридном раствору за таложење, као и густине струје таложења, на хемијски састав, морфологију и корозиону постојаност легура. Коришћени су раствори са истим укупним садржајем метала, без додатака, и таложење је вршено на собној температури. Показано је да је таложење тројних легура аномално и да однос јона никла и кобалта у раствору за таложење, као и густина струје таложења, имају зна-

чајан утицај на хемијски састав и корозиону стабилност ових легура. Заједничко присуство Ni и Co је имало повољан утицај на корозиону постојаност легура. Показано је да су морфологија и порозност превлака легура веома важни фактори који утичу на њихову корозиону стабилност. Превлака добијена таложењем из раствора са већим односом јона легирајућих елемената густином струје од 8 A dm^{-2} се састојала од мањих агрегата кристалних зрна, била је мање храпавости и порозности и показала је највећу корозиону стабилност.

(Примљено 28 августа, ревидирано 31. октобра, прихваћено 13. новембра 2014)

REFERENCES

1. K. R. Sriraman, S. Brahimi, J. A. Szpunar, J. H. Osborne, S. Yue, *Electrochim. Acta* **105** (2013) 314
2. E. M. de Oliveira W. Rubin, I. A. Carlos, *J. Appl. Electrochem.* **39** (2009) 1313
3. O. Girčienė, L. Gudavičiūtė, R. Juškėnas, R. Ramanauskas, *Surf. Coat. Technol.* **203** (2009) 3072
4. C. N. Panagopoulos, D. A. Lagaris, P. C. Vatista, *Mater. Chem. Phys.* **126** (2011) 398
5. J. L. Ortiz-Aparicio, Y. M. G. Trejo, R. Ortega, T. W. Chapman, E. Chainet, P. Ozil, *J. Appl. Electrochem.* **41** (2011) 669
6. M. H. Gharahcheshmeh, M. H. Sohi, *J. Appl. Electrochem.* **40** (2010) 1563
7. I. H. Karahan, *J. Mater. Sci.* **42** (2007) 10160
8. S. L. Dıaz, O. R. Mattos, O. E. Barcia, F. J. Fabri Miranda, *Electrochim. Acta* **47** (2002) 4091
9. M. M. Younan, *J. Appl. Electrochem.* **30** (2000) 55
10. N. Eliaz, K. Venkatakrishna, A. C. Hegde, *Surf. Coat. Technol.* **205** (2010) 1969
11. M. M. Abou-Krisha, H. M. Rageh, E. A. Matter, *Surf. Coat. Technol.* **202** (2008) 3739
12. M. M. Abou-Krisha, *Mater. Chem. Phys.* **125** (2011) 621
13. T. Dikici, O. Culha, M. Toparli, *J. Coat. Technol. Res.* **7** (2010) 787
14. R. S. Bhat, U. Bhat, A. C. Hegde, *Anal. Bioanal. Electrochem.* **3** (2011) 302
15. J. B. Bajat, M. D. Maksimović, V. B. Mišković-Stanković, S. Zec, *J. Appl. Electrochem.* **31** (2001) 335
16. J. B. Bajat, V. B. Mišković-Stanković, Z. M. Kačarević-Popović, *Prog. Org. Coat.* **45** (2002) 379
17. A. Brenner, *Electrodeposition of Alloys*, Vols. 1 and 2, Academic Press, New York, 1963
18. A. C. Hegde, K. Venkatakrishna, N. Eliaz, *Surf. Coat. Technol.* **205** (2010) 2031
19. O. Hammami, L. Dhouibi, E. Triki, *Surf. Coat. Technol.* **203** (2009) 2863
20. M. S. Chandrasekar, S. Srinivasan, M. Pushpavanam, *J. Solid State Electrochem.* **13** (2009) 781
21. C. H. Hsu, F. Mansfeld, *Corrosion* **57** (2001) 747
22. M. R. Lambert, G. R. Hart, H. E. Townsend, *SAE Tech. Pap. Series* No 831817, Detroit, MI, 1983, p. 81
23. N. R. Short, A. Abibsi, J. K. Dennis, *Trans. Inst. Met. Finish.* **67** (1989) 73
24. M. C. Bernard, A. Hugot-Le Goff, N. Philips, *J. Electrochem. Soc.* **142** (1995) 2162
25. P. L. Neto, A. N. Correia, R. P. Colares, W. S. Araujo, *J. Braz. Chem. Soc.* **18** (2007) 1164
26. N. Boshkov, K. Petrov, D. Kovacheva, S. Vitkova, S. Nemska, *Electrochim. Acta* **51** (2005) 416
27. S. Peulon, D. Lincot, *J. Electrochem. Soc.* **145** (1988) 864.

Journal of the Serbian Chemical Society
eVersion electronic
JSCS@tmf.bg.ac.rs • www.shd.org.rs/JSCS
J. Serb. Chem. Soc. 80 (1) S13–S14 (2015)
Supplementary material

SUPPLEMENTARY MATERIAL TO

Ternary Zn–Ni–Co alloy: anomalous codeposition and corrosion stability

MILORAD V. TOMIĆ[1], MILOŠ M. PETROVIĆ[2], SLAVKA STANKOVIĆ[3], SANJA I. STEVANOVIĆ[4] and JELENA B. BAJAT[3]*

[1]*University of Eastern Sarajevo, Faculty of Technology Zvornik, Republic of Srpska, B & H,* [2]*Institute of Materials Research and Engineering, A*STAR (Agency for Science, Technology and Research) 3 Research link, Singapore 117602, Department of Mechanical Engineering, National University of Singapore, Singapore 117576,* [3]*Faculty of Technology and Metallurgy, University of Belgrade, P. O. Box 3503, 11120 Belgrade, Serbia and* [4]*ICTM – IEC, P. O. Box 473, 11001 Belgrade, Serbia*

J. Serb. Chem. Soc. 80 (1) (2015) 73–86

The Zn content in the ternary alloys for deposition solutions with different $[Co^{2+}]/[Ni^{2+}]$ ratios, along with the corresponding CRLs indicate that the amount of Zn does not change much with the deposition current density (Fig. S-1a and b) and in both plating solutions it is well above the CRLs, suggesting preferential Zn deposition.

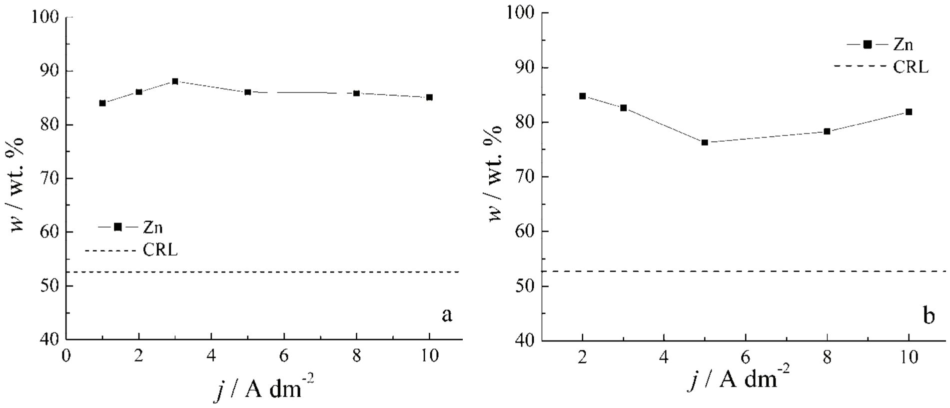

Fig. S-1. Dependence of Zn content in the Zn–Ni–Co alloys on deposition current density for alloys deposited from the solution with $[Co^{2+}]/[Ni^{2+}]$: a) 0.12 and b) 0.90.

---

* Corresponding author. E-mail: jela@tmf.bg.ac.rs

The long-term protection was evaluated by following the change in the open circuit potential with time of exposure to a 3 % NaCl solution. The time dependence of E_{ocp} for steel coated with Zn–Ni–Co alloys deposited from different plating solutions at different current densities is shown in Fig. S-2. The open circuit potential of bare steel surface in 3 % NaCl is marked with a line in Fig. S-2 (–640 mV *vs*. SCE).

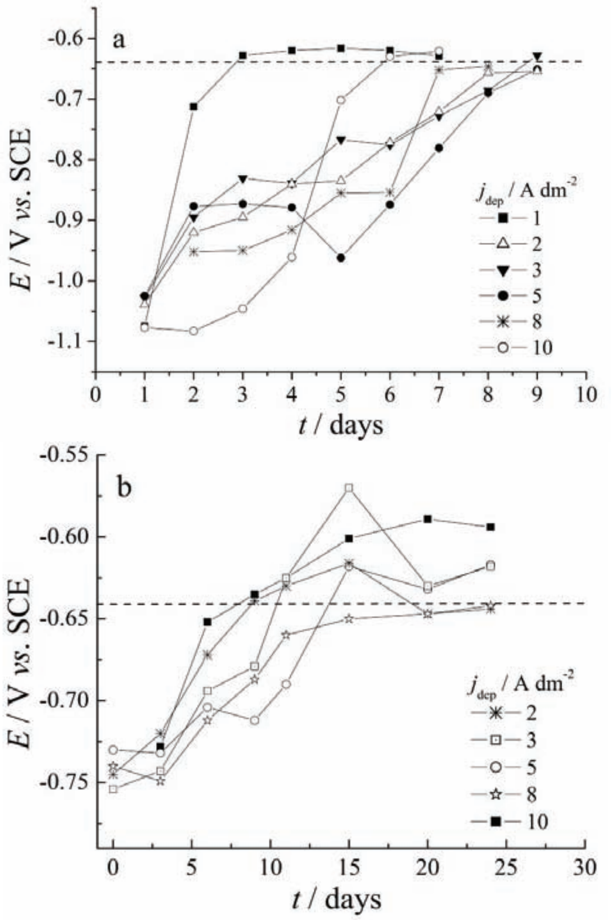

Fig. S-2. The dependence of E_{ocp} for Zn–Ni–Co alloys deposited on steel from solution with $[\mathrm{Co}^{2+}]/[\mathrm{Ni}^{2+}]$: a) 0.12 and b) 0.90.

Journal of
the Serbian
Chemical Society
ersion
lectronic

JSCS-info@shd.org.rs • www.shd.org.rs/JSCS

J. Serb. Chem. Soc. 80 (1) 87–96 (2015)
JSCS–4699

UDC 547.677.5+546.47+577.213.3:
539.196+543.552
Original scientific paper

Polarographic determination of DNA based on its interaction with the phenanthroline–zinc(II) complex

NI HUI[1]*, AIQIN LIANG[1], CHANGHUI XUE[1] and WEI SUN[2]

[1]*College of Chemistry and Pharmacy, Qingdao Agriculture University, Qingdao 266109, P. R. China and* [2]*College of Chemistry and Chemical Engineering, Hainan Normal University, Haikou, 571158, P. R. China*

(Received 18 February, revised 28 November, accepted 2 December 2014)

Abstract: By using the linear sweep voltammetric technique, a phenanthroline (Phen) and zinc(II) (Phen–Zn(II)) complex was used as the electrochemical probe for the determination of double-stranded (ds) DNA. In pH 9.0 Britton–Robinson (B–R) buffer solution, Phen can interact with Zn(II) to form a stable electroactive [Phen–Zn(II)] complex, which had a sensitive second order derivative polarographic reductive peak at –1.300 V (*vs.* SCE). After the addition of dsDNA into a solution of Phen–Zn(II) complex, the reduction peak current decreased with a negative shift of the reduction peak potential and without the appearance of new peaks. The results showed that a new supramolecular complex was formed *via* interaction of the Phen–Zn(II) complex with dsDNA. The conditions of interaction and the electrochemical detection were carefully investigated. Under the optimum conditions, the decrease in the reduction peak current was directly proportional to the dsDNA concentration in the range of 0.4–18.0 mg L^{-1} with the linear regression equation: $\Delta Ip''/\mathrm{nA} = 349.48 + 84.647(c/\mathrm{mg\ L^{-1}})$ ($n = 13$, $\gamma = 0.991$) and a determination limit of 0.20 mg L^{-1} (3σ). The relative standard deviation (*RSD*) for 10 parallel determinations of 10.0 mg L^{-1} dsDNA was found to be 2.03 %. The method was successfully applied to the detection of synthetic samples with satisfactory results.

Keywords: phenanthroline; zinc; DNA; interaction; linear sweep voltammetry.

INTRODUCTION

The interaction of small molecules with double-stranded (ds) DNA has been widely investigated in recent years because of the specific functions of dsDNA in life processes. Some interactions could damage the structure of dsDNA and influence the replication of dsDNA.[1] In addition, the investigations could be used for the design of new drugs targeted on dsDNA.[2,3] Generally speaking, small molecules, such as dyes,[4–6] drugs[7–9] and metal coordination compounds,[10–13]

---

* Corresponding author. E-mail: huini1029@163.com
doi: 10.2298/JSC140218120H

can bind to dsDNA in three ways, *i.e.*, electrostatic binding, intercalation and groove binding.[14–16] The quantitative determination of DNA is also important in bioanalytical chemistry and clinical tests. Various analytical methods for the detection of DNA, such as spectrophotometry,[17–19] fluorometry,[20,21] light scattering technique,[22,23] *etc*., have been established based on the interaction of small molecules with dsDNA. However, most of these methods suffer from low sensitivity, high costs or complicated procedures. Compared with the above methods, the electroanalytical method has some advantages. Such as cheaper and smaller devices, wider linear range and lower detection limits.[24] In addition, as the electrochemical reaction occurs at the electrode interface, only a small amount of sample is required in the detection procedure. Wang *et al.*[25] established an electrochemical equation for examining the interaction of irreversible redox compounds, such as bis-benzimidazole derivative (Hoechst 33258) with dsDNA using cyclic voltammetry and other electrochemical techniques. Paleček *et al.*[26] studied the interaction between the anticancer drug mitomycin C and DNA by cyclic voltammetry on a hanging mercury drop electrode, which resulted in a decrease in the voltammetric signal. Jiao *et al.* used some organic dyes, such as toluidine blue,[27] rhodamine B[28] and malachite green,[29] for the detection of dsDNA based on the formation of electroinactive complexes on mixing a mixture of dsDNA with the dyes in solution. Bard *et al.*[30,31] reported the interaction of metal chelates of tris (1,10-phenanthroline) cobalt (III) with DNA in an aqueous medium and established a redox current equation for the intercalator–DNA complex. Moreover, some polarographic methods for the detection of dsDNA were established using electroactive dyes, such as pyronine B,[32] phenosafranine,[33] neutral red[34] and brilliant cresyl blue.[35]

Phenanthroline (Phen) is a heterocyclic organic compound that is often used as a bidentate ligand in coordination chemistry. Phen reacts with most metal ions to yield strong stable metal complexes, such as with cobalt(III)[30] and copper(II).[36] It was employed in the determination of zinc(II) by polarography.[37,38] Experimental results indicated that the Phen–Zn(II) complex had a sensitive polarographic reduction peak at –1.300 V (*vs.* SCE) on a dropping mercury working electrode. After the addition of dsDNA into a Phen–Zn(II) complex solution, a large decrease in the reduction peak current and a negative shift of the reductive peak potential appeared, which indicated that Phen–Zn(II) complex could interact with dsDNA to form a supramolecular complex in the mixture solution. In this study, the phenanthroline (Phen) and zinc complex was investigated as a new polarographic probe for dsDNA detection.

EXPERIMENTAL

Apparatus and reagents

All the polarographic determinations were performed on a model JP-303 polarography (Chengdu Apparatus Factory, China) with the second order derivative linear sweep polarography. A conventional three-electrode system, which was composed of a dropping mercury working electrode (DME), a saturated calomel reference electrode (SCE) and a platinum wire auxiliary electrode, was used throughout. A pHS-25 acidimeter (Shanghai Leici Instrument Factory, China) was used for the pH value measurement and all the experiments were performed at 25±1 °C.

A stock solution (1.0 g L^{-1}) of double-stranded (ds) herring sperm DNA (Sigma, USA) was prepared by dissolving it in doubly distilled water and storing at 4 °C.[39-41] The skeleton of dsDNA is very stable and apart from strong acids and high temperature, other environments cannot destroy it.[42] Experiments showed that the A_{260} of the dsDNA solution kept in 4 °C did not change, indicating that the low temperature environment prevented it from unwinding. The purity of dsDNA was examined by the absorbance ratio of A_{260}/A_{280} that was 1.85, which indicated that the dsDNA was sufficiently free of protein. The concentration of dsDNA was calculated from the absorbance value at 260 nm using $\varepsilon_{\rm DNA}$ = 6600 dm^3 mol^{-1} cm^{-1}. Single-stranded DNA (ssDNA) was acquired by heating the solution of native herring sperm DNA at 100 °C in a waterbath for 10 min and cooling in an ice–water bath.[41] A 1.0×10^{-3} mol L^{-1} phenanthroline (Phen, Shanghai Sanpu Chemical Reagent Factory, China) solution was prepared by dissolving 0.1802 g Phen in water and diluting to 250 mL. Britton–Robinson (B–R) buffers (0.2 mol L^{-1}) were used to adjust the pH values of test solution. When B–R buffer was adjusted to pH of 9.0, its ionic strength was 0.104.[43] All the other reagents were of analytical reagent grade and doubly distilled water was used throughout.

Procedures

Into a dry 10 mL volumetric flask, the following reaction solutions were added in turn: 2.0 mL of 0.2 mol L^{-1} B–R buffer solution, 1.0 mL of 1.0×10^{-3} mol L^{-1} Phen, 0.5 mL of 1.0×10^{-3} mol L^{-1} Zn(II) and different amounts of dsDNA solution. The mixtures were diluted to 10 mL with water, mixed thoroughly and allowed to stand for 20 min at 25 °C. Then the solution mixture was transferred to a 10 mL electrochemical cell and the second order derivative linear sweep polarographic curve was recorded in the potential range from –0.8 to –1.6 V (*vs.* SCE) and the reduction peak current (Ip″) of the solution was measured. The peak current of the blank solution (Ip$_0$″) without dsDNA was obtained under the same conditions and the difference of peak currents (ΔIp″= Ip$_0$″– Ip″) was used for dsDNA determination.

RESULT AND DISCUSSION

Second order derivative linear sweep polarography

Typical second order derivative linear sweep voltammograms of the buffer, the Phen–Zn(II) complex and two Phen–Zn(II)–dsDNA reaction solutions are shown in Fig. 1. Curve 1 is the polarogram of the B–R buffer solution without any polarographic peak. Curve 2 is the polarogram of the Phen–Zn(II) complex solution with a reduction peak at –1.300 V (*vs*. SCE), which is the typical Phen––Zn(II) wave on a mercury electrode. The formation and the electrochemical behavior of the [Phen–Zn(II)] complex were explained in detail in the literature.[37,38] Curves 3 and 4 are polarograms of the mixture containing different amounts of dsDNA and the Phen–Zn(II) complex. It can be seen that the reduction peak current decreased gradually with the negative shift of the reduction peak potential, which indicated electrostatic binding of the Phen–Zn(II) complex with dsDNA to form a supramolecular complex. The decrease in the peak current was proportional to the concentration of dsDNA, which could be further used for the determination of dsDNA.

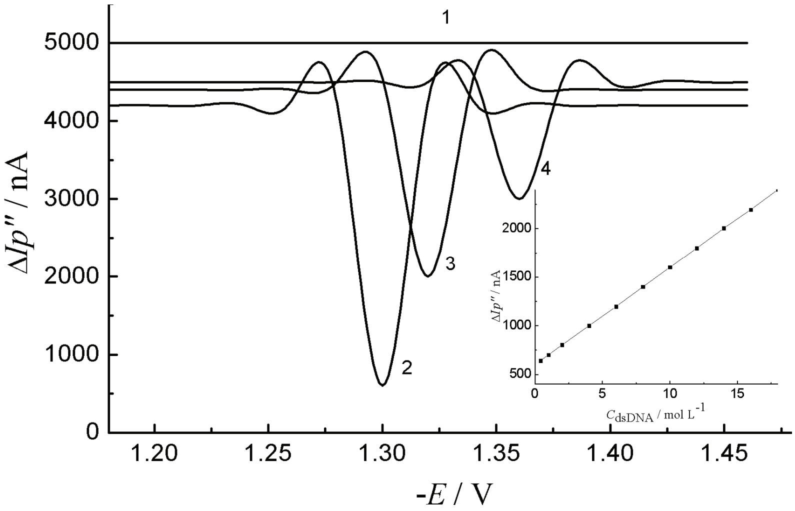

Fig. 1. Second order derivative linear sweep voltammograms of the Phen–Zn(II)–dsDNA reaction system. Inset: the linear calibration curve of dsDNA. 1: pH 9.5, B–R buffer; 2: 1 + 1.0×10^{-4} mol L^{-1} Phen + 5.0×10^{-5} mol L^{-1} Zn(II); 3: 2 + 8.0 mg L^{-1} dsDNA; 4: 2 + 18.0 mg L^{-1} dsDNA.

Optimization of the reaction conditions

The effect of buffer acidity on the difference in the peak current (Δ*I*p″) was investigated in the pH range between 7.0 and 12.0 and the results are shown in Fig. 2. It could be seen that the value of Δ*I*p″ reached its maximum at pH 9.0; hence, pH 9.0 was selected for this assay. The volume of B–R buffer solution added into the solution was also investigated and 2.0 mL of B–R buffer solution was suitable as the supporting electrolyte having sufficient buffer capacity.

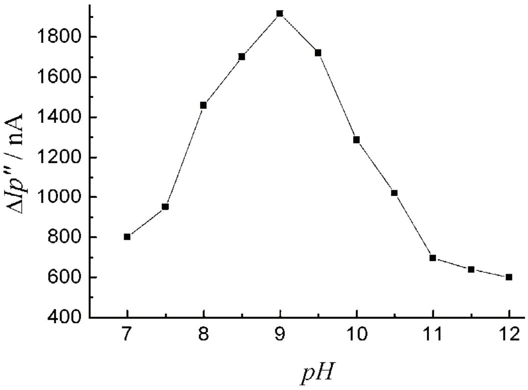

Fig. 2. The influence of pH on the binding interaction. 1.0×10^{-4} mol L^{-1} Zn(II) +1.0×10^{-4} mol L^{-1} Phen + 10.0 mg L^{-1} dsDNA in B–R buffers of different pH values.

The effect of the mole ratio of Phen and Zn(II) on the value of Δ*I*p″ was studied by fixing the dsDNA concentration at 10.0 mg L^{-1}, the Zn(II) concentration at 5.0×10^{-5} mol L^{-1} and changing the concentration of Phen. The value of Δ*I*p″ reached a maximum when the Phen concentration was 1.0×10^{-4} mol L^{-1}. Hence, the ratio of Phen to Zn(II) was kept at 2:1 in the following experiments.

After mixing Phen, Zn(II) with dsDNA in the solution, the value of Δ*I*p″ reached a maximum within 20 min and remained constant for 2 h. Hence, an incubation time of 20 min was used in the experiments, and thus the system gave sufficient time for routine measurements.

The influence of the order of the additions of the different solution on the value of Δ*I*p″ was also studied. The optimal addition order was selected as B–R, Phen, Zn(II) and dsDNA. The results indicated that in the selected pH buffer, the formation of Phen–Zn(II) complex was crucial to the interaction.

The effect of the reaction temperature on the interaction was also tested in the range of 10–40 °C and no obviously differences on ΔI*p*″ was found in the selected temperature range. Thus, a reaction temperature of 25 °C was used throughout.

The effect of instrumental conditions such as the scan rate and the mercury dropping time were carefully tested in turn. The results expressed that the value of Δ*I*p″ increased with the increase of potential scan rate in the range of 300 to 1000 mV s^{-1}. Thus, 1000 mV s^{-1} was selected as the scan rate for detection. The dropping mercury developing time for the assay was optimized and selected as 8 s.

Effect of ionic strength

The effect of ionic strength on the interaction was also investigated by the addition of different amounts of 0.10 mol L^{-1} NaCl to the mixture. The value of Δ*I*p″ decreased with increasing salt concentration in the solution, indicating that the ionic strength had significant influence on the interaction. Thus, the interaction of Phen–Zn(II) complex with dsDNA was caused by a highly favored electrostatic attraction. The addition of NaCl to the reaction solution could weaken the electrostatic force between the Phen–Zn(II) complex and dsDNA.

Effect of ssDNA and dsDNA on peak current

The effect of ssDNA and dsDNA on the change of reduction peak current was further investigated. It could be seen that both ssDNA and dsDNA can cause a decrease in the reduction peak current, but that ssDNA had a smaller effect on the peak current than did dsDNA. The results indicated that the Phen–Zn(II) complex could interact with phosphate groups outside the DNA strand by electrostatic interaction and the fact that there are more phosphate groups on dsDNA than on ssDNA resulted in a great decrease in the reduction peak currents.

Influences of coexisting substances

The influences of co-existing substances on the determination of 12.0 mg L^{-1} dsDNA were also tested and the results are listed in Table I. It could be seen that most of the compounds did not disturb the determination. However, some metal ions, such as Al^{3+} and Co^{2+}, exhibited some influence, which may be due to the formation of metal complex with Phen.

TABLE I. Influence of co-existing substances on the determination of 12.0 mg L^{-1} dsDNA

Co-existing substance, 2.0 mg L^{-1}	Relative error, %	Co-existing substance, 5.0 μmol L^{-1}	Relative error, %
L-Glutamine	3.23	Ca^{2+}	–1.94
L-Tyrosine	5.02	Mg^{2+}	0.65
L-Cystine HCl monohydrate	1.29	Mn^{2+}	5.00
L-Arginine	4.34	Al^{3+}	8.48
L-Leucine	2.20	Co^{2+}	9.78
L-Cysteine	10.4	Pb^{2+}	1.48
Glycine	3.92	*β*-CD	0.00
Glucose	3.91	SDS	–5.63
L-Glutamic acid	–3.23		

Calibration curve

Under the optimal conditions, the decrease of reduction peak current was proportional to the concentration of dsDNA in the range from 0.4 to 16.0 mg L^{-1} with the linear regression equation:

$$\Delta Ip''/\text{nA} = 349.48 + 84.647(c\ /\ \text{mg L}^{-1})$$
$$(n = 13,\ \gamma = 0.991)$$

The *RSD* of 10 parallel determinations of 10.0 mg L^{-1} dsDNA was 2.03 %, indicating the good reproducibility of the detection. The limit of detection (*LOD*) for dsDNA was calculated using the equation:

$$LOD = 3S_0/S$$

where 3 is the factor at the 99 % confidence level, S_0 is the standard deviation of the blank measurement, and *S* is the slope of the calibration curve. The *LOD* was calculated to be 0.20 mg L^{-1}

The proposed method is compared with other methods in Table II. It could be concluded that although the sensitivity of this method was not comparable to

TABLE II. Comparison of the analytical results for the determination of DNA with those in the literature

Method	Linear range, mg L^{-1}	*LOD* / mg L^{-1}	Ref.
Light-scattering technique	0.112–4.64	0.112	44
Fluorometry	0.02–0.80	0.007	45
LSV at DME	0.4–16.0	0.198	This paper

that of the light-scattering technique and fluorometry, the widest linear range with good selectivity made this method more practical for routine tests.

Sample determinations

Three synthetic samples containing some metal ions, amino acids, *etc*. were analyzed by the proposed method with the standard addition method and the obtained results are listed in Table III. A good recovery was obtained in the range of 95.1–99.5 %, indicating that this new method was practical and reliable for the determination of dsDNA in synthetic samples.

TABLE III. Determination results of dsDNA in synthetic samples (*n* = 5); conditions: L-leucine, L-arginine, L-tyrosine, glycine, L-glutamine, L-glutamic acid glucose, 2.0 mg L^{-1}; Ca^{2+}, Pb^{2+}, Mn^{2+}, Al^{3+}, Mg^{2+}, *β*-CD, 5×10^{-6} mol L^{-1}

No.	Foreign co-existing substances	dsDNA, mg L^{-1}		Recovery %	*RSD* %
		Added	Found		
1	Ca^{2+}, Mg^{2+}, L-arginine, L-tyrosine	10.00	9.71	97.1	2.12
2	Pb^{2+}, Ca^{2+}, L-teucine, glycine, *β*-CD	10.00	9.95	99.5	1.02
3	Mn^{2+}, Al^{3+}, glucose, L-glutamine, L-glutamic acid	10.00	9.51	95.1	3.20

Measurement of the binding ratio

The binding ratio of Phen–Zn(II) complex with dsDNA was calculated by the commonly used mole ratio method. By keeping the Phen–Zn(II) complex concentration constant at 4.5×10^{-5} mol L^{-1} and changing the dsDNA concentration, the relationship between *I*p″ and c_{dsDNA} was obtained and is plotted in Fig. 3. It can be seen that when the concentration of dsDNA was higher than 18.0 mg L^{-1}, the reduction peak current remained stable, indicating that the interaction had reached its equilibrium. Then the intersection point of the two linear curves was obtained as 14.61 mg L^{-1} (4.48×10^{-5} mol L^{-1}) dsDNA. Thus, the stoichiometry of Phen–Zn(II) complex with dsDNA was calculated as 1:1, which indicated that a Phen–Zn(II)–dsDNA supramolecular complex was formed under the selected conditions.

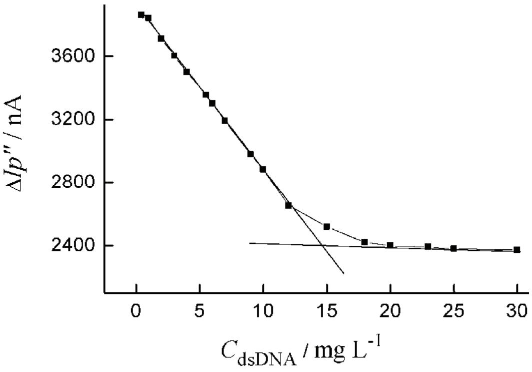

Fig. 4. Determination of the coordination number by molar ratio method pH 9.0 B–R buffer + 4.5×10^{-5} mol L^{-1} Phen–Zn(II) complex with different amounts of dsDNA.

CONCLUSIONS

A new electroanalytical method for the determination of dsDNA using the Phen–Zn(II) complex was investigated in this study. On addition of dsDNA to a solution of the Phen–Zn(II) complex, a decrease in the reduction peak current occurred, which could be employed for the micro-determination of dsDNA. Under the selected conditions, a new supramolecular complex was formed by electrostatic binding and the binding ratio of Phen–Zn(II) complex with dsDNA was calculated by the mole ratio method to be 1:1. Under the optimal conditions, dsDNA could be detected in the concentration range from 0.4 to 16.0 mg L^{-1} with a detection limit of 0.20 mg L^{-1} (3σ). The proposed method is practical and reliable with a simple procedure and could be used for dsDNA quantification in real samples.

ИЗВОД

ПОЛАРОГРАФСКО ОДРЕЂИВАЊЕ ДНК БАЗИРАНО НА ИНТЕРАКЦИЈАМА СА ФЕНАНТРОЛИН–ЦИНК(II) КОМПЛЕКСОМ

NI HUI[1], AIQIN LIANG[1], CHANGHUI XUE[1] и WEI SUN[2]

[1]*College of Chemistry and Pharmacy, Qingdao Agriculture University, Qingdao 266109, P. R. China* и
[2]*College of Chemistry and Chemical Engineering, Hainan Normal University, Haikou, 571158, P. R. China*

Применом волтаметрије са линеарном променом потенцијала, комплекс фенантролина и цинка(II) (Phen–Zn(II)) је коришћен за електрохемијско испитивање и одређивање ДНК у форми дволанчане спирале (dsDNA) Фенантролин реагује са цинком(II) у Бритон–Робинсоновом пуферу, pH 9,0, градећи стабилан електроактиван Phen–Zn(II) комплекс, који даје полярографски редукциони сигнал (у удносу на засићену каломелову електроду) и показује осетљив пик добијен као извод другог реда на потенцијалу од –1,300 V. После додатка dsDNA у раствор Phen–Zn(II) комплекса, струја редукционог пика се смањује, уз померање потенцијала пика ка негативнијим вредностима и без појаве нових пикова. Резултати указују на формирање супрамолекуларног комплекса, преко интеракција Phen–Zn(II) комплекса са дволанчаном спиралом ДНК. Испитивани су услови интеракције и електрохемијске детекције. При оптималним условима, смањење струје редукционог пика је директно сразмерно концентрацији dsDNA у опсегу 0,4–18,0 mg L^{-1} са регресионом једначином $\Delta Ip''/\mathrm{nA} = 349.48 + 84.647(c\ /\ \mathrm{mg\ L^{-1}})$ $(n = 13, \gamma = 0{,}991)$ и границом одређивања од 0,20 mg L^{-1} (3σ). Релативна стандардна девијација (RSD) за 10 паралелних одређивања 10,0 mg L^{-1} dsDNA износи 2,03 %. Метода је успешно примењена за детекцију синтетичких узорака и добијени су задовољавајући резултати.

(Примљено 18. фебруара, ревидирано 28. новембра, прихваћено 2. децембра 2014)

REFERENCES

1. E. Paleček, M. Fojta, *Anal. Chem.* **73** (2001) 75A
2. M. J. Waring, in *Drug Action at the Molecular Level Symposium Proceedings – Biological Council Symposia on Drug action*, G. C. K. Roberts, Ed., Pub. Palgrave Macmillan, London, 1977, p. 167
3. A. Bergamo, C. Gaiddon, J. H. M. Schellens, J. H. Beijinen, G. Sava, *J. Inorg. Biochem.* **106** (2012) 90

4. E. Paleček, *Nature* **188** (1960) 656
5. D. W. Pang, M. Zhang, Z. L. Wang, *J. Electroanal. Chem.* **403** (1996) 183
6. S. A. M. J. Patricia, J. M. P. T. Arturo, *Anal. Bioanal. Chem.* **378** (2004) 104
7. P. Kara, K. Kerman, D. Ozkan, B. Meric, A. Erdem, Z. Ozkan, M. Ozsoz, *Electrochem. Commun.* **4** (2002) 705
8. X. Hu, K. Jiao, W. Sun, J. Y. You, *Electroanalysis* **6** (2006) 613
9. M. S. Ibrahim, M. M. Kamal, Y. M. Temerk, *Anal. Bioanal. Chem.* **375** (2003) 1024
10. P. B. Dervan, *Science* **232** (1986) 464
11. S. Rauf, J. J. Gooding, K. Akhtar, M. A. Ghauri, M. Rahman, M. A. Anwar, A. M. Khalid, *Pharmaceut. Biomed.* **37** (2005) 205
12. A. Radi, M. A. El Ries, S. Kandil, *Anal. Chim. Acta* **495** (2003) 61
13. D. Dospivova, K. Smerkova, M. Ryvolova, D. Hynek, V. Adam, P. Kope, M. Stiborova, T. Eckschlager, J. Hubalek, R. Kizek, *Int. J. Electrochem. Sci.* **7** (2012) 3072
14. G. M. Zhang, S. M. Shuang, C. Dong, D. S. Liu, M. M. F. Choi, *J. Photochem. Photobiol., B* **74** (2004) 127
15. C. Li, S. L. Liu, L. H. Guo, D. P. Chen, *Electrochem. Commun.* **7** (2005) 23
16. R. Y. Zhang, D. W. Pang, R. X. Cai, *Chem. J. Chin. Univ.* **20** (1999) 1210
17. C. C. Ge, Z. Y. Fang, J. H. Chen, J. Liu, X. W. Lu, L. W. Zeng, *Analyst* **137** (2012) 2032
18. H. Deng, Y. Xu, Y. H. Liu, Z. J. Che, H. L. Guo, S. X. Shan, Y. Sun, X. F. Liu, K. Y. Huang, X. Y. Ma, Y. Wu, *Anal. Chem*. **84** (2012) 1253
19. C. Z. Huang, Y. F. Li, P. Feng, *Talanta* **55** (2001) 321
20. X. Q. Liu, L. J. Li, J. J. Sun, Y. S. Yan, X. Shu, B. Q. Liu, W. Sha, H. Feng, S. Sun, J. Zhu, *Inorg. Chem*. **51** (2012) 188
21. C. Q. Ma, K. A. Li, W. T. Hua, S. Y. Tong, *Microchem. J.* **59** (1998) 417
22. Y. F. Li, C. Z. Huang, M. Li, *Anal. Chim. Acta* **452** (2002) 285
23. R. T. Liu, J. H. Yang, X. Wu, T. Hu, *Anal. Chim. Acta* **448** (2001) 85
24. M. T. Carter, M. Rodriguez, A. J. Bard, *J. Am. Chem. Soc.* **111** (1989) 8901
25. S. F. Wang, T. Z. Peng, F. Y. Catherine, *Electroanalysis* **14** (2002) 1648
26. D. Marin, P. Perez, C. Teijeiro, E. Paleček, *Biophys. Chem.* **75** (1998) 87
27. K. Jiao, Q. J. Li, W. Sun, Z. J. Wang, *Electroanalysis* **17** (2005) 997
28. K. Jiao, Q. J. Li, W. Sun, Z. Y. Wang, *Chem. Res. Chinese U.* **21** (2005) 145
29. X. Hu, K. Jiao, W. Sun, J. Y. You, *Electroanalysis* **18** (2006) 613
30. M. T. Carter, A. J. Bard, *J. Am. Chem. Soc.* **109** (1987) 7528
31. R. Marisol, A. J. Bard, *Anal. Chem.* **62** (1990) 2658
32. W. Sun, J. Y. You, X. Hu, K. Jiao, *Anal. Lett.* **39** (2006) 33
33. W. Sun, J. Y. You, X. Hu, K. Jiao, *Anal. Sci.* **22** (2006) 691
34. W. Sun, J. Y. You, Q. X. Wang, K. Jiao, *Indian J. Chem., A* **45** (2006) 1173
35. W. Sun, J. Y. You, C. K. Gong, K. Jiao, *Ann. Chimica* **96** (2006) 259
36. C. W. Yaw, W. T. Tan, W. S. Tan, C. H. Ng, W. B. Yap, N. H. Rahman, M. Zidan *Int. J. Electrochem. Sci.* **7** (2012) 4692
37. X. L. Li, Y. Lu, C. L. Zhou, W. B. He, *J. Anal. Sci.* **15** (1999) 480
38. L. M. Li, X. B. Jia, X. G. Mu, *PTCA (Part B: Chem. Anal.)* **42** (2006) 430
39. W. Sun, J. Y. You, X. Hu, K. Jiao, *Anal. Lett.* **39** (2006) 33
40. W. Sun, J. Y. You, Q. X. Wang, *Chem. Anal.* **51** (2006) 477
41. G. Y. Xu, K. Jiao, J. S. Fan, *Acta Chim. Slov.* **53** (2006) 486
42. G. M. Malacinski, D. Freifeder, *Essentials of Molecular Biology*, Science Press, Beijing, 2002, p. 202
43. C. Mongay, V. Cerda, *Ann. Chimica* **64** (1974) 409

44. H. Zheng, X. L. Chen, C. Q. Zhu, D. H. Li, Q. Y. Chen, J. G. Xu, *Microchem. J.* **64** (2000) 263
45. Y. T. Wang, F. L. Zhao, K. A. Li, S. Y. Tong, *Spectrochim. Acta, A* **56** (2000) 1827.

Journal of the Serbian Chemical Society
JSCS-info@shd.org.rs • www.shd.org.rs/JSCS

J. Serb. Chem. Soc. 80 (1) 97–106 (2015) UDC 678.744:544.5+544.14+547.298.4
JSCS–4700 *Original scientific paper*

Influence of the amount of poly(vinyl alcohol) on the *in situ* production of photo-crosslinked thioamide functionalized nanofiber membranes

BIHTER ZEYTUNCU[1]*, MEHMET HAKAN MORCALI[2], SULEYMAN AKMAN[3] and ONURALP YUCEL[2]

[1]Istanbul Technical University, Applied Research Center of Materials Science and Production Technology, 34469, Istanbul, Turkey, [2]Istanbul Technical University, Faculty of Chemical and Metallurgical Engineering, 34469, Istanbul, Turkey and [3]Istanbul Technical University, Faculty of Science and Letters, Department of Chemistry, 34469, Istanbul, Turkey

(Received 17 March, revised 31 July, accepted 7 August 2014)

Abstract: Poly(vinyl alcohol)/maleic anhydride/acryloyl thioamide monomer (PVA/MA/ATM) photo-cured nanofiber membranes and pure PVA nanofiber membranes were produced by the electrospinning technique. *In situ* UV radiation was applied during the electrospinning in order to provide polymerization during the jet flight and promote crosslinking of ATM and MA with PVA. The cross-linking was examined by Fourier transform infrared spectroscopy (FTIR). The morphology of the electrospun nanofibers was characterized by scanning electron microscope (SEM). The surface area of the nanofiber membranes was measured by Brunauer–Emmert–Teller (BET) analysis. Furthermore, their water durability was examined. The water durability test demonstrated that the *in situ* photo-cured PVA/MA/ATM nanofiber membrane had the lowest average mass loss. The surface areas of PVA/MA/ATM nanofiber membranes were 160–280 $m^2 g^{-1}$. The surface area and diameter of PVA/MA/ATM nanofibers decreased with increasing PVA content. The diameter of the obtained nanofibers was less than 100 nm. The results showed that water-insoluble nanofiber membranes with good chemical and thermal resistance were obtained. These nanofiber membranes may be promising candidates for usage in water treatment.

Keywords: electrospinning; nanofiber membrane; poly(vinyl alcohol); photocurable; thioamide.

INTRODUCTION

Nanofibers are an exciting new class of materials that have been extensively studied due to their uniquely light weight, high porosity, small inter-fiber pore size, large surface area and well-modified surface properties.[1,2] Many potential

---

* Corresponding author. E-mail: bihter_zeytuncu@hotmail.com

doi: 10.2298/JSC140317083Z

applications for nanofibers, such as tissue engineering, sensors, biomaterials, device wipes, electrical applications, wound dressings material and filtrations and adsorptions, have been proposed and investigated.[3–9]

In recent years, electrospinning has become the most common technique for the generation of nanofibers because it is comparatively simple, convenient, effective, low cost and with a relatively high production rate.[10] However, most important is that nanofibers with a diameter in the range of 100–1000 nm could be achieved by electrospinning. This technique has three basic components, *i.e.*, a syringe pump, a high voltage supply and a collector. In the process, a polymer solution or melt is placed into the syringe with a millimeter size nozzle and is subjected to a high voltage. Under the applied electrostatic force, the polymer is ejected from the nozzle, the diameter of which is reduced significantly, as it is transported to and deposited on a collector, which also serves as the ground for the electrical charges.[11–14]

Poly(vinyl alcohol) (PVA) is a water-soluble, non-toxic and biocompatible polyhydroxy polymer with good chemical and thermal stability.[15,16] However, the aqueous solubility PVA would limit its use for water treatment.[15] Therefore, when fabricated for aqueous applications, such as filtration and adsorption (*i.e.*, water treatment), PVA must be modified to minimize swelling in water.[17,18] The most popular way of decreasing the solubility of PVA in water is to crosslink the polymer.

The main purpose of this study was to produce a water-insoluble PVA nanofiber membrane by the electrospinning technique. Chemical crosslinking of PVA with maleic anhydride (MA) and acryloyl thioamide (ATM) during the electrospinning process was realized by the effects of *in situ* UV radiation. Then the obtained PVA/MA/ATM nanofiber membranes were characterized by FTIR, SEM and BET, and their aqueous stabilities were examined.

EXPERIMENTAL

Reagents

Poly(vinyl alcohol) (PVA; 87–89 % hydrolyzed, $\bar{M}_w$ 146,000–186,000 g mol^{-1}), maleic anhydride (MA), acryloyl chloride (C_3H_3ClO) and the radical photo-initiator, 2-hydroxy-2-methyl-1-phenyl-1-propan-1-one (Darocur® 1173), were purchased from Sigma–Aldrich. Thiourea (TU; $SC(NH_2)_2$), triethylamine (TEA) and dimethylformamide (DMF) were purchased from Merck. Distilled water was used throughout.

Synthesis of acryloyl thioamide monomer (ATM)

Thiourea (0.15 mol) was dissolved in 20 mL DMF at 40 °C and the mixture was charged into a 500 mL three-necked flask fitted with a reflux condenser. After the solution had cooled, TEA (0.15 mol) was added. Then, at 0 °C under nitrogen, acryloyl chloride (0.15 mol) was added slowly drop wise to the reaction mixture under continuous stirring. After 1 h at 0 °C, the reaction was continued at room temperature for an additional 1 h. Then, the solvent was evaporated. The synthesized acryloyl thioamide monomer (ATM) was dried under vacuum at 30 °C for 24 h.

Preparation of the solutions for electrospinning

First, 8, 10 and 12 % PVA solutions were prepared by adding slowly the required amount of PVA powder to distilled water at room temperature. The mixtures were then stirred at 80 °C for 2 h to obtain homogenous solutions and refrigerated overnight to when the solutions become transparent. MA (0.98 g) was added into 50 g of the prepared PVA solutions in the presence of 10 mL of 1 M NaOH with vigorously stirring at 70 °C for 5 h (Scheme 1).

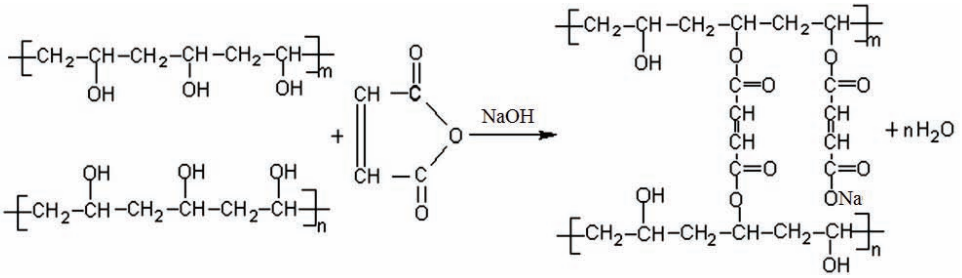

Scheme 1. The esterification reaction between PVA and MA.

Then, the synthesized ATM and Darocur® 1173 as a photo initiator were added at 3 wt. % of the total weight for all formulations and then immediately electrospun. The composition of all nanofiber membrane formulations are given in Table I.

TABLE I. The composition of the formulations used in the synthesis of nanofiber membranes; PVA solution: 50 g

Formulation	MA g	ATM g	Darocur® 1173 %	Sulfur content wt. %	Nitrogen content wt. %
8 % PVA	0	0	0	0	0
	0.98	1.53	3	0.72	0.63
10 % PVA	0	0	0	0	0
	0.98	1.53	3	0.72	0.63
12 % PVA	0	0	0	0	0
	0.98	1.53	3	0.72	0.63

Synthesis of nanofiber membranes

The schematic diagram of electrospinning process combined with UV radiation is shown in Fig. 1. The prepared solution was placed in the syringe. The negative terminal of the high

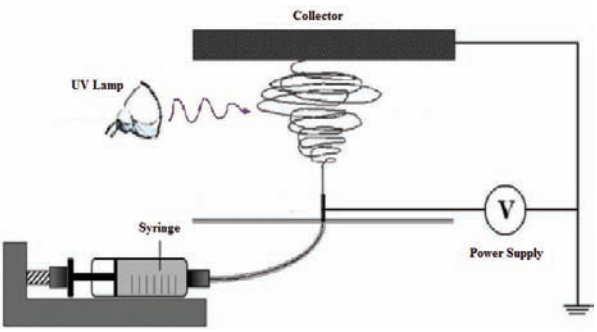

Fig. 1. Schematic diagram of the electrospinning process.

voltage power supply was connected to a conductive drum covered with aluminum foil, which functioned as the collector for the fibers. The positive terminal was connected to the metallic syringe tip. A voltage of 25 kV with a tip-to-target distance of 15 cm at a speed of 0.1 mL h^{-1} was applied to the solution that was simultaneously radiated with a high pressure UV lamp (λ_{max} = 365 nm, OSRAM 300W) and the nanofiber membranes were collected on the aluminum foil. After preparation, the nanofiber membranes were dried for 12 h at 100 °C and then refluxed in ethanol/HCl (mole ratio 10:1) for 24 h at 70 °C to remove the template. Finally, the nanofibers were dried for 6 h at 30 °C under vacuum.

Characterization

The infrared spectra of the prepared membranes were obtained on an FTIR spectrometer (Spectrum 100, PerkinElmer) in the wave number region of 4000–400 cm^{-1} to define the characteristic peaks of the functional groups of the nanofiber membranes. The surface morphology of the electrospun nanofiber was examined with an SEM (JEOL JSM 7000F). The specific surface area and pore volume were determined using BET analysis (ASAP 2020). In the water durability test, the nanofiber membranes were treated with boiling water for 1 h and the mass loss measured.

RESULTS AND DISCUSSION

ATM was synthesized by reaction between thiourea and acryloyl chloride and the representation of this reaction is shown in Scheme 2. The FTIR spectrum of ATM is given in Fig. 2. According to the spectrum, thioamide group showed an absorption band at 3528 cm^{-1}, due to –NH– stretching of the amide group. The carbonyl stretching of the amide appeared at 1658 cm^{-1}. The C=S group of thioamide showed a band at 1255 cm^{-1}. The peaks at 1089 and 1384 cm^{-1} are attributed to –C–N groups. Furthermore, –C–H stretching bands were recorded at 2857 and 2928 cm^{-1}. FTIR spectral measurements confirmed the structure of ATM.

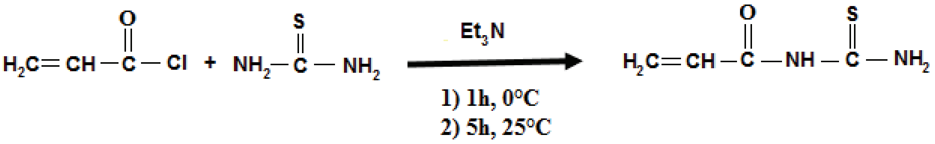

$$H_2C{=}CH{-}\overset{O}{\overset{\|}{C}}{-}Cl + NH_2{-}\overset{S}{\overset{\|}{C}}{-}NH_2 \xrightarrow[\text{1) 1h, 0°C; 2) 5h, 25°C}]{Et_3N} H_2C{=}CH{-}\overset{O}{\overset{\|}{C}}{-}NH{-}\overset{S}{\overset{\|}{C}}{-}NH_2$$

Scheme 2. Proposed structure of the synthesized acryloyl thioamide monomer (ATM).

FTIR spectra of the synthesized 10 % PVA and 10 % PVA/MA/ATM nanofiber membranes are given in Fig. 3. The FTIR spectrum of pure PVA nanofiber (Fig. 3a) showed a broad peak at 3307 cm^{-1} attributed to the hydroxyl (–OH) and at 2910 cm^{-1} that is due to $–CH_2$ asymmetric stretching. The peak observed at 1731 cm^{-1} indicated the (–C=O) carbonyl stretching bond.[16,18] As shown in Fig. 3b, an absorption band at 1661 cm^{-1} due to –C=O stretching of the amide group and a carbonyl stretching (–O–C=O) at 1730 cm^{-1}, a C=S stretching bands at 1247 cm^{-1} and a –C–N stretching bands at 1091–1375 cm^{-1} were found.[19,20] The proposed structure of the synthesized PVA/MA/ATM nanofiber membrane is given in Scheme 3.

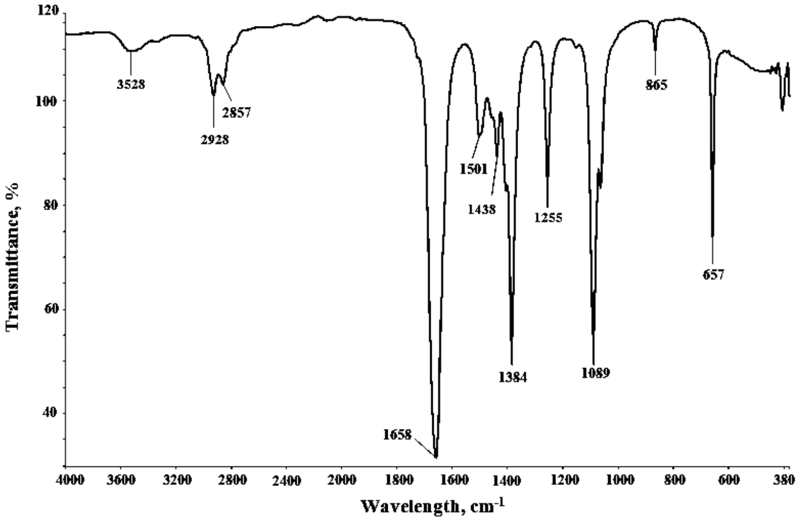

Fig. 2. FTIR spectrum of ATM.

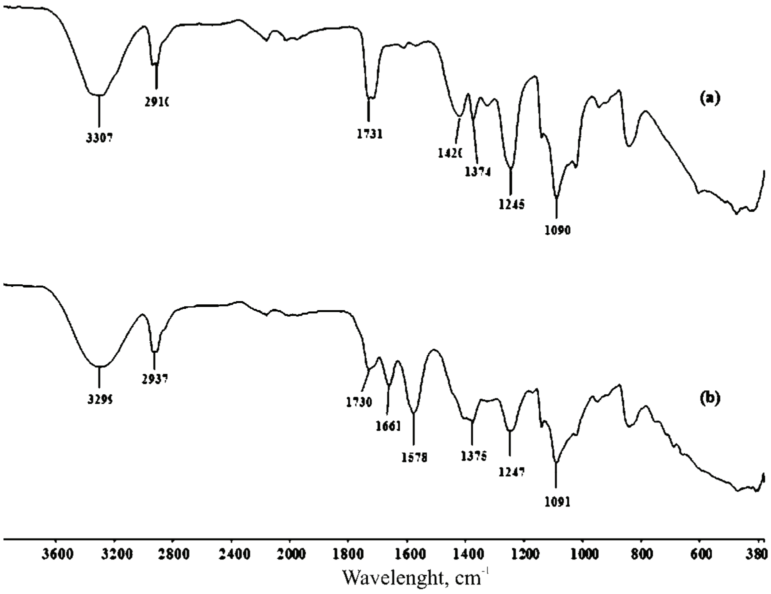

Fig. 3. FTIR spectra of a) 10 % PVA and b) 10 % PVA/MA/ATM nanofiber membranes.

The water durability test involved boiling the synthesized pure PVA, PVA/MA and PVA/MA/ATM nanofiber membranes in water for 1 h. The average mass losses are given in Table II. As seen from the results, pure PVA nanofiber membranes dissolved completely in a short period at room temperature. However, when PVA was crosslinked with dianhydride and thioamide groups, the

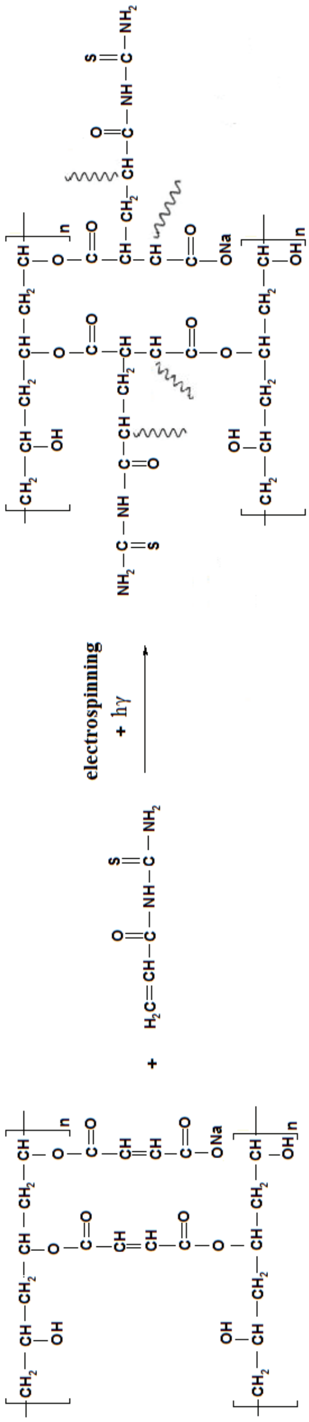

Scheme 3. Proposed structure of the 10 % PVA/MA/ATM nanofiber membrane.

resulting PVA/MA/ATM nanofiber membranes were slightly soluble during boiling in water for 1 h. This was mainly due to the efficient crosslinking of PVA with MA and ATM by exposure to UV radiation during electrospinning. Compared to the 8 % PVA/MA/ATM and 12 % PVA/MA/ATM nanofiber membranes, the 10 % PVA/MA/ATM nanofiber membrane had the lowest average mass loss because of being the most efficiently crosslinked. This could be due to the non-efficient crosslinking for the 8 % and the dissolving of unreacted MA for the 12 % PVA/MA/ATM fibers. Yang *et al.*[21] prepared PVA/MA crosslinked nanofiber membrane by electrospinning directly. In the present work, the thioamide nanofiber membranes were prepared by simultaneously electrospinning and UV radiation. It was found that this method enabled more efficient crosslinking due to photopolymerization and less water-soluble the obtained nanofiber membranes were less soluble.

TABLE II. Physical properties of nanofiber membranes

Nanofiber membrane	Water solubility, %	Surface area, $m^2 g^{-1}$	Nanofiber diameter, nm
8 % PVA	Soluble	57.72	106–126
10 % PVA	Soluble	48.89	163–190
12 % PVA	Soluble	38.91	236–259
8 % PVA/MA/ATM	3.84	282.71	91–96
10 % PVA/MA/ATM	1.09	225.48	126–134
12 % PVA/MA/ATM	1.83	161.94	244–326

The morphologies of nanofiber membranes and the nanofiber diameters were determined by SEM analysis and the SEM images are shown in Fig. 4. It could be seen that the membranes were composed of numerous, randomly oriented nanofibers. The diameters of the nanofibers increased with increasing amount of PVA. The pure PVA nanofibers were smooth and uniform with diameters in the range of 106–259 nm. The diameters of the 8 % PVA nanofibers were between 106 and 126 nm while diameters of 10 % PVA and 12 % PVA nanofiber were between 163–190 nm and 236–259 nm, respectively (Fig. 4A–C). With the introduction of the dianhydride and thioamide groups to PVA, the nanofibers became more intertwined and there were more crosslinks between the fibers (Fig. 4D–F). As a result, the fiber scaffold became stronger. The diameters of PVA/MA/ATM nanofibers were smaller than those of the corresponding pure PVA fibers. The diameters of the 8 % PVA/MA/ATM nanofibers were less than 100 nm. As the PVA content increased in modified membranes, the diameters increased from 90 to 326 nm, as in the pure PVA nanofiber membranes. It should be noted that the addition of MA and ATM may have caused a possible increase in the conductivity of the solution.[5] However, there were some beads in the PVA/MA/ATM nanofiber membranes, especially in the 12 % PVA/MA/ATM nanofiber membrane. Furthermore, the Brunauer–Emmet–Teller (BET) surface area values of nanofibers indicated that the surface area decreased with increasing amount of PVA. The nanofiber diameters and surface areas are given in Table II.

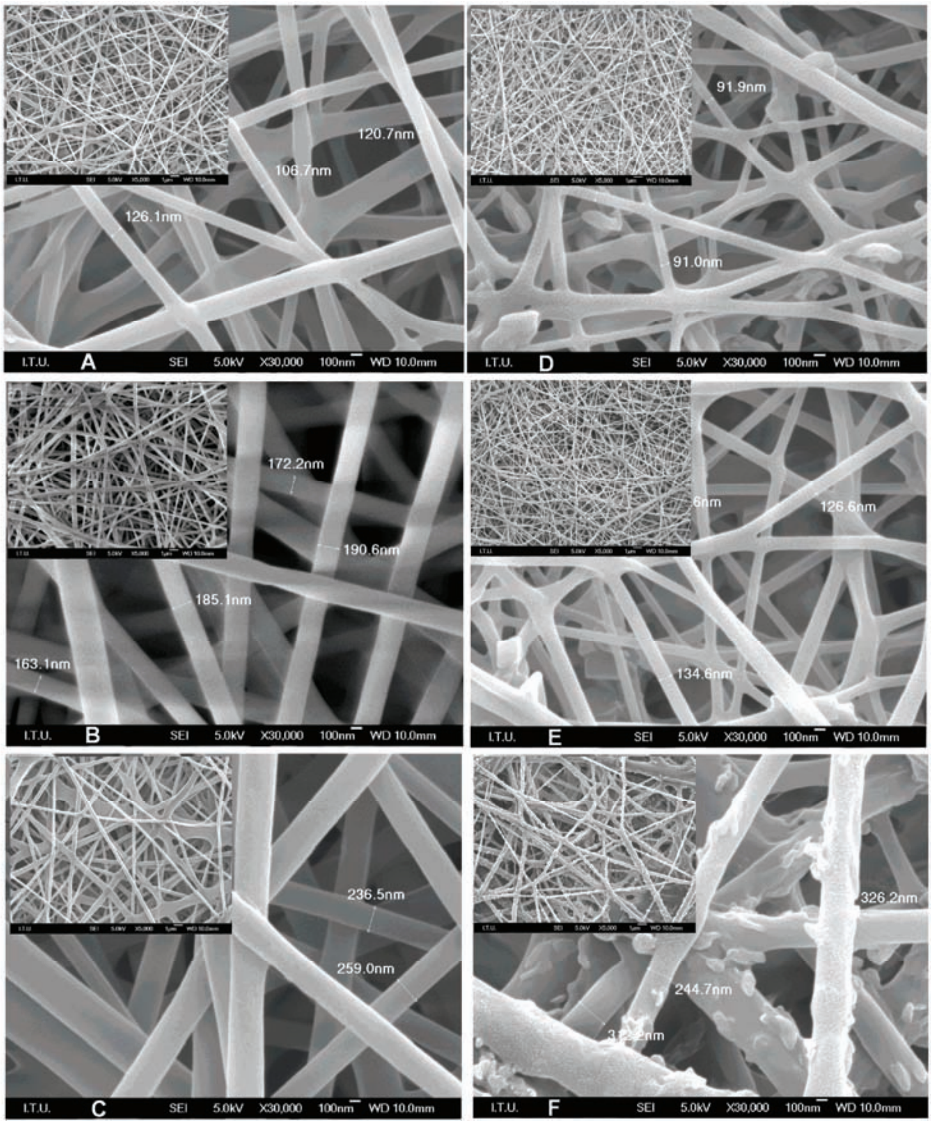

Fig. 4. SEM images of: A) 8, B) 10 and C) 12 % PVA; D) 8, E) 10 and F) 12 % PVA/MA/ATM nanofiber membranes.

CONCLUSIONS

The aim of this study was to synthesize more dynamic nanofiber membranes by combining the electrospinning technique with UV radiation. Photo-crosslinking of the thioamide-functionalized fibers was successfully achieved. Moreover, the effect of PVA content on the properties of the synthesized photo-cured nanofiber membranes was investigated. While pure PVA nanofiber membranes completely dissolved in water, the photo-cured membranes resisted hot water. SEM images showed that the diameters of the nanofibers ranged from 90 to 320 nm and increased with increasing content of PVA. The diameters of the PVA/MA/ /ATM nanofibers in membranes were smaller than those of the pure PVA nanofibers and their BET surface area was larger. When compared to pure PVA nanofiber membranes, they were tougher and insoluble membranes, had lower fiber diameter and higher surface area. The results illustrated that these photo-crosslinked thioamide functionalized nanofiber membranes possess an enormous potential with the chemical resistance for usage in water treatment as, for example, adsorption media.

Acknowledgements. This study is a part of Bihter Zeytuncu PhD dissertation at the Istanbul Technical University. The authors wish to thank Istanbul Technical University for financial support under BAP project 36460. Grateful acknowledgements are given to Associate Prof. M. Vezir Kahraman and Dr. Emrah Cakmakci, Marmara University, for providing the electrospinning equipment and the FTIR spectra; Prof. Dr. Gültekin Göller, Technician Hüseyin Sezer and Talat Alpak Istanbul Technical University, for the SEM analysis.

ИЗВОД

УТИЦАЈ САДРЖАЈА ПОЛИ(ВИНИЛ-АЛКОХОЛА) НА ПОСТУПАК ИЗРАДЕ МЕМБРАНА *IN SITU* ФОТО-УМРЕЖАВАЊЕМ НАНОВЛАКАНА ФУНКЦИОНАЛИЗОВАНИХ ТИОАМИДОМ

BIHTER ZEYTUNCU[1], MEHMET HAKAN MORCALI[2], SULEYMAN AKMAN[3] и ONURALP YUCEL[2]

[1]Istanbul Technical University, Applied Research Center of Materials Science and Production Technology, 34469, Istanbul, Turkey, [2]Istanbul Technical University, Faculty of Chemical and Metallurgical Engineering, 34469, Istanbul, Turkey и [3]Istanbul Technical University, Faculty of Science and Letters, Department of Chemistry, 34469, Istanbul, Turkey

У овом раду је приказано добијање мембрана поступком електроспининга чистих PVA нановлакана као и *in situ* фото-умрежавањем поли(винил-алкохол)/анхидрид малеинске киселине/акрилоил-тиоамид мономера (PVA/MA/ATM). Примена *in situ* UV зрачења у поступку електроспининга омогућава да се реакција умрежавања ATM и MA са PVA одиграва истовремено са формирањем влакана. Ток реакције умрежавања је праћен помоћу инфрацрвене спектроскопије (FTIR). Док су морфологија и термичка својства добијених нановлакана анализирана скенирајућом електронском микроскопијом (SEM). Специфична површина нановлакана добијених мембрана је одређена помоћу Брунауер–Емерт–Телер (BET) методе. Затим је анализирана отпорност нановлакана на воду. Тестови отпорности на воду су потврдили да мембране фото-умрежених PVA/MA/ /ATM нановлакана показују најмањи губитак масе. Специфична површина PVA/MA/ATM нановлакана у мембранама је износила 160–280 m^2 g^{-1}. Установљено је да специфична површина и пречник нановлакана опадају са порастом садржаја PVA у полазном раствору. Пречник добијених нановлакана је био мањи од 100 nm. Резултати су потврдили да се овим поступком могу добити мембране од водонерастворних PVA

нановлакана са бољом хемијском и термичком отпорношћу. Мембране сачињене од умрежених PVA нановлакана могу наћи примену у поступцима за пречишћавање вода.

(Примљено 17. марта, ревидирано 31. јула, прихваћено 7. августа 2014)

REFERENCES

1. D. H. Reneker, A. L. Yarin, *Polymer* **49** (2008) 2387
2. S. Ramakrishna, K. Fujihara, W.-E. Teo, T. Yong, Z. Ma, R. Ramaseshan, *Mater. Today* **9** (2006) 40
3. H. H. Tonnesen, J. Karlsen, *Drug Dev. Ind. Pharm.* **28** (2002) 621
4. E. Cakmakci, A. Gungor, N. Kayaman-Apohan, S. E. Kuruca, M. B. Cetin, K. A. Dar, *J. Bio. Sci. Polymer Ed.* **23** (2012) 887
5. T. J. Sill, H. A. von Recum, *Biomaterials* **29** (2008) 1989
6. D. Aussawasathien, J. H. Dong, L. Dai, *Synth. Met.* **154** (2005) 37
7. P. Gibson, H. Schreuder-Gibson, D. Rivin, *Colloids Surfaces, A* **187–188** (2001) 469
8. X. Li, C. Zhang, R. Zhao, X. Lu, X. Xu, X. Jia, C. Wang, L. Li, *Chem. Eng. J.* **229** (2013) 420
9. Z. Ma, K. Masaya, S. Ramakrishna, *J. Memb. Sci.* **282** (2006) 237
10. L. Li, R. Hashaikeh, H. A. Arafat, *J. Memb. Sci.* **436** (2013) 57
11. W. Wang, Q. Yang, L. Sun, H. Wang, C. Zhang, X. Fei, M. Sun, Y. Li, *J. Hazard. Mater.* **194** (2011) 185
12. K. Saeed, S. Haider, T.-J. Oh, S.-Y. Park, *J. Memb. Sci.* **322** (2008) 400
13. S. Haider, S.-Y. Park, *J. Memb. Sci.* **328** (2009) 90
14. M. Aliabadi, M. Irani, J. Ismaeili, H. Piri, M. J. Parnian, *Chem. Eng. J.* **220** (2013) 237
15. C. A. Finch, Polyvinyl alcohol; properties and applications, Wiley, New York, 1973
16. B. Zeytuncu, S. Akman, O. Yucel, M. V. Kahraman, *Mater. Res.* **17** (2014) 565
17. S. Wu, F. Li, Y. Wu, R. Xu, G. Li, *Chem. Commun.* **46** (2010) 1694
18. K. Sasipriya, R. Suriyaprabha, P. Prabu, V. Rajendran, *Mater. Res.* **16** (2013) 824
19. O. E. Fayemi, A. S. Ogunlaja, P. F. M. Kempgens, E. Antunes, N. Torto, T. Nyokong, Z. R. Tshentu, *Miner. Eng.* **53** (2013) 256
20. T. L. Lin, H. L. Lien, *Int. J. Mol. Sci.* **14** (2013) 9834.
21. H. Yang, R. Xu, X. Xue, F. Li, G. Li, *J. Hazard. Mater.* **152** (2008) 690.

Journal of the Serbian Chemical Society
JSCS-info@shd.org.rs • www.shd.org.rs/JSCS

J. Serb. Chem. Soc. *80* (1) 107–113 (2015)
JSCS–4701

UDC 548.15+546.57+551.312.1+544.654.2+
621.385.833
Original scientific paper

Randomly oriented twin domains in electrodeposited silver dendrites

EVICA R. IVANOVIĆ[1]*, NEBOJŠA D. NIKOLIĆ[2#] and VELIMIR R. RADMILOVIĆ[3]**

[1]Faculty of Agriculture, University of Belgrade, Nemanjina 6, Belgrade-Zemun, Serbia,
[2]ICTM – Institute of Electrochemistry, University of Belgrade, Njegoševa 12, P. O. Box 473,
11001 Belgrade, Serbia and [3]Faculty of Technology and Metallurgy, University of Belgrade,
Karnegijeva 4, P. O. Box 3503, 11001 Belgrade, Serbia

(Received 6 March, revised 16 April, accepted 18 April 2014)

Abstract: Silver dendrites were prepared by electrochemical deposition. The structures of the Ag dendrites, the type of twins and their distribution were investigated by scanning electron microscopy (SEM), Z-contrast high angle annular dark field transmission electron microscopy (HAADF), and crystallographically sensitive orientation imaging microscopy (OIM). The results revealed that the silver dendrites were characterized by the presence of randomly distributed 180° rotational twin domains. The broad surface of dendrites was of the {111} type. The directions of growth of the main dendrite stem and all branches were of the <112> type.

Keywords: dendrite; silver; electrodeposition; twinning; scanning electron microscopy; high angle annular dark field microscopy; orientation imaging microscopy.

INTRODUCTION

Dendritic growth is one of the most complex patterns that evolves through the dynamic processes of crystal growth and therefore has remained an active subject for experimental and theoretical studies for an extended period. During the past several decades, dendritic growth has attracted a large number of researchers in the broad areas of material science, condensed matter physics, fluid dynamics, applied mathematics, *etc.*[1–3] It has been regarded as a typical example of a variety of pattern formations in nature and technology. Among various metals, the preparation of Ag dendrites has been widely investigated because of their unique optical properties and potential applications in surface-enhanced

---

*,** Corresponding authors. E-mail: (*)ivaeva@agrif.bg.ac.rs; (**)VRRadmilovic@tmf.bg.ac.rs
[#] Serbian Chemical Society member.

doi: 10.2298/JSC140306045I

Raman spectroscopy (SERS),[4,5] catalysis,[6,7] sensors[8] and the fabrication of superhydrophobic surfaces.[9]

Several methods were explored to synthesize dendritic Ag structures, including electrochemical deposition,[10] the galvanic replacement reaction,[4,11,12] electroless deposition,[10] sonoelectrochemistry,[13,14] microwave irradiation,[15] hydrothermal reduction,[6] photoreduction[16] and the template method.[17] Electrochemical deposition has an advantage over the other methods because the driving force, *i.e.*, overpotential, is more controllable and is able to produce dendritic structures with high purity. Therefore, electrodeposition represents a powerful technique that provides versatility in tailoring the architecture of metals on the micro/nanoscale.

Several mechanisms, such as the diffusion-limited aggregation (DLA) model,[18] oriented attachment growth,[19–21] nanoparticle-aggregated self-assembly crystallization,[22] anisotropic crystal growth,[23] site-specific sequential nucleation,[11,24] multistep self-assembly process[12] and the cluster–cluster aggregation model (CCA) model,[25] were proposed to explain Ag dendritic growth in various systems. The electrochemical literature has defined the problem of roughening in electrodeposition.[10] Mullins–Sekerka linear stability analysis[26] and the Barton–Bockris dendrite-propagation model[27] are popular methods used to describe cathodic roughening and dendritic growth in electrochemical deposition. These commonly cited theories employ kinetic relationships that differ in mathematical form, but both contain the effects of surface tension and local concentration deviations induced by surface roughening.

However, intrinsic dendritic structures, *i.e.*, the appearance of well-defined and fairly regular branching and directions of growth, cannot be explained by the nonspecific models mentioned above. The twin plane reentrant edge (TPRE) mechanism or WHS model[28,29] is also a much-cited model of dendritic growth. In this mechanism, crystal growth arises through the formation of reentrant grooves at the intersection by the twin planes, which make this location a favorable site for nucleation. Based on this model, a dendrite is a twin crystal with at least one twin boundary, which extends throughout the dendrite and is parallel to the main dendrite plane.

The aim of this research effort was to investigate the role of twinning, the type and shape of twins, and the presence of twin domains and their distribution in silver dendrites obtained by electrochemical deposition.

EXPERIMENTAL

The electrodeposition was realized using a typical set-up consisting of a platinum cathode with geometric surface area of 0.53 cm^2. The reference and counter electrodes were of pure silver. The counter electrode was silver foil of surface area approximately 0.80 dm^2, placed close to the cell walls. The reference electrode was a silver wire, the tip of which was positioned at a distance of ≈0.2 cm from the surface of the working electrode. The working electrode was placed in the center of the cell. The electrolyte solution consisted of 0.06 M $AgNO_3$ + 1.2 M $NaNO_3$ + 0.05 M HNO_3. Double distilled water was used for preparing the solutions. The total electrolyte volume was 100 mL and the electrodeposition was performed at 100 mV, at room temperature. The electrodeposition time was 72 s. The as-prepared Ag dendrites were sequentially rinsed with distilled water and ethanol for further characterization.

The morphology and microstructure of silver dendrites were characterized and analyzed by SEM and crystallographically sensitive orientation imaging microscopy (OIM) using a DB235 FIB system, and by Z-contrast high angle annular dark field transmission electron microscopy (HAADF) using a TEAM 0.5 transmission electron microscope operating at 300 kV. Orientation imaging microscopy (OIM) is based on electron-backscattered diffraction (EBSD), generated from the top 10 to 50 nm of the material surface. When exposed to the atmosphere, silver dendrites can rapidly oxidize, covering the surface with Ag_2O. A silver oxide film would decrease the signal to noise ratio and make it difficult to analyze silver dendrite twin structures using the EBSD tool. To solve this problem, Ferrer *et al.*[30] proposed the solution of having an EBSD system installed on a dual-beam focused ion beam system (FIB). This concept allows the EBSD analysis to be performed immediately after material surface preparation,[31] using a focused ion beam (FIB), without breaking the vacuum.

RESULTS AND DISCUSSION

The polarization curve for silver electrodeposition from 0.06 M $AgNO_3$ + 1.2 M $NaNO_3$ + 0.05 M HNO_3 is shown in Fig. 1a. The plateau of the limiting diffusion current density corresponds to the range of overpotentials between 75 and 175 mV. The dependence of the current density on the time of electrodeposition obtained at an overpotential of 100 mV is presented in Fig. 1b. A fast increase in the current density with electrodeposition time was observed during the electrodeposition process at this overpotential.

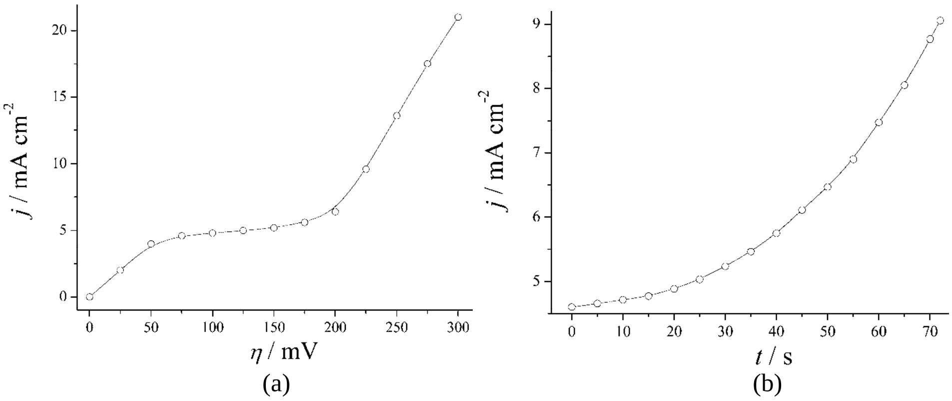

(a) (b)

Fig. 1. a) Polarization curve for silver electrodeposition from 0.06 M $AgNO_3$ + 1.2 M $NaNO_3$ + 0.05 M HNO_3. b) Dependence of the current density on the time of electrodeposition obtained at an overpotential of 100 mV. The electrodeposition time was 72 s.

The typical morphology of electrodeposited silver dendrites obtained at an overpotential of 100 mV, characterized by scanning electron microscopy (SEM), is shown in Fig. 2a. The simplest dendrites consisted of only the stem and primary branches and are referred to as primary (P) dendrites. If the primary branches in turn developed secondary branches, the dendrites are called secondary (S). With an additional set of branches, tertiary (T) dendrites were formed.

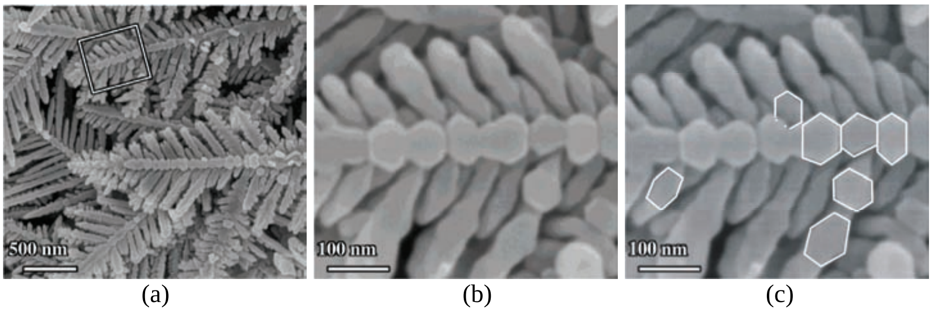

(a) (b) (c)

Fig. 2. a) Scanning electron micrograph of electrodeposited silver dendrites. b) Enlarged detail (see rectangle in a) showing twinned (stacked) octahedrons in the dendrite stem. c) Drawing indicating how Ag dendrite stems and branches are formed by the stacking of hexagonal units.

From the SEM image, it appears that these dendrites were two-dimensional patterns with the main stem and all branches being in the same plane; such dendrites are often referred to as two-dimensional or 2D crystals.[32] Figure 2b shows that the main stem of a dendrite is formed by the stacking of octahedrons mostly in the elongated form undergoing longitudinal propagation along the specific crystallographic direction. Primary and secondary hexagons (mostly irregular) develop and grow outwards from the main stem, as is shown in Fig. 2c.

A high angle annular dark field (HAADF) transmission electron micrograph of a silver dendrite is shown in Fig. 3. Both, the primary and secondary branches exhibited much the same or similar contrast, indicating they were all of approximately the same or similar thicknesses. The exceptions are the bright dots on the main stem, which indicate that some of the primary branches had grown perpendicular to the main stem and to the broad main dendrite surface.

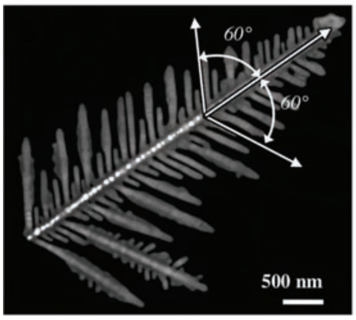

Fig. 3. High angle annular dark field (HAADF) transmission electron micrograph of silver dendrite showing the angles between the stem and the branches.

The angles between the main stem and primary branches, as well as between primary and secondary branches were 60°. This angular relationship between branches indicates that the main axis of the dendrite was parallel to the <112> direction and all branches were also parallel to the same family of crystallographic directions.

A 100 pole figure of an Ag dendrite is shown in Fig. 4a. From this pole figure, it is obvious that the crystallographic orientation of this silver dendrite was close to 111, indicated by the 111 pole being in the center of the stereographic projection. There are two sets of 100 poles present in this pole figure, related to each other by rotation of 180° around the [111] direction.

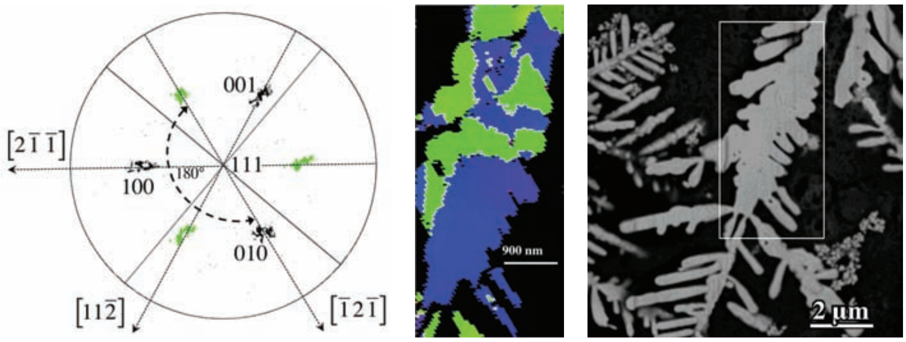

(a) (b) (c)

Fig. 4. a) 100 pole figure of Ag twins with crystallographic orientation close to the 111 twin plane. b) Color-coded map of two 180° rotational twins. c) Back scattered scanning electron image obtained after FIB shaving; the white rectangle indicates the region from where the OI map was taken.

These results confirm that the growth direction of the main stem of the dendrite was close to $[\bar{1}\bar{1}2]$ and the directions of the branches were $[1\bar{2}1]$ and $[\bar{2}11]$. These results clearly show that, besides the commonly accepted presence of a twin plane parallel to the broad dendrite surface plane,[28,29] this silver dendrite structure was characterized by the presence of two types of twins, related to each other by 180° rotation around the [111] crystallographic direction, as indicated in the 100 pole figure (Fig. 4a). From the color-coded map (Fig. 4b), taken from the region shown by the white rectangle in the back-scattered scanning electron image in Fig. 4c, it appears that the 180° rotational twin domains were randomly distributed. Colors of the twins in stereographic projection (Fig. 4a) correspond to the appropriate twin variances in the color-coded map (Fig. 4b). Not all details shown in Fig. 4c are present in the color-coded map. Since the map was obtained at a 70° tilt angle, any closely spaced branches, shown in Fig. 4c, cannot be separated. Both twin domains are random in terms of size and shape, and the 111 pole in the center of the 100 pole figure confirms that they have the same (111) plane parallel to the main broad twin surface in common. High susceptibility for twinning of these dendrites comes from very low stacking fault energy of silver of ≈16 mJ m^{-2}.[33]

In summary, the structures of electrodeposited Ag dendrites were investigated by SEM, Z-contrast HAADF and OIM. The results revealed that the Ag dendrites exhibited the presence of well-defined randomly distributed twin domains of irregular size and shape. These twin domains were related to each other by 180° rotation around the common [111] crystallographic axis, which is normal to the main broad dendrite surface. The growth direction of the main dendrite stem was found to be close to $[\bar{1}\bar{1}2]$ and the direction of the branches were $[1\bar{2}1]$ and $[\bar{2}11]$.

Acknowledgements. V.R.R. acknowledges support by the Ministry of Education, Science and Technological Development of the Republic of Serbia, under contract No. 172054. Electron microscopy was performed at the National Center for Electron Microscopy, which is supported by the Office of Science, Office of Basic Energy Sciences, of the U.S. Department of Energy under Contract No. DE-AC02-05CH11231.

ИЗВОД

ПРОИЗВОЉНО ОРИЈЕНТИСАНИ ДОМЕНИ ДВОЈНИКА У ЕЛЕКТРОХЕМИЈСКИ ИСТАЛОЖЕНИМ ДЕНДРИТИМА СРЕБРА

ЕВИЦА Р. ИВАНОВИЋ[1], НЕБОЈША Д. НИКОЛИЋ[2] и ВЕЛИМИР Р. РАДМИЛОВИЋ[3]

[1]*Пољопривредни факултет, Универзитет у Београду, Немањина 6, Београд-Земун,* [2]*ИХТМ – Центар за електрохемију, Универзитет у Београду, Његошева 12, Београд и* [3]*Технолошко–металуршки факултет, Универзитет у Београду, Карнегијева 4, Београд*

Дендрити сребра припремљени су поступком електрохемијског таложења. Испитивани су структура, тип двојника и њихова расподела коришћењем скенирајуће електронске микроскопије (SEM), високо-угаоне трансмисионе електронске микроскопије тамног поља са контрастом атомског броја (HAADF) и кристалографски осетљиве оријентационе микроскопије (OIM). Резултати су показали да дендрите сребра карактерише присуство произвољно распоређених двојникованих домена, међусобно ротираних за 180° око заједничког кристалографског правца [111]. Основна фронтална раван дендрита је {111} типа. Главно стабло дендрита и све дендритне гране расту у кристалографским правцима типа <112>.

(Примљено 6. марта, ревидирано 16. априла, прихваћено 18. априла 2014)

REFERENCES

1. J. S. Langer, *Rev. Mod. Phys*. **52** (1980) 1
2. E. Ben-Jacob, P. Garik, *Nature* **343** (1990) 523
3. M. C. Cross, P. C. Hohenberg, *Rev. Mod. Phys*. **65** (1993) 851
4. S. Xie, X. Zhang, D. Xiao, M. C. Paau, J. Huang, M. M. F. Choi, *J. Phys. Chem., C* **115** (2011) 9943
5. Z. Zheng, S. C. Tang, S. Vongehr, X. K. Meng, *Mater. Chem. Phys.* **129** (2011) 594
6. M. H. Rashid, T. K. Mandal, *J. Phys. Chem., C* **111** (2007) 16750
7. X. Qin, H. Wang, X. Wang, Z. Miao, Y. Fang, Q. Chen, X. Shao, *Electrochim. Acta* **56** (2011) 3170

8. X. Wen, Y. Xie, M. W. C. Mak, K. Y. Cheung, X. Li, R. Renneberg, S. Yang, *Langmuir* **22** (2006) 4836
9. C. Gu, T. Y. Zhang, *Langmuir* **24** (2008) 12010
10. K. I. Popov, S. S. Djokić, B. N. Grgur, *Fundamental Aspects of Electrometallurgy*, Kluwer Academic/Plenum Publishers, New York, 2002, pp. 1–305
11. Z. Jiang, Y. Lin, Z. Xie, *Mat. Chem. Phys.* **134** (2012) 762
12. Q. Zhou, B. Wang, P. Wang, C. Dellago, Y. Wang, Y. Fang, *CrystEngCom.* **15** (2013) 5114
13. J. Zhu, S. Liu, O. Palchik, Y. Koltypin, A. Gedanken, *Langmuir* **16** (2000) 6396
14. Y. Socol, O. Abramson, A. Gedanken, Y. Meshorer, L. Berenstein, A. Zaban, *Langmuir* **18** (2002) 4736
15. R. He, X. Qian, J. Yin, Z. Zhu, *Chem. Phys. Lett*. **369** (2003) 454
16. S.-D. Wu, Z. Zhu, Z. Zhang, L. Zhang, *J. Chem. Res.* **2002** (2002) 342
17. Z. Wang, F. Tao, D. Chen, L. Yao, W. Cai, X. Li, *Chem. Lett.* **36** (2007) 672
18. T. A. Witten, L. M. Sander, *Phys. Rev. Lett*. **47** (1981)1400
19. J. X. Fang, H. J. You, P. Kong, Y. Yi, X. P. Song, B. J. Ding, *Cryst. Growth. Des.* **7** (2007) 864
20. Y. C. Han, S. H. Liu, M. Han, J. C. Bao, Z. H. Dai, *Cryst. Growth. Des.* **9** (2009) 3941
21. R. L. Penn, J. F. Banfield, *Science* **281** (1998) 969
22. G. X. Zhang, S. H. Sun, M. N. Banis, R. Y. Li, M. Cai, X. L. Sun, *Cryst. Growth. Des.* **11** (2011) 2493
23. H. P. Ding, G. Q. Hin, K. C. Chen, M. L. Zhang, Q. Y. Liu, J. C. Hao, H. G. Liu, *Colloids Surfaces, A* **353** (2010) 166
24. M. A. Meyers, L. E. Murr, *Acta Met*. **26** (1978) 951
25. S. Hayashi, R. Koga, M. Ohtuji, K. Yamamoto, M. Fujii, *Solid State Commun*. **76** (1990) 1067
26. W. W. Mullins, R. F. Sekerka, *J. Appl. Phys*. **35** (1964) 444
27. J. L. Barton, J. O’M. Bockris, *Proc. Roy. Soc., A* **268** (1962) 485
28. R. S. Wagner, *Acta Met*. **8** (1960) 57
29. D. R. Hamilton, R. G. Seidensticker, *J. Appl. Phys.* **31** (1960) 1165
30. J. K. Farrer, M. C. Chipman, M. Tiner, *Microsc. Microanal*. **8** (2002) 544 CD
31. T. L. Matteson, S. W. Schwartz, E. C. Houge, B. W. Kempshall, L. A. Gianuzzi, *J. Electronic. Mater*. **31** (2002) 33
32. G. Wranglen, *Electrochim. Acta* **2** (1960) 130
33. R. E. Smallman, R. J. Bishop, *Modern Physical Metallurgy and Materials Engineering*, Butterworth–Heinemann, Oxford, 1999, p. 101.

Journal of
the Serbian
Chemical Society

JSCS-info@shd.org.rs • www.shd.org.rs/JSCS

J. Serb. Chem. Soc. 80 (1) 115–125 (2015)
JSCS–4702

UDC 63.875+665.944.7:66.099.72+628.3
Original scientific paper

The feasibility of *Cassia fistula* gum with polyaluminum chloride for the decolorization of reactive dyeing wastewater

YUAN SHING PERNG and MANH HA BUI*

Department of Environmental Engineering, Dayeh University, No.168, University Rd., Dacun, Changhua- 51591, Taiwan, China

(Received 2 January, revised 10 April, accepted 11 April 2014)

Abstract: In order to find a new environmentally friendly coagulant that could partially replace conventional polyaluminum chloride (PAC), which was shown to be toxic to aquatic environments, gum extracted from the seeds of *Cassia fistula* Linn. (*CF*) was investigated for the decolorization of reactive dyes Blue 19 (RB19) and Black 5 (RB5) using jar-test experiments. The optimal results showed that crude *CF* gum did not achieve high degrees of decolorization of RB5 and RB19 when compared with PAC coagulant under the same conditions. Whereas when *CF* gum was used in combination with PAC, decolorization efficiencies of both dyes reached over high values at 40 % volume fraction of gum. These results indicated the potential of using *CF* gum as a "green" coagulant or as a contributing factor to color removal in textile wastewater.

Keywords: coagulation; dye removal; natural coagulant; reactive blue 19; reactive black 5.

INTRODUCTION

With rapid technological developments, dyes are commonly used in many industries, particularly the textile sector. It was found that the main components in the wastewater are activated dyes that are completely soluble in water and their complex chemical structures contain non-biodegradable groups. Without an effective treatment of dyes before wastewater discharge, serious damage to water sources, wildlife and human health could result even at low dye concentrations.[1,2]

To reduce the reactive dyes, coagulation is one of the most often used techniques, in which inorganic coagulants (alum, ferric chloride, PAC, *etc*.), or organic polymers (polyacrylamide, poly(diallyldimethylammonium chloride), poly(acrylic-acid-*co*-acrylamide), *etc*.). Both coagulant groups are successful in

---

[*] Corresponding author. E-mail: manhhakg@yahoo.com.vn

doi: 10.2298/JSC140102041P

color removal.[2,3] However, these chemicals and their adjustments for pH, temperature of the sample (before or after treatment) produce a huge volume of sludge, which is sometimes difficult to thicken and increases operational costs. In addition, recently there was a report suggesting that there may be a possible link between the use of metal-based coagulants or excessive organic polymers and cancer in human or infliction of harm to aquatic organisms.[4]

Due to the limited accessibility, high costs and potential environmental issues associated with conventional coagulants, there is a trend to use locally available natural coagulants: *Plantago psyllium*,[5] *Ipomoea dasysperma*,[6] *Moringa oleifera*,[7] *etc*., as point-of-use treatment in the developing countries. They have proved that extractable gums (polysaccharides) have functional groups that serve as coagulants. These groups also help to reduce the dosages of the traditional coagulants by 40 to 50 %. Furthermore, the gums are biodegradable and produce sludge of low toxicity, which abates the possibility of secondary pollution.

In the field of natural coagulants, *Cassia* seed gums seem to be an emerging coagulant. Their endosperms contain an amount of the galactomannan polysaccharides including *cis*-hydroxyl group interacting with colloidal particles.[8,9] Some of seeds in the *Cassia* genus, such as *C. angustfolia*,[10] *C. javahikai*,[11] and *C. grandis*[12] were found to be effective in the removal of pollutants in wastewater. They could be employed as alternative coagulants or partial alternatives to PAC.

In Vietnam, *Cassia fistula* Linn. (*CF*) or Golden Shower tree is an ornamental tree widely planted on many roads and parks because of its beautiful flowers. However, according to Hoornweg *et al*.[13] *CF* pods are major agricultural wastes that cause increases in the capital costs of solid waste treatment. In an effort to utilize this *Cassia* waste, Hanif *et al*.[14,15] presented a method in which dried internal pod mass of *CF* was used as an alternative absorbent for the successful removal of Ni from industrial wastewater (91 to 99 %) and for decreasing the chemical oxygen (COD) of textile wastewater (71 %) in the laboratory. To the best of our knowledge, there have been few studies attempting to assess characteristic of *CF*, and no publication related to the efficiency of *CF* seed gum in wastewater treatment.[16]

Thus, the present study focused on the potential of gums extracted from *CF* and PAC to reduce the color of reactive black 5 (RB5) and reactive blue 19 (RB19), together with the determination of the optimal factors, such as pH, agitation speed, initial dye concentration (*IDC*), coagulants dosage (*CF* gum and PAC) and reaction time. The performance of gum and PAC was evaluated individually and in combination through measuring the decrease in maximum absorbance of the dyes. Furthermore, the chemical composition of *CF* gum was investigated by utilizing Fourier transform infrared spectroscopy (FTIR), high performance liquid chromatography (HPLC), and gel permeation chromatography (GPC).

EXPERIMENTAL

Material: Cassia fistula *gum.*

Collection. The seeds of the *Cassia fistula* Linn. (*CF*) tree were collected in a park (Phu Nhuan district, Ho Chi Minh city, Vietnam) in January 2013. The ripe fruits are black. They were sun-dried and split into two halves to obtain the seeds.

Isolation. The extraction of polysaccharide from *CF* seeds was performed according to Singh *et al.*[9] with some modifications. Briefly, dried seeds were ground into powder in a blender. The dry powder was defatted and decolorized by Soxhlet extraction; the powder was then dissolved in 1 % CH_3COOH solution and precipitated by ethanol to form a fibrous masses. Next, the fibrous masses was dissolved in distilled water and precipitated again to purify the gum. The crude *CF* gum was collected, crushed and dried.

Reactive dye stock

Both dyes RB5 (C.I. 20505, purity 68 %, λ_{max} 599 nm) and RB19 (C.I. 61200, purity 47 %, λ_{max} 590 nm) used in this study were purchased from Sigma–Aldrich, and their structures are given in Fig. 1.

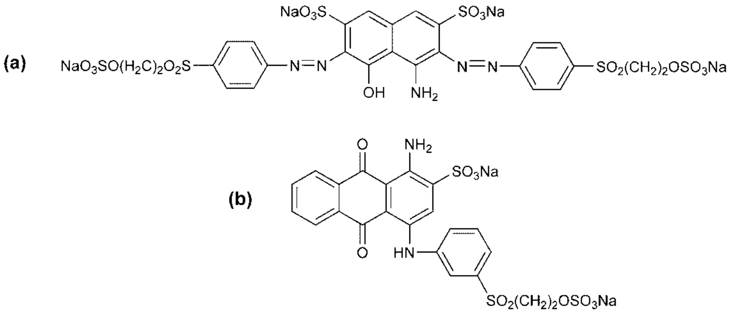

Fig. 1. Chemical structures of the studied dyes: (a) RB5 and (b) RB19.

At room temperature, the solubility of reactive dyes is limited. To prepare the dyeing solution for the coagulant process, the operating condition of the dyeing processes had to be mimicked, similar to the procedure described by Joo *et al.*,[17] to obtain a dye stock solution of 1000 mg L^{-1} in the “hydrolyzed” form. Other dye concentrations, varying between 10 and 140 mg L^{-1}, were obtained by dilution of this stock solution.

Coagulant stock solutions

Besides *CF* gum, the other coagulant used in this study was PAC, a product of South Basic Chemicals Co. Ltd., Vietnam; with a bulk density of 0.5 g cm^{-3} and a specific gravity of 1.31 kg L^{-1}, containing a mass fraction of 15 % Al_2O_3.

The stock solutions of the coagulants were prepared by dissolving 500±1 mg of powder (*CF* gum or PAC) into 100 mL distilled water (5000 mg L^{-1}) using a magnetic stirrer for 5 min and sonication for 60 min to obtain homogenous solutions. These solutions were stored in a refrigerator at 5°C. To obtain the appropriate mass concentrations (80 to 350 mg L^{-1}), these solutions were diluted before use.

Decolorization experiments

The coagulation studies were conducted by using a jar-test apparatus (Stuart flocculator, SW6) based on the traditional methods reported by Ndabigengesere and Subba Narasiah[7] with 5 factors and some modifications such as the effects of a slow mixing phase on the agitation speed and reaction time. In particular, the parameters and the ranges of their value are given in Table I. The initial conditions for both *CF* gum and PAC treatment were pH 10, coagulant dosage 100 mg L^{-1}, initial dye concentrations (*IDC*) 100 mg L^{-1}, time 30 min, and agitation speed 60 rpm. This study was designed based on a controlled, or one-factor-at-a-time, experiment, *i.e.* in every series of experiments; only one independent factor was varied while all other factors were kept constant. Overall, 5 series of experiment were performed to evaluate the effects of all 5 factors.

TABLE I. The factors evaluated and the established range for the decolorization of dyes

Factor	Values
pH	3, 7, 10 and 12
Agitation speed, rpm	15, 30, 45, 60 and 90
Initial dye concentration, mg L^{-1}	10, 20, 50, 80, 100, 120 and 140
Coagulant dosage, mg L^{-1}	
1. Gum	100, 150, 200, 250, 300 and 350
2. PAC	80, 100, 120, 140, 160, 180, 200, 220,240, 260 and 280
Reaction time, min	15, 30, 45 and 60

Characterization of the obtained gum

The obtained gum was characterized in terms of its chemical composition and molar mass. The details of its characterization are given and presented as Figs. S-1–S-3 in the Supplementary material to this paper.

Input and output water analysis

Dye decolorization efficiency could be measured by using the decreasing percentage of the maximum absorbance (599 nm for RB5 and 590 nm for RB19) between initial and final value (after 30 min settling) of dye solutions using Thermo a Fisher Scientific Inc., UV–Vis Genesys 10 spectrophotometer, and the pH was determined using a digital pH meter model 744, Metrohm Ltd., Switzerland. All analyses were conducted in duplicate and the results presented herein are the mean of duplicate ± standard deviations (*SD*).

RESULTS AND DISCUSSION

Characterization of CF *gum*

The results of the characterization of the gum are given in the Supplementary material to this paper (Figs. S-1–S-3). In summary, the analysis data of *CF* gum, obtained by FTIR, GPC and HPLC spectrum, combined with galactomannan information in previous studies,[6,8] revealed a possible galactomannan structure of *CF* seed gum as shown in Fig. 2.

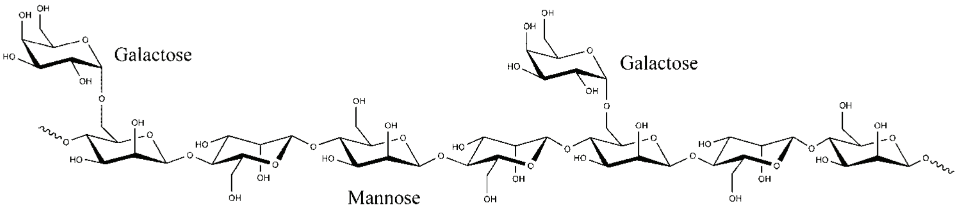

Fig. 2. A hypothetic fragment structure of the *CF* gum.

Coagulation studies

The color removal effects of *CF* gum and PAC were studied using the one-factor-at-a-time jar-test method. Here, the influences of each factor in the order in which they were performed in the actual experiments are discussed.

Effect of pH. It was established that pH plays an important role in the performance of dye coagulation process because it not only affects the specialization of coagulant and the hydrolysis behavior of dyes, but also their solubility.[2,3,6] The variation in the effectiveness of decolorization with pH is presented in Fig. S-4 of the Supplementary material to this paper.

In the case of *CF* gum, color removal efficiency at alkaline pH was higher than at neutral and acidic pH values. Particularly, at pH 10, the decolorization for both RB19 and RB5 reached the highest values (56.7 and 31.7 %, respectively). This pH value quite matched earlier research on *Ipomeoa dasysperma* gum at pH 9.5.[6]

At pH 10, the relative dyes are primarily in a hydroxyethyl sulfone structure as described in Fig. 3.[18] It can react with galactomannans by intermolecular force between the π electron system of the dyes and the *cis*-hydroxy groups in the constituent sugars.[8] Indeed, dyes can be easily removed by *CF* gum at this pH value in a mechanism illustrated in Fig. 4.

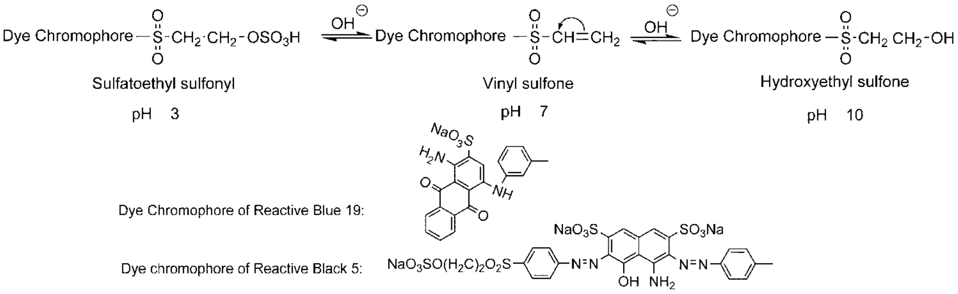

Fig. 3. Structure of the reactive groups of the dyes at various pH values.

In the presence of stronger alkali (pH 12), the carbohydrate bone of *CF* gum may be broken into complex particles that might not react effectively with dye molecules even though the dyes still retained the hydroxyethyl sulfone structure.[19] Hence, this decreased the yield of decolorization.

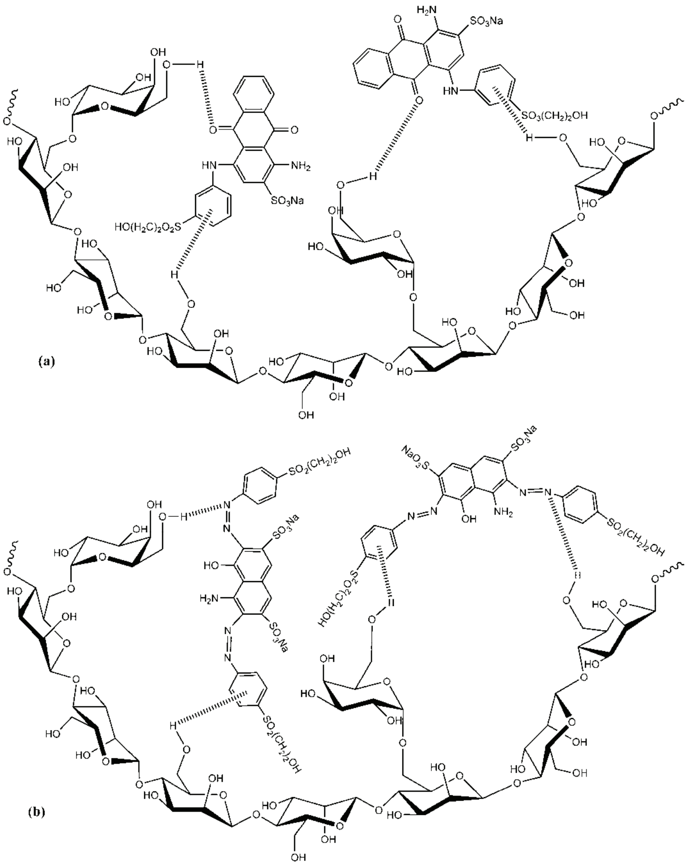

Fig. 4. The hypothetic mechanism of *CF* gum and dyes: a) RB19 and b) RB5.

In contrast, at pH ≤ 7, the dyes become protonated, and positive charges appear in their molecules. The acidic medium also causes the formation of cross-linking bisacetal on the mannose backbone of the gum. The net effect is that electrostatic repulsion occurs between the positively charged surface of the gum and the positively charged dye molecules, resulting in a decrease in the efficiencies of color removal.

In the case of PAC, the best results for RB19 and RB5 removal at 100 mg L^{-1} dosage were 40.7 and 32.2 %, respectively, both achieved at pH 7. These show that at low dosages, PAC exhibited poor efficiencies even at the optimum pH. This phenomenon could be explained by the positive charges caused when diluted PAC is not sufficient to destabilize the dye particles.[3] This result is interesting because even though at high dosages, PAC exhibited much higher efficiencies than *CF* gum (see section on coagulant dosage), at low dosage, PAC was less efficient than *CF* gum. Moreover, when compared to *CF* gum (9), the lower optimum pH of PAC (7) makes the decolorization process using PAC costlier than using *CF* gum because of the necessity to neutralize the normally highly alkaline reactive dyeing wastewater.[3,17]

Effect of agitation speed. In jar-test experiments, the agitation process is separated into rapid mixing phase and then slow mixing phase. The rapid phase was employed to ensure complete mixing of the colloids in the wastewater with the coagulant. A speed of 200 rpm for 1 min was used for both the PAC and the *CF* gum.[17] In the slow phase, each coagulant needs a suitable agitation speed to keep the particles suspended at a sufficient level without shearing them, so that larger and larger aggregates can form. Thus, it was critical to investigate the effect of agitation speed in the slow mixing phase and the obtained results are shown in Fig. S-5 of the Supplementary material.

Thus, the highest color removal percentages by *CF* gum and PAC were obtained in both the dye solutions at 60 and 45 rpm, respectively. It is obvious that gum needs to be mixed faster than PAC due to the high viscosity of the *CF* gum. In other words, the gum flocs are more stable than PAC. This result is quite similar to the agitation speed recommended by Tatsi *et al.*[20] Hence, an agitation speed of 60 rpm was chosen for *CF* gum and of 45 rpm for PAC in the subsequent study.

Effect of initial dye concentration. The color removal percentages of RB19 and RB5 *vs*. the initial dye concentration (*IDC*) are shown in Fig. S-6 of the Supplementary material. As the *IDC* of RB19 increased up to 100 mg L^{-1}, the removal efficiencies were relatively constant; their values were around 56.7 and 48.1 % for *CF* gum and PAC, respectively. However, above this concentration, the effects of both *CF* gum and PAC dropped rapidly to 18.2 and 20.8 %, respectively. In the case of RB5, even though decolorization efficiencies almost constantly decreased with increasing *IDC*, the slopes of the decrement in the low concentration part up to 50 mg L^{-1} were lower than in the high concentration part above 50 mg L^{-1}, especially in the case of *CF* gum.

These "flat then drop" variations could be explained by the relatively fixed ratio between the coagulant particles and the decolorized dye particles. This ratio is determined by the binding strength between the two kinds of particles.[21] As the concentration of dye increased but the dosage of coagulant was fixed, the amount of decolorized dye particles was relatively fixed an increasing amount of particles were left not decolorized. This led to the decrease in the decolorization efficiency. With decreasing dye concentration, the decolorization yield first increased but then remained almost unchanged after the dye concentration passed a threshold relative to the fixed coagulant dosage. These thresholds, *i.e.*, 100 mg L^{-1}

for RB19 and 50 mg L^{-1} for RB5, were chosen to be the *IDC* in subsequent experiments.

Furthermore, there was a large difference in the efficiency of *CF* gum (44.2 %) and of PAC (75.9 %), Fig. S-6b of the Supplementary material. The lower efficiency of the gum could be explained by the weakness of the bonds between the *CF* gum particles and the dye particles that are shown in Fig. 4b.

Effect of the coagulant dosage. The effects of the coagulant dosage on the decolorization efficiency of PAC and *CF* are presented in Fig. S-7 of the Supplementary material. Thus, PAC achieved efficiencies over 94 % for both RB19 and RB5. At low dosages, the color removal of RB5 was higher than that of RB19. However, the difference became unclear when the coagulant dosage was increased above 220 mg L^{-1}. These results confirm that PAC is a coagulant with highly positive charges and a very effective polymer for dye removal.[3]

With *CF* gum treatment, the removal yield initially increased to 62.0 and 53.8 % with dosages up to 200 and 300 mg L^{-1} for RB19 and RB5, respectively. However, decreasing efficiency trends were evident with further increasing of the gum dosages. A possible explanation is that the appropriate dosage of *CF* gum could cause dye particles to aggregate (destabilization) and settle out, so that gum–dye bridging occurs.[6,8] Then, when the *CF* gum dosage in the solution exceeds an optimal threshold, there will not be enough bare dye particles with unoccupied surface available for attachment of *CF* gum segments.[11] This results in a reduction in the *CF* gum–dye bridging and the solution restabilizes. Hence, the optimal *CF* gum dosages of 200 and 300 mg L^{-1} for RB5 and RB19, respectively, were chosen for next series of experiments.

Reaction time. Along with agitation speed, reaction time at slow mixing phase between coagulant and dye solution also plays relevant role. It mostly depends on coagulant and wastewater characteristics. The effects of reaction time on the efficiencies of dye removal are presented in Fig. S-8 of the Supplementary material. Thus, with increasing reaction time, the dye removal efficiency of *CF* gum was improved. The yields were 62.0 (RB19) and 55.7 % (RB5). Nevertheless, when the optimal reaction time of 30 and 45 min for RB19 and RB5, respectively, were increased, the efficiencies became constant and even slightly decreased. This may be due to restabilization of the aggregated particles.[10] A similar trend was also found in the experiment using PAC at 94.4 % (RB19) and 97.2 % (RB5).

Thus under the optimized conditions, it was possible with CF gum to remove 62.0 % of RB19 and 55.7 % of RB5, while the corresponding removal efficiencies with PAC were more than 94 %. This difference may due to the original characteristics of gum and PAC. While PAC is easy to dissolve in water and produce a positive charged polymer that can react directly with negative colloids (dyes), *CF* gum dissolve limitedly in water and its removal mechanism mostly depends on bond interaction that is weaker than ionic bonds mechanism of PAC.[9,17]

Combination of CF gum and PAC

In order to investigate the effect of combining gum and PAC on dye removal, a series of experiment was conducted for the full range of volume fractions from 0 % gum with 100 % PAC to 100 % gum with 0 % PAC at optimal conditions of *CF* gum for RB19 and RB5. The volume fractions matched with mass concentrations of each coagulant are given in Table S-I of the Supplementary material.

The relationship between the decolorization efficiency and the percentage ratios between *CF* gum and PAC is described in Fig. 5. At first, as the gum fraction increased from 0 to 20 %, the efficiency decreased because *CF* gum is much less efficient than PAC, as shown in previous sections. However, as more gum was added, the efficiencies arrived at 92.6 % (RB19) and 94.2 % (RB5) when the gum fraction was 40 %. This suggests that the combination of *CF* gum and PAC could provide for a strong chelation of PAC–gum–dye or gum–PAC––dye that allows the dye particles to settle easily as was demonstrated in a previous study.[8] A possible chelation of *CF* gum with PAC and dye in solution is illustrated in Fig. 6. With further increasing of gum fraction from 40 to 100 %, the dye removal significantly decreased. This might relate to inadequate dosages of *CF* gum and PAC. Therefore, this leads to inefficiency of the interaction between gum and PAC.

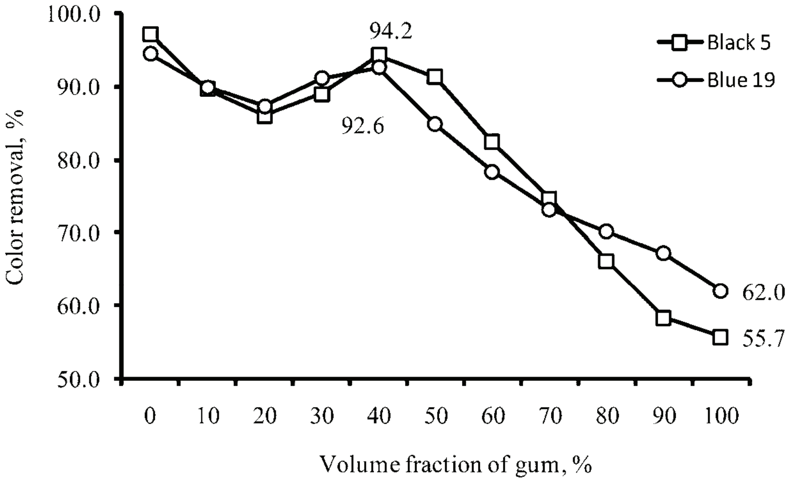

Fig. 5. Effect of combinations of *CF* gum and PAC on color removal efficiencies.

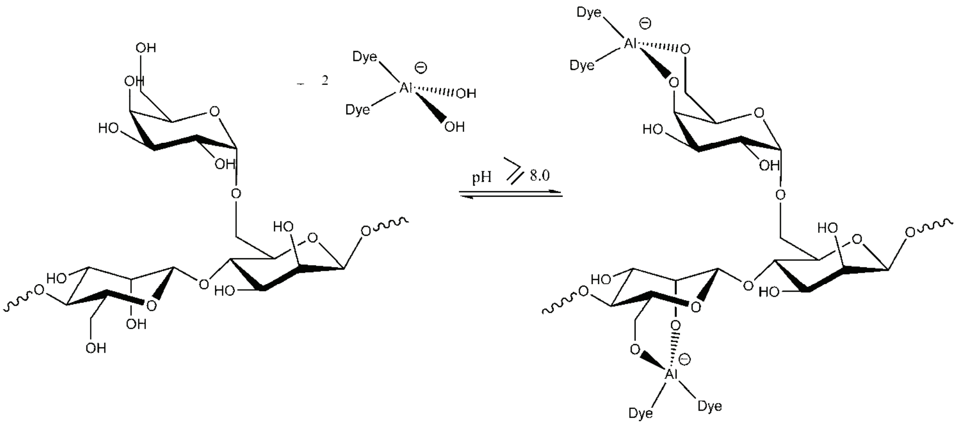

Fig. 6. Complexation of *cis*-hydroxyl group on the CF gum backbone with PAC and dyes.

CONCLUSIONS

Cassia fistula Linn. seed gum was investigated as a coagulant in the color removal process of two reactive vinyl sulfone dyes, blue 19 and black 5. The decolorization of these dyes by *CF* gum depended highly on pH because it may affect the structure of dyes, gum and their interactions. The best result was gained at pH 10. When only gum was used for RB19 and RB5 removal, the best treatment efficiencies reached 62.0 and 55.7 %, respectively. However, a combination of low dosages of gum (80 and 120 mg L^{-1}) and PAC (132 mg L^{-1}) showed rather high removal efficiencies of over 92 %. Therefore, the natural and inexpensive gum extracted from *Cassia* waste was shown to be an effective aiding factor for the color removal process using PAC, which helped to reduce the usage of the inorganic coagulant PAC by up to 40 %.

SUPPLEMENTARY MATERIAL

The details of the characterization of *CF* gum and optimization of the dye removal are available electronically from http://www.shd.org.rs/JSCS/, or from the corresponding author on request.

Acknowledgements. The authors are grateful to Prof. Le Ngoc Thach from University of Science Ho Chi Minh City, Vietnam, for contributing his idea of using *Cassia Fistula* seed gum as a coagulant.

ИЗВОД

МОГУЋНОСТ КОРИШЋЕЊА КАУЧУКА ИЗ *Cassia fistula* СА ПОЛИАЛУМИНИЈУМ--ХЛОРИДОМ ЗА ОБЕЗБОЈЕЊЕ ОТПАДНЕ ВОДЕ ОД РЕАКТИВНОГ БОЈЕЊА

YUAN SHING PERNG и MANH HA BUI

Department of Environmental Engineering, Dayeh University, No.168, University Rd., Dacun, Changhua-51591, Taiwan, Republic of China

Како би се нашао коагулант прихватљив за животну средину који може делимично да замени конвенционални полиалуминијум-хлорид (PAC), који се показао токсичним у воденој средини, испитан је каучук екстрахован из семена *Cassia fistula Linn.* (*CF*) у обезбојавању од реактивних боја blue 19 (RB19) и black 5 (RB5) коришћењем JAR-тест експеримената. Оптимални резултати су показали да сиров *CF* каучук (на pH 10, почетне концентрације боје од 100 и 50 mg L^{-1}, дозе каучука од 200 и 300 mg L^{-1}, времена реакције од 30 и 45 min и брзина мешања од 60 o/min) није постигао тако високе степене обезбојавања од RB5 и RB19 (55,7, односно 62,0 %) као коагулант PAC (97,2, односно 94,4 %) при истој почетној концентрацији боје. С друге стране, када је каучук *CF* коришћен у комбинацији са PAC, ефикасност обезбојавања са обе боје је превазишао 92, односно 40 % запреминских фракција каучука. Ови резултати указују на потенцијал коришћења каучука од *CF* као "зеленог" коагуланта или као додатне компоненте при обезбојавању отпадне воде од бојења текстила.

(Примљено 2. јануара, ревидирано 10. априла, прихваћено 11. априла 2014)

REFERENCES

1. A. Gottlieb, C. Shaw, A. Smith, A. Wheatley, S. Forsythe, *J. Biotechnol.* **110** (2003) 49
2. V. Golob, A. Vinder, M. Simonic, *Dyes Pigm.* **67** (2005) 93
3. A. Assadi, M. Amin, R. Nateghi, *Int. J. Environ. Health Eng.* **2** (2013) 5
4. N. Z. Al-Mutairi, *Ecotoxicol. Environ. Saf.* **65** (2006) 74
5. A. Mishra, R. Srinivasan, M. Bajpai, R. Dubey, *Colloid Polym. Sci.* **282** (2004) 722
6. R. Sanghi, B. Bhattacharya, A. Dixit, V. Singh, *J. Environ. Manage.* **81** (2006) 36
7. A. Ndabigengesere, K. Subba Narasiah, *Water Res.* **32** (1998) 781
8. R. S. Blackburn, *Environ. Sci. Technol.* **38** (2004) 4905
9. V. Singh, R. Sethi, A. Tiwari, *Int. J. Biol. Macromol.* **44** (2009) 9
10. R. Sanghi, B. Bhattacharya, V. Singh, *Green Chem.* **4** (2002) 252
11. R. Sanghi, B. Bhattacharya, V. Singh, *Bioresour. Technol.* **97** (2006) 1259
12. V. Singh, S. Tiwari, A. K. Sharma, R. Sanghi, *J. Colloid Interface Sci.* **316** (2007) 224
13. D. A. Hoornweg, L. Thomas, *What a Waste: Solid Waste Management in Asia*, World Bank, Urban Development Sector Unit, East Asia and Pacific Region, 1999
14. M. A. Hanif, R. Nadeem, M. N. Zafar, K. Akhtar, H. N. Bhatti, *J. Hazard. Mater.* **145** (2007) 501
15. M. A. Hanif, R. Nadeem, M. N. Zafar, H. N. Bhatti, R. Nawaz, *J. Chem. Soc. Pak.* **30** (2008) 385
16. M. A. Ali, M. A. Sayeed, N. Absar, *J. Chin. Chem. Soc.* **51** (2004) 647
17. D. J. Joo, W. S. Shin, J. H. Choi, S. J. Choi, M. C. Kim, M. H. Han, T. W. Ha, Y. H. Kim, *Dyes Pigm.* **73** (2007) 59
18. A. Ojstršek, A. Doliška, D. Fakin, *Anal. Sci.* **24** (2008) 1581
19. R. L. Whistler, J. N. BeMiller, *Advances in Carbohydrate Chemistry*, Academic Press, New York, 1958, p. 289–329
20. A. A. Tatsi, A. I. Zouboulis, K. A. Matis, P. Samaras, *Chemosphere* **53** (2003) 737
21. S. Buthelezi, A. Olaniran, B. Pillay, *Molecules* **17** (2012) 14260.

Journal of the Serbian Chemical Society
JSCS@tmf.bg.ac.rs • www.shd.org.rs/JSCS
J. Serb. Chem. Soc. 80 (1) S15–S23 (2015)
Supplementary material

SUPPLEMENTARY MATERIAL TO

The feasibility of *Cassia fistula* gum with polyaluminum chloride for the decolorization of reactive dyeing wastewater

YUAN SHING PERNG and MANH HA BUI*

Department of Environmental Engineering, Dayeh University, No.168, University Rd., Dacun, Changhua- 51591, Taiwan, China

J. Serb. Chem. Soc. 80 (1) (2015) 115–125

CHARACTERIZATION OF *CF* GUM

Fourier transform infrared (FTIR) spectrum of CF *gum*

The infrared spectrum of the *CF* gum was measured on a Bruker Equinox 55 FTIR spectrometer in the form of tablets KBr pellets. The spectrum was recorded from 400 cm^{-1} to 4000 cm^{-1} with 64 scans collected at a resolution of 4 cm^{-1}.

The infrared spectrum of *CF* gum shown in Fig. S-1 indicates the typical peak characteristic of polysaccharides and confirms the presence of many similar sugar residues.

The broad band of 950 to 1151 cm^{-1} is assigned to galactomannan composition in gum by the contribution of bending C–OH modes. The peak at 1151 cm^{-1} results from stretching modes of the C–O present in the pyranose ring while the absorption peaks at 1026 and 1093 cm^{-1} correspond to bending vibrational modes of C–OH. In the anomeric region (700 to 950 cm^{-1}), the obvious peaks at 814 and 875 cm^{-1} reveal the presence of α-linked D-galactopyranose and β-linked D-mannopyranose unit, respectively. These bands identified a galactomannan polysaccharide structure with the same characteristics as in a previously published study.[1]

Carbohydrate profile

The constituent saccharides (mannose and galactose) were measured by HPLC under following conditions: 250 mm×4.6 mm i.d. NH$_2$P-50 column (Asahi Kasei Ltd.), mobile phase including water:acetonitrile of 20:80, flow rate 0.6 mL min^{-1} and with a refractive index (RI) detector at 25 °C.

The resulting chromatogram is depicted in Fig. S-2, which shows that the average molar ratio of mannose to galactose in the *CF* gum was about 3.5:1. This

---

* Corresponding author. E-mail: manhhakg@yahoo.com.vn

seems to be quite consistent with the result of Ali *et al.*[2] This ratio indicates a limited solubility of this gum in water due to the formation of strong intramolecular hydrogen bonds.

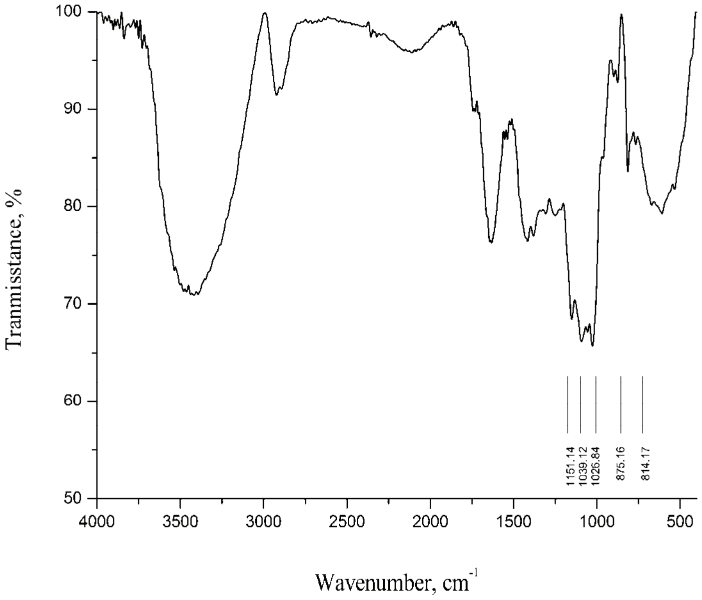

Fig. S-1. FT-IR spectra of the *CF* gum.

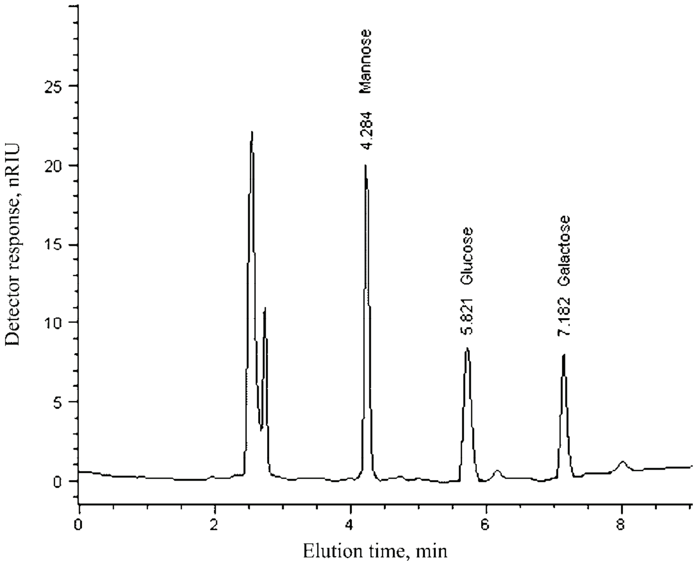

Fig. S-2. HPLC profile of the hydrolyzate of the crude *CF* gum.

Molar mass determination of the CF *gum*

The number-average molar mass ($\bar{M}_\mathrm{n}$) and weight-average molar mass ($\bar{M}_\mathrm{w}$) of the samples were determined by gel permeation chromatography (GPC) with an Agilent instrument (serial LC 1100) using an ultrahydrogel linear column (7.8 i.d.×300 mm, Waters, USA), a flow rate of 0.6 mL min^{-1}, a *CF* gum concentration of 2 mg L^{-1}, water as the solvent and $NaHCO_3$ buffer (pH 11) as the eluent using an RI detector at room temperature.

The GPC chromatogram of the *CF* gum is presented in Fig. S-3. The weight-average molar mass ($\bar{M}_\mathrm{w}$) of the *CF* gum was 4.70×10^5 g mol^{-1} and the polydispersity index (*D*) was 2.483. The weight value was lower, but the *D* value of this gum was higher than the values for other galactomannans extracted from some plant sources, such as *Dimorphandra gardneriana*[3] ($\bar{M}_\mathrm{w}$ 3.9×10^7 g mol^{-1}, *D* 2.06), *Caesalpinia ferrea*[4] ($\bar{M}_\mathrm{w}$ 6.04×10^5 g mol^{-1}, *D* 1.55) and *Mimosas cabrella*[5] ($\bar{M}_\mathrm{w}$ 8.48×10^5 g mol^{-1}, *D* 1.3). Thus, the *CF* gum could dissolve faster than the gums investigated in other studies. However, this product needs to be purified or subjected to some modification steps to become a commercial coagulant.[5,6]

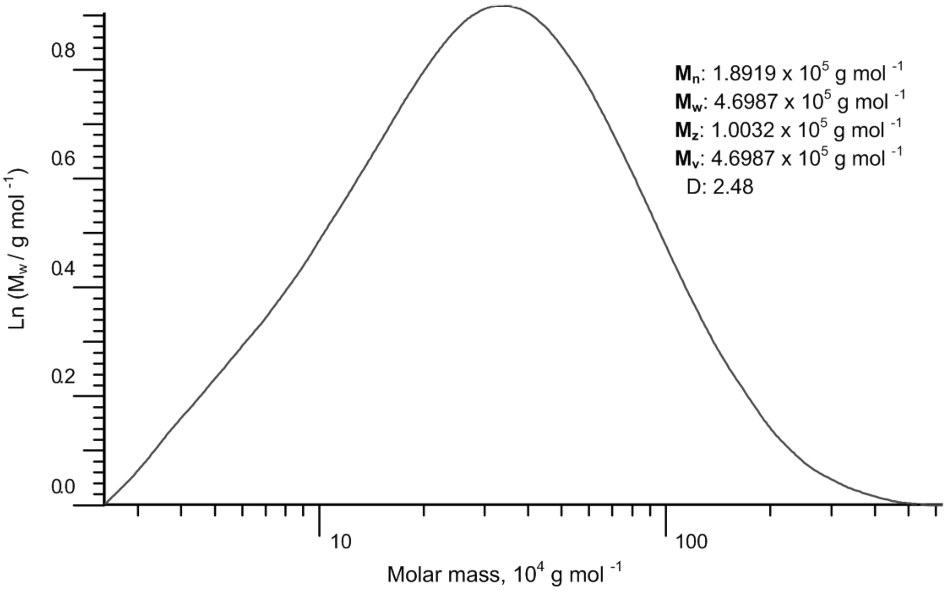

Fig. S-3. Molecular weight distribution of the *CF* gum.

RESULTS FOR THE OPTIMIZATION OF THE REMOVAL OF THE DYES

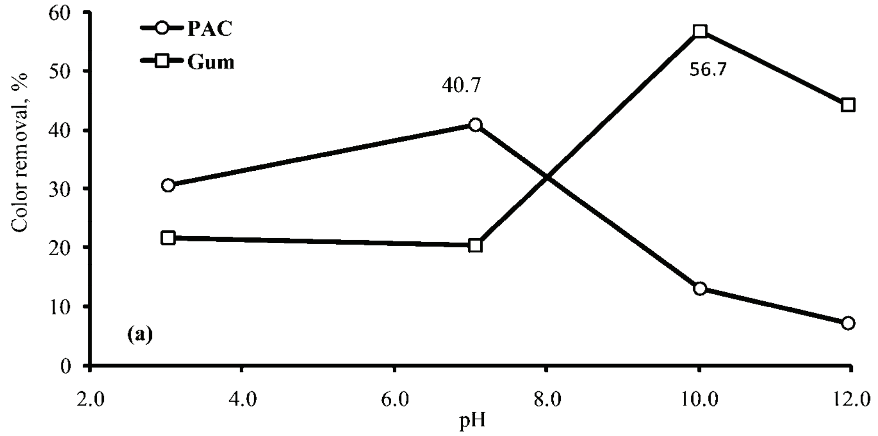

(a)

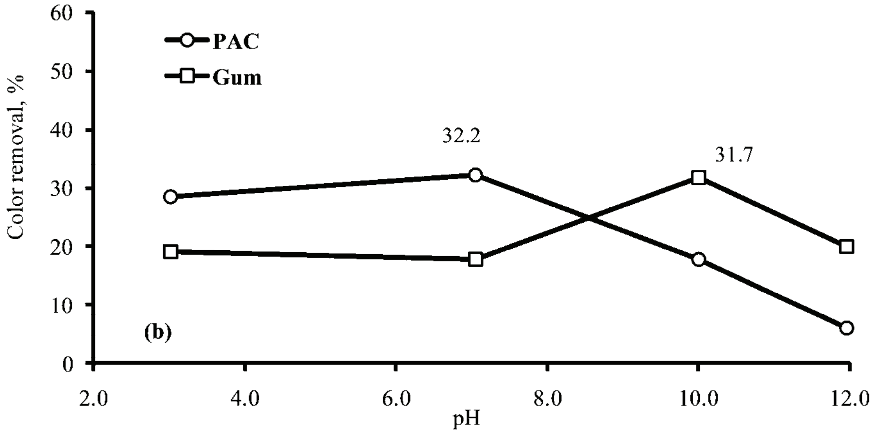

(b)

Fig. S-4. Effect of pH on the color removal for a) RB19 and b) RB5.

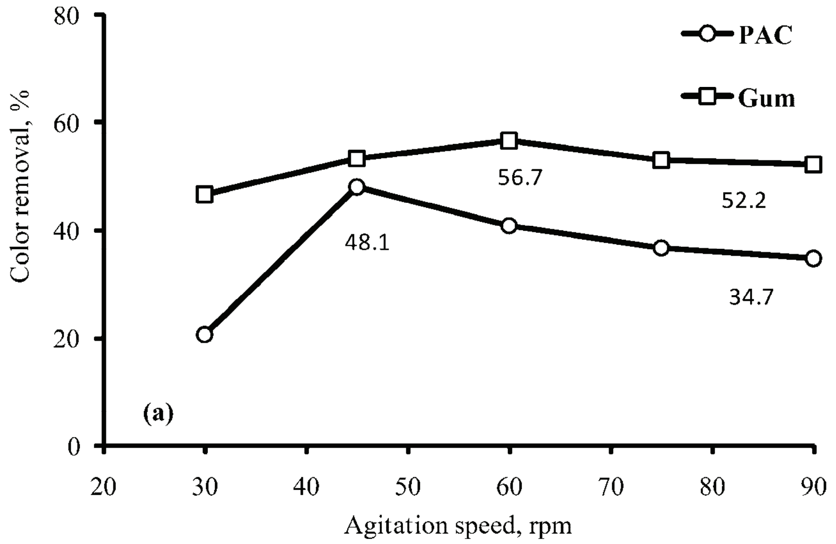

(a)

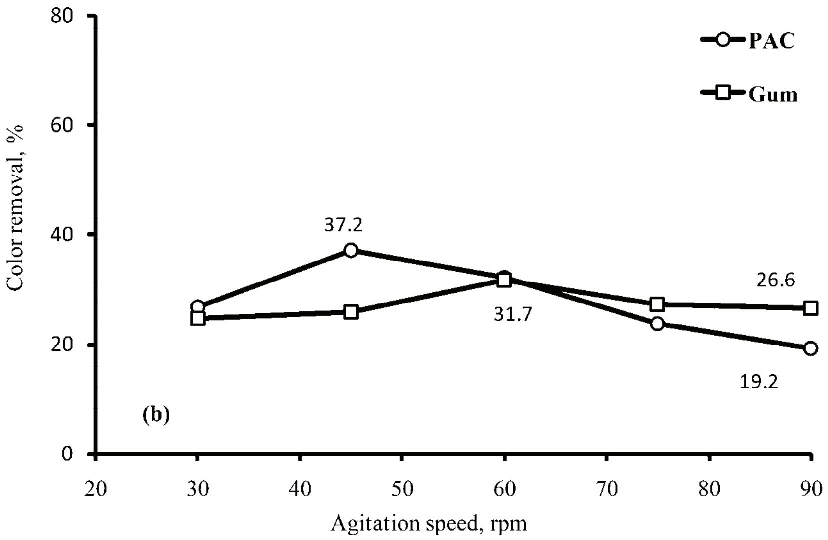

(b)

Fig. S-5. Influence of agitation speed on color removal for a) RB19 and b) RB5.

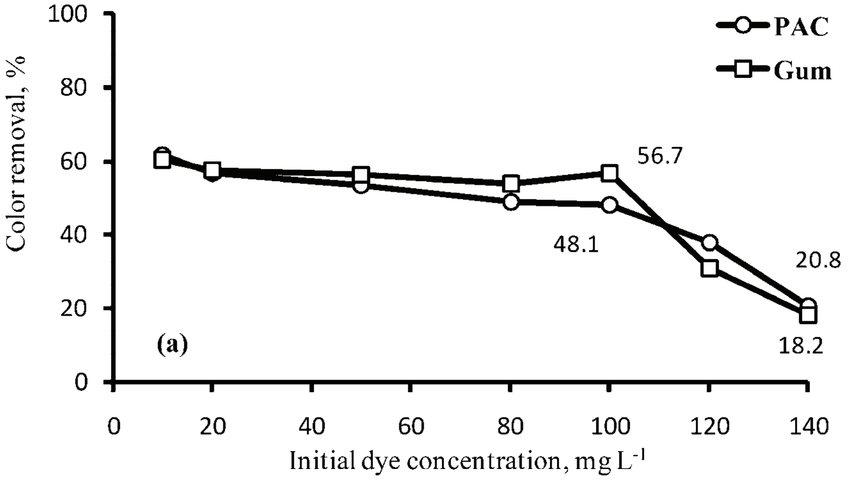

(a)

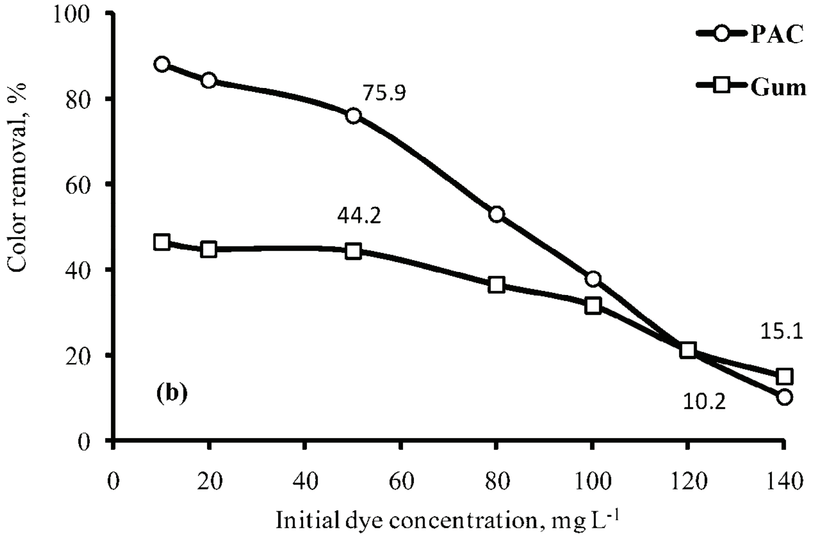

(b)

Fig. S-6. Effect of initial dye concentration on color removal for a) RB19 and b) RB5.

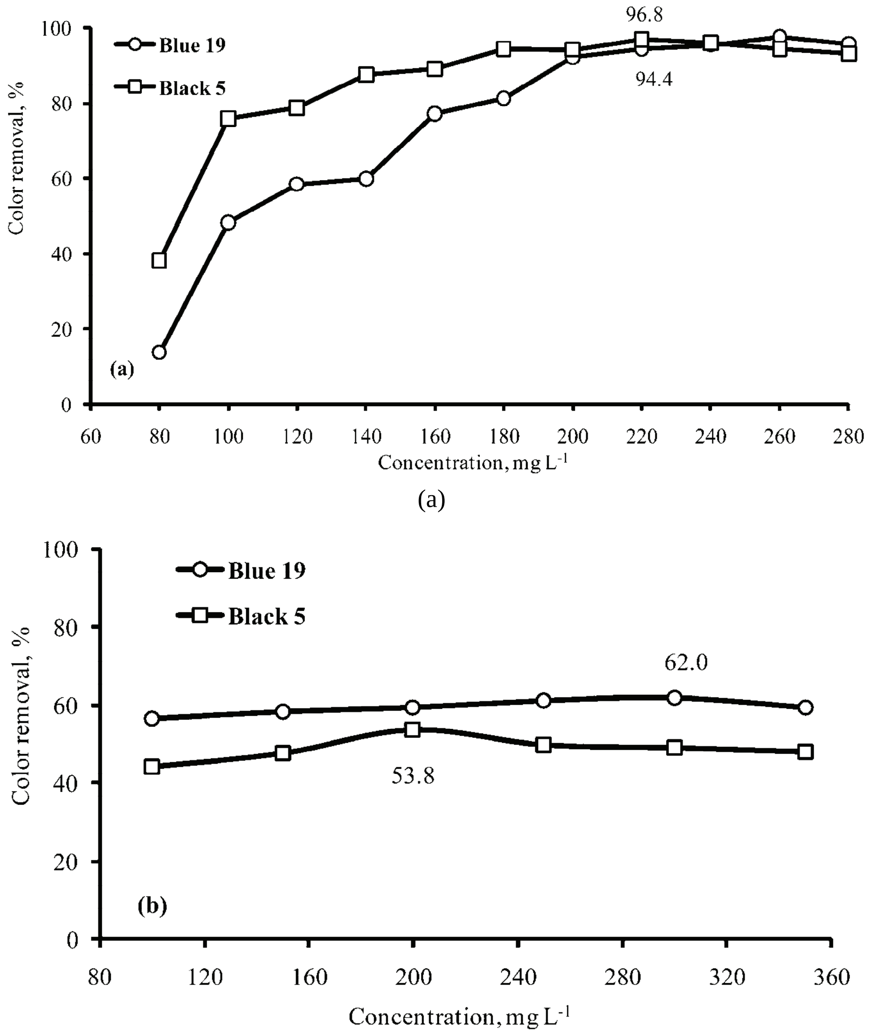

(a)

(b)

Fig. S-7. Effect of coagulant concentration on dye removal efficiencies for a) PAC and b) gum.

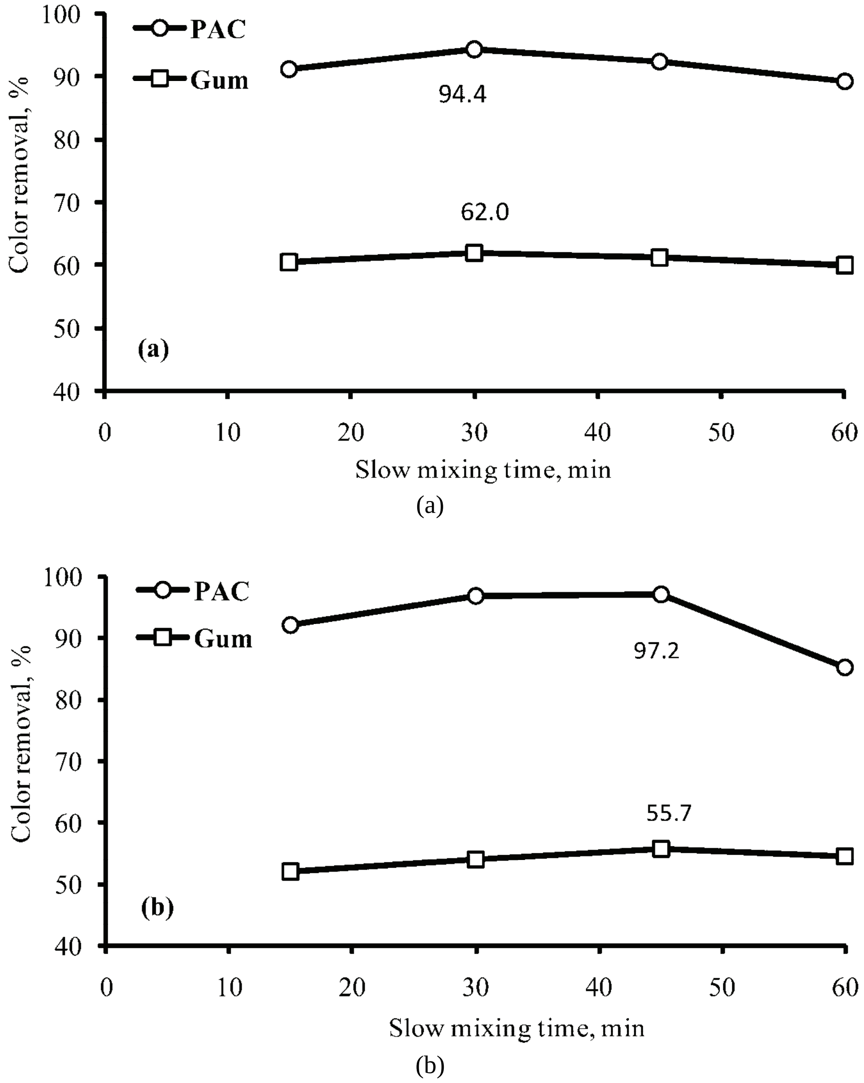

(a)

(b)

Fig. S-8. Effect of reaction time on dye removal efficiencies for a) RB19 and b) RB5.

Table S-I. Volume fractions and associated concentrations of each coagulant

Dye	Gum			PAC	
	Volume fraction %	Volume mL	Mass concentration mg L^{-1}	Volume mL	Mass concentration mg L^{-1}
Blue 19	0	0	0	50	220
	10	5	20	45	198
	20	10	40	40	176
	30	15	60	35	154
	40	20	80	30	132
	50	25	100	25	110
	60	30	120	20	88
	70	35	140	15	66
	80	40	160	10	44
	90	45	180	5	22
	100	50	200	0	0
Black 5	0	0	0	50	220
	10	5	30	45	198
	20	10	60	40	176
	30	15	90	35	154
	40	20	120	30	132
	50	25	150	25	110
	60	30	180	20	88
	70	35	210	15	66
	80	40	240	10	44
	90	45	270	5	22
	100	50	300	0	0

REFERENCES

1. M. A. Cerqueira, B. W. S. Souza, J. Simões, J. A. Teixeira, M. R. M. Domingues, M. A. Coimbra, A. A. Vicente, *Carbohydr. Polym.* **83** (2011) 179
2. M. A. Ali, M. A. Sayeed, N. Absar, *J. Chin. Chem. Soc.* **51** (2004) 647
3. P. L. R. Cunha, Í. G. P. Vieira, Â. M. C. Arriaga, R. C. M. De Paula, J. P. A. Feitosa, *Food Hydrocoll.* **23** (2009) 880
4. C. F. De Souza, N. Lucyszyn, F. A. Ferraz, M. R. Sierakowski, *Carbohydr. Polym.* **82** (2010) 641
5. C. W. Vendruscolo, C. Ferrero, E. A. G. Pineda, J. L. M. Silveira, R. A. Freitas, M. R. Jiménez-Castellanos, T. M. B. Bresolin, *Carbohydr. Polym.* **76** (2009) 86
6. V. Singh, S. Tiwari, A. K. Sharma, R. Sanghi, *J. Colloid Interface Sci.* **316** (2007) 224.